



HAL
open science

Measurement of the cosmic lepton and electron fluxes with the AMS detector on board of the International Space Station. Monitoring of the energy measurement in the calorimeter

Li Tao

► **To cite this version:**

Li Tao. Measurement of the cosmic lepton and electron fluxes with the AMS detector on board of the International Space Station. Monitoring of the energy measurement in the calorimeter. Other [cond-mat.other]. Université Grenoble Alpes, 2015. English. NNT : 2015GREAY016 . tel-01178917

HAL Id: tel-01178917

<https://theses.hal.science/tel-01178917>

Submitted on 21 Jul 2015

HAL is a multi-disciplinary open access archive for the deposit and dissemination of scientific research documents, whether they are published or not. The documents may come from teaching and research institutions in France or abroad, or from public or private research centers.

L'archive ouverte pluridisciplinaire **HAL**, est destinée au dépôt et à la diffusion de documents scientifiques de niveau recherche, publiés ou non, émanant des établissements d'enseignement et de recherche français ou étrangers, des laboratoires publics ou privés.

THÈSE

Pour obtenir le grade de

DOCTEUR DE L'UNIVERSITÉ GRENOBLE ALPES

Spécialité : **Physique Subatomique et Astroparticules**

Arrêté ministériel : 7 août 2006

Présentée par

Li TAO

Thèse dirigée par **Corinne GOY**

préparée au sein du **Laboratoire d'Annecy-le-Vieux de
Physique des Particules**
dans l'**École Doctorale de Physique de Grenoble**

Measurement of cosmic lepton and electron fluxes with the AMS detector on board the International Space Station. Monitoring of the energy measurement in the calorimeter

Thèse soutenue publiquement le **6 juillet 2015**,
devant le jury composé de :

Jean-Pierre LEES

Directeur de recherche, LAPP, Président

Isabelle LHENRY-YVON

Directeur de recherche, IPNO, Rapporteur

Eric NUSS

Maître de conférences, LUPM, Rapporteur

Fernando BARAO

Professeur, LIP - Lisbonne, Examineur

Pascal COYLE

Directeur de recherche, CPPM, Examineur

Corinne GOY

Directeur de recherche, LAPP, Directeur de thèse



© 2015

LI TAO

ALL RIGHTS RESERVED

Acknowledgments

I would like to begin by thanking my Ph.D. advisor, Corinne Goy, whose broad perspective and experience in particle physics and astrophysics have greatly helped and inspired me at various stages of my researches in the past three years. I am also grateful for her careful reading and valuable suggestions of this thesis. I would like to thank Sylvie Rosier for her valuable and constructive guidance during my Ph.D. period as well as my internship of M2.

I want to acknowledge the jury members: Isabelle Lhenry-Yvon, Eric Nuss and Paschal Coyle for their careful proofreading and sharing of their unique perspectives; Fernando Barao with whom I worked closely and benefited from a lot on the studies of triggers and the original calibration method using geomagnetic cutoff; Jean-Pierre Lees for presiding my defense and offering me help in administrative affairs.

I am grateful to all the people who worked with me in the past years. I want to thank Vincent Poireau for his introduction to RooFit and solutions to uncertainty estimation. I thank Jean-Pierre Vialle and Guy Coignet for their valuable and crucial suggestions through all my analyses. I thank Pierre Salati for his passionate teaching and instructive ideas on theoretical analysis. I also give my thanks to my young colleagues, Manuela Vecchi, Antje Putze, Sami Caroff, Jie Feng, Mathieu Boudaud and Yoann Genolini, who have worked with me and lunched with me. I would like to thank Armand Fiasson and Laurent Basara for their helping me start my analysis on leptons and minimum ionizing protons.

I also want to thank the administration team at LAPP, Myriam who helped every year to ob-

tain my residence card and Chantal for my registration. I thank Natalie and Brigitte for their arranging of all my missions. I thank Nicole for being there when I need help in the library. And I owe my thanks to all my other friends at LAPP, together we have shared interesting discussions at coffee time.

This thesis would not be possible without the contributions from past and present AMS collaboration members. I thank all AMS members for their work.

In the end, I thank my parents and all my friends for their unconditional love and support during all these years.

Abstract

The Alpha Magnetic Spectrometer (AMS) is a particle detector installed on the International Space Station; it has been recording data since May 2011. The experiment aims at identifying the nature of charged cosmic rays and photons and measuring their fluxes in the energy range of GeV to TeV. These measurements allow to refine the cosmic ray propagation models, to perform indirect research of dark matter and to search for primordial antimatter ($\bar{H}e$). In this context, the data of the first years have been utilized to measure the electron flux and lepton flux (electron + positron) in the energy range of 1 GeV to 700 GeV. Identification of electrons requires an electron-proton separation power of the order of 10^4 , which is obtained by combining the information from different sub-detectors of AMS, in particular the electromagnetic calorimeter (ECAL), the tracker and the transition radiation detector (TRD). In this analysis, the numbers of electrons and leptons are estimated by fitting the distribution of ECAL estimator and are verified using TRD estimator: 11 million leptons are selected and analyzed. The systematic uncertainties are determined by changing the selection cuts and the fit procedure. The geometric acceptance of the detector and the selection efficiency are estimated using simulated data. The difference from observations on data control samples allows to correct the simulation. The systematic uncertainty associated to this correction is estimated by varying the control samples. In total, at 100 GeV (resp. 700 GeV), the statistic uncertainty of the lepton flux is 2% (30%) and the systematic uncertainty is 3% (40%).

As the fluxes generally follow a power law as a function of energy, it is important to control the

energy calibration. We have controlled in-situ the energy measurement in the ECAL by comparing the electrons from flight data and from test beams, using in particular the E/p variable, where p is momentum measured by the tracker. A second method of absolute calibration at low energy, independent from the tracker, is developed based on the geomagnetic cutoff effect. Two models of geomagnetic cutoff prediction, the Störmer approximation and the IGRF model, have been tested and compared. These two methods allow to control the energy calibration to a precision of 2% and to verify the stability of the ECAL performance over time.

Contents

1	Introduction	1
1.1	Cosmic rays	1
1.1.1	Cosmic ray composition	2
1.1.2	Cosmic ray electrons and positrons	3
1.1.2.1	Energy loss mechanisms	4
1.1.2.2	Diffusion-loss equation	8
1.2	Dark matter	8
1.2.1	Nature of dark matter	9
1.2.2	Detection of dark matter	10
1.2.3	DM analysis with cosmic ray positron fraction	11
1.3	Astroparticle detection	13
1.3.1	Challenges	14
1.3.2	Local environment for near-Earth detection	15
1.3.2.1	Solar modulation	15
1.3.2.2	Geomagnetic field	16
1.3.2.3	Geomagnetic cutoff rigidity (R_{cut})	19
1.4	Conclusion	22
2	AMS Experiment and Lepton Identification	23
2.1	AMS sub-detectors	24

2.1.1	Transition radiation detector (TRD)	24
2.1.2	Time of flight (TOF)	28
2.1.3	Silicon tracker and magnetic field	29
2.1.4	Ring imaging Cherenkov detector (RICH)	30
2.1.5	Electromagnetic calorimeter (ECAL)	31
2.1.5.1	Energy reconstruction	33
2.1.5.2	Lepton-proton separation with ESE_{V3}	36
2.1.6	Anti-coincidence counter	37
2.2	Lepton identification summary	39
2.2.1	E/P variable	40
2.2.2	TRD_{LER} and ESE_{V3}	41
2.3	AMS data acquisition and organization	43
2.3.1	AMS trigger system	43
2.3.2	AMS data flow	44
2.3.3	AMS datasets	46
3	Control of the energy measurement	49
3.1	Energy scale with test beam data	49
3.1.1	Distributions of E_{rec}/E_{beam}	50
3.1.2	Energy dependence of E_{rec}/E_{beam}	50
3.1.3	E_{rec}/E_{beam} for different angles	52
3.2	E/P control with test beam and ISS data	54
3.2.1	Distribution of E/P	54
3.2.2	Energy dependence of E/P with ISS data	57
3.2.3	Comparison of E/P peak position between test beam and ISS data	58
3.2.4	Time dependence of E/P with ISS data	58
3.3	Energy control at low energy with R_{cut}	60
3.3.1	Störmer cutoff rigidity map	61
3.3.2	Geomagnetic cutoff rigidity measurement	61
3.3.3	Comparison of measured and predicted R_{cut}	66
3.3.4	Energy control with R_{cut} obtained from IGRF model	66
3.3.5	Time variation of measurement/prediction with IGRF model	68
3.3.6	Conclusions on energy scale with R_{cut}	69

3.4	Energy reconstruction in simulation	70
3.4.1	$E_{\text{rec}}/E_{\text{true}}$	71
3.4.2	E/P control	72
3.5	Conclusions on the ECAL energy measurement	73
4	Lepton and Electron Counting	75
4.1	Event preselection	76
4.2	Lepton selection	78
4.3	Proton and electron templates for ESE_{V3}	84
4.3.1	Templates at low energy: below 15 GeV	85
4.3.2	Templates at intermediate energy range: 15 - 200 GeV	86
4.3.3	Templates at high energy: above 200 GeV	88
4.3.4	Summary of the template building	89
4.4	Lepton and electron numbers counting	90
4.5	Lepton and electron numbers	92
4.6	Cross check using TRD_{LER}	94
4.6.1	TRD_{LER} cut efficiency	94
4.6.2	ESE_{V3} cut efficiency	96
4.6.3	Comparison of results from ESE_{V3} and from TRD_{LER}	97
4.7	Systematic uncertainties	98
4.7.1	Template uncertainties	98
4.7.2	Different TRD_{LER} cuts	100
5	Electron Flux Measurement	103
5.1	Exposure time	104
5.1.1	Systematic uncertainty due to geomagnetic cutoff	105
5.2	Physics Trigger Efficiency	105
5.2.1	Physics trigger efficiency for electrons	106
5.2.2	Systematic uncertainty of the trigger efficiency using the electron trigger	107
5.2.3	TOF and ECAL triggers yearly monitoring	110
5.3	Acceptance and selection efficiency	111
5.3.1	MC reweighting	111
5.3.2	Estimation of the acceptance with MC events	112
5.3.3	Data-driven correction on the acceptance	112

5.3.3.1	Control of the preselection efficiency	113
5.3.3.2	Selection efficiency estimated with ISS electrons	116
5.3.3.3	Selection efficiency estimated with MC electrons	117
5.3.3.4	Data-MC efficiency correction	120
5.3.3.5	Systematic uncertainty of the data-MC efficiency correction . .	121
5.3.4	Study of the impact of MC reweighting	124
5.4	Charge confusion for electrons	125
5.4.1	Impact of track pattern on charge confusion	126
5.4.2	Charge confusion correction of electron number	127
5.4.3	Systematic uncertainty of the charge confusion correction	128
5.5	Summary of uncertainties in flux measurement	129
5.6	Results of the flux measurement	132
5.7	Consistency check of unfolding	136
5.7.1	Mathematical formulation	137
5.7.2	Unfolding result	137
6	Conclusion and outlook	141
A	Solar Energetic Particles events during AMS flight	143
	Bibliography	145

Chapter 1

Introduction

More than a century after the discovery of cosmic rays by Hess in 1912, several questions are still unanswered, such as

- the origin of cosmic rays and their composition
- the nature of dark matter, which is revealed through observation of gravitational effects
- search for anti-nuclei, like $\bar{H}e$, \bar{C}

To better understand these questions, many astrophysical experiments are carried out, including AMS. Among all the cosmic ray species, electrons and positrons arise a particular interest, because they may reveal characteristics of their primary sources and of features of our local environment.

1.1 Cosmic rays

The cosmic ray story began about 1900 when it was discovered that electroscopes discharged even if they were kept in the dark well away from sources of natural radioactivity. The big

breakthrough came in 1912 and 1913 when first Hess and then Kolhörster made manned balloon ascents in which they measured the ionization of the atmosphere increasing with altitude. This was clear evidence that the source of the ionizing radiation must be located above the Earth's atmosphere [2], which is now known as cosmic radiation.

In the 1930s, air showers initiated by charged cosmic ray particles were observed extending over dimensions greater than 100 meters on the ground and contained millions of ionizing particles. It is inferred that the particles responsible for initiating the showers must have had energies exceeding 10^{15} eV at the top of the atmosphere. Detection and discovery of the cosmic rays continued since then.

Figure 1.1 provides an overview of the complete cosmic ray spectrum. A very wide range of energies is observed and the spectrum can be described by power-law distributions over many decades in energy. Cosmic rays in the lower energy range (below 10^{15} eV) are mainly detected by particle detectors in space observatories and at the higher energies, cosmic ray air-shower technique is used.

1.1.1 Cosmic ray composition

About 98% of the cosmic-ray particles are protons and nuclei while about 2% are electrons. Of the protons and nuclei, about 87% are protons, 12% are helium nuclei and the remaining 1% are heavier nuclei [2]. Figure 1.2 shows the energy spectra of cosmic ray nuclei species. Energy spectra of the major nuclei species in comparison with electrons, positrons and antiprotons are shown in Figure 1.3.

Two categories of cosmic rays are defined according to their creation mechanism. Particles such as H, He, C, O and electrons are known as primary species, defined as those accelerated in the astrophysical sources. Other particles such as Li, Be, B, positrons and antiprotons are known as secondary species, which are primarily created in nuclear collisions, also known as spallation, of the primary species with the nuclei of atoms and molecules of the interstellar gas. The observed composition of the cosmic rays is similar to the abundances of the elements in the Sun with exceptions for the secondary species, which can be attributed to spallation. [2]

The energy spectra of cosmic ray electrons and electrons+positrons have been determined both from high flying balloon experiments and from satellites. Figure 1.4 and Figure 1.5 show the fluxes measured by earlier experiments, which follow a power-law distribution. Below 10 GeV, the observations are influenced by the effects of solar modulation, which is discussed in

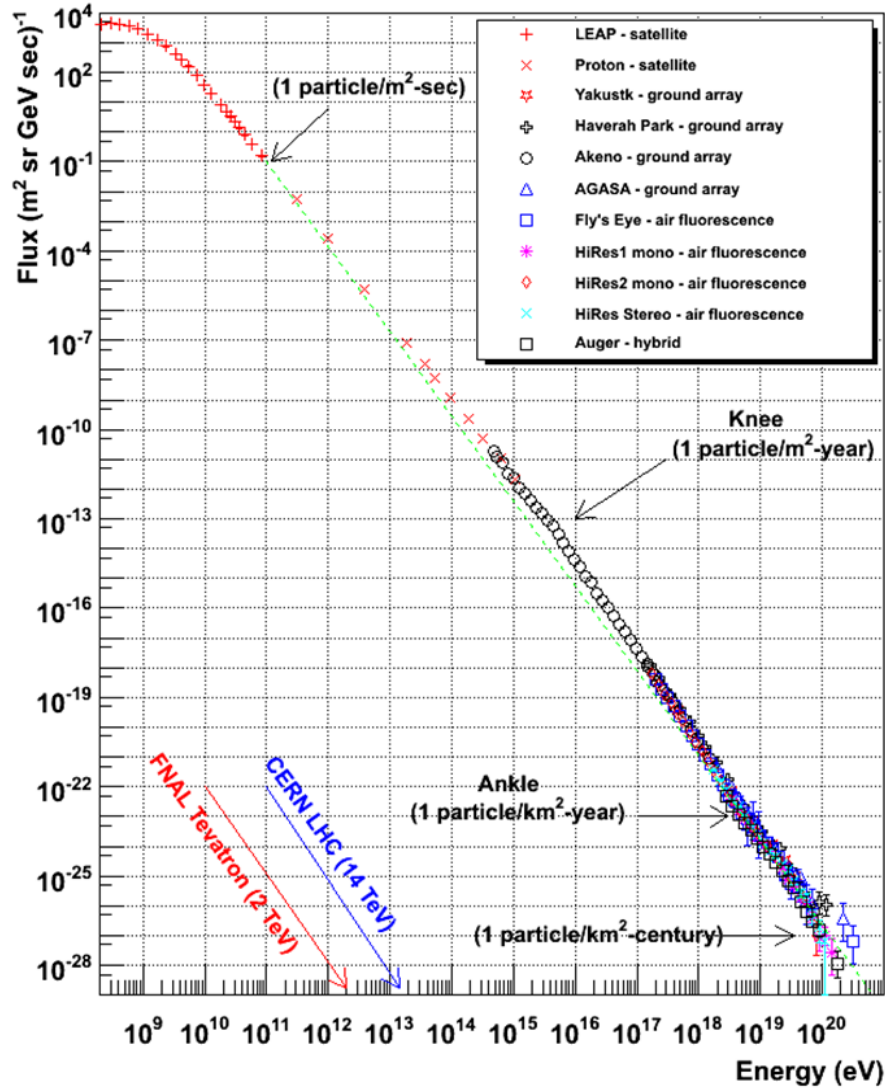


Figure 1.1: The overall differential energy spectra of cosmic rays from various experiments. Prominent features in the spectrum are indicated - the *knee* at 10^{15} eV and the *ankle* at 10^{18} eV. The frequencies of arrival of particles of different energies are indicated, as well as the energies attainable in various accelerator experiments [2].

Section 1.3.2.1.

1.1.2 Cosmic ray electrons and positrons

Though electrons constitute only 1% of cosmic ray particles, they are important to astrophysical studies because of their unique properties. TeV electrons accelerated in the sources at distances larger than ~ 1 kpc, or ages greater than a few 10^5 yr cannot reach the solar system. Therefore, they can only be signatures of some nearby sources. This suggests that the features in the electron spectrum provide an ideal probe to help clarifying the origins of cosmic rays and their

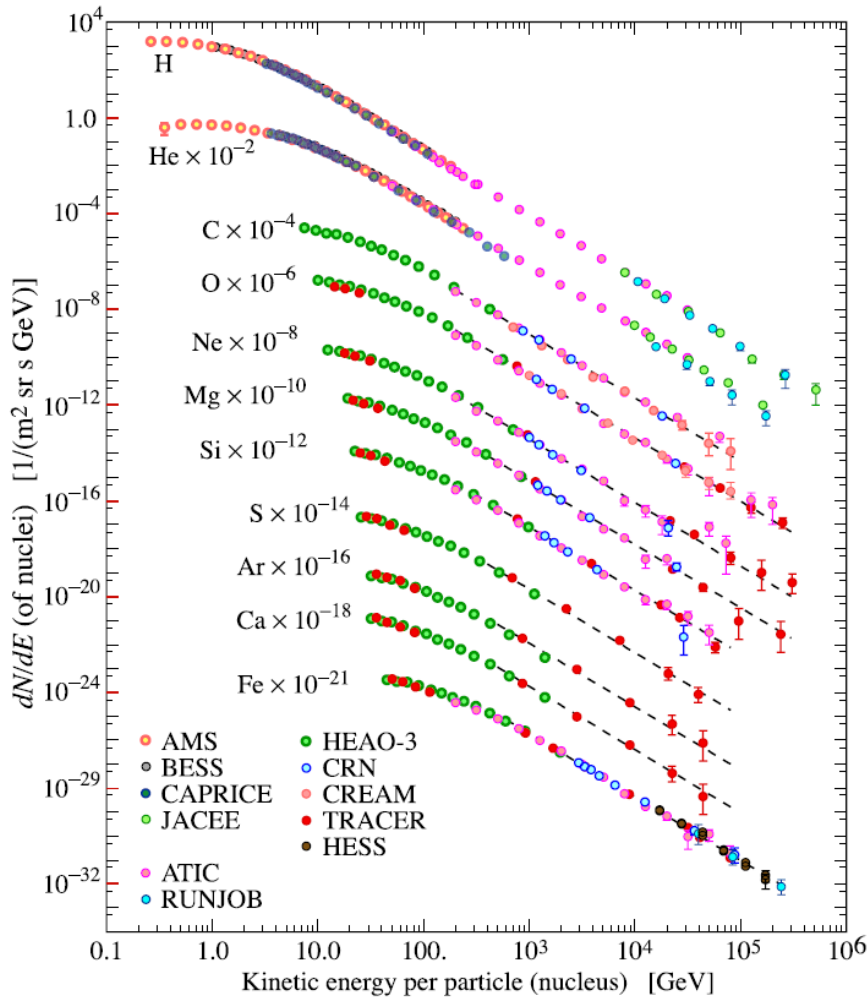


Figure 1.2: The differential energy spectra of different cosmic ray species as a function of kinetic energy. The scaling factors used to display the spectra of the different elements are shown on the diagram [3].

propagation mechanisms in the Galaxy. For example in Figure 1.5, the bump of $(e^+ + e^-)$ flux at ~ 450 GeV observed by ATIC might be indication of unknown sources.

Two possible sources of cosmic ray electrons are identified. One is primary sources, such as supernova remnants. The other is decay product resulting from nuclear interactions of nuclei with the interstellar medium (ISM) [5]. Positrons were thought to be only secondary particles, until later experiments show that above 10 GeV, the positron fraction increases with energy, which cannot be explained by a pure secondary production.

1.1.2.1 Energy loss mechanisms

High energy electrons observed at the top of the atmosphere are a representative sample of those present throughout the ISM. However, the observed spectra are distorted with respect

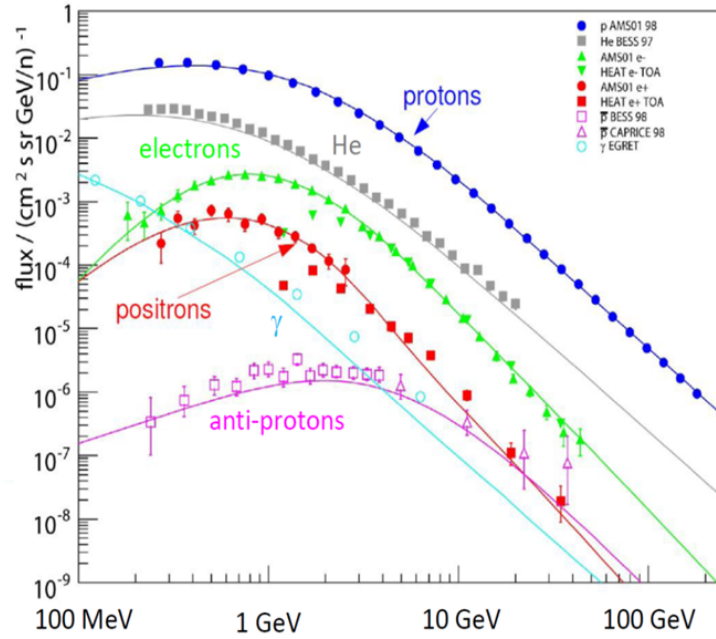


Figure 1.3: Fluxes of protons measured by AMS-01 (blue), helium by HESS 97 (grey), electrons by AMS-01 and HEAT (green), positrons by AMS-01 and HEAT (red), photons by EGRET (cyan) and antiprotons by BESS and CAPRICE (magenta). [4]

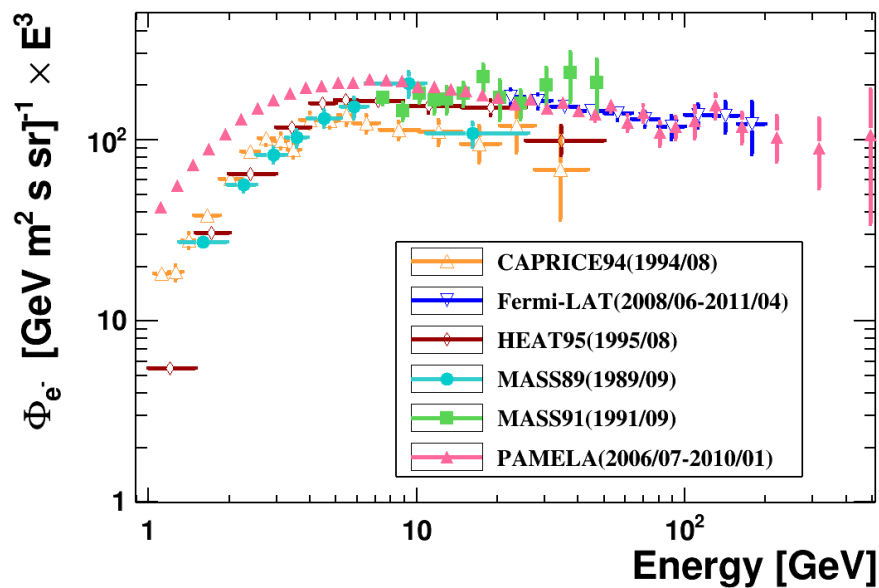


Figure 1.4: Electron flux plotted as $\Phi \times E^3$, measured by earlier experiments CAPRICE, Fermi-LAT, HEAT, MASS, and PAMELA (*Database of Charged Cosmic Rays*: <http://lpsc.in2p3.fr/cosmic-rays-db/>).

to their injection spectra, by a number of energy loss processes as electrons propagate through the ISM from their sources. The loss mechanisms involve radiation, interactions with magnetic fields and matter.

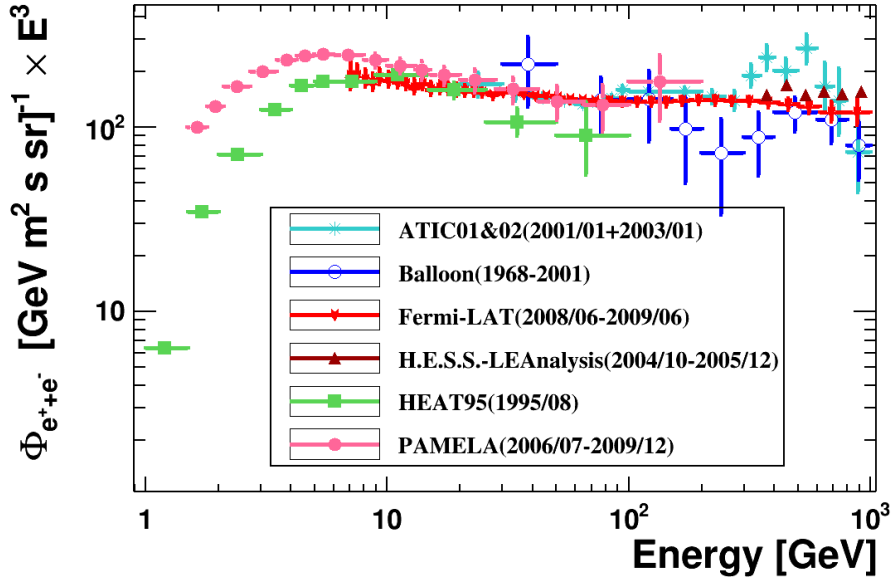


Figure 1.5: Positron+electron flux plotted as $\Phi \times E^3$, measured by earlier experiments ATIC, Balloon, Fermi-LAT, HESS, HEAT, and PAMELA (*Database of Charged Cosmic Rays*: <http://lpsc.in2p3.fr/cosmic-rays-db/>).

Synchrotron radiation, dominant channel of energy loss for high energy electrons, is the emission of high energy photons by electrons gyrating in a magnetic field. The energy loss rate by synchrotron radiation is proportional to E^2 with E the energy of electron, given by [2]

$$\frac{dE}{dt} = -\frac{4}{3} \frac{\sigma_T c}{(m_e c^2)^2} U_{mag} E^2 \quad (1.1)$$

where σ_T is the Thompson cross section, $U_{mag} = B^2/2\mu_0$ is the energy density of the magnetic field.

Inverse Compton scattering, another dominant channel of energy loss, is the process in which electrons scatter low energy photons to high energies. The energy loss rate by inverse Compton scattering in a radiation field of energy density U_{rad} is also proportional to E^2 , given by [2]

$$\frac{dE}{dt} = -\frac{4}{3} \frac{\sigma_T c}{(m_e c^2)^2} U_{rad} E^2 \quad (1.2)$$

The average energy density U_{rad} is about $6 \times 10^5 \text{ eV} \cdot \text{m}^{-3}$.

Ionization of cosmic ray electrons is the process by which satellite electrons are torn off of ISM atoms by the electrostatic forces. The energy loss rate of cosmic electrons by ionization [2]

is given by

$$\frac{dE}{dt} = 7.64 \times 10^{-15} n (3 \ln \gamma + 19.8) \quad [eV \cdot s^{-1}] \quad (1.3)$$

where n is the number density of hydrogen atoms in *particles/m³*, typically $\sim 10^6 m^{-3}$, γ is the Lorentz factor of the cosmic ray electron.

Bremsstrahlung is electromagnetic radiation produced by the deceleration of electrons when deflected by an atomic nucleus. The energy loss rate by Bremsstrahlung is proportional to E , given by [2]

$$\frac{dE}{dt} = -4nZ^2r_e^2\alpha c\bar{g}E \quad (1.4)$$

where Z is the charge of the nucleus, r_e is the electron radius, α is the fine structure constant and \bar{g} is a Gaunt factor dependent on the state of the nuclei.

Adiabatic losses take place if the electrons are confined within an expanding volume, doing work which reduces the internal energy of the gas. The loss rate is proportional to E and dependent on the dynamics of the expansion. In the case of a uniformly expanding sphere with an outer radius R , it is given by [2]

$$\frac{dE}{dt} = -\left(\frac{1}{R} \frac{dR}{dt}\right)E \quad (1.5)$$

To conclude the ionization loss varies as a function of $\ln(E)$, which dominates at low energy; Bremsstrahlung and adiabatic losses are proportional to E ; synchrotron radiation and inverse Compton scattering losses are proportional to E^2 , which dominate at high energy. The total energy loss rate of electrons, $b(E)$, can be summed up as

$$b(E) = -\left(\frac{dE}{dt}\right) = \underbrace{A_1 \left(\ln \frac{E}{m_e c^2} + 19.8\right)}_{\text{Ionization}} + \underbrace{A_2 E}_{\text{Br. \& Ad.}} + \underbrace{A_3 E^2}_{\text{Sync. \& IC}} \quad (1.6)$$

At high energy, the last term $A_3 E^2$ dominates the energy loss. Therefore, Equation (1.6) becomes $b(E) = A_3 E^2$, which can be solved with the initial condition $E(0) = E_0$,

$$E(t) = \frac{E_0}{1 + A_3 E_0 t} \quad (1.7)$$

It can be seen that $E(t) \rightarrow \infty$ as $t \rightarrow -1/(A_3 E_0)$. Therefore, for an electron observed with energy E_0 , it cannot be older than

$$T_{max}(E_0) = 1/(A_3 E_0) \quad (1.8)$$

For an electron of $E_0 = 1$ TeV, $T_{max} \sim 2.10^5$ years, which is much shorter than the lifetime of protons in the Galaxy ($\sim 10^7$ years) [6].

1.1.2.2 Diffusion-loss equation

The transport of cosmic ray electrons can be modeled as a diffusion process, described by [2]

$$\frac{dN(E)}{dt} = D\nabla^2 N(E) + \frac{\partial}{\partial E}[b(E)N(E)] + Q(E) \quad (1.9)$$

where $N(E)$ is the gradient of particle density, D is a scalar diffusion coefficient, $b(E)$ is the energy loss rate described above, and $Q(E)$ is the injection rate per unit volume. The equation can be simplified by neglecting diffusion and assuming that the spectrum does not vary with time. For a given injection spectrum $Q(E) = \kappa E^{-p}$, Equation (1.9) turns into:

$$\frac{d}{dE}[b(E)N(E)] = -Q(E) \quad \Rightarrow \quad N(E) = \frac{\kappa E^{-p+1}}{(p-1)b(E)} \quad (1.10)$$

At high energy (above 10 GeV) where $b(E) \propto E^2$, $N(E)$ is proportional to E^{-p-1} . The spectrum is steeper than the injection spectrum by one power of E .

In the diffusion approximation, the mean distance which could be passed by high energy electrons during their lifetime is determined by $r_{max} \sim \sqrt{2DT_{max}}$, with D the diffusion coefficient of the form $D_0(E/GeV)^\delta$, where δ and D_0 are confined diffusion parameters. It can be derived that $r_{max}(1TeV, \delta = 0.6) \sim 1.5$ kpc [6]. Therefore, electrons with 1 TeV cannot come from sources farther than 1.5 kpc. They must originate from nearby sources.

1.2 Dark matter

The present understanding of the known universe indicate that only 5% of the known universe is composed of luminous matter and the rest remains “dark”. The “dark” matter was revealed

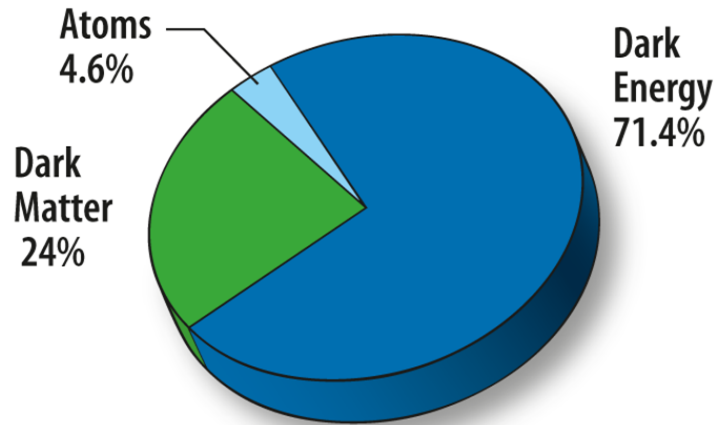


Figure 1.6: Breakdown of the total energy density in the universe [7].

only be its gravitational effects. To understand the nature of dark matter (DM), intensive experimental searches are carried out.

1.2.1 Nature of dark matter

In 1930s, Fritz Zwicky and others inferred the presence of dark matter while studying clusters of galaxies. The calculated gravitational mass of the galaxies are much greater than expected from their luminosity. Since then, the hypothesis of dark matter builds up gradually with more

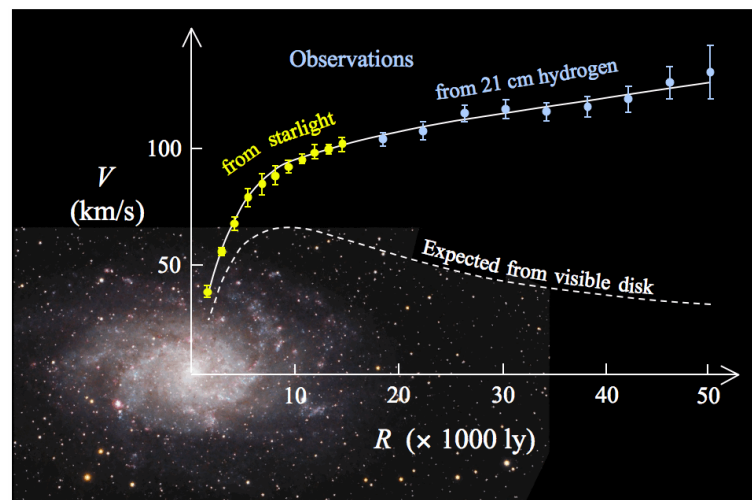


Figure 1.7: Rotation curve of the typical spiral galaxy M33 (yellow and blue points). Discrepancy between the two curves (white line) is accounted for by adding a dark matter halo surrounding the galaxy. [8]

developed theoretical models and observations.

Early theories of dark matter concentrate on massive compact halo objects or MACHOs, such

as black holes and brown dwarfs. But evidence from surveys like MACHO, EROS and others indicated that such “dark” baryonic matter constitute only a small portion. Furthermore, evidence indicated that the dark matter does not interact with the electromagnetic force. Consequently, it is commonly accepted that dark matter is primarily non-baryonic, made of one or more elementary particles other than the usual ones.

Leading candidates for dark matter are weakly interacting massive particles, or WIMPs, which interact only through gravity and weak force with an annihilation cross section close to $3 \times 10^{-26} \text{cm}^3 \text{s}^{-1}$. WIMPs are non-baryonic matter, which come from speculations that since the universe was very dense and hot in the early moments following the Big Bang, the dark matter may be made of particles produced shortly after the Big Bang. One of the primary motivations for building “supercolliders” is to try to produce this new particle in the laboratory.

1.2.2 Detection of dark matter

The search for WIMP dark matter detection is carried out by three different and complementary methods: direct detection, detection at colliders and indirect detection [9].

Direct detection relies on the fact that DM particles should be omnipresent in the universe, typically moving with normal galactic velocities of ~ 200 km/s: the principle is to detect the scattering of DM on atoms of large mass detector. The experiments are usually in deep underground laboratories to reduce the background from cosmic rays. Two technologies are often adopted:

- Cryogenic detectors: Operating at temperatures below 100 mK, they detect the heat produced when a particle hits an atom in a crystal absorber such as germanium. Applied in experiments including CDMS, CRESST, EDELWEISS, EURECA.
- Noble liquid detectors: detect the flash of scintillation light produced by a particle collision in liquid xenon or argon. Applied in experiments including XENON, DEAP, ArDM, WARP, DarkSide, PandaX and LUX.

Detection at accelerators: The idea is to produce WIMPs in collision of energetic particles in the laboratory. Because a WIMP has negligible interactions with matter, it may be detected

indirectly as missing energy or missing transverse momentum. Figure 1.8 shows the limits from the LHC compared with those of other direct detection experiments on the WIMP-nucleon cross section as a function of the WIMP mass. The two approaches are complementary especially at

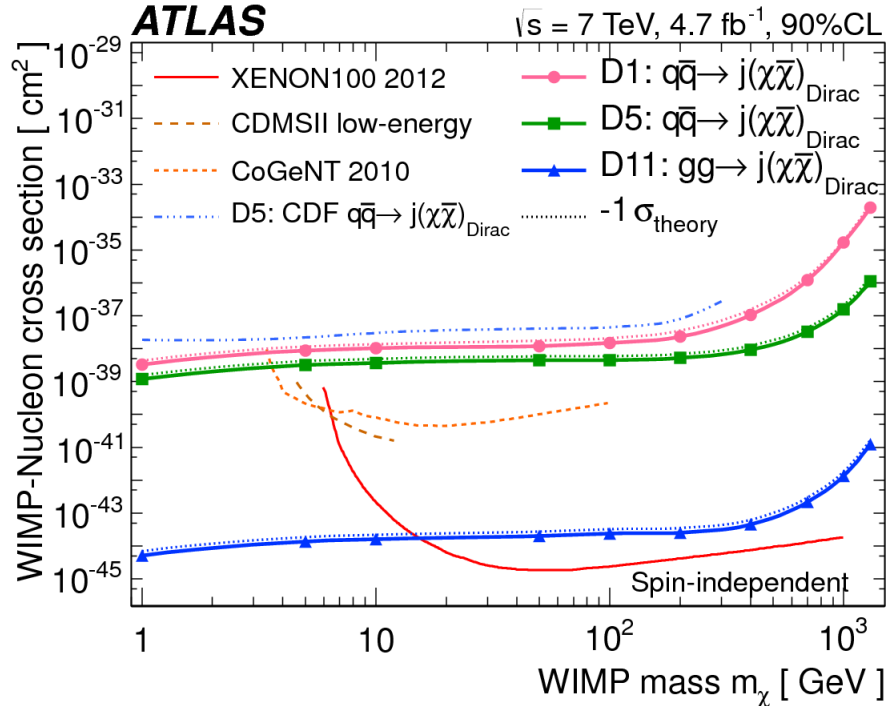


Figure 1.8: ATLAS limits on WIMP-nucleon scattering. Cross sections are shown versus WIMP mass m_χ . For comparison, 90% CL limits from the XENON100, CDMSII, CoGeNT, CDF, and CMS experiments are shown. [10]

low mass.

Indirect detection searches for the products of dark matter annihilation from regions of high dark matter density like the galactic center, dwarf spheroidal galaxies, galaxy clusters. Knowing the halo density distribution, one can estimate the probability for DM particle annihilation into final states containing detectable Standard Model particles, such as γ , $e^+ + e^-$, $\bar{p} + p$. These processes could be detected preferably through an excess of antiprotons or positrons, as they are suppressed in cosmic rays due to the baryon asymmetry of the universe.

1.2.3 DM analysis with cosmic ray positron fraction

As previously mentioned, evidence of DM can be detected indirectly through the excess of positrons, which is developed here. Full details can be found in [11].

The cosmic ray positron flux at the Earth exhibits above 10 GeV an excess with respect to the astrophysical background produced by the interactions of high energy protons and helium nuclei with the ISM. The excess is also present in the positron fraction, which is defined as $\Phi_{e^+}/(\Phi_{e^+} + \Phi_{e^-})$. Figure 1.9 shows that the observed excess steadily increases with energy.

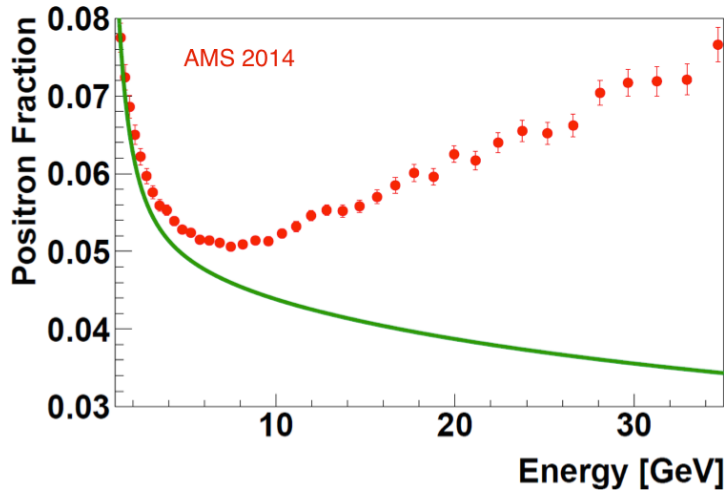


Figure 1.9: Result of positron fraction measured by AMS experiment (red dots) in contrast to the prediction of secondary positrons only (green line). [12]

To explain the excess, different DM annihilation channels are explored. By taking into account the WIMP annihilation cross section and mass, and the branching ratios for each channel, one example of best fit results is shown in Figure 1.10. The model fit and the measurement are in good agreement. However, the needed cross section is $1.05 \times 10^{-23} \text{cm}^3 \text{s}^{-1}$, which is larger than the cross-section required to explain the relic density.

An alternative explanation for the positron excess is the pulsar hypothesis. Pulsars are highly magnetized, rotating neutron star that emit a beam of electromagnetic radiation. The emitted positron spectrum at the source can be parametrized by a power law as a function of energy. An example of best fit to data using combination of three pulsars is shown in Figure 1.11. The fit reproduces well the experimental data, though it does not reach the highest energy data points.

In future, only more precise measurements of e^+ and e^- at higher energies can help to conclude on the positron excess. However, measurements of other channels, such as \bar{p} and γ , also provide evidence to the indirect DM analysis.

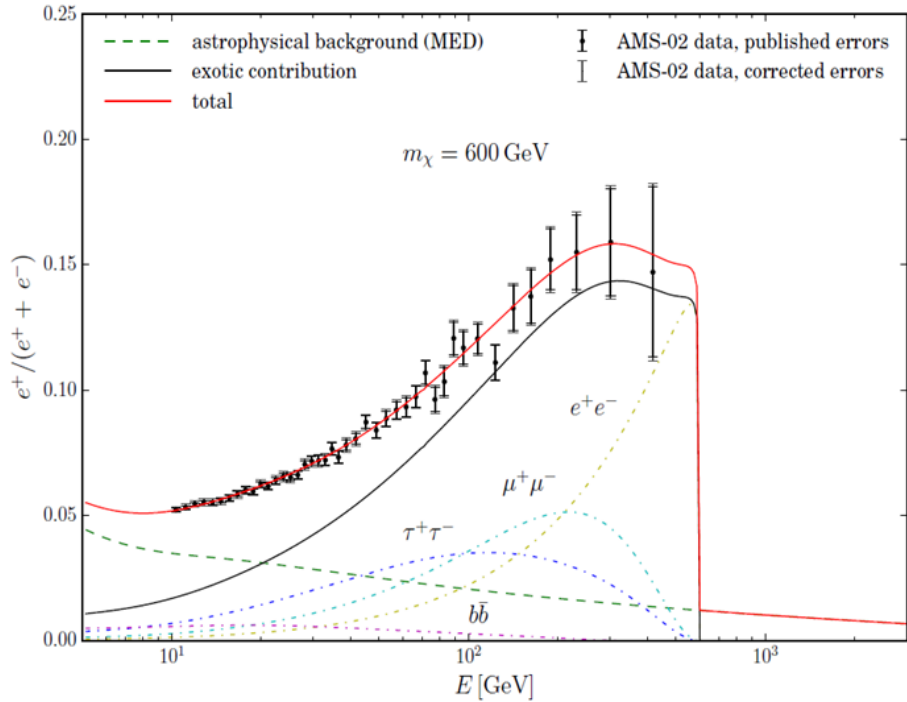


Figure 1.10: Positron fraction as a function of the positron energy, for a DM mass $m_\chi=600$ GeV, compared to AMS-02 data. The contribution of DM annihilation into lepton and $b\bar{b}$ channels is indicated. [11]

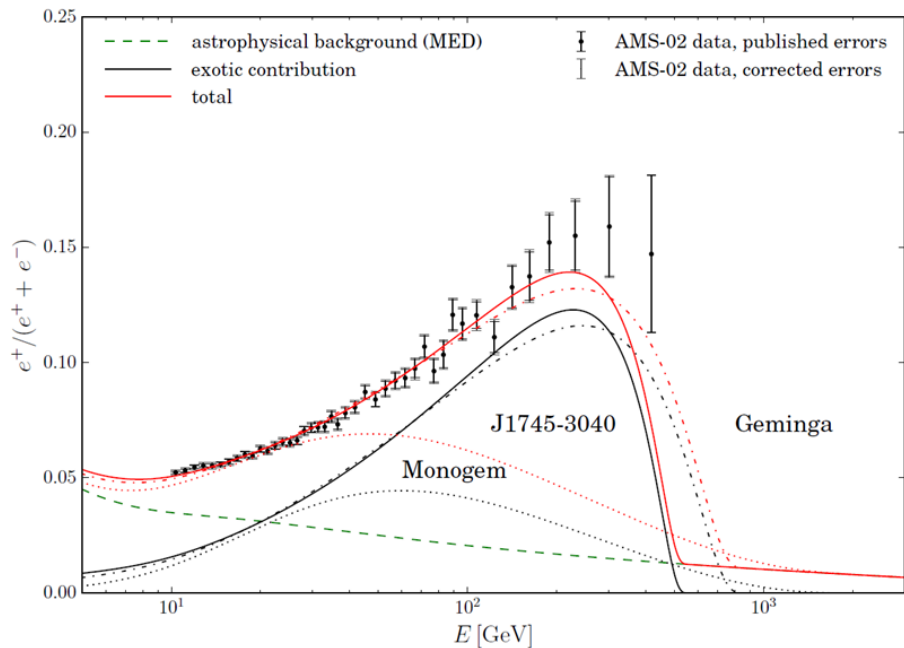


Figure 1.11: Positron fraction for the best fits for the pulsars J1735-3040 (solid line), Geminga (dashed-dotted line), and Monogem (dotted line). [11]

1.3 Astroparticle detection

From the measurement of ionization in the air at the Eiffel Tower to today's high precision space-based particle detectors, experimental astroparticle physics has undergone rapid development

since last century. Challenges of astroparticle detection lie in the requirements for precision and large energy range, especially for leptons.

1.3.1 Challenges

- **Statistical precision:** as we know, the cosmic ray fluxes follow power laws as a function of energy. Protons at 1 TV are $\sim 100^{2.7}$ times fewer than at 10 GV. To obtain enough statistics at high energy, large detector acceptance and long detection duration are required.
- **Energy/momentum reconstruction:** to measure cosmic-ray fluxes and to reveal the possible structures in them, the energy or momentum resolution of the detector must be less than 5% - 10%: this can only be achieved by placing particle detectors in space, such as Fermi, PAMELA, AMS, which have undergone beam tests and are free from air showers. Moreover, no traditional absolute calibration can be performed in space. Alternative methods and redundancy of energy/momentum measurements by different sub-systems are indispensable.
- **Particle identification:** protons constitute 90% of cosmic rays. For analysis of electrons and positrons, background rejection is one of the most important issues. Especially for positrons, which have the same charge as protons, they are 1000 times fewer than protons. Accurate identification of positrons requires proton rejection power greater than 10^5 .
- **Control of charge confusion:** charge confusion indicates the level at which the particle charge sign is mis-measured, which is of great importance for anti-matter detection. Usually, astroparticle detectors use curvature of particle trajectory in magnetic field to measure the charge sign. At high energy, where the curvature is small, it is difficult to correctly estimate charge sign. The control of charge confusion determines the detector's sensitivity to anti-matter research.

In the next chapter, we will describe precisely how the experiment of Alpha Magnetic Spectrometer (AMS) on board the International Space Station was designed to resolve the above difficulties. At an altitude of 400 km, AMS is immersed in the Earth's magnetic field and is sensitive to the influence of the Sun. These points are developed in the next section.

1.3.2 Local environment for near-Earth detection

Earth is the third planet in solar system, at a distance of 150 million kilometers from the Sun. Near-Earth observations of cosmic rays are possibly affected by the solar activities. Moreover, the shielding of the geomagnetic field also deviates the trajectory of charged particles and traps the low energy particles.

1.3.2.1 Solar modulation

Galactic cosmic rays (GCR) encounter a turbulent solar wind with an embedded heliospheric magnetic field (HMF) when entering the heliosphere. This leads to significant global and temporal variations in their intensity and in their energy as a function of position inside the heliosphere. This process is identified as the solar modulation of cosmic rays [13]. Fluxes of low energy particles decrease during periods of high solar activity and are at a maximum during phases of low solar activity. This is due to the fact that the greater the solar activity, the greater the disturbances in the interplanetary magnetic field which impede the propagation of particles with energies less than about 10 GeV/nucleon to the Earth [2].

The solar modulation of the cosmic ray flux $J(E)$ is usually approximated by

$$J(E) = J_{IS}(E + \Phi eZ) \frac{E^2 - M^2}{(E + \Phi eZ)^2 - M^2} \quad (1.11)$$

where J_{IS} is the inter-stellar flux outside the solar cavity, M is the mass of the particle, eZ is electric charge of particle and Φ is the solar modulation parameter [14]. The parameter Φ is dependent on time and has the same period as the solar activity cycle, which is about 11 years. It varies between 100 MV and 1000 MV [15].

Figure 1.12 shows the time dependence of cosmic nuclei energy spectra measured by Advanced Composition Explorer (ACE) in the energy range of 40 - 500 MeV/nucleon. Due to the reversal of the HMF during each period of extreme solar activity, another important cycle of 22 years, is also observed. Figure 1.13 illustrates observation of these two cycles.

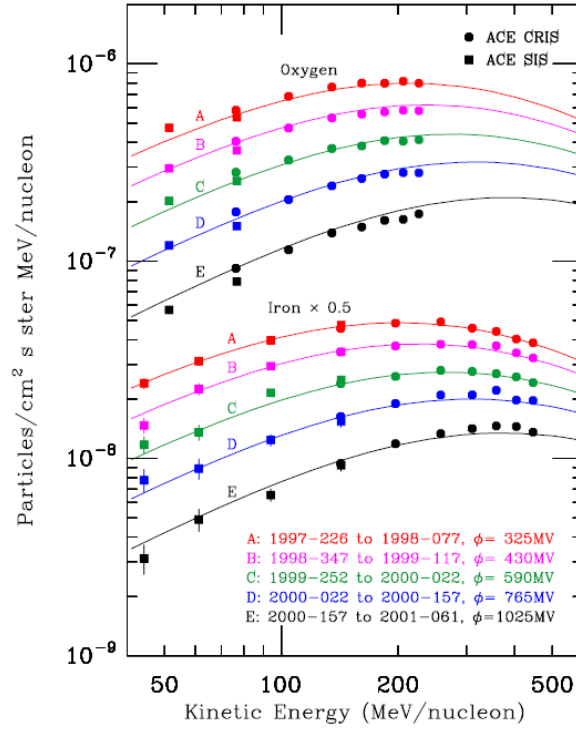


Figure 1.12: Oxygen and iron energy spectra measured by ACE during five time periods from August 1997 through February 2001, fitted using a GCR propagation model [16].

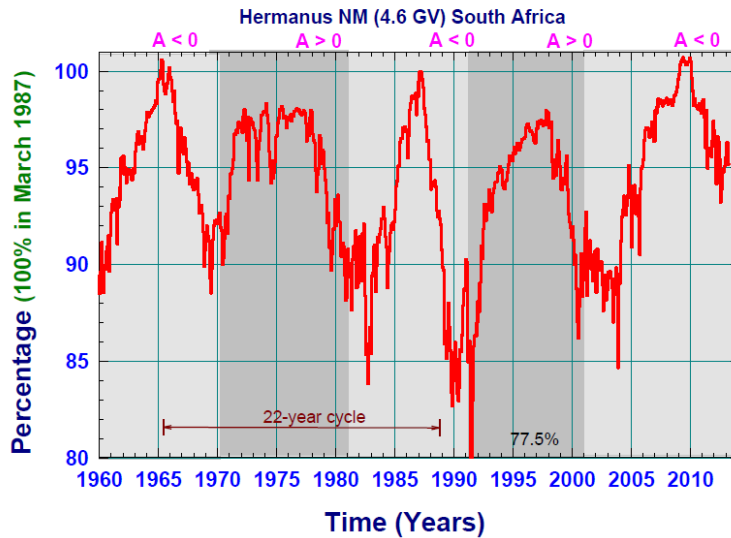


Figure 1.13: An illustration of the 11-year and 22-year cycles in the solar modulation of CRs as observed by the Hermanus NM in South Africa at a cut-off rigidity of 4.6 GV in terms of percentage with March 1987 at 100. A > 0 epochs signify the years when HMF is directed in the northern hemisphere; A < 0 when the HMF is directed in the southern hemisphere. [13]

1.3.2.2 Geomagnetic field

Around the Earth, the shielding of geomagnetic field protects us from the intrusion of charged particles of cosmic rays and solar wind. Presence of magnetic fields has been observed in the

Earth as well as other major planets, in the Sun and other active stars, and also in spiral galaxies like the Milky Way. The global magnetic fields are believed to be maintained by a rotating, convecting and electrically conducting fluid in the celestial body's core, which is called hydromagnetic dynamos [17]. The simulation of this mechanism is illustrated in Figure 1.14, where the magnetic field lines show the predominantly dipole field.

Because the geomagnetic field is constantly changing, continuous observations on the changes

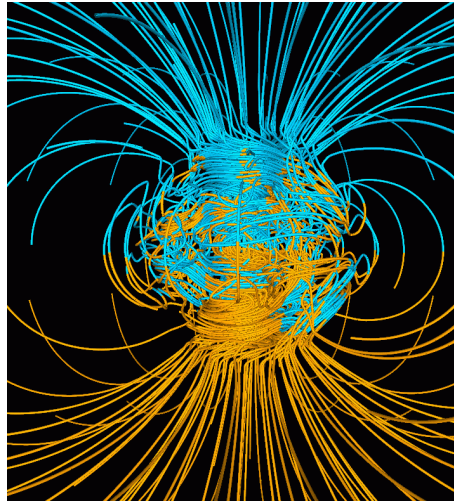


Figure 1.14: 3D magnetic field structure simulated with the Glatzmaier-Roberts geodynamo model. Magnetic field lines are blue where the field is directed inward and yellow where directed outward. The rotation axis of the model Earth is vertical and through the center. [18]

of the field are made over a period of years. Using this information, it is possible to create a mathematical representation of the Earth's main magnetic field. The dipole model and International Geomagnetic Reference Field (IGRF) are here presented as examples.

Dipole model

A simple approximation of the geomagnetic field is the dipole model supposing that a magnet dipole is positioned at the center of the earth and tilted with an angle of $\sim 10^\circ$ with respect to the rotational axis of the Earth. In spherical polar coordinates, the components of the geomagnetic field intensity B are

$$\begin{cases} B_r &= -2B_0\left(\frac{R_E}{r}\right)^3 \sin \lambda \\ B_\lambda &= B_0\left(\frac{R_E}{r}\right)^3 \cos \lambda \\ B_\phi &= 0 \end{cases} \quad (1.12)$$

where B_0 is the mean value of the field on the equator at the Earth's surface ($3.12 \times 10^{-5}\text{T}$), r is the radial distance, R_E is the earth radii (6370 km) and λ is the geomagnetic latitude. The

dipole field is symmetric about its axis so that B_ϕ is 0 everywhere [19].

The geomagnetic field lines are obtained using the Equation (1.12).

$$\frac{dr}{r d\lambda} = \frac{B_r}{B_\lambda} = -\frac{2 \sin \theta}{\cos \lambda} \Rightarrow r/R_E = L \times \cos^2 \lambda \quad (1.13)$$

where L, known as the McIlwain parameter, is the radial distance (in Earth radius unit) of a field line crossing the geomagnetic equator. The simulation results of the field lines are shown in Figure 1.15.

The International Space Station (ISS), which is situated at an altitude of ~ 400 km, traverses

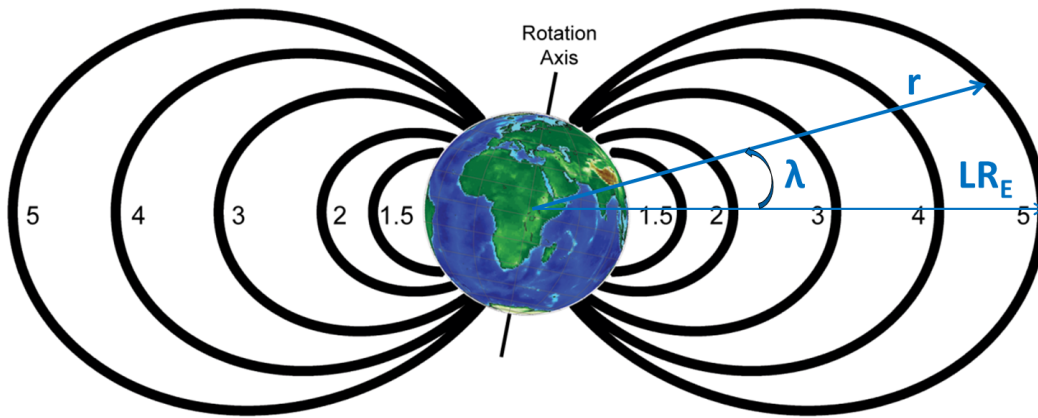


Figure 1.15: Geomagnetic field lines for L-shells 1.5, 2, 3, 4 and 5 using a dipole model [20].

the regions of L from 1.1 (near the Earth’s Equator) to 4.2 (near the polar regions). The dipole model is a good approximation for low L regions, $L < 3$. At higher L regions, more complex models are recommended for accurate estimation.

IGRF model

Multi-pole expansion is often utilized when a more precise model is required to describe the geomagnetic field. By solving the Maxwell’s equations and setting $B = -\nabla V$, the geomagnetic potential field is

$$V(r, \phi, \theta) = R_E \sum_{n=1}^{\infty} \left(\frac{R_E}{r}\right)^{n+1} \sum_{m=0}^n (g_n^m \cos m\phi + h_n^m \sin m\phi) P_n^m(\cos \theta) \quad (1.14)$$

where ϕ is east longitude, θ is colatitude, g_n^m and h_n^m are Gauss coefficients and P_n^m are the Schmidt normalized associated Legendre functions. In fact, the dipole approximation is the lowest order, but dominant term in Equation (1.14) with $n = 1, m = 0$.

The IGRF is a series of mathematical models of the geomagnetic field using the multi-pole

expansion potential at order 13. The Gauss coefficients are determined by best fits to survey data and are computed every five years by the International Association of Geomagnetism and Aeronomy (IAGA) [21].

However, the geomagnetic field cannot be accurately modeled due to the many variations. First, temporal variations occur about every 27 days when the active solar area of the Sun faces the Earth. Another type is the diurnal variations due to partial movement within the ionosphere, such as auroral and equatorial electro-jets. The last variation is the magnetic storm during solar flares [22].

Earth's magnetosphere

Magnetosphere is the area of space around the Earth that is controlled by the geomagnetic field, whose shape is the direct result of being blasted by the solar wind [23]. The external current systems in the magnetosphere are additional sources that affect the geomagnetic field. A number of magnetospheric models have been developed to add to the IGRF magnetic field model, such as Tsyganenko model.

In the inner region of the Earth's magnetosphere are located radiation belts of energetic charged particles, which are held by the geomagnetic field. The main belts extend from an altitude of about 1000 to 6000 kilometers above the Earth's surface. However, in a certain geographical area called South Atlantic Anomaly (SAA), the distance between the inner belt and the Earth's surface is merely 200 km. The flux of charged particles in this region is significantly increased, which leads to high-level exposure of aircrafts, such as the ISS.

1.3.2.3 Geomagnetic cutoff rigidity (R_{cut})

Within the magnetosphere, trajectories of charged particles are deviated from the Earth. The complex system of the magnetosphere provides shielding against the solar disturbances while redistributing the energy and mass throughout.

Low-energy charged particles cannot penetrate the magnetosphere or reach the Earth's surface. The minimum rigidity required for a charged particle to reach a specified region is called geomagnetic cutoff rigidity, denoted as R_{cut} . Determinations of R_{cut} were initially accomplished by Störmer in 1930s, through hand calculations of particle motion in a dipole field. With the development of digital computers, simulations of cosmic ray trajectories in the geomagnetic field became possible and the cutoff rigidity estimation has been greatly improved [24].

Geomagnetic cutoff observation with AMS

The geomagnetic cutoff phenomenon has been observed by many experiments in the flux measurements. Figure 1.16 shows proton spectra measured at different geomagnetic latitudes by AMS-01. The dependence of the cutoff rigidity with latitude is clear. The fluxes measured

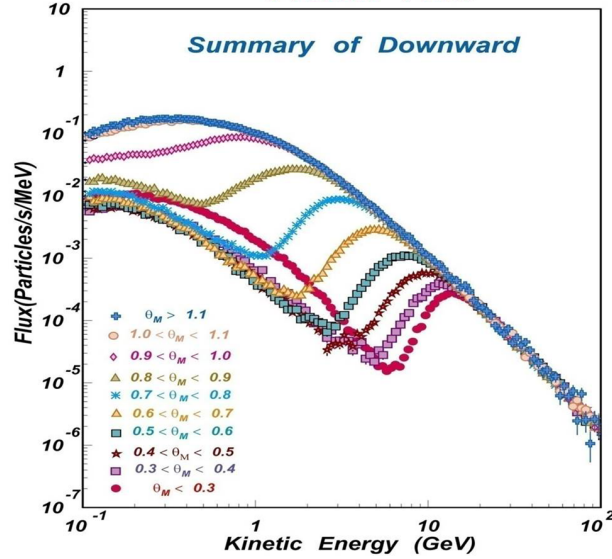


Figure 1.16: Proton spectra measured by AMS-01 at different geomagnetic latitudes (θ_M) from 0.1 to 100 GeV. Each color represents one latitude range [25].

below the cutoff are due to secondary particles that are trapped in the geomagnetic field.

R_{cut} determined from the Störmer approximation

It was found by Störmer that the cutoff rigidity, R_{cut} in a dipole field is approximately:

$$R_{\text{cut}} = M \left(\frac{R_E}{r} \right)^2 \frac{\cos^4 \lambda}{\left(1 + \sqrt{1 - \frac{z}{|z|} \cos \alpha \cos^3 \lambda} \right)^2} \quad (1.15)$$

where M is the dipole moment and has a normalized value of 58 [26], R_E is the earth radii, r is the distance from the earth origin, λ is geomagnetic latitude of the observation point (denoted as λ_{LatC}), α is the angle between the direction of arrival of the particle with the eastward direction and z is the particle electric charge. The definition of λ and α is illustrated in Figure 1.17.

At a specified distance from the earth, only 2 free parameters remain in the equation. The geomagnetic cutoff rigidity only depends on λ and α . For electrons with charge $Z=-1$, the maximum R_{cut} is obtained at $\alpha_{\text{EW}} \rightarrow 180^\circ$ and $\lambda_{\text{LatC}} \rightarrow 0^\circ$. While for protons with charge $Z=1$, R_{cut} reaches maximum at $\alpha_{\text{EW}} \rightarrow 0^\circ$ and $\lambda_{\text{LatC}} \rightarrow 0^\circ$.

Particularly for vertical direction particles, $\cos \alpha$ is zero. The vertical geomagnetic cutoff rigidity

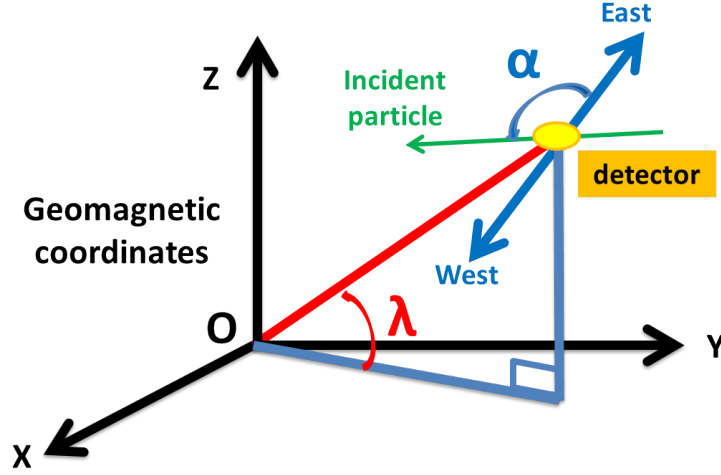


Figure 1.17: Illustration of variables in Equation (1.15), where O is the origin of magnetosphere of the earth, yellow circle is the position of the detector, λ is the geomagnetic latitude of the detector, green arrow is the direction of arrival of the particle and α is defined as east-west angle.

R_{cut}^V is simplified into

$$R_{\text{cut}}^V = \frac{M}{4} \left(\frac{R_E}{r} \right)^2 \cos^4 \lambda = \frac{14.5}{L^2} \text{GV} \quad (1.16)$$

R_{cut} determined from the IGRF model

In Equation (1.17), the general equation for the motion of a charged particle of charge q in a magnetic field B is expressed in three dimensional coordinates r, θ, ϕ [26]:

$$\frac{d(m\gamma \vec{v})}{dt} = q \vec{v} \times \vec{B} \Rightarrow \begin{cases} \frac{dv_r}{dt} = \frac{e(v_\theta B_\phi - v_\phi B_\theta)}{m\gamma c} + \frac{v_\theta^2}{r} + \frac{v_\phi^2}{r} \\ \frac{dv_\theta}{dt} = \frac{e(v_\phi B_r - v_r B_\phi)}{m\gamma c} - \frac{v_r v_\theta}{r} + \frac{v_\phi^2}{r \tan \theta} \\ \frac{dv_\phi}{dt} = \frac{e(v_r B_\theta - v_\theta B_r)}{m\gamma c} - \frac{v_r v_\phi}{r} - \frac{v_\theta v_\phi}{r \tan \theta} \end{cases} \quad (1.17)$$

The magnetic field \vec{B} is calculated by the IGRF model for each specified location. The system of equations can be solved by specifying the starting point of the trajectory.

The common method of calculating cosmic ray trajectories is to calculate the trajectory in the reverse direction, also known as back-tracing. Thus the starting point is the top of the detector. The tracing result is illustrated in Figure 1.18 for 15 charged particles with different energies. The trajectories undergo increased geomagnetic bending as the particle energy is decreased. The cutoff rigidity is determined as the energy below which charged particles trajectories are trapped in the geomagnetic field. However, a region of penumbra is observed in Figure 1.18, where

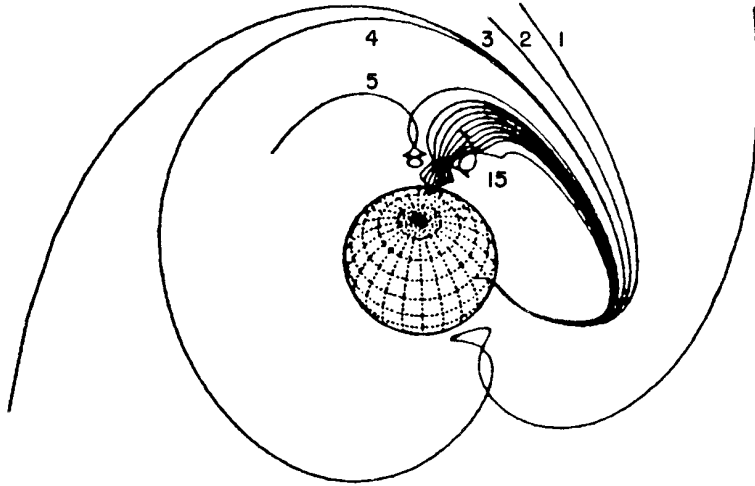


Figure 1.18: Illustration of charged particle trajectories traced out in the vertical direction from the same location. Particles from 1 to 15 have decreasing energies [27].

trajectories develop intermediate loops and the determination of R_{cut} become complex [27].

1.4 Conclusion

In this chapter, the main motivations and challenges of cosmic-ray physics are presented. In the following of the dissertation, these points are developed in details:

- Description of the detector, performance of the sub-detectors, lepton/proton separation variables, and AMS datasets (chapter 2)
- In situ control of energy scale in the calorimeter (chapter 3)
- Lepton identification and the extraction of lepton and electron numbers (chapter 4)
- Calculation of the lepton and electron fluxes, as well as their systematic uncertainties (chapter 5)

Chapter 2

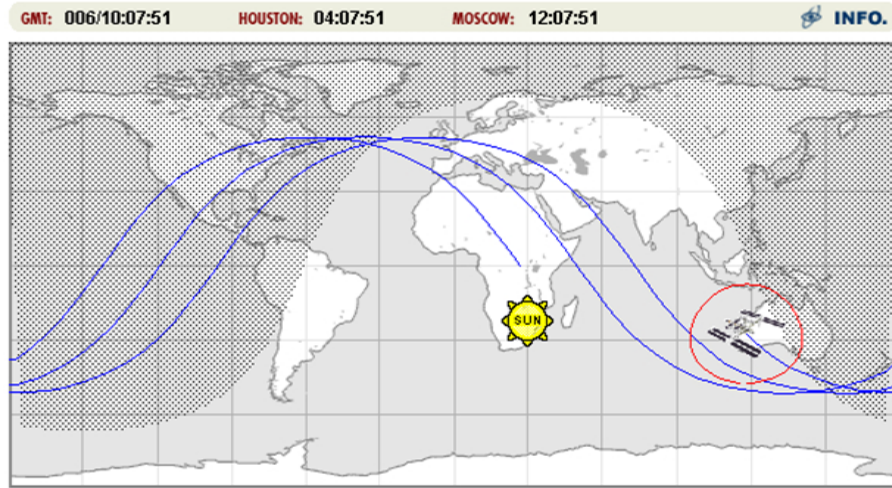
AMS Experiment and Lepton Identification

AMS-02 is a particle detector, launched in 2011, mounted on the main truss of International Space Station (ISS), which orbits the Earth at an altitude of about 400 km. In this chapter,



Detector of AMS on the ISS.

the AMS experiment is reviewed from its sub-detector design and performance to the data



ISS path on the map - ISS tracker [28].

acquisition and organization, with emphasis on the lepton identification.

2.1 AMS sub-detectors

AMS-02 consists of five sub-detectors: transition radiation detector, time of flight, tracker inserted in a dipole magnetic field, ring imaging cherenkov detector and electromagnetic calorimeter. Each of them measures different features of particles, such as charge, rigidity(P/Z), velocity and energy. The redundancy of measurements from different sub-detectors allows cross-calibration of energy and charge, which ensures a more reliable estimation. An overview of the sub-systems of AMS-02 is given in Figure 2.1.

In AMS coordinates, the magnetic field direction is defined as X, the bending direction as Y and the zenith-pointing direction as Z (cf Section 2.1.3).

2.1.1 Transition radiation detector (TRD)

Transition radiation is a form of electromagnetic radiation emitted when a charged particle passes through inhomogeneous media, such as a boundary between two media with very different dielectric constants. Particles with a high Lorentz factor, typically light particles such as electrons, induce radiation in the X-rays range.

The TRD of AMS, located on top of the detector, between Layer 1 of the tracker and the planes of the Time of Flight is designed for the purpose of identifying particles through the detection

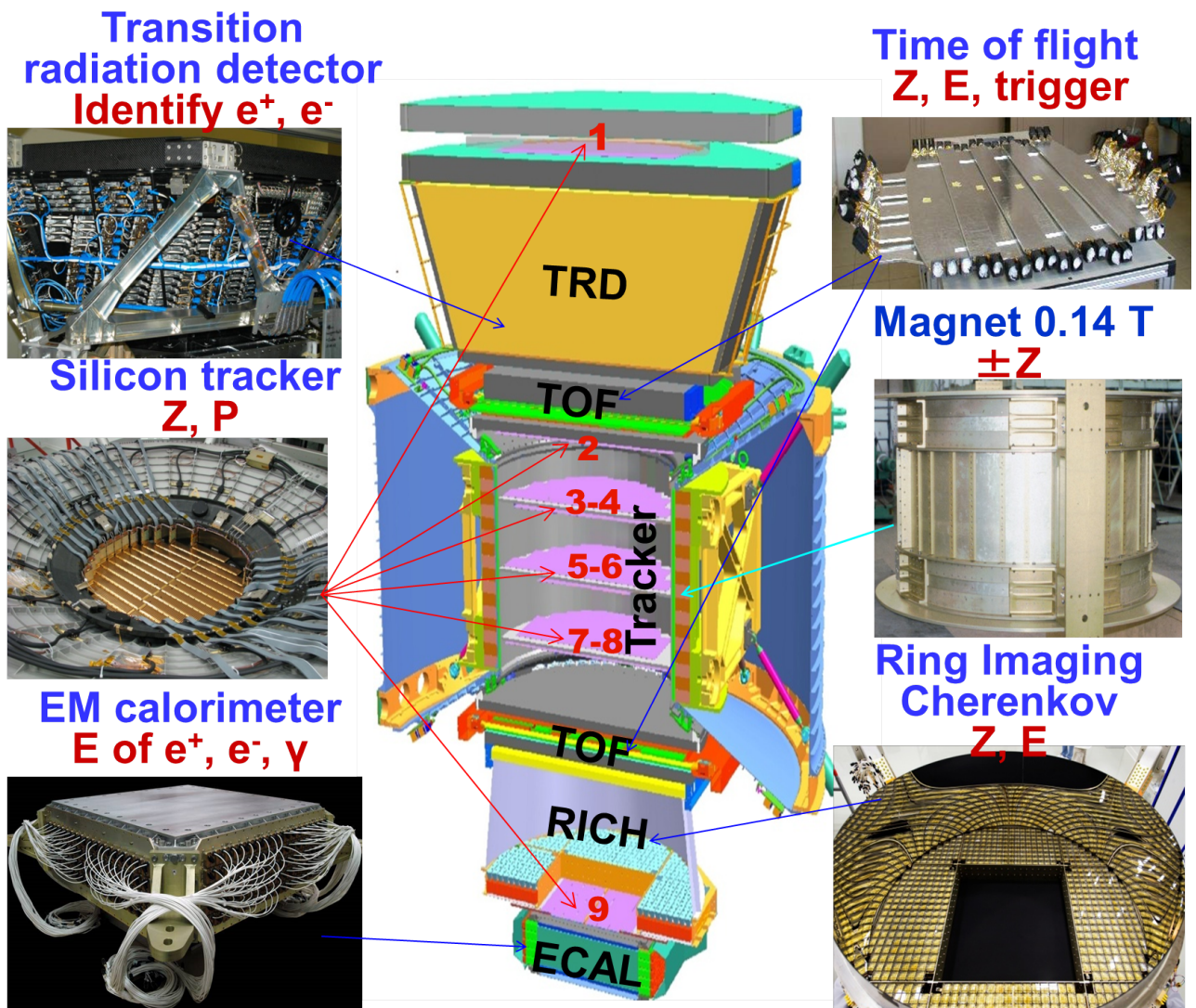


Figure 2.1: Sub-detectors of AMS: transition radiation detector (TRD), time of flight (TOF), tracker and the magnet, ring imaging cherenkov detector (RICH) and electromagnetic calorimeter (ECAL).

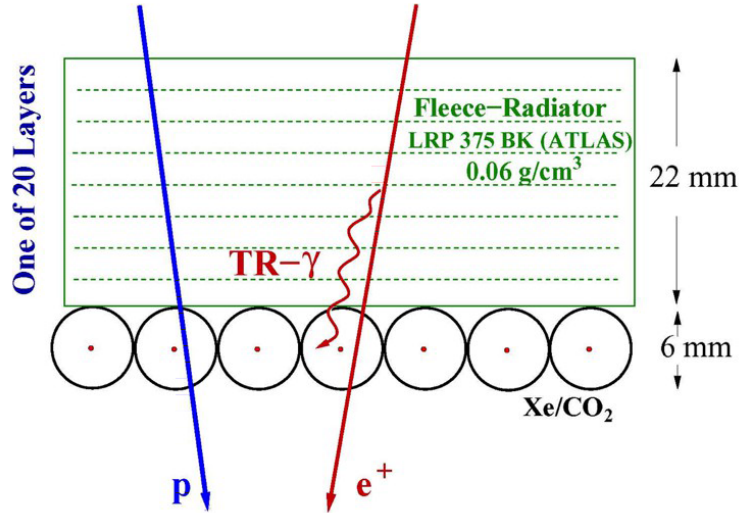


Figure 2.2: Principle schema of transition radiation detector [29].

of emitted X-rays. It consists of 20 layers with 8 in X direction and 12 in Y. Each TRD layer is composed of 22 mm of fiber fleece that induces the transition radiation and 16 straw tubes filled with Xe and CO_2 gas mixture that produces ionization avalanche and converts the X-rays into electric signals. The working principle of TRD is illustrated in Figure 2.2. Positrons and electrons produce extra X-rays, whereas protons and heavy nuclei don't. This difference provides means for lepton and proton separation. Lepton hereinafter indicates electrons and positrons.

Lepton-proton estimator TRD_{LER}

Behaviors of leptons and protons in the TRD are studied with test beam and Monte Carlo simulation as shown in Figure 2.3, where protons and electrons exhibit different signal features. By parameterizing these features, a TRD likelihood ratio (TRD_{LER}) is developed based on the signal amplitude in each layer of TRD. The likelihood functions are normalized probability functions, defined as

$$\begin{aligned}
 \text{Protons : } P_p &= \sqrt[n]{\prod_i^n P_p^{(i)}(E_{TUBE})} \\
 \text{Electrons : } P_e &= \sqrt[n]{\prod_i^n P_e^{(i)}(E_{TUBE})}
 \end{aligned} \tag{2.1}$$

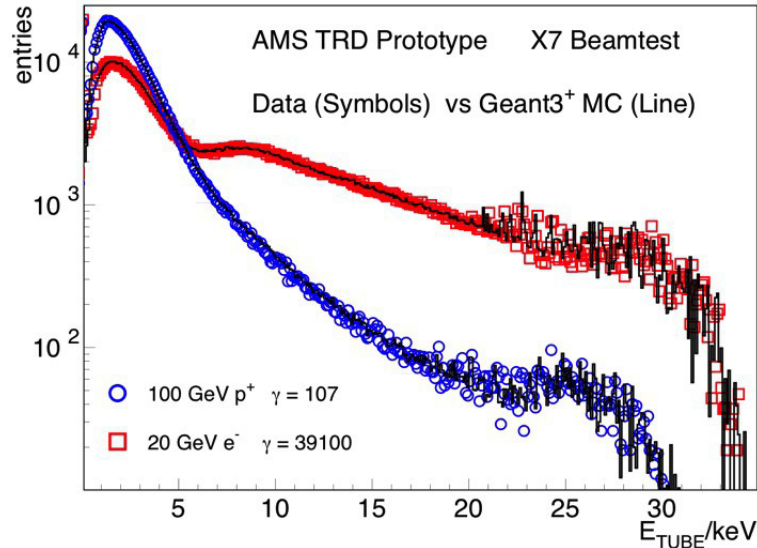


Figure 2.3: Distributions of detected radiation energy for protons at 100 GeV (blue) and electrons at 20 GeV (red) from test beam (colored markers) and MC simulation (black line) [29].

where n is the number of TRD layers used for the measurement. The TRD likelihood ratio estimator is thus given by

$$TRD_{LER} = -\ln\left(\frac{P_e}{P_e + P_p}\right)$$

Distributions of TRD_{LER} are shown in Figure 2.4 with lepton peak below 0.7 and proton peak above 0.7. Shape of the TRD_{LER} distributions can be described by Novosibirsk function [30], which is a logarithmic Gaussian function defined as:

$$\mathcal{F}(x) = N \exp\left(-\frac{1}{2\sigma_0^2} \ln^2\left(1 - \frac{x - x_p}{\sigma} \eta\right) - \frac{\sigma_0^2}{2}\right) \quad (2.2)$$

where N is the normalization factor, x_p is the peak value, η is the asymmetry parameter, σ is the width and σ_0 is $(1/\sqrt{\ln 4}) \sinh^{-1}(\eta\sqrt{\ln 4})$. The TRD_{LER} distribution shape changes with energy, so does its proton rejection power.

The dependence of the proton rejection power with energy is shown in Figure 2.4. Rejection factor is defined as $\epsilon_{electron}/\epsilon_{proton}$, where $\epsilon_{electron}$ and ϵ_{proton} are respectively efficiency of TRD_{LER} cut for electrons and protons. It is observed that the proton rejection factor calculated from ISS data (defined in Section 2.3.3) and from Toy MC ¹ follow the same trend, both are greater than 10^3 below 100 GeV and gradually drop to 10 at 500 GeV. The drop of efficiency at high energy is due to the fact that ultra-relativistic protons also induce X-rays, which make it more difficult to separate from leptons.

¹Toy MC is simplified MC program generating particles on top of the detector in a power-law energy spectrum; the TRD information from ISS data is used.

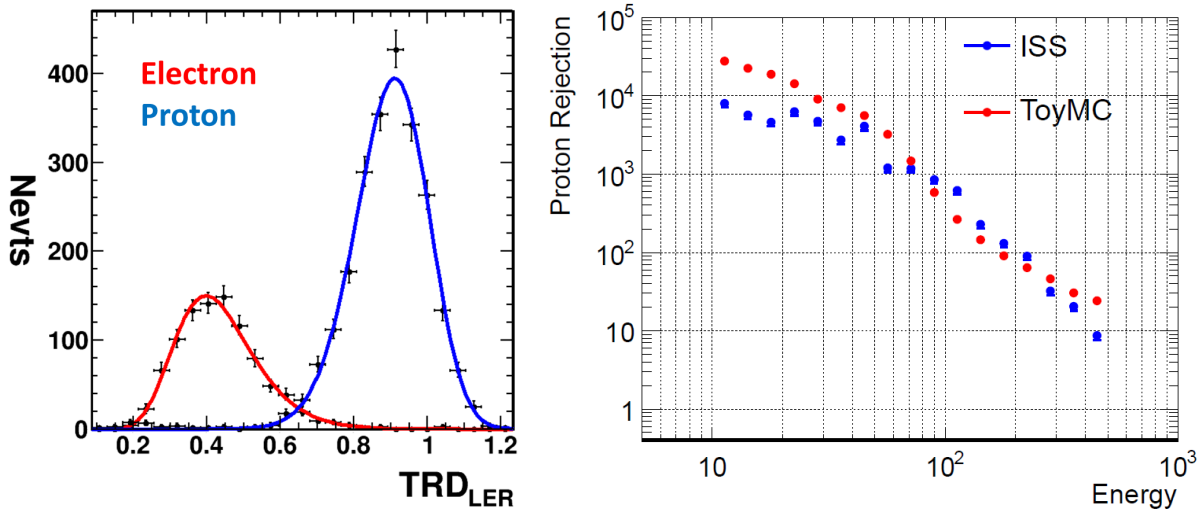


Figure 2.4: Left: TRD_{LER} proton and electron distributions from ISS data (black dots) fitted by Novosibirsk function, proton in blue and electron in red, at 92.5 - 100 GeV. Right: TRD_{LER} proton rejection factor as a function of energy at 90% efficiency for leptons, result from ISS data in blue and from Toy MC in red [31].

Additionally, TRD also provides powerful tools (TRD_{eHe}) for helium rejection using the same principle as for protons.

2.1.2 Time of flight (TOF)

The TOF of AMS consists of four planes of scintillation counters, two above the magnet and two below, giving a total acceptance of approximately $0.4 \text{ m}^2 \cdot \text{sr}$. The four planes contain, beginning from top, 8, 8, 10 and 8 scintillator paddles. TOF is a multi-purpose system designed for:

- providing main trigger (Section 2.3.1)
- distinguishing upward and downward going particles at a level of 10^{-9} , crucial for anti-matter $\bar{H}e$ detection
- measuring the particle velocity with a resolution improving as charge increases, about 4% for protons, 2% for He and 1.2% for C [32]
- measuring the particle charge by scintillating signals, $dE/dX \propto Z^2$

When a particle passes through a TOF plane, the Time-to-Digital Converter (TDC) starts running and stops when the particle exits from the other side of the magnet barrel and passes

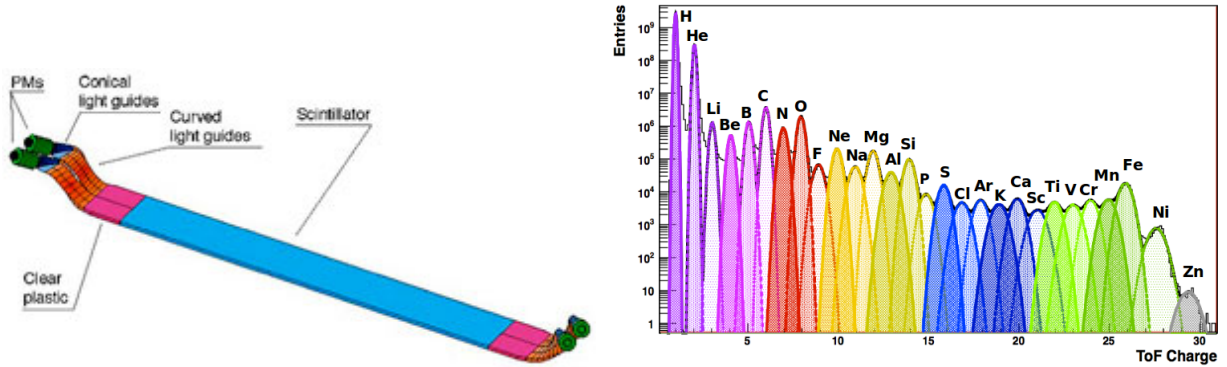


Figure 2.5: Left: One paddle of the scintillation counters of TOF. Right: charge measurement with TOF up to $Z=30$ [32].

through the opposite TOF plane. Transit time of the particle is measured with a precision of about 150ps.

2.1.3 Silicon tracker and magnetic field

The silicon tracker is in the central position of the AMS-02, inserted in a permanent dipole magnet of 0.15 Tesla. The tracker is designed to measure the rigidity, sign of charge and charge for charged particles traversing the instrument.

The tracker consists of 9 layers with an effective area of 6.2 m^2 [33]. Specifically layer 1, 2 and 9 labeled external to the magnet as shown in Figure 2.6, where layer 1 is above the TRD, layer 2 is just above the magnet and layer 9 is between the RICH and ECAL; 3 to 8 are internal layers placed on both sides of the three silicon planes. Each layer is made of double-sided micro-strip sensors placed in orthogonal directions, which allows to determine the hit position in X and Y directions. By tracking the particle passage at 9 different positions with an accuracy of $10 \mu\text{m}$, the curvature of the trajectory, κ , in the magnetic field of density B is precisely measured and the rigidity is calculated by $R=P/Z=B\kappa$. With the AMS tracker, the maximum detectable rigidity (MDR) is 2 TeV. At MDR, the rigidity measurement resolution is 100%.

Quality of the track reconstruction depends on the hits pattern, since not all hits can be used or exist for the reconstruction . To differentiate the cases, 5 exclusive categories according to the external hit patterns are defined:

1. Inner: no hit on layer 1 or 2 or 9
2. L2: hits on layer 2; no hit on layer 1 or 9

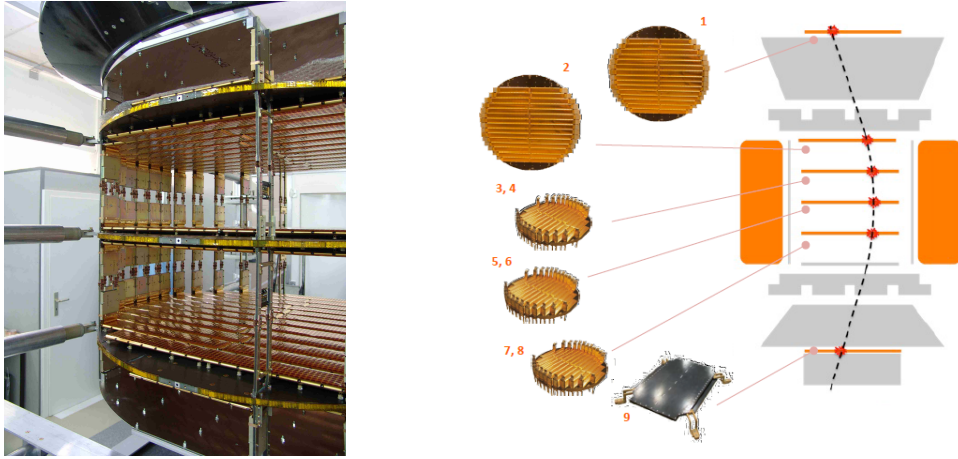


Figure 2.6: Left: photo of AMS silicon tracker layers. Right: AMS-02 tracker design: 9 layers and the dipole magnet in orange.

3. L1: hits on layer 1; no hit on layer 9
4. L9: hit on layer 9; no hit on layer 1 or 2
5. L2L9: hit on layer 2 and 9; no hit on layer 1
6. L1L9: hit on both layer 1 and 9

These patterns and their fractions are studied in Section 5.4 in relation with the charge confusion estimation.

2.1.4 Ring imaging Cherenkov detector (RICH)

The RICH measures the particle velocity and charge. With the rigidity measured by the tracker, the RICH is also able to precisely estimate the mass, particularly helpful in isotope identification.

The detection principle of RICH is Cherenkov radiation, which is electromagnetic radiation (light cone) emitted when a charged particle passes through a dielectric medium at a speed greater than the phase velocity of light in that medium. The Cherenkov light cone angle is proportional to the particle velocity and the light intensity proportional to the charge. In the RICH, such light cone is generated, reflected and detected (Figure 2.7).

The radiator of RICH is composed of aerogel, a mixture of SiO_2 and H_2O . With its central surface equipped with NaF , particles passing through the central part emit larger cones so as to avoid the $64 \times 64 cm^2$ hole in the detection plane, corresponding to the active area of the

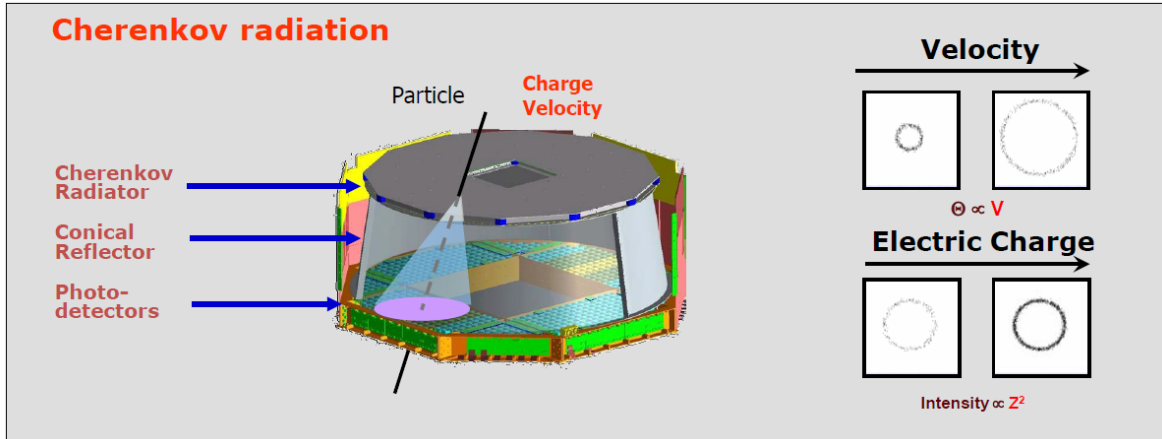


Figure 2.7: Left: configuration of RICH, radiator material in aerogel and central surface equipped with NaF . Right: RICH working schema [34].

electromagnetic calorimeter. The reflector of RICH is a multilayer structure of carbon fiber with epoxy resin, attaining a reflectivity greater than 85% and roughness less than 15 nm. The RICH provides AMS-02 with precision measurement of velocity with an accuracy of 0.1% for protons, and measurement of charge with resolution better than 10% for $Z \leq 26$ [34].

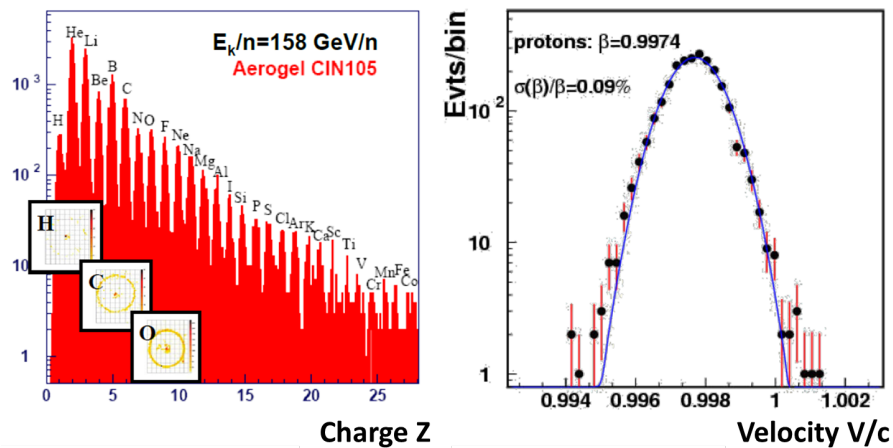


Figure 2.8: RICH prototype test at CERN with collision products, measurements of charge for different nuclei (red area) and velocity of protons in black dots fitted by a Gaussian (blue line) [34].

2.1.5 Electromagnetic calorimeter (ECAL)

The ECAL of AMS is a 3D imaging calorimeter located at the bottom of the AMS-02 detector, measuring the particle deposited energy, serving as standalone trigger for unconverted photons and separating hadrons from leptons. It performs a destructive measurement of the energy of electromagnetic particles and is the only sub-detector with which the unconverted photons

interact.

The ECAL consists of 9 superlayers of 18.5 mm thickness, each composed of 11 grooved lead foils (1.68 mm thick) interleaved with scintillating fibers with diameter of 1 mm (Figure 2.9). Particles entering the ECAL interact with the lead and develop showers, which are sampled

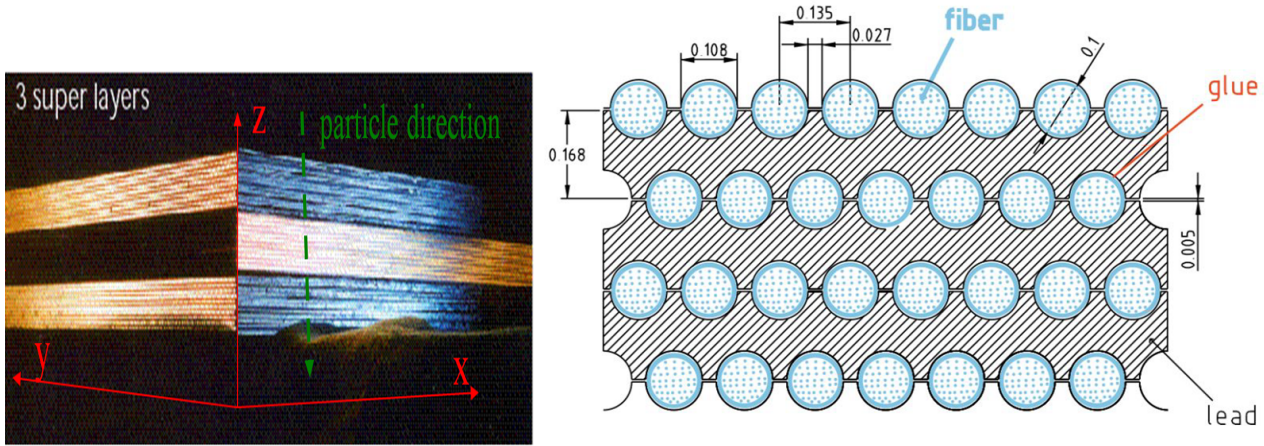


Figure 2.9: Left: 3 superlayers of ECAL, 1 in X direction and 2 in Y. Right: zoomed schema of 3 lead foils interleaved with four layers of scintillating fibers. Each fiber has a diameter of 1 mm.

by scintillating fibers. The scintillating light is transported to photomultiplier tubes (PMTs) situated at one end of the fibers. The PMTs then transform the fiber light into electrical pulse proportional to the released energy. Each superlayer is equipped with 36 PMTs and each PMT consists of 4 (2×2) pixels, which segments the superlayer into 2 layers in depth and in 72 cells laterally. Cell is defined as the active area covered by each anode of the PMTs, which corresponds to 35 fibers and an area of $9 \times 9 \text{ mm}^2$ [35]. The shower longitudinal profile is thus measured at 18 different depths and the lateral profile is sampled with a granularity of about 0.5 Moliere radius². The 9 superlayers are stacked alternatively parallel to the X axis (4) and Y axis (5). With the profile information, a 3D ECAL shower is reconstructed, as well as the particle energy and direction.

The radiation length of the ECAL, X_0 ,³ is 1.05 layer unit compared to the nuclear interaction length, λ_I ,⁴ of 28 layer unit. With $17.2X_0$, the ECAL of AMS-02 allows measurement of energy with a good resolution up to 1 TeV.

²Moliere radius is the radius of a cylinder containing on average 90% of the shower's energy deposition.

³Radiation length, measured in $g \cdot \text{cm}^{-2}$, is the mean distance over which a high-energy electron loses all but $1/e$ of its energy by bremsstrahlung [3].

⁴Nuclear interaction length is the mean traveled by a hadronic particle before undergoing an inelastic nuclear interaction.

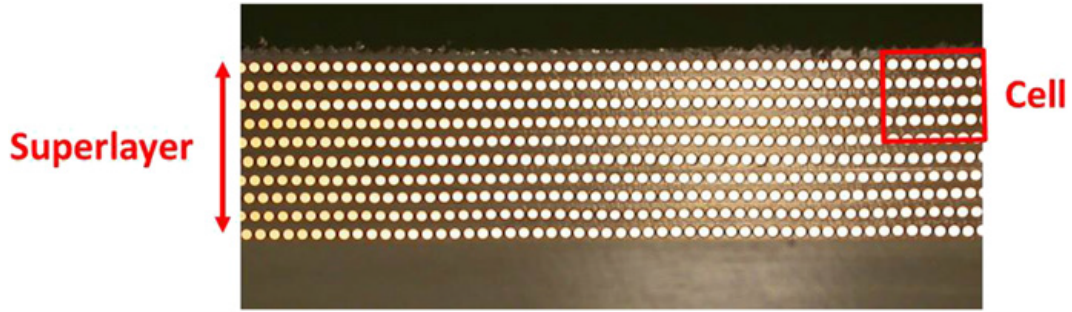


Figure 2.10: Schema of 1 superlayer and cell dimension [35].

2.1.5.1 Energy reconstruction

[1] In each pixel, energy collected by the scintillating fibers is converted into digital counts through analogue-to-digital converter (ADC). To cover the required electronics dynamic range of 60 000, 2 channels of low gain (LG) and high gain (HG) with a conversion ratio of 33 are applied for each pixel. The response of each ADC hit is equalized using minimum ionizing particles (MIPs). MIPs, typically protons, traverse the ECAL without interacting with the lead nuclei but only losing little energy by ionization. The ADC to GeV conversion factor are

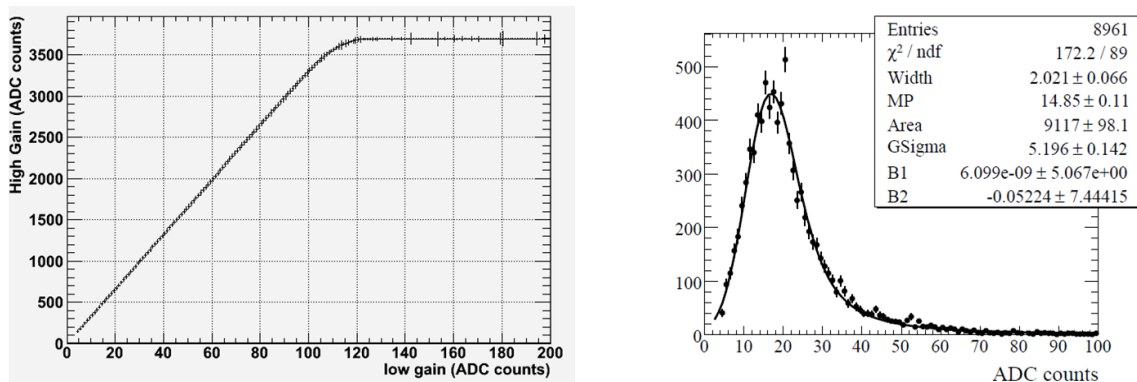


Figure 2.11: Left: ADC HG counts vs LG counts. The part of HG below 3700 counts can be fitted by a linear function with a slope of 33, which is the gain ratio. Above 3700, the HG saturates and the LG is used instead [36]. Right: ADC counts distribution of MIP protons, fitted with a Landau function convoluted with a Gaussian plus an exponential background. Value MP is noted as mean ADC count [37].

determined with MIPs.

The energy reconstruction is here explained with the EnergyA developed by LAPP, one of the official reconstructed energies in AMS software. After equalization, temperature and attenuation corrections at the cell level, the ECAL hits are clustered into showers. An overall normalization of shower energy is determined using test beam events well contained in the ECAL, which is applied as a correction. Three other shower corrections are here presented in

details.

Impact correction is to account for the energy loss between the cells. The correction is based on the S1/S3, which is a ratio sensitive to the impact position. S1/S3 is computed per layer, where S1 is the energy of the cell with the maximum deposited energy or the center of gravity of the layer and S3 is S1 plus the energy deposited in the two neighboring cells of S1. The dependence of S1/S3 on the center of gravity of the layer and the dependence of deposited energy on the S1/S3 are shown in Figure 2.12.

The impact correction is derived from test beam and applied on all the datasets. It was also

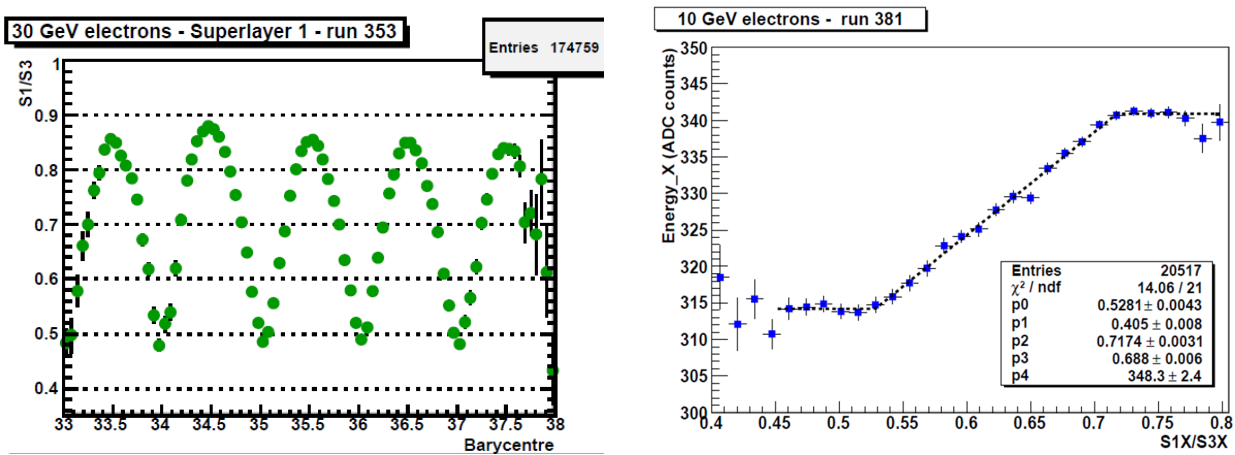


Figure 2.12: Left: S1/S3 as a function of center of gravity of the superlayer 1 from test beam- 30 GeV electrons. Right: Energy of X direction in ADC counts as a function of the S1/S3 in X direction from test beam- 10 GeV electrons [37].

controlled on ISS data which also allows to study the angle dependence [38].

Rear leakage correction is to account for the energy loss of the shower tail which is not contained in the ECAL. The rear leakage is estimated using the longitudinal segmentation of the shower. The longitudinal profile of a shower, dE/dZ , is described by [3]

$$\frac{dE}{dZ} = E_0 \beta \frac{e^{-\beta Z} (\beta Z)^{\alpha-1}}{\Gamma(\alpha)} \quad (2.3)$$

where E_0 is the particle true energy, α and β are two parameters, Γ is the Gamma function⁵. The rear leakage can be estimated by integration of dE/dZ at the tail. To simplify the work, a triangle approximation is adopted to describe the rear leakage as illustrated in Figure 2.13. The area of the blue triangle is applied as rear leakage correction, which is proportional to the

⁵Gamma function: $\Gamma(a) = \int_0^\infty x^{a-1} e^{-x} dx$

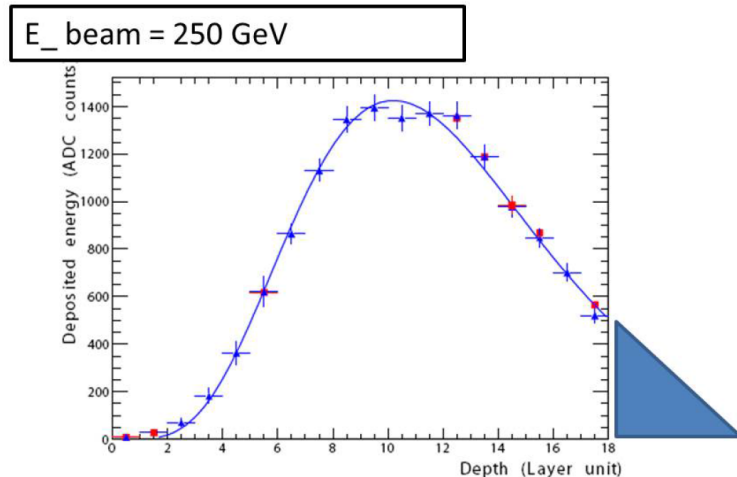


Figure 2.13: Illustration of rear leakage correction from test beam 2007 @250 GeV. Blue dots are measured deposited energy per layer fitted by the blue line and the blue triangle is the approximated extrapolation of the profile [1].

fraction of energy in the last two layers.

$$\frac{E}{E_{true}} = 1/Corr_{rearleak} = A + S \times Frac_{last2layers} \quad (2.4)$$

where A and S are determined by fitting the Test Beam 2010 electrons and positrons in the energy range of 10 to 290 GeV.

Systematic uncertainty of this rear leakage correction is estimated using ISS data and MC data. An uncertainty of 2% is attributed to the parameter A and 15% to the S. In total, at 1 TeV, the systematic uncertainty due to rear leakage correction is $\sim 5\%$ [1].

Dead cells correction is applied for the dead PMTs and cells. After the launch 1 PMT died, for which the deposited energy is not measured and therefore needs to be estimated. A first simple approach is to take the mean energy of the two neighboring cells of the dead one. To better estimate the energy loss, an improved method is to parameterize ECAL shower and calculate the deposited energy in the dead cell. This new correction is applied in EnergyA and the result is compared in Figure 2.14, using test beam data.

The same correction is applied to compensate for saturation in the cells at high energy. Figure 2.15 shows the distributions of reconstructed energy over true energy (E_{true}) with MC electrons of 1.8 TeV - 2 TeV. Without the saturation correction, EnergyA/ E_{true} peaks at 0.7. After the correction, the distribution nicely peaks at 1.

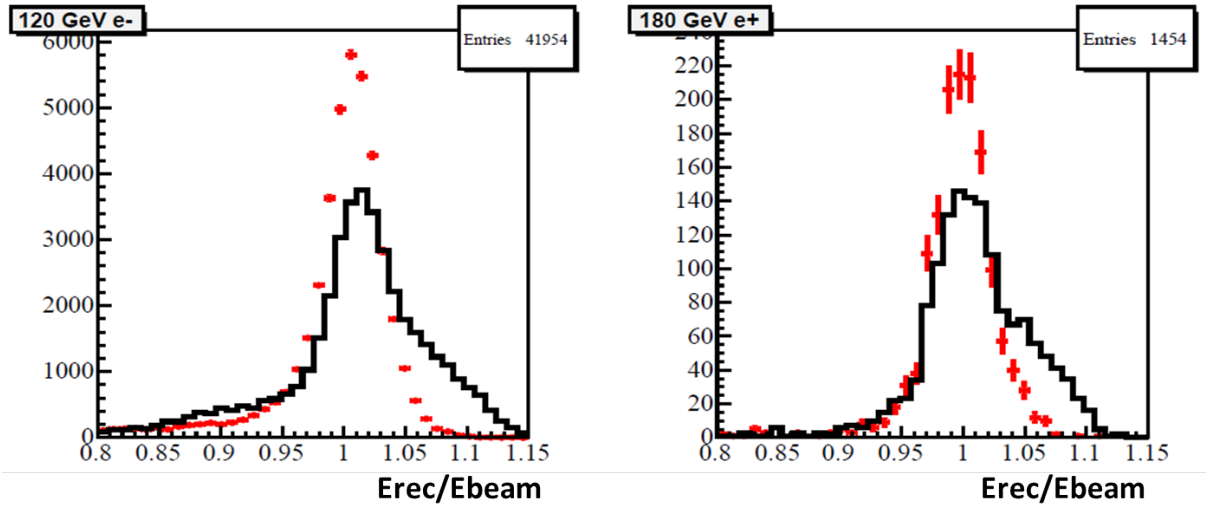


Figure 2.14: Improvement of new dead cell correction on E_{rec}/E_{beam} : mean-energy approach (black) and new parameterization approach (red). Events are selected in the region of the dead PMT. [1]

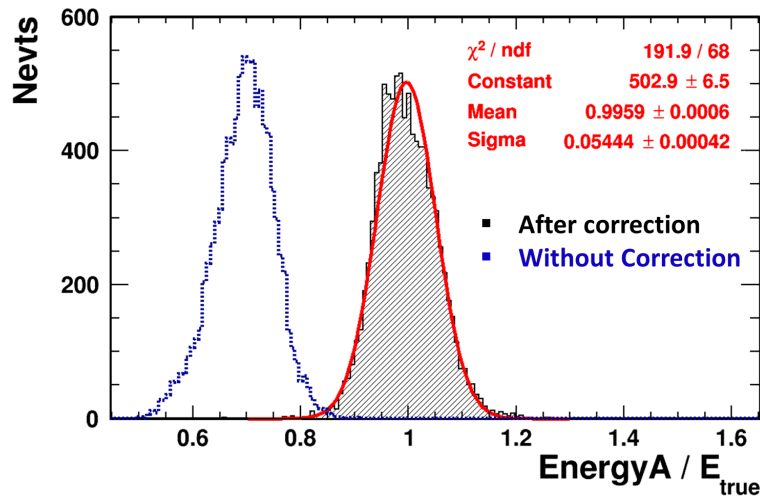


Figure 2.15: Distributions of $EnergyA/E_{true}$ using MC electrons of $1.8 \text{ TeV} < E_{true} < 2 \text{ TeV}$: with saturation correction (black) fitted by Gaussian function, without the correction (blue dashed).

2.1.5.2 Lepton-proton separation with ESE_{V3}

Another important objective of the ECAL is to distinguish leptons from proton background. The rejection ratio can achieve 10^{-4} with the high segmentation and the ratio of λ_I/X_0 greater than 26.

When a high-energy e^+ , e^- or γ passes through ECAL, an electromagnetic shower is produced by the interplay of the bremsstrahlung and the pair production. In contrast, protons or nuclei pass through ECAL either as MIPs or developing hadronic showers. MIPs are easily identified

by their unique features, one or two hits per layer with very little deposited energy, typically 10 MeV/layer for protons. Hadronic showers are less compact than the electromagnetic shower as is shown in Figure 2.16 and Figure 2.17. Therefore an ECAL standalone estimator (ESE_{V3})⁶ for

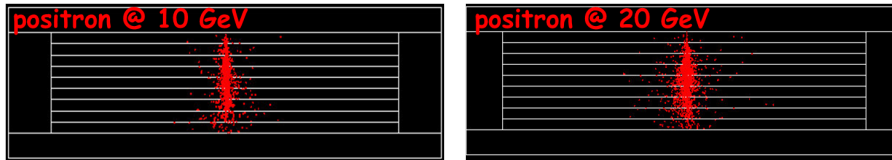


Figure 2.16: Illustration of electromagnetic behaviors of particles traversing ECAL.

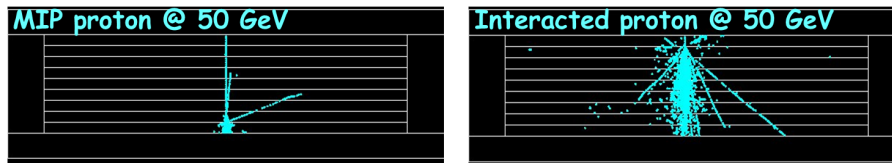


Figure 2.17: Illustration of 2 types of hadronic showers of protons at 50 GeV traversing ECAL.

lepton-proton separation is developed by LAPP based on the different shower shapes. ESE_{V3} is a boosted decision tree trained on Monte Carlo electrons and smeared with Test Beam electrons and positrons. The training and performance of the estimator are detailed in [36].

The shape of ESE_{V3} distribution for protons and electrons are shown in Figure 2.18, which is an asymmetric Gaussian varying from -1 to 1. Precisely, the proton shape is described by Novosibirsk function and the electron shape is described by Crystal Ball function [39], composed of a Gaussian core portion and a power-law low-end tail, defined by

$$f(x; \alpha, n, \bar{x}, \sigma) = N \cdot \begin{cases} \exp\left(-\frac{(x-\bar{x})^2}{2\sigma^2}\right) & \text{for } \frac{x-\bar{x}}{\sigma} > -\alpha \\ A \cdot \left(B - \frac{x-\bar{x}}{\sigma}\right)^{-n} & \text{for } \frac{x-\bar{x}}{\sigma} \leq -\alpha \end{cases} \quad (2.5)$$

where A and B are functions of α and n. The four parameters of Crystal Ball function are α , n, \bar{x} and σ .

2.1.6 Anti-coincidence counter

ACC is designed to reject events with bad topology, such as particles coming sideways. These events may interact with the materials of AMS (magnet, aluminium honeycomb, etcetera) and

⁶V3 means the third version

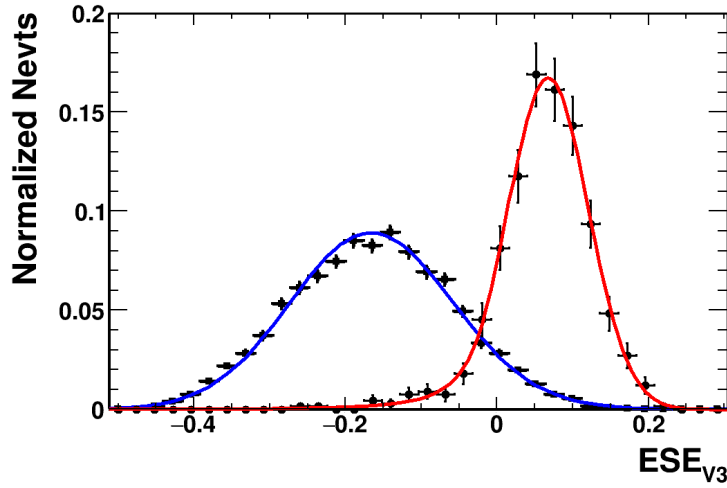


Figure 2.18: Normalized ESE_{V3} proton and electron distributions using proton and electron samples selected from ISS data (black dots) at 92.5 - 100 GeV, protons fitted by Novosibirsk function (blue) and electron fitted by Crystal Ball function (red). The sample selection is defined in Section 2.3.3.

confuse the event reconstruction. Thus an ACC veto trigger is present to remove them from the analysis.

The ACC of AMS has 16 scintillating paddles surrounding the tracker and 8 PMTs to collect

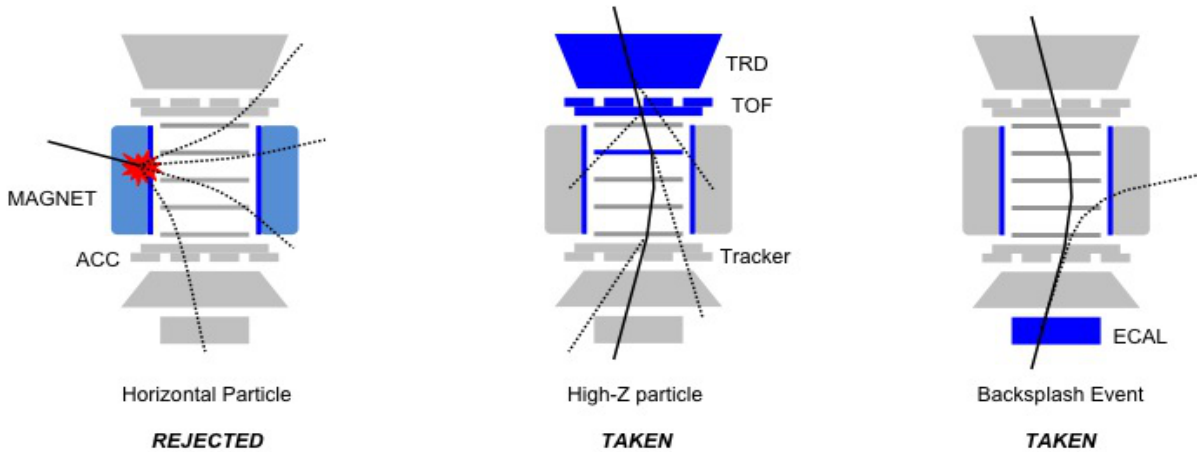


Figure 2.19: 3 cases for ACC: (1) horizontal particle fires the ACC and is rejected. (2) high Z particle that emits δ - rays is accepted by disabling the ACC veto. (3) backplash event is also accepted if ToF is triggered and no more than 4 ACC paddles are fired.

the signal. Its working principle is illustrated in Figure 2.19: particles from a horizontal direction trigger the ACC veto; particles coming vertically are accepted if less than 4 ACC paddles fired.

2.2 Lepton identification summary

Each sub-detector of AMS-02 contributes to one or several measurements for the particle detection. The identification of the particle is based on the combination of the information from all the sub-systems, their lorentz factor, charge and sign of charge, rigidity, velocity, energy and electromagnetic interaction. Illustration of particle identification process is shown in Figure 2.20.

The determination of **charge** is done by RICH, TOF and tracker. The charge measurement

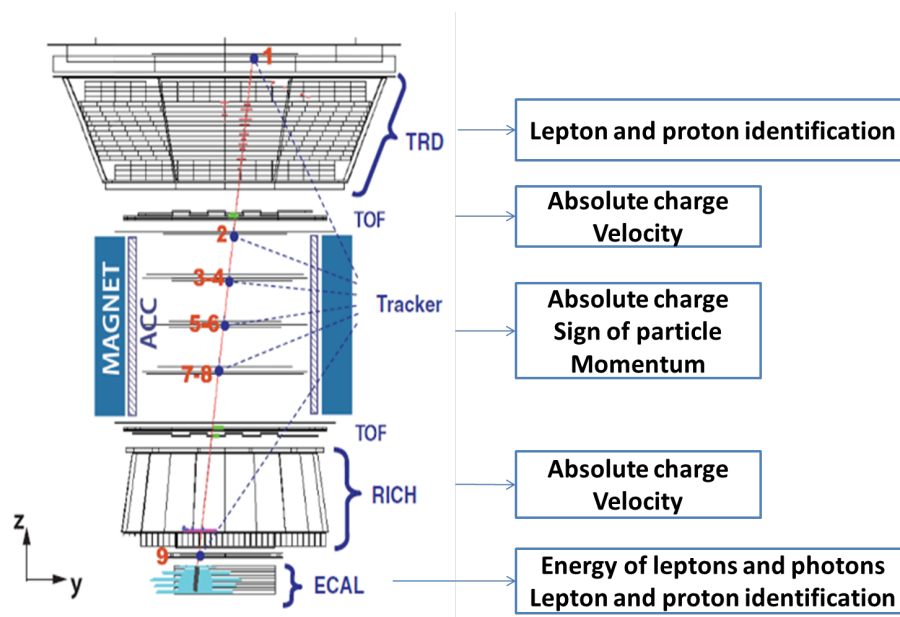


Figure 2.20: Display of a particle passing through AMS and particle identification using the sub-detectors of AMS.

in RICH is derived from the number of photons collected on the ring and in TOF and tracker, the estimation comes from the energy loss by ionization. The **velocity** is measured by TOF with the flight time between different TOF layers and by RICH with the radius of the RICH ring. The **rigidity** and **energy** are respectively measured by tracker and ECAL. Finally, TRD and ECAL are used to separate leptons from protons.

Protons are easily identified. Most of the cosmic ray particles are protons.

Nuclei are easily identified by their high charge. By requiring Z measured by TOF and tracker, leptons and protons are effectively reduced.

Photons have two possible behaviors in AMS-02. Most of the time, a photon passes through TRD, TOF, tracker and RICH without trace. The only detectable interaction is in the ECAL. In contrast, 20% of photons are converted into an e^+/e^- pair in the TRD. Then in the lower sub-detectors, they are treated as two charged particles.

Lepton samples are principally selected by charge $Z=1$, velocity positive and close to 1, clean trace in the detector with a good ECAL shower. Helium and heavy nuclei are effectively removed. However, many protons survive these basic selections as they are relativistic and have the same absolute charge as electrons and positrons. Positron identification is even more difficult since positrons have the same charge sign as protons. To purify the lepton samples, three variables are commonly used for proton rejection, TRD_{LER} and ESE_{V3} introduced in the previous section and E/P .

2.2.1 E/P variable

E/P is the ratio of the energy deposited in ECAL and the momentum measured by tracker. For leptons, energy deposited in ECAL is very close to its true energy, or rigidity, which means E/P value is about one. In contrast, protons and other hadrons traverse the ECAL with few or no interaction, depositing little energy compared to their true energy; the E/P value is close to zero. These different behaviors make E/P a natural discriminator of leptons and protons.

$$E/P = E_{dep}/E_{true} = \begin{cases} \sim 1 & \text{for leptons} \\ \ll 1 & \text{for protons} \end{cases}$$

The separation is illustrated with Monte Carlo electrons and Test Beam protons. In Figure 2.21, electrons peak at 1 with a power-law tail on the right side due to bremsstrahlung; protons peak near 0 with a tail quickly dropping to 0.

Besides lepton-proton separation, E/P is also used for energy control (cf. Section 3.2).

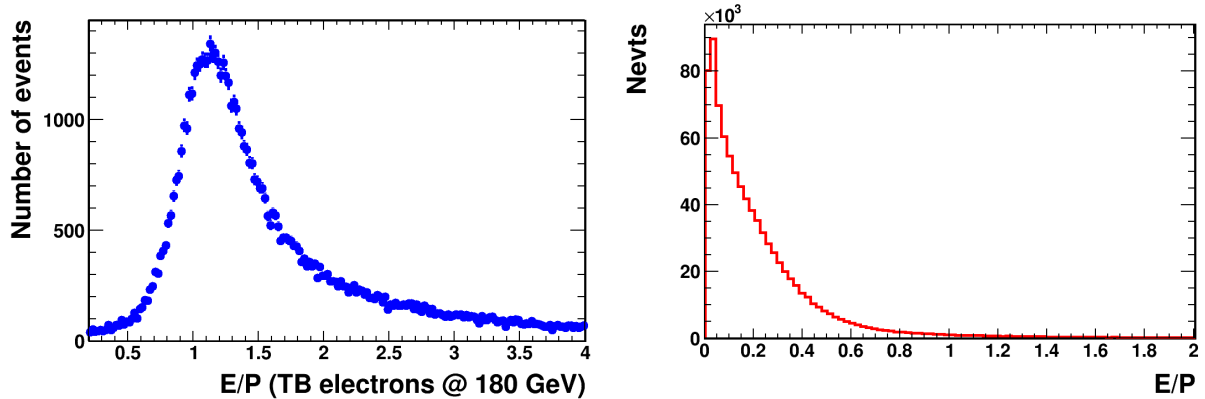


Figure 2.21: E/P distribution using test beam electrons at 180 GeV (left) and test beam protons at 400 GeV (right).

2.2.2 TRD_{LER} and ESE_{V3}

TRD_{LER} and ESE_{V3} , presented in Section 2.1.1 and Section 2.1.5.2, are two independent discriminators for proton rejection. By cutting on either of them, proton background is effectively reduced. Advantages of each estimator are listed below.

- TRD_{LER}
 1. good separation power of electrons and protons at low energy
 2. smooth asymmetric Gaussian shape over the whole energy range
- ESE_{V3}
 1. increasing separation power with energy and good separation at high energy
 2. Gaussian shape for a large energy range
 3. standalone ECAL estimate, independent from other sub-detectors

Separation power of TRD_{LER} and ESE_{V3} is quantified in Figure 2.22. From 30 to 700 GeV, the two estimators are fitted with analytical functions. Comparison of the fitted mean and RMS for leptons and protons again confirms that TRD_{LER} has a better separation at low energy and ESE_{V3} exhibits an excellent separation above 200 GeV.

Accordingly, drawbacks of TRD_{LER} are that the separation power drops at high energy and it is sensitive to the track reconstruction quality and the sign of charge of incoming particles. For ESE_{V3} , the separation power is weak below 10 GeV and proton shapes are not stable at high

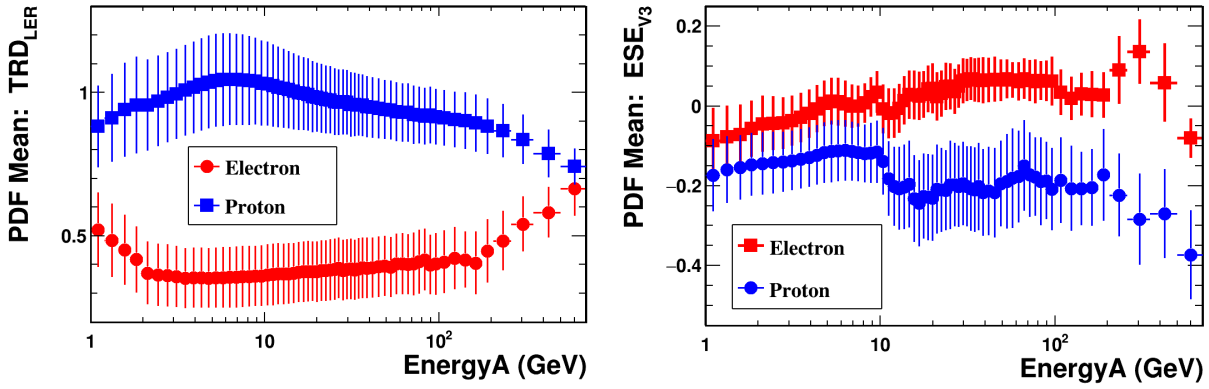


Figure 2.22: Mean (dots) and width (error bars) from fit results of ISS leptons (in red) and protons (in blue), TRD_{LER} on the left and ESE_{V3} on the right.

energy, which will be discussed in the systematics of the analysis (cf. Section 4.4).

To conclude, combining the redundant measurements from TRD, tracker and ECAL. The proton rejection power of AMS reaches 10^5 , as shown in Figure 2.23.

Pure electron and proton samples can be selected from ISS data by cutting on TRD_{LER} , E/p

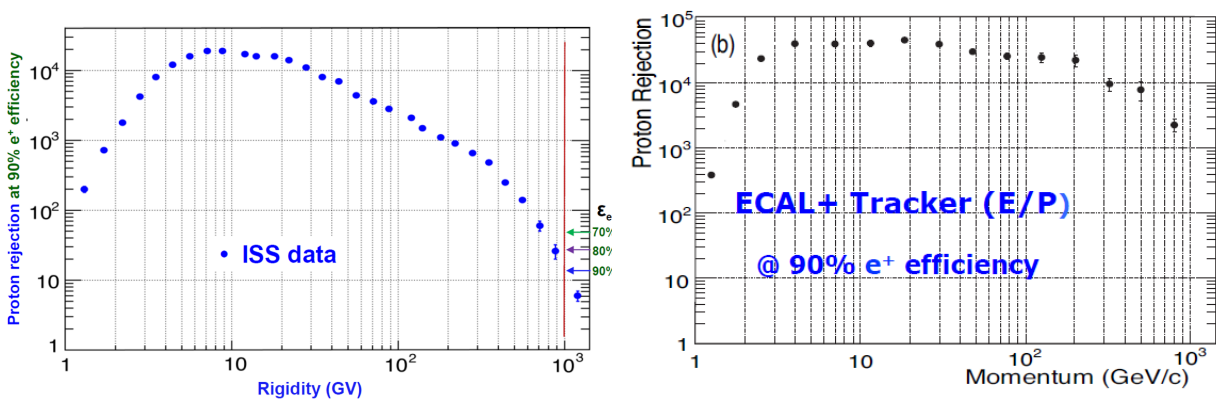


Figure 2.23: Proton rejection power of AMS, with TRD at 90% e^+ efficiency (left) and with ECAL and E/P at 90% e^+ efficiency (right) [40].

and ESE_{V3} , which will be used for template building in Chapter 4 and efficiency estimation in Chapter 5. The purity can be controlled to be greater than 99% at the expense of low statistics.

2.3 AMS data acquisition and organization

2.3.1 AMS trigger system

An event is recorded if the particle satisfies one of the trigger conditions. For the ISS data, the trigger rate is on average 500 events per second.

Among the sub-detectors presented above, TOF and ECAL have independent trigger sys-

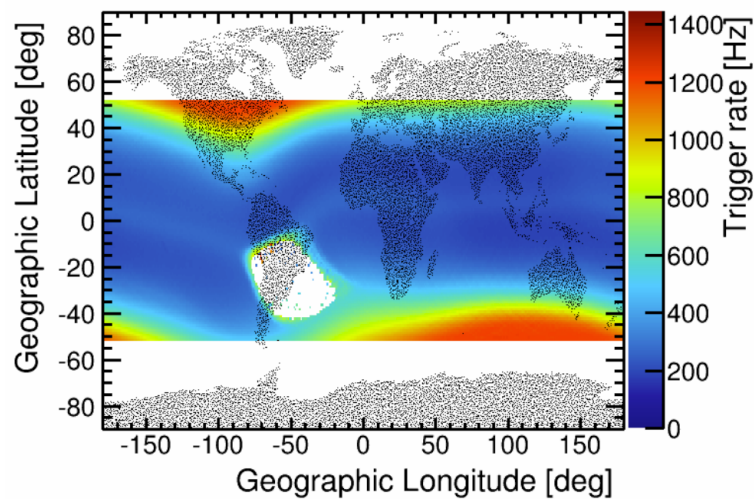


Figure 2.24: Trigger rate as a function of orbital position [41].

tems [42]. They generate fast triggers with a delay of 40 ns. The fast triggers FTC and FTZ, respectively designed for charged particles and high Z particles, are generated by the TOF; the fast trigger FTE, specially designed for neutral particle detection, is generated by ECAL.

Seven physics triggers are then defined with complementary information from the ACC and ECAL. Their definitions are listed in Table 2.1. The trigger pattern abbreviations are

- FTCP0 (fast trigger charged particle): three out of four TOF planes are fired
- FTCT1 (fast trigger central TOF): all of the four TOF planes are fired
- ACC0: number of ACC hits $N_{acc}=0$
- ACC1: $N_{acc}<5$
- ECALF&: ECAL fast trigger using AND of the two projections (xz and yz) decisions
- ECALF|: ECAL fast trigger using OR of the two projections decisions

Bit name	FTCP0	FTCT1	FTZ	ACC0	ACC1	BZ	ECALF&	ECALF	ECALA&
0 Unbiased TOF	0	1	1	1	1	1	1	1	1
1 Protons $Z \geq 1$	1	0	1	0	1	1	1	1	1
2 $Z \geq 2$	1	1	1	1	0	0	1	1	1
3 Slow $Z \geq 2$	1	1	0	1	1	1	1	1	1
4 Electrons	1	0	1	1	1	1	0	1	1
5 Photons	1	1	1	1	1	1	1	1	0
6 Unbiased ECAL	1	1	1	1	1	1	1	0	1

Table 2.1: The trigger system setting mask for physics triggers. Bits 1 to 5 are defined as physics triggers. Bits 0 and 6 are unbiased triggers.

- ECALA&: ECAL fast trigger using AND plus the incoming particle angle decisions

Particularly, two unbiased triggers are designed for trigger efficiency estimation, which accept the events with lower thresholds. These events are not usable for analysis and thus called non-physics events. The unbiased triggers are also denoted as non-physics triggers. The downscaling factor is 100 for unbiased TOF and 1000 for unbiased ECAL.

2.3.2 AMS data flow

Data acquisition (**DAQ**) system of AMS-02 collects signals from over 200K analog channels of the different sub-detectors: TRD (U), TOF and ACC (S), Tracker (T), RICH (R), ECAL (E) and Level-1 Trigger module (LV1). ([43]) The DAQ process tree is illustrated in Figure 2.25. Analog signals from the sub-detectors are digitized and compressed in Data Reduction (DR) boards. The next node in this tree, the JINF, receives data from up to 24 xDR. In the JINF data from the xDRs are collated, buffered and sent to the top level JINJ boards. The JINJ collates, buffers and passes data to a Main DAQ Computer (MDC). The MDC receives the complete event and analyses it to ensure that it contains interesting physics. The selected events are then buffered and sent out the High Rate Dynamic Link (HRDL). Since AMS operates at high trigger rates up to 2 kHz, the DAQ parameters are optimized for not increasing the dead time due to data processing with an efficiency greater than 90% as is seen in Figure 2.26, where the low-efficiency region in blue is the South Atlantic Anomaly (SAA).

Finally, the selected events are transferred back to earth, the Science Operation Center (SOC) at CERN, for off-line data reconstruction.

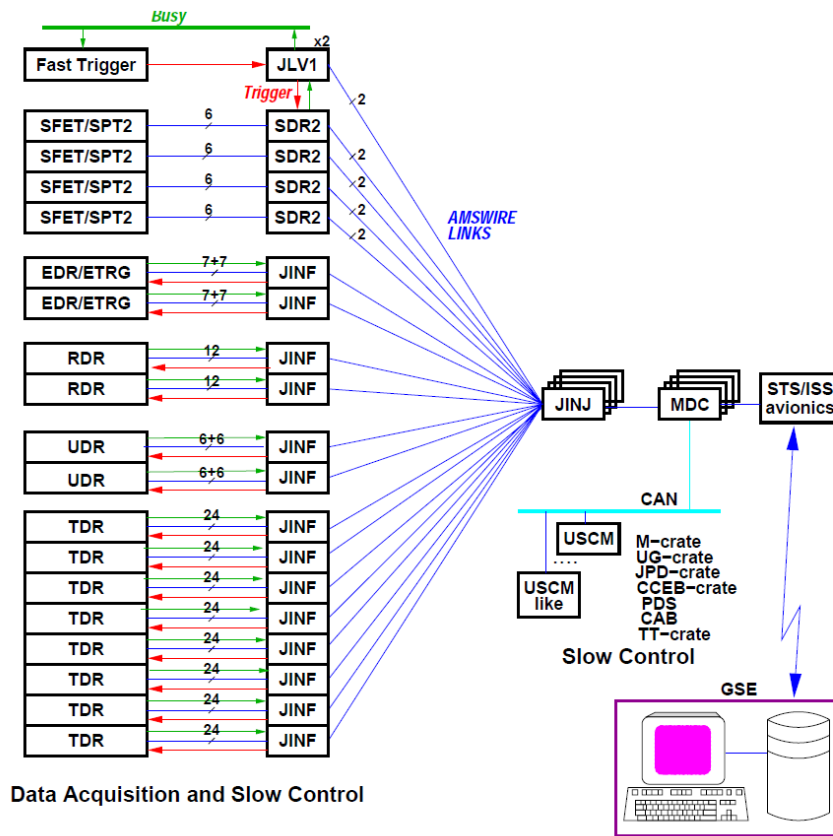


Figure 2.25: DAQ tree diagram. The blocks xDR stands for data reduction of a sub-detector: U, S, T, R or E. ([43])

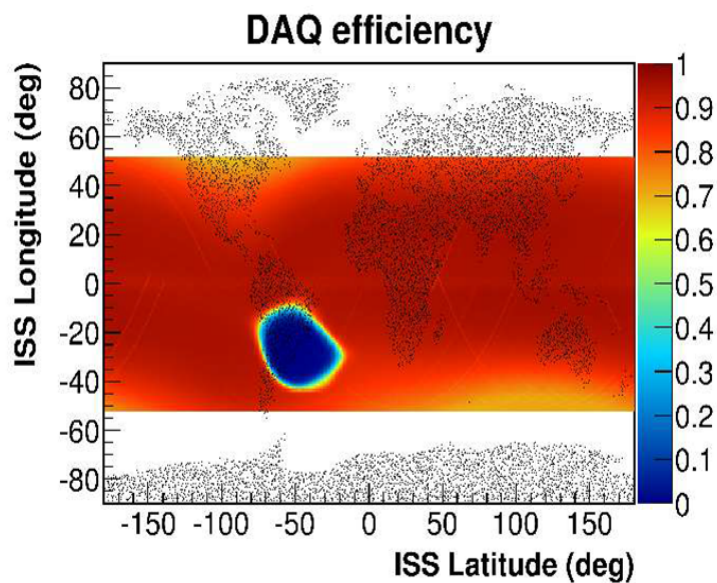


Figure 2.26: Data acquisition efficiency map.

2.3.3 AMS datasets

Three datasets are used in the analysis: ISS data, positron and electron test beam and electron MC data.

ISS data: The ISS data is the flight data taken since the launch on the 16th May 2011. More than 50 billions of events have been collected over last three years. These events are organized in ntuples and reprocessed for different calibration, alignment and reconstruction. Each ntuple is attributed a run number, which is the Unix time of the first event. Bad runs due to operational deficiencies and those taken in the SAA are removed.

Test beam data: The AMS has gone through several beam tests at CERN before the launch, which include proton beams of 7 discrete energy values from 20 to 400 GeV, positron beams of 6 discrete energy values from 10 to 180 GeV and electron beams of 4 energy values from 100 to 300 GeV. These beams of controlled particles are used to check the detector performance and to calibrate the ECAL. Details of the positron and electron test beam are listed in Table 2.2.

Dataset	10	20	80	100	120	180	300
Positrons	5k	150k	53k	33k	97k	350k	–
Electrons	–	–	–	2.4M	2.7M	2M	32k

Table 2.2: test beam positrons and electrons energy category and the number of events for each category.

MC events: To overcome the limitations of statistics, impurity and other drawbacks of ISS data and test beam, the interactions with the detector of different particles are simulated with Monte Carlo version GEANT4. The simulated particles currently include positron, electron, photon, muon, proton, antiproton, helium and other heavy nuclei. For electromagnetic study, electrons are generated isotropically from a square plane of $3.9 \times 3.9 \text{ m}^2$ located at 1.95 m above

the detector center. The generation acceptance A_{gen} is calculated by

$$\begin{aligned}
 A_{gen} &= \int_S \int_{\Omega} \vec{dS} \cdot \vec{n} d\Omega \\
 &= \int_S \int_{\phi=0}^{2\pi} \int_{\theta=0}^{\pi/2} \cos \theta \sin \theta d\theta d\phi \\
 &= 2\pi S \times \frac{1}{2} [\sin^2 \theta]_0^{\pi/2} \\
 &= 2\pi \times 3.9^2 \times \frac{1}{2} \simeq 47.8 m^2 \cdot sr
 \end{aligned} \tag{2.6}$$

The MC electrons are respectively generated in 3 energy ranges, from 0.25 GeV to 5 GeV, from 5 GeV to 100 GeV, and from 100 GeV to 2 TeV. The statistics of version B620 for each energy range are given in Table 2.3. The generation spectrum is a power law function of degree of -1 of

Energy (GeV)	0.25 - 5	5 - 100	100 - 2000
Generated events	44×10^9	27×10^9	2×10^8

Table 2.3: Statistics of electron MC data version B620 type p11.

generated energy, referred to as E_{true} , as is shown in Figure 2.27, covering a continuous energy range up to 2 TeV. A re-weighting of the MC spectrum to the measured one is still necessary in some case. It represents a compromise between the true cosmic ray spectrum decreasing with energy and the interest to have large statistics at high energy.

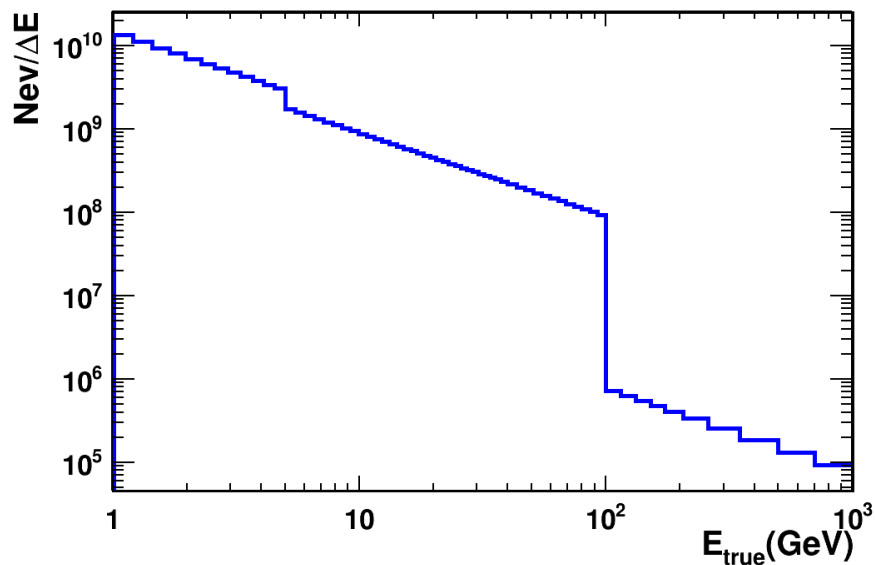


Figure 2.27: MC generation spectra as a function of energy. Number of events divided by the bin width is drawn in Y to reduce the binning effect.

Chapter 3

Control of the energy measurement

The lepton flux, which follows a power law of energy, E^α with $\alpha \sim -3$, is measured in bins of lepton energies. Therefore the correct determination of ECAL energy scale is crucial for this measurement. The absolute energy scale of ECAL has been determined using test beam data before the launch of AMS-02. During the flight, the energy scale has been monitored using the E/P method. A method based on the geomagnetic cutoff has also been developed to verify this scale.

In this chapter, we describe the calibration and the uncertainties of the ECAL energy, using test beam data and ISS data.

3.1 Energy scale with test beam data

The absolute energy scale is obtained using minimum ionizing protons in test beam. And in the case of EnergyA, it is also completed by using well contained electron events from test beam data at 10 and 20 GeV. The lepton energy is reconstructed after several corrections as explained in Section 2.1.5.1. Therefore the distribution of reconstructed energy over beam energy ($E_{\text{rec}}/E_{\text{beam}}$) should be peaked at one if the ECAL energy scale is correct. In the

following, this linearity is controlled at different beam energies and the behavior with different incidence angles is studied.

3.1.1 Distributions of $E_{\text{rec}}/E_{\text{beam}}$

Figure 3.1 shows the $E_{\text{rec}}/E_{\text{beam}}$ distributions for positrons at 20 GeV and electrons at 180 GeV, with incidence angle of $\theta < 2^\circ$, where θ is calculated from the tracker track extrapolated to the ECAL. The distributions are fitted with a Gaussian function with a procedure as follow,

1. fit with a Gaussian on the interval (0.85, 1.1); obtain the mean value μ_0 and width σ_0 .
2. repeat the Gaussian fit on the interval $(\mu_0 - 1.5\sigma_0, \mu_0 + 1.5\sigma_0)$; Mean and Sigma from the second fit result are noted as mean and sigma of the $E_{\text{rec}}/E_{\text{beam}}$ distribution.

The error of the ECAL energy scale is found to be within 0.2% and 0.6% for 20 GeV positrons and 180 GeV electrons, respectively.

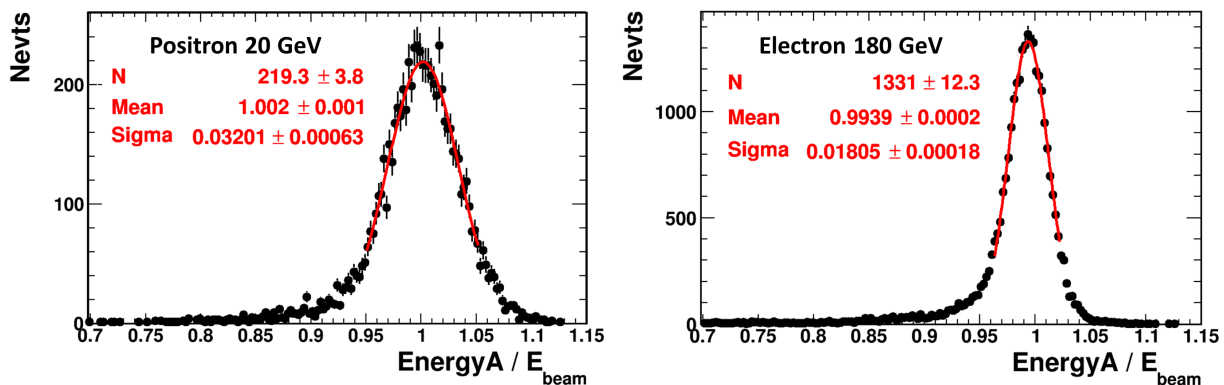


Figure 3.1: Distributions of $E_{\text{rec}}/E_{\text{beam}}$ with EnergyA for test beam positrons at 20 GeV (left) and test beam electrons at 180 GeV (right), with a fitted Gaussian function shown in red curve. The mean of the Gaussian is used to determine the energy scale, and the width refers to the energy resolution.

3.1.2 Energy dependence of $E_{\text{rec}}/E_{\text{beam}}$

The precise beam energy of each dataset is given in Table 3.1. With the fit results of Mean and Sigma presented previously, variation of $E_{\text{rec}}/E_{\text{beam}}$ as a function of energy is obtained. In Figure 3.2 and Figure 3.3, energy scale and the resolution for test beam e^+ and e^- with incidence angle $\theta < 2^\circ$ are shown.

Energy (GeV)	10	20	80	100	120	180	300
Positron beam	10	20	80	100	120	179.5	–
Electron beam	–	–	–	100	120	178.6	290.8

Table 3.1: Beam energy for test beam positron and electron datasets.

The peak position of $E_{\text{rec}}/E_{\text{beam}}$, Mean, is stable and close to 1 for all energies. Most of them

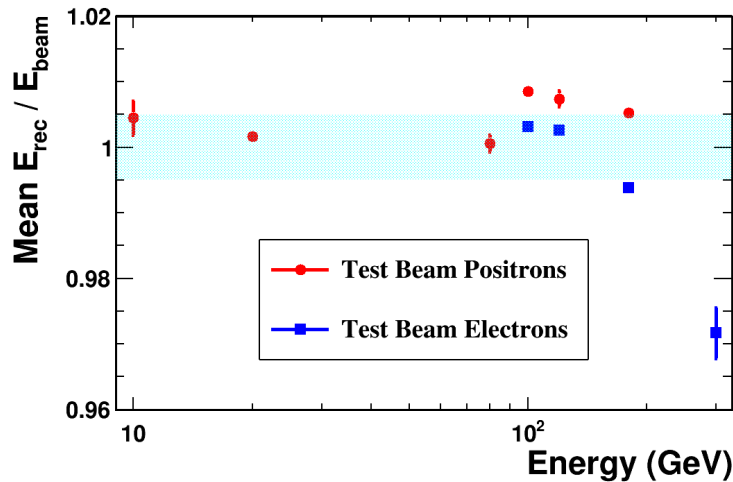


Figure 3.2: Variation of the Mean $E_{\text{rec}}/E_{\text{beam}}$ as a function of energy for vertically incident positrons in red and electrons in blue. Error bars are fit errors of the parameter Mean. The cyan band indicates boundaries of 1 ± 0.005 .

are compatible within the cyan band, which indicates a region of 0.5%. The energy resolution

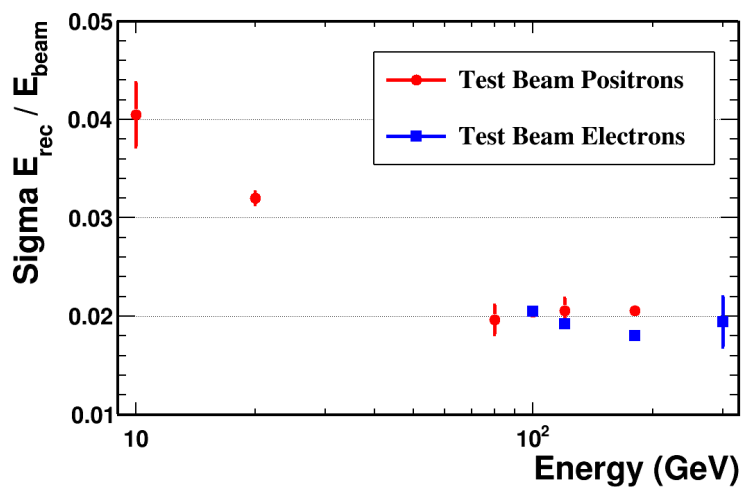


Figure 3.3: Variation of $E_{\text{rec}}/E_{\text{beam}}$ resolution as a function of energy, positrons in red and electrons in blue. Error bars are fit errors of the parameter Sigma.

of EnergyA improves with energy, approximately 4% at 10 GeV and 2% at 300 GeV.

3.1.3 $E_{\text{rec}}/E_{\text{beam}}$ for different angles

Positron and electron test beams are not isotropic. Distributions of the incidence angles are shown in Figure 3.4 and Figure 3.5 for all the test beam datasets.

Five peaks are observed in the angle distribution, at 0° , 3° , 5° , 10° and 15° . The dependence of

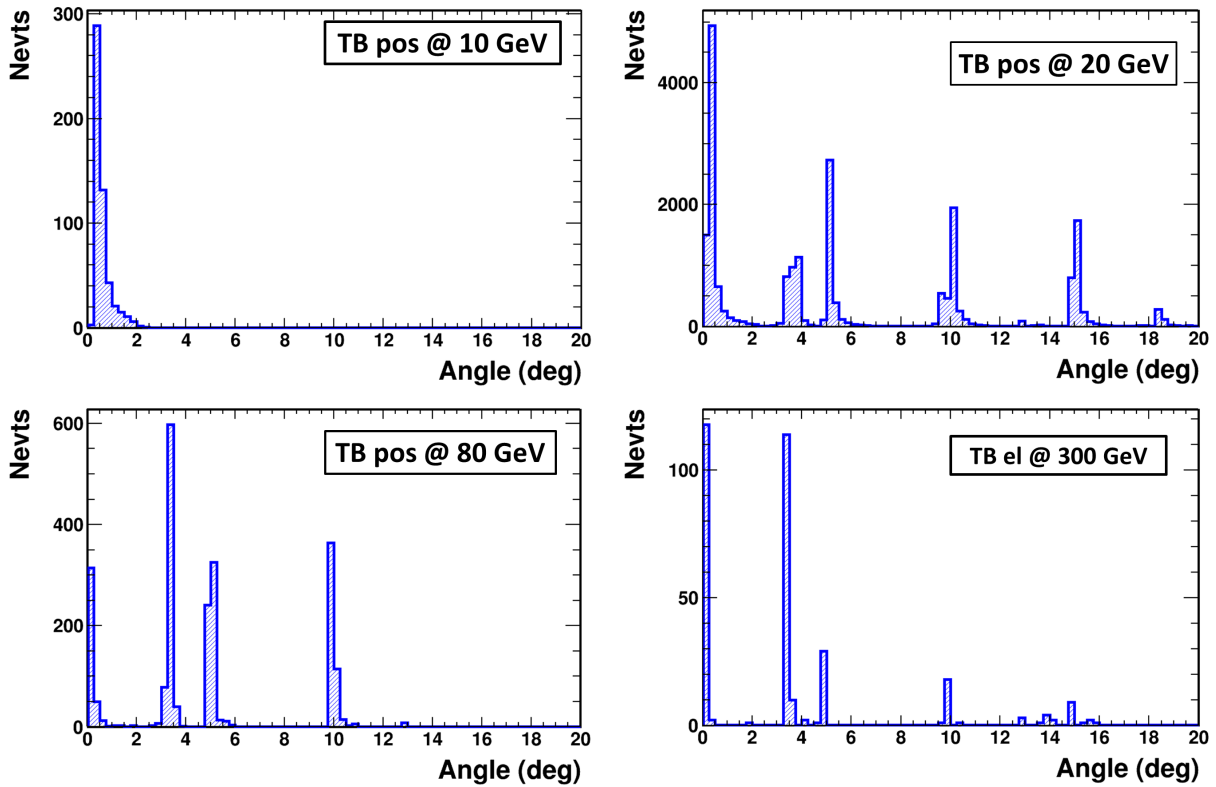


Figure 3.4: Distributions of particle incidence angle (angle between axis Z and track extrapolation at ECAL entry) for test beam positrons and electrons. The angle unit is degree.

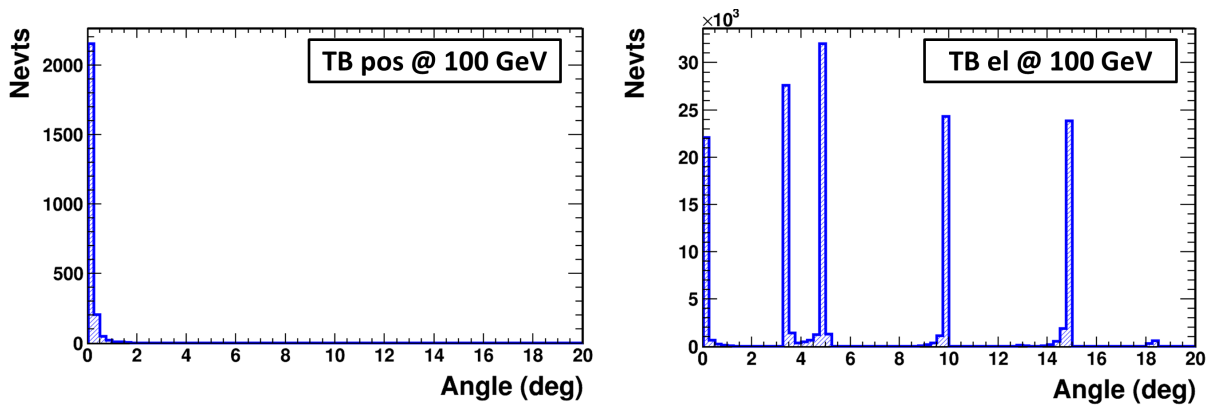


Figure 3.5: Distributions of particle incidence angle for test beam positrons and electrons at 100 GeV. The angle unit is degree.

$E_{\text{rec}}/E_{\text{beam}}$ as a function of incidence angle is shown in Figure 3.8 and Figure 3.9 for 20 GeV e^+

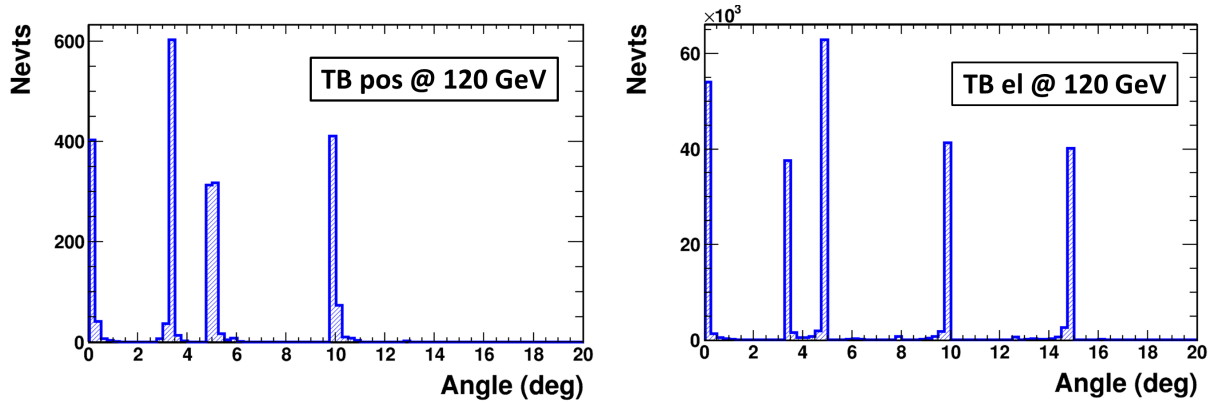


Figure 3.6: Distributions of particle incidence angle for test beam positrons and electrons at 120 GeV. The angle unit is degree.

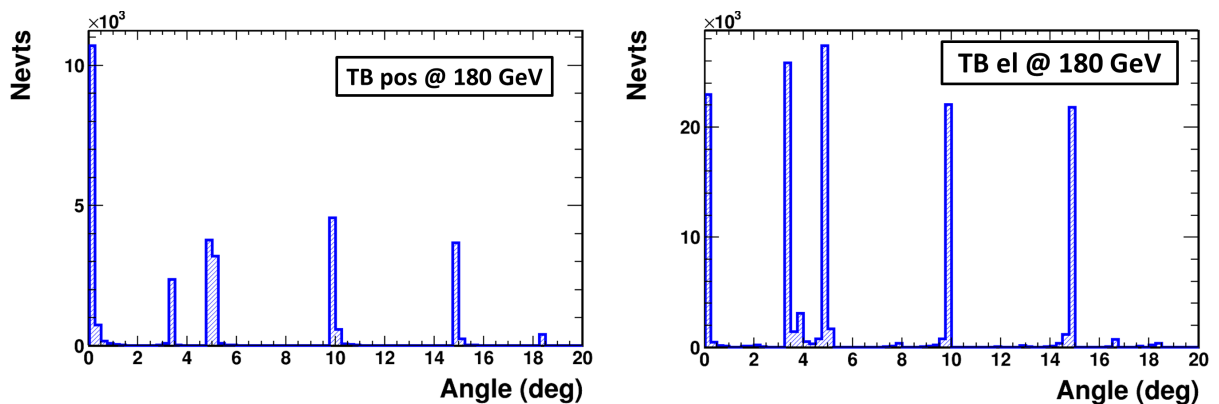


Figure 3.7: Distributions of particle incidence angle for test beam positrons and electrons at 180 GeV. The angle unit is degree.

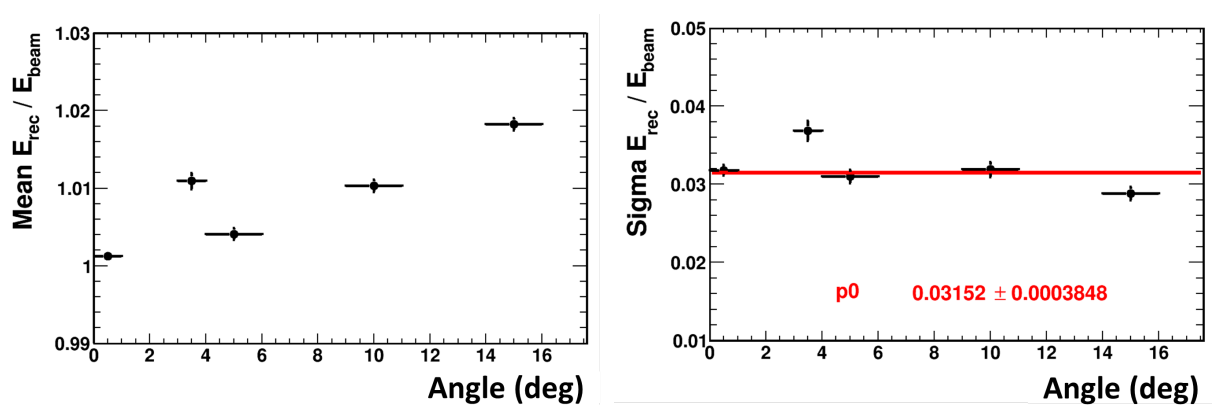


Figure 3.8: Angle dependence of $E_{\text{rec}}/E_{\text{beam}}$ with test beam positrons at 20 GeV. Mean (left) and Sigma (right) are shown as a function of angle (angle between the track extrapolation and Z axis). The sigma is fitted with a constant, fit results in red.

and 120 GeV e^- . In EnergyA, no angle correction is applied. Therefore, $E_{\text{rec}}/E_{\text{beam}}$ becomes larger as shower gets more inclined. Energy resolution stays stable with angle, no dependence observed.

$E_{\text{rec}}/E_{\text{beam}}$ Mean is measured for all test beam datasets as a function of incidence angle. The

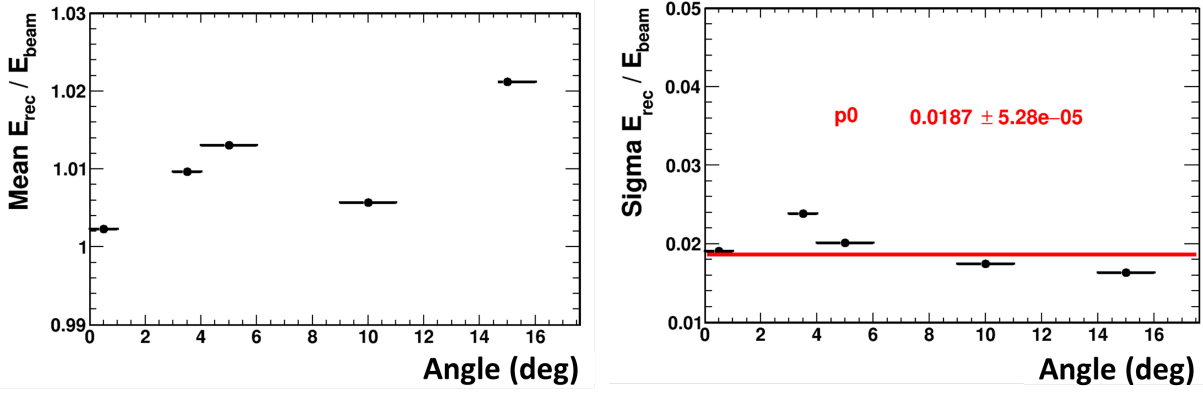


Figure 3.9: Angle dependence of E_{rec}/E_{beam} with test beam electrons at 120 GeV. The sigma is fitted with a constant, fit results in red.

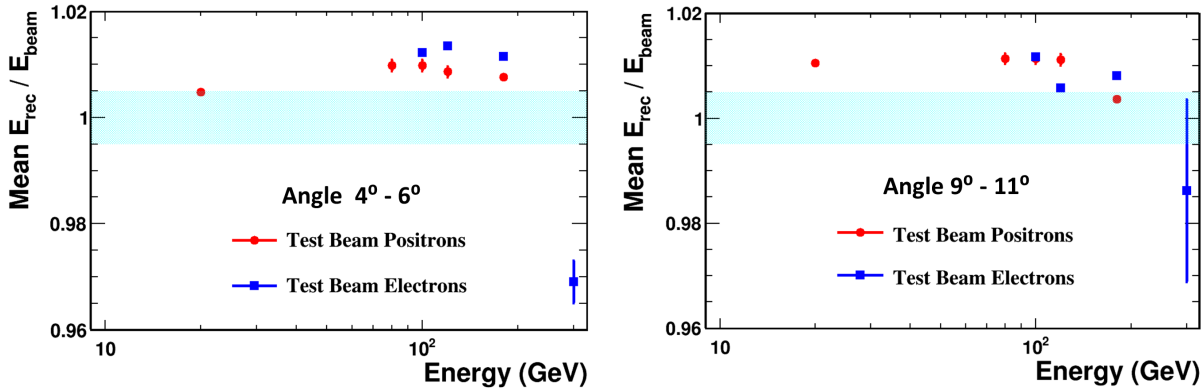


Figure 3.10: Variation of the Mean E_{rec}/E_{beam} as a function of energy, incident angle between 4°- 6°(left) and between 9°- 11°(right). The cyan bands indicate boundaries of $1 \pm 0.5\%$.

results of e^+ and e^- beams with angle between 4°- 6°and between 9°- 11°are shown in Figure 3.10. Compared to Figure 3.2, the mean value is larger for particles with larger incidence angles.

3.2 E/P control with test beam and ISS data

E/P, ratio of reconstructed energy measured by the ECAL over rigidity measured by the tracker, provides a calibration method with ISS electrons, which are selected with cuts on TRD_{LER} and ESE_{V3} .

3.2.1 Distribution of E/P

First, pure electron samples are selected with tight cuts on TRD_{LER} , ESE_{V3} , tracker track and ECAL shower quality, TOF charge and tracker charge and Tracker-ECAL matching, which

are explained in details in **lepton selection** (Section 4.2).

- $TRD_{LER} < 0.65$
- $ESE_{V3} > -0.05$
- TOF charge < 1.8 and tracker charge < 1.5
- Track
 - only 1 tracker track present
 - χ^2 of the track fit is smaller than 10
 - track hit pattern is L1L9 (hit on both layer 1 and 9)
 - negative rigidity required for ISS data and test beam electrons; positive rigidity required for test beam positrons
- ECAL
 - only 1 ECAL shower reconstructed
 - the inclination angle of the shower is within 4°
 - shower fiducial cut: the shower axis is 4 cells away from the ECAL border
- Tracker-ECAL matching within 3 cm in X direction and 5 cm in Y

Pure electron samples are obtained by applying the selection on both test beam and ISS data. Efficiency of the selection is $\sim 25\%$ for electrons. E/P distributions of the samples are fitted with Crystal Ball function on the interval of 0.6 to 4 (Figure 3.11). The fitted mean is greater than 1 due to the fact that photons produced by bremsstrahlung in the tracker are not captured in the track reconstruction, but are collected in the ECAL shower. As a result, the measured P is smaller than E.

ISS electrons are divided into 12 energy bins from 10 to 300 GeV (cf. Table 3.2). The E/P distributions of ISS electrons for different categories are shown in Figure 3.12, fitted with Crystal Ball as well.

The E/P distributions of leptons are hence described by Crystal Ball function with its four

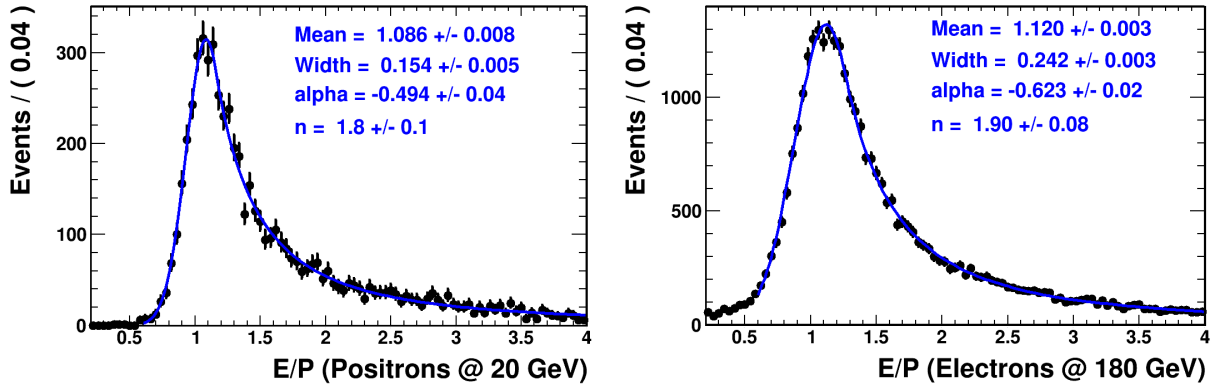


Figure 3.11: E/P distributions with test beam positrons at 20 GeV and electrons at 180 GeV (black dots), fitted with Crystal Ball function (blue) on the interval (0.6, 4). Fit results of the four parameters are shown in blue.

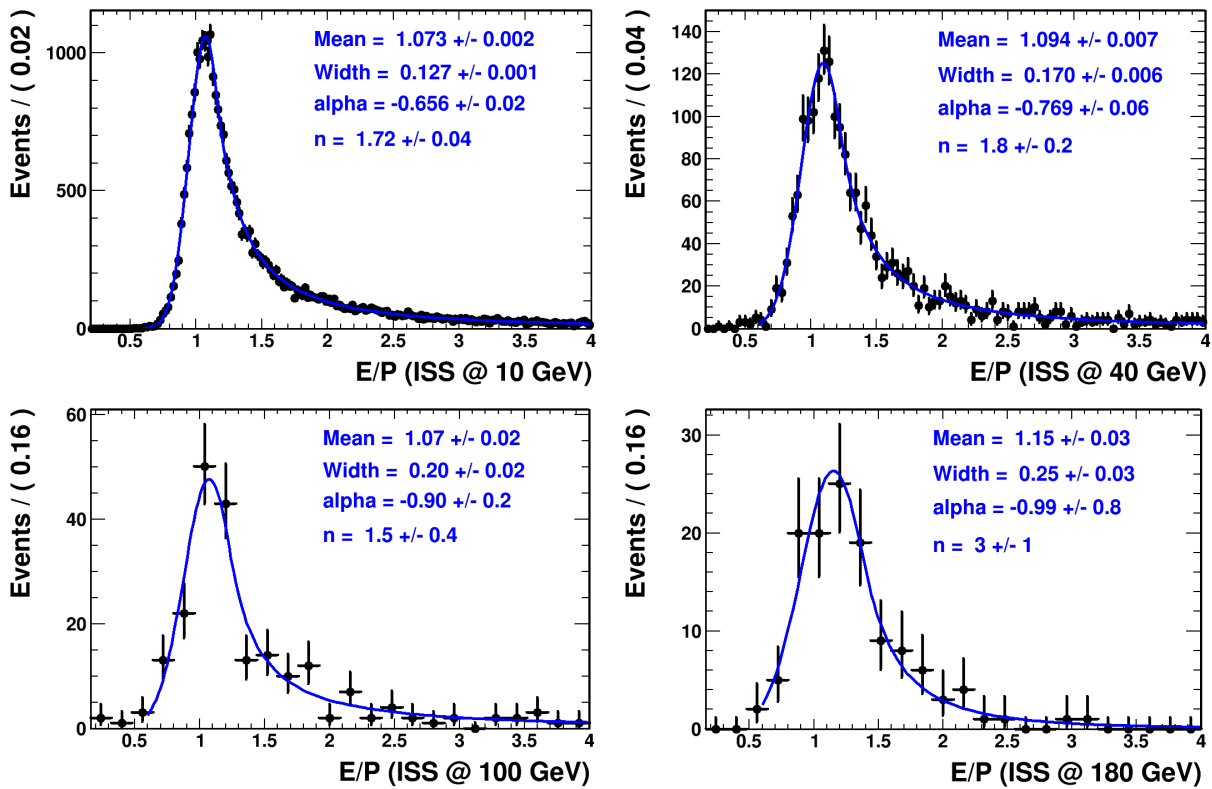


Figure 3.12: E/P distribution with ISS electrons at 10 GeV, 40 GeV, 100 GeV and 180 GeV (black dots), fitted with Crystal Ball function (blue) on the interval (0.6, 4). Fit results of the four parameters are shown in blue.

parameters. The mean value corresponds to the E/P peak position, which is an important indicator in energy control study.

3.2.2 Energy dependence of E/P with ISS data

As observed in Figure 3.12, fitted value of Mean changes with energy. To study the energy dependence of E/P peak position, 12 energy ranges are chosen for ISS electrons, including the 7 test beam energies. The energy range selection is listed in Table 3.2.

The 12 E/P distributions of ISS electrons are respectively fitted with Crystal Ball function.

Datasets (GeV)	TB pos	TB el	ISS
10	10		9 - 11
15			13.5 - 16.5
20	20		18 - 22
30			27 - 33
40			36 - 44
50			45 - 55
64			57.6 - 70.4
80	80		72 - 88
100	100	99.9	90 - 110
120	119.9	120	108 - 132
180	179.5	178.6	144 - 216
300		290.8	240 - 360

Table 3.2: Energy ranges used for E/P study. test beam: beam energy. ISS: energy intervals used to select electron sub-samples.

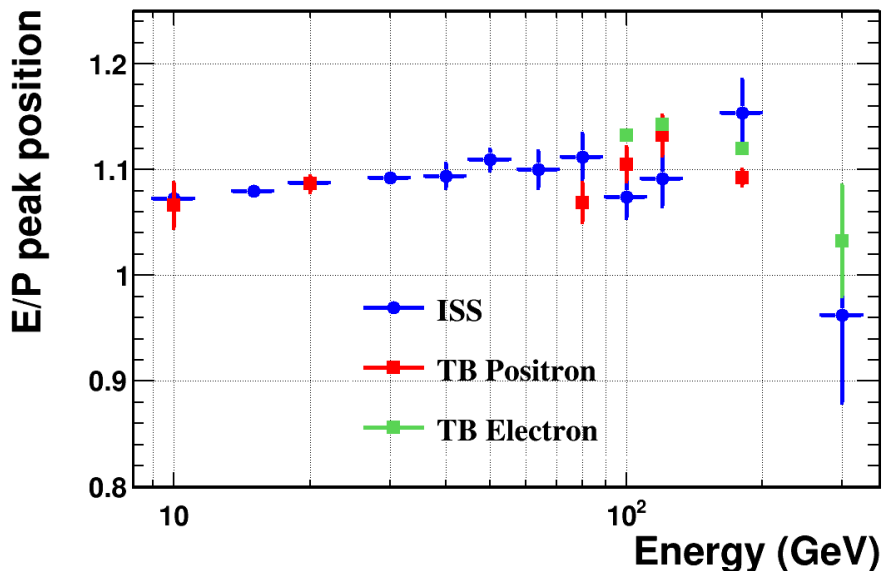


Figure 3.13: E/P peak position of ISS electrons as a function of energy (blue), in comparison with the peak positions of test beam positrons (red) and electrons (green). Error bars are uncertainty of the parameter Mean from the fit.

Their Mean values are given in Figure 3.13 as a function of energy. It is observed that below

200 GeV, E/P peak position slowly increases with energy and at 300 GeV, the peak position drops partly due to rear leakage of the ECAL shower.

The Peak positions of test beam positrons and electrons are also drawn in Figure 3.13, which are in good agreement with the ISS results. The same trend of increase with energy is observed.

3.2.3 Comparison of E/P peak position between test beam and ISS data

Peak positions of ISS data and test beam positrons and electrons are compared for each energy bin of test beam. The ratio of ISS over test beam is shown in Figure 3.14. The ratios are

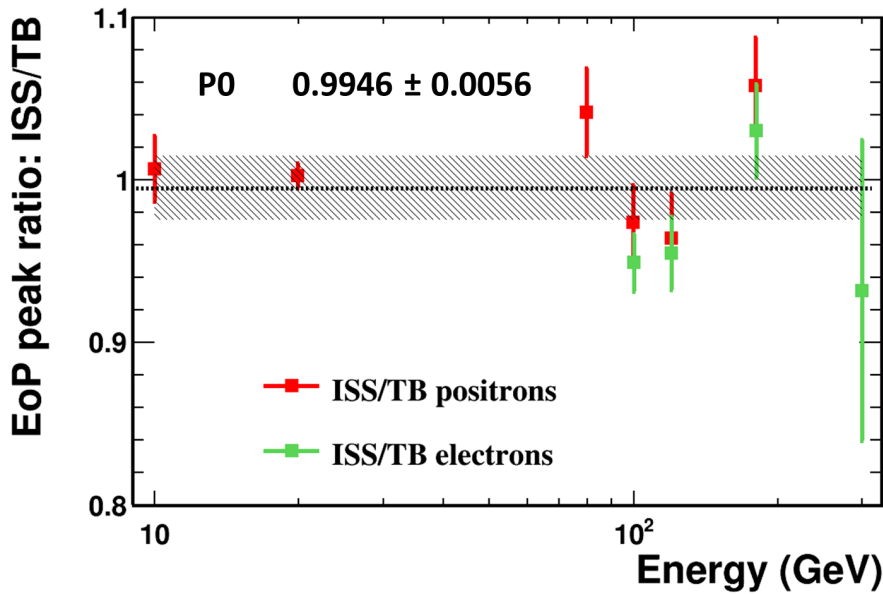


Figure 3.14: Ratio of ISS E/P peak position over the test beam peak position, fitted with constant function $f(x)=P_0$. Conservative uncertainty of 2% is drawn in black shade.

distributed close to 1, fitted by the constant function of 0.99 ± 0.01 . Conservative uncertainty of 2% is attributed to account for the angular dependence of energy.

3.2.4 Time dependence of E/P with ISS data

Variation of E/P peak position as a function of time allows to monitor the calibration of ECAL on the ISS. The time dependence of E/P is studied for four energy ranges with 29 months of ISS electrons.

Time correction of ECAL energy is obtained from variation of minimum ionizing protons in

ISS data along time. Figure 3.15 shows the MIP variation from June 2011 to November 2013.

Figure 3.16 shows the time dependence of E/P, with and without the time correction obtained

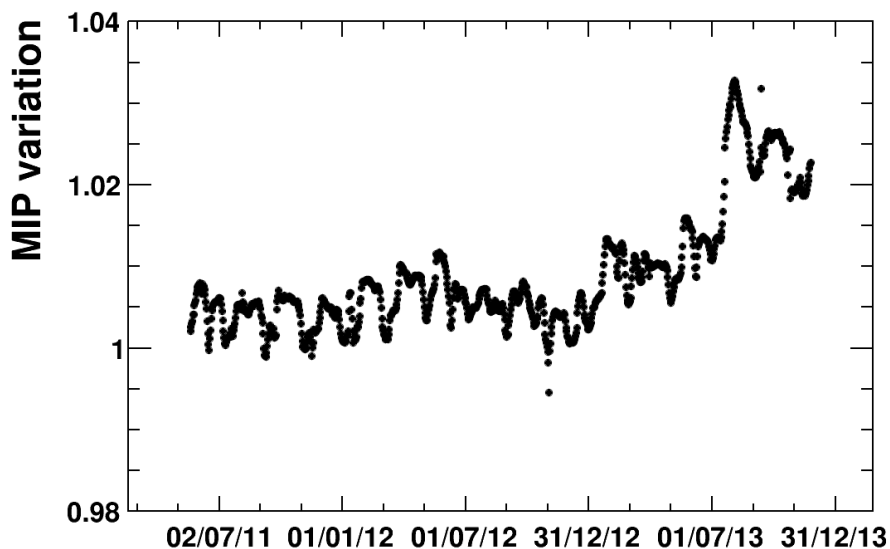


Figure 3.15: Variation of MIP signal in the ECAL with time [44]. The small fluctuations are due to instabilities of temperature and high voltage of the ECAL. The big jump in July 2013 is due to change of equalization method.

from MIP variation along time. The corrected values in blue are flatter and more stable with time.

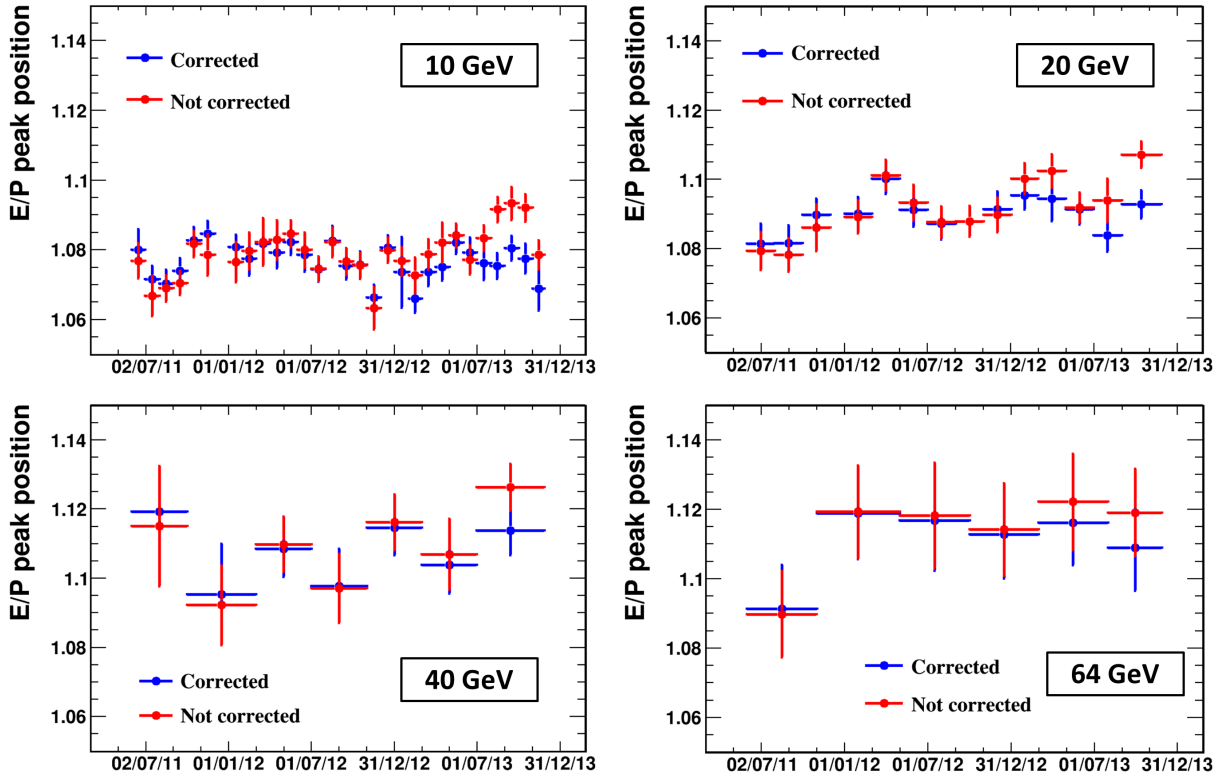


Figure 3.16: Variation of E/P peak as a function of time with ISS electrons at 10 GeV (upper left), 20 GeV (upper right), 40 GeV (lower left) and 64 GeV (lower right) for the period of June 2011 to November 2013. E/P at 10 GeV is checked per month, 20 GeV per two months, 40 GeV per 4 months and 64 GeV per 5 months. The red dots are E/P with uncorrected energy and the blue dots are with corrected energy.

3.3 Energy control at low energy with geomagnetic cut-off rigidity

The previous method using E/P relies on the stability of the rigidity measurement and of the tracker alignment, which introduces additional systematic uncertainty. To verify the absolute energy scale with ECAL alone in the space, it is necessary to find sources with spectral features such that the energy peak and shape are well known. The geomagnetic cutoff effect provides exactly such spectral features, if the cutoff rigidities are perfectly known.

Principle of this method is to compare, for a specified zone where particles are submitted to the same geomagnetic cutoff rigidity (R_{cut}), the measured R_{cut} and the one predicted by models (Section 1.3.2.3). The measurement of R_{cut} is realized by fitting the peak of energy distribution of ISS electrons (Section 3.3.2). The comparison between the predicted and measured R_{cut} allows to monitor the ECAL energy scale at low energy, particularly below 20 GeV. Similar

approach has been explored by Fermi-LAT experiment [45], which has obtained an energy scale accuracy to $\sim 5\%$ level.

3.3.1 Störmer cutoff rigidity map

The R_{cut} is calculated with Equation (1.15), which depends on two parameters the east-west angle (α_{EW}) and the geomagnetic colatitude (λ_{LatC}). The formula for negatively charged particles simplifies to:

$$R_{\text{cut}} = A \frac{\cos^4 \lambda_{\text{LatC}}}{(1 + \sqrt{1 + \cos \alpha_{\text{EW}} \cos^3 \lambda_{\text{LatC}}})^2} \quad (3.1)$$

where A is a known coefficient. The dependence of R_{cut} on α_{EW} and λ_{LatC} is shown in Figure 3.17 as well as the R_{cut} dispersion. The angular precision of the map is 0.5×0.5 . The model uncertainty is not included. It is observed in the map that the cutoff rigidity distribution is

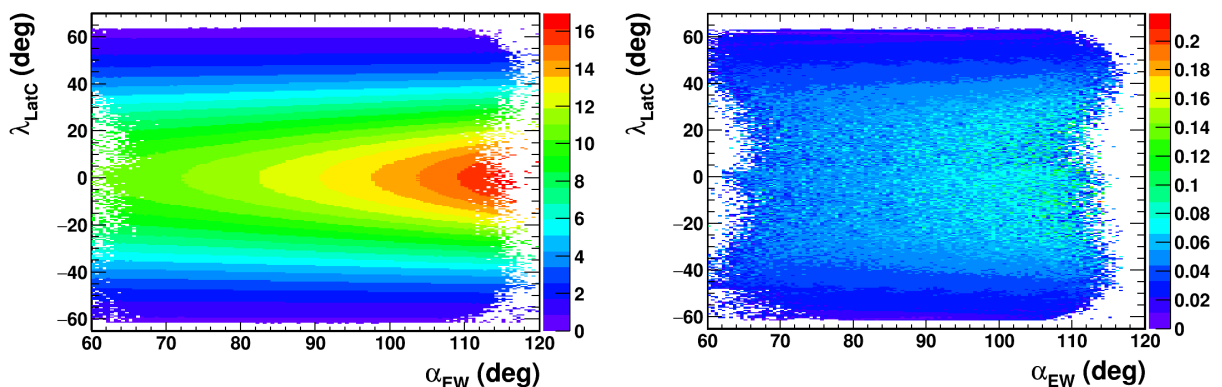


Figure 3.17: Geomagnetic cutoff rigidity (R_{cut}) predicted by Störmer approximation for electrons (left) and the R_{cut} dispersion map (right). λ_{LatC} is geomagnetic colatitude and α_{EW} is east-west angle. The unit of Z axis is GeV.

symmetric about the axis of $\lambda_{\text{LatC}} = 0^\circ$ and decreasing as approaching the magnetic north and south poles, $\lambda_{\text{LatC}} \rightarrow -90^\circ$ or 90° , as expected from Equation (3.1). The highest predicted R_{cut} is ~ 16 GeV at the equator with an α_{EW} of 120° . In this map, α_{EW} is only shown between 60° and 120° due to the limited azimuthal angle of AMS; λ_{LatC} is only shown between 20° and 160° due to the lack of available data near the two poles, where ISS seldom passes by.

3.3.2 Geomagnetic cutoff rigidity measurement

Dependence of R_{cut} on the λ_{LatC} observed with cosmic-ray protons has been shown in Figure 1.16. It suggests that the R_{cut} for a given latitude can be deduced from the cutoff feature of

the measured spectra. Similar measurement is repeated in the following analysis with cosmic-ray electrons. The R_{cut} is obtained by fitting the electron spectrum measured at a specified bin of α_{EW} and λ_{LatC} .

Equi- R_{cut} zone on R_{cut} map

Electrons with the same $(\alpha_{\text{EW}}, \lambda_{\text{LatC}})$ have the same R_{cut} . The cutoff feature at R_{cut} should be observed in their spectrum. An example of the bin in the map center with coordinates $(\alpha_{\text{EW}} = 90^\circ, \lambda_{\text{LatC}} = 0^\circ)$ is shown in Figure 3.18. In this specific bin, the predicted R_{cut} is $\text{geo} \sim 12.65$

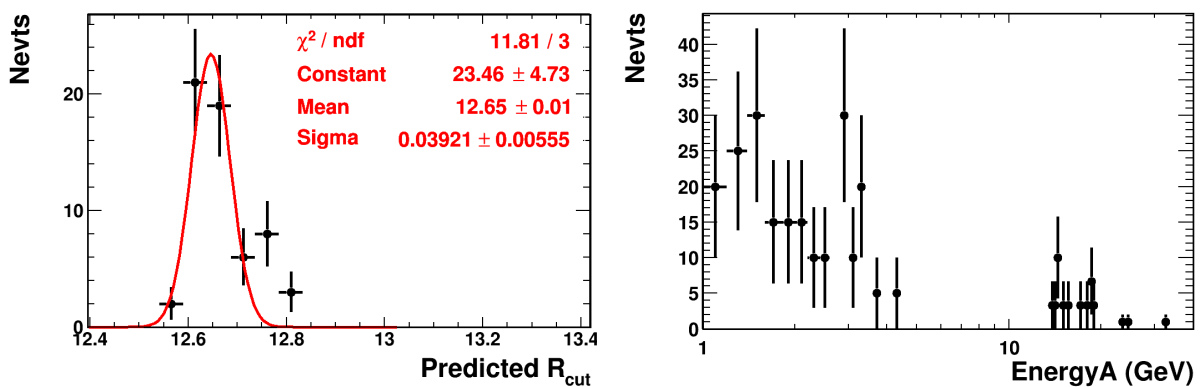


Figure 3.18: Projection of the R_{cut} map in the center cell ($\alpha_{\text{EW}} = 90^\circ, \lambda_{\text{LatC}} = 0^\circ$), predicted R_{cut} distribution fitted with a Gaussian function (left). Measured electron spectrum for the same cell (right).

GV with a dispersion of ~ 0.04 GV and the measured spectrum exhibits a cutoff feature at above 10 GeV. However, the low statistics does not allow a reliable fitting.

To increase the statistics of electrons with the same R_{cut} , two methods are possible: enlarge the bins or combine them. The former method results in an larger dispersion of R_{cut} whereas the latter better keeps the original dispersion. Therefore, electron samples from bins with the same predicted R_{cut} values (**equi- R_{cut} zone**) are combined.

In Figure 3.19 left column, the equi- R_{cut} zone with R_{cut} between 3.9 GV and 4.1 GV is selected from the R_{cut} map. The predicted R_{cut} distribution and the measured electron energy spectrum in the specified zone are shown. On the right column, example of a higher R_{cut} between 12.9 GV and 13.1 GV is shown.

Electron spectrum fit

In order to measure the R_{cut} of a specified equi- R_{cut} zone, the obtained electron spectrum (eg. the two spectra on the bottom of Figure 3.19) is fitted with a parametrized function $\mathcal{F}(E)$.

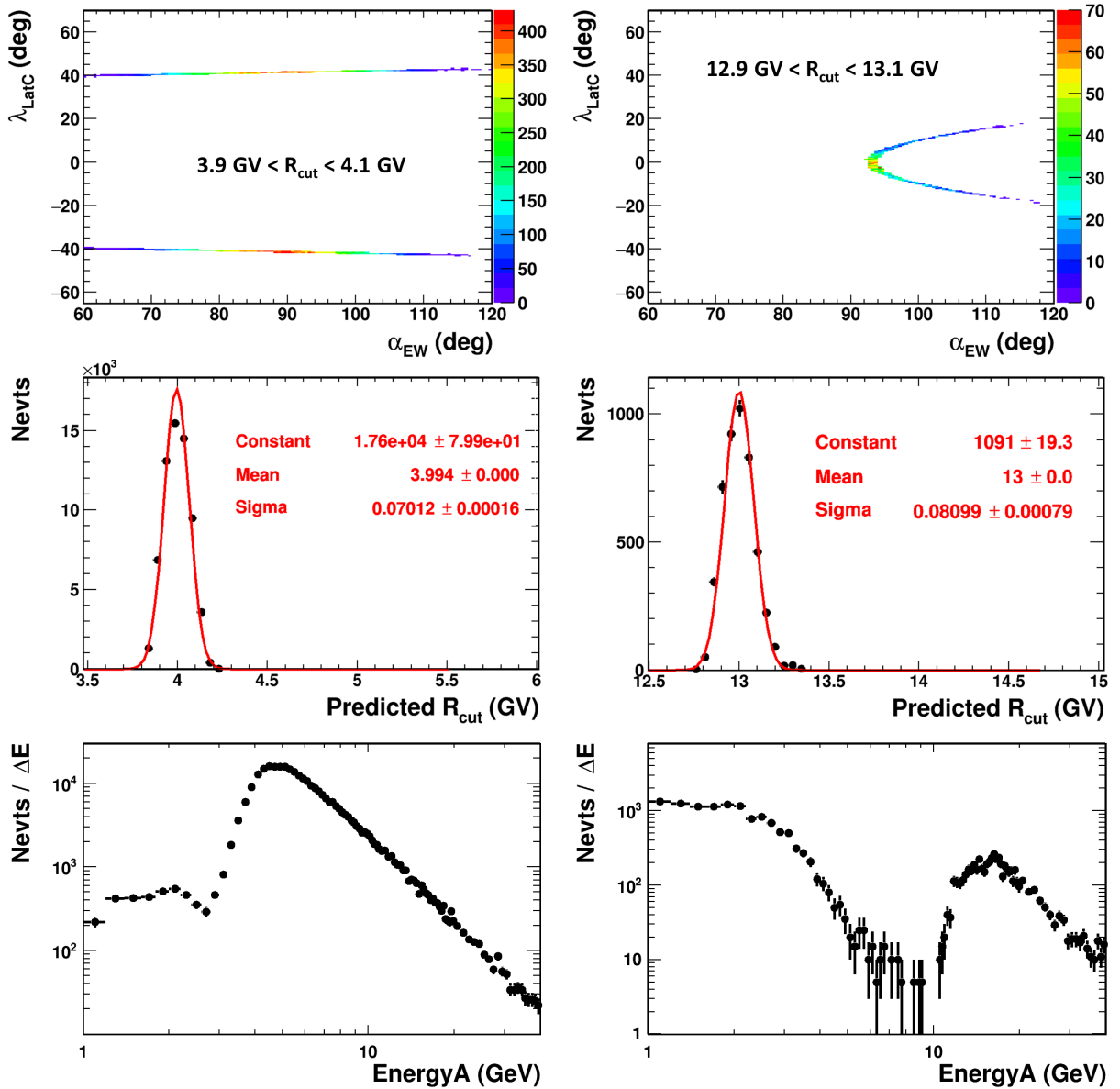


Figure 3.19: Column left: (top) bands with the R_{cut} between 3.9 GV and 4.1 GV, axis Z is number of events; (middle) distribution of theoretical R_{cut} in the selected bands; (bottom) energy spectrum of electrons in the selected bands with 29 months ISS data. Column right: the same distributions for R_{cut} between 12.9 GV and 13.1 GV.

Suppose that for a given equi- R_{cut} zone, the true R_{cut} distribution $\mathcal{R}(x)$ is a Gaussian function

with a mean of c and a width of σ . The measured spectrum should be:

$$\begin{aligned}
 \mathcal{F}(E) &= \int_0^\infty \Phi(E)H(E-x)\frac{1}{\sigma\sqrt{2\pi}}\mathcal{R}(x)dx \\
 &= \frac{\Phi(E)}{\sigma\sqrt{2\pi}}\int_0^E e^{-\frac{(x-c)^2}{2\sigma^2}}dx \\
 &= \frac{\Phi(E)}{\sqrt{\pi}}\int_{-\frac{c}{\sqrt{2}\sigma}}^{\frac{E-c}{\sqrt{2}\sigma}} e^{-t^2}dt \\
 &= \frac{\Phi(E)}{2}\left(\text{Erfc}\left(-\frac{c}{\sqrt{2}\sigma}\right) - \text{Erfc}\left(\frac{E-c}{\sqrt{2}\sigma}\right)\right)
 \end{aligned} \tag{3.2}$$

where $\Phi(E)$ is the spline function¹ of primary electron rate in Figure 3.20, $H(E-x)$ is Heaviside

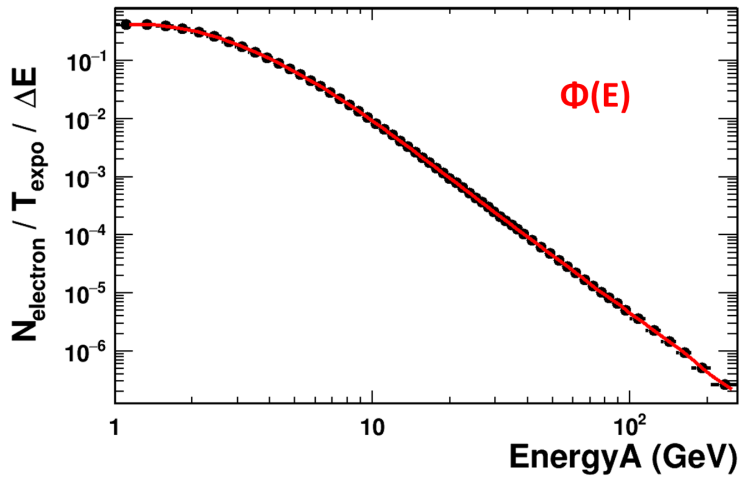


Figure 3.20: Number of electrons divided by exposure time and bin width (black dots) measured with 29 months of ISS data. The obtained histogram is fitted with a spline function up to 200 GeV (red).

step function defined as 0 if $E < x$ and 1 if $E > x$ and Erfc is the complementary error function. $\mathcal{F}(E)$ is used to fit the two electron spectra in Figure 3.21. The second parameter of fit is the measured R_{cut} .

Verification of the fit procedure with MC data

The fit method is repeated with MC data. The input spectrum and cutoff spectra in EnergyA are given in Figure 3.22, for cutoff at 5 GeV and 13 GeV. The input spectrum is the renormalized $\Phi(E)$ in Figure 3.20. The geomagnetic cutoff effect is simulated by cutting on the E_{true} . In this case, the predicted R_{cut} distribution is a Dirac delta function.

¹Spline is a numeric function that is piecewise-defined by polynomial functions, and which possesses a sufficiently high degree of smoothness at the places where the polynomial pieces connect (which are known as knots).

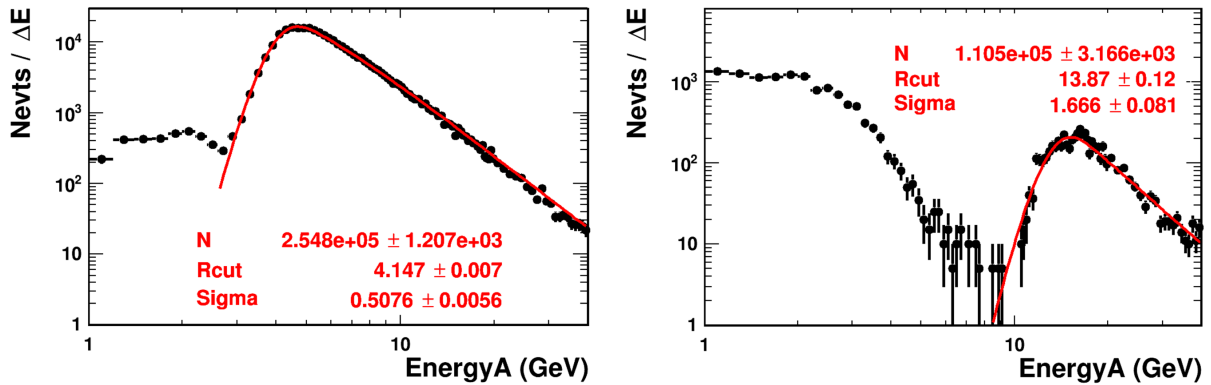


Figure 3.21: Electron spectra fitted with $\mathcal{F}(x)$ for R_{cut} between 3.9 - 4.1 GV (left) and between 12.9 - 13.1 GV (right). The measured R_{cut} results are respectively 4.1 GV and 13.9 GV with an error of less than 1%.

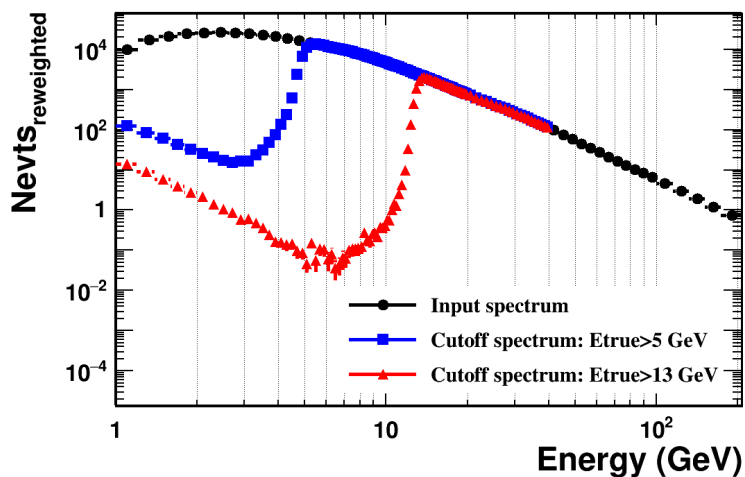


Figure 3.22: With MC data: input spectrum in E_{true} without cutoff (black), cutoff spectra in EnergyA for cutoff energy at 5 GeV (blue) and 13 GeV (red).

The spectra are fitted with $\mathcal{F}(E)$ in Equation (3.2), in which the $\Phi(E)$ is replaced by the input spectrum in Figure 3.22. The fit results for cutoff at 5 GeV and 13 GeV are shown in Figure 3.23. The measured R_{cut} are respectively 4.96 GeV and 13.07 GeV, which are in good agreement with the predicted values. The comparison results are shown in Figure 3.24 for 12 different predicted R_{cut} in the range of 3 GeV to 14 GeV.

The linear dependence of measured R_{cut} on predicted R_{cut} with MC data shows that the uncertainty of this fit method is about 1%.

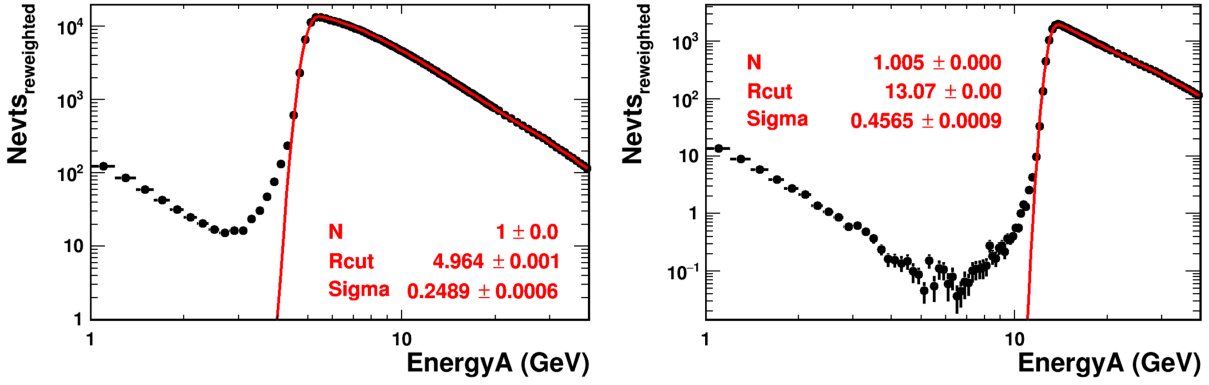


Figure 3.23: MC simulation of cutoff spectra fitted with $\mathcal{F}(E)$, R_{cut} at 5 GeV (left) and at 13 GeV (right).

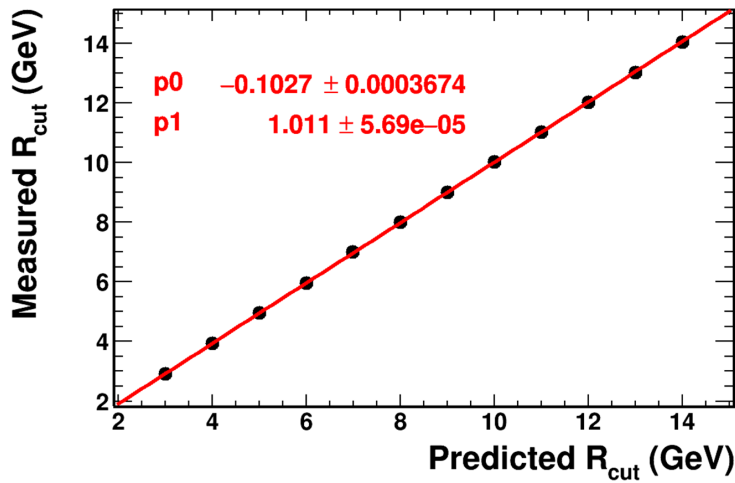


Figure 3.24: Measured R_{cut} as a function of predicted values (MC data). The dependence is fitted with a linear function (red): $f(x) = p_0 + p_1 \times x$.

3.3.3 Comparison of measured and predicted R_{cut}

The measured and predicted R_{cut} values are compared for 41 equi- R_{cut} zones, from 2.5 GV to 14.5 GV. The result is shown in Figure 3.25. The measured R_{cut} is higher than predicted and small structures are observed. This possibly comes from the limit of the Störmer approximation. Other models such as IGRF method should provide more precise cutoff estimation.

3.3.4 Energy control with R_{cut} obtained from IGRF model

The same study is repeated using the R_{cut} obtained from the IGRF model instead of Störmer approximation.

The IGRF R_{cut} does not explicitly depend on the α_{EW} . Therefore, the map is drawn as a

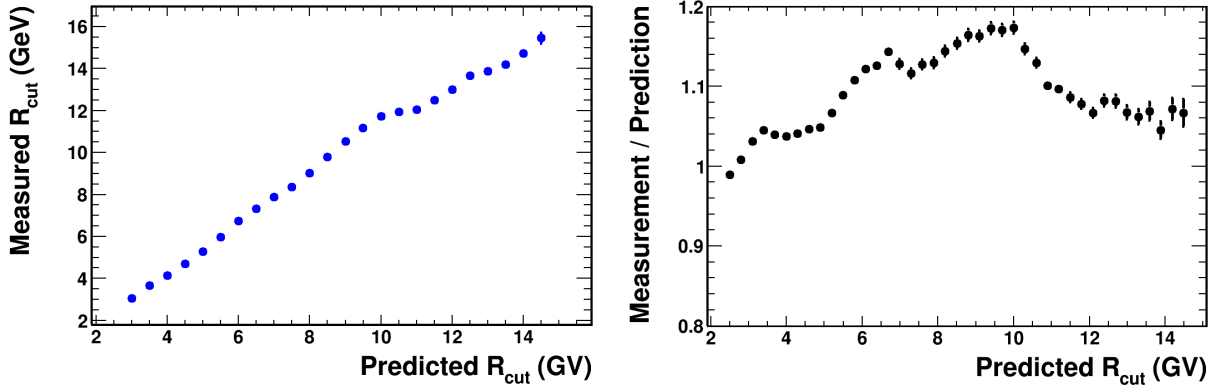


Figure 3.25: Measured R_{cut} values as a function of the predicted R_{cut} for the 41 equi- R_{cut} zones. The ratio of measurement over prediction is shown in the right plot. 29 months of ISS data are used.

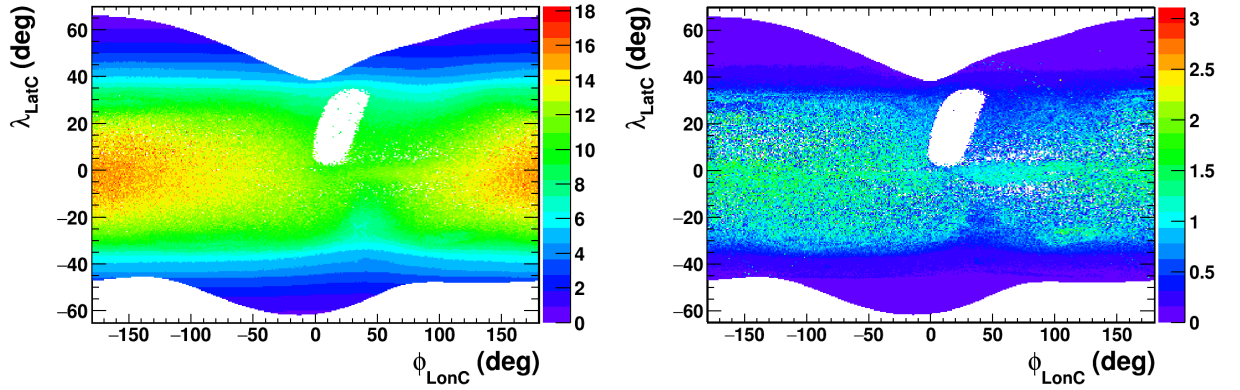


Figure 3.26: R_{cut} predicted by IGRF model for electrons (left) and the R_{cut} dispersion map (right). ϕ_{LonC} is geomagnetic longitude. The unit of Z axis is GeV. The white spot represents the SAA region.

function of ϕ_{LonC} - λ_{LatC} in Figure 3.26, where ϕ_{LonC} is the geomagnetic longitude.

Figure 3.27 illustrates the fit procedure repeated for all the equi- R_{cut} zones. The resolution of

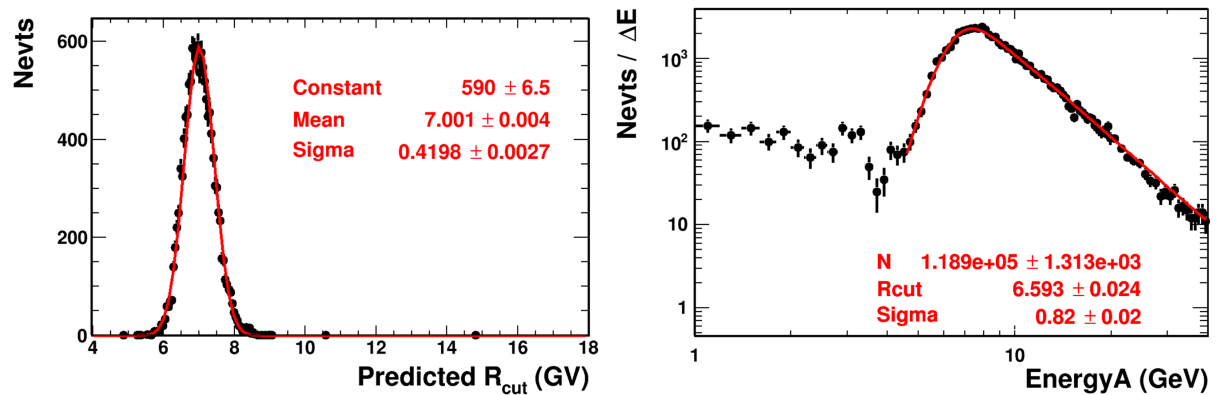


Figure 3.27: Left: distribution of the predicted R_{cut} in the equi- R_{cut} zone of 6.9 - 7.1 GV, fitted with Gaussian function. Right: electron spectra fitted with $\mathcal{F}(x)$ for the same equi- R_{cut} zone. The measured R_{cut} is 6.59 ± 0.02 GeV.

predicted R_{cut} distribution is larger than that with Störmer approximation.

Comparison of measured R_{cut} values and the predicted ones is shown in Figure 3.28. A linear

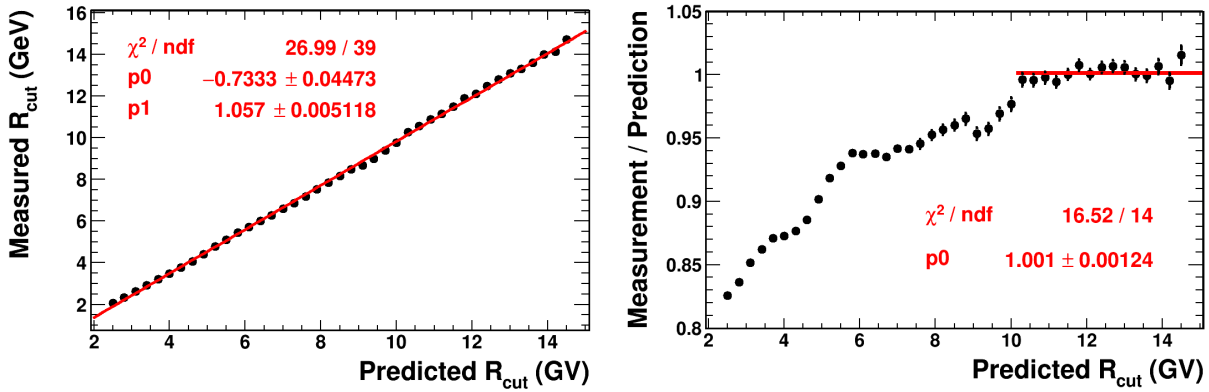


Figure 3.28: Left: measured R_{cut} values as a function of the predicted R_{cut} for 41 equi- R_{cut} zones from 2.5 GV to 14.5 GV, fitted by linear function of $f(x) = p0 + p1 \times x$. Right: ratio of measurement over prediction. The ratios above 10 GeV are fitted by constant function of $f(x) = 1.001$.

dependence of measured R_{cut} on the predicted R_{cut} is observed. Compared to the results from Störmer approximation shown in Figure 3.25, the results calculated with IGRF model are much improved in the range of $R_{\text{cut}} > 6$ GV. And in the region of $R_{\text{cut}} > 10$ GV, the ratio of measurement over prediction can be precisely fitted by constant 1.

The value of R_{cut} with IGRF model is obtained after the particles are back-traced in the magnetosphere. However, the tracing procedure is especially complex for low energy particles. The use of IGRF model and backtracing introduces extra uncertainty to this method, which is not estimated here. This uncertainty may explain the difference observed in regions of $R_{\text{cut}} < 10$ GV.

3.3.5 Time variation of measurement/prediction with IGRF model

The variation of R_{cut} measurement/prediction as a function of time is studied with 29 months of ISS data from July 2011 to November 2013. Every five or six months are regrouped into one time period. The R_{cut} is measured with data of each time period using the IGRF model. Figure 3.29 shows the R_{cut} measurement results of equi- R_{cut} zones 5.7 - 5.9 GV and 13.4 - 13.6 GV with six months of data in 2012. The uncertainty of the fit result is larger than that measured with 29 months of data in Figure 3.21 due to reduced statistics.

The measurement/prediction results for all the predicted R_{cut} values are shown in Figure 3.30. Below 10 GeV, the electron spectra are affected by solar modulation, which explains part of the time variation.

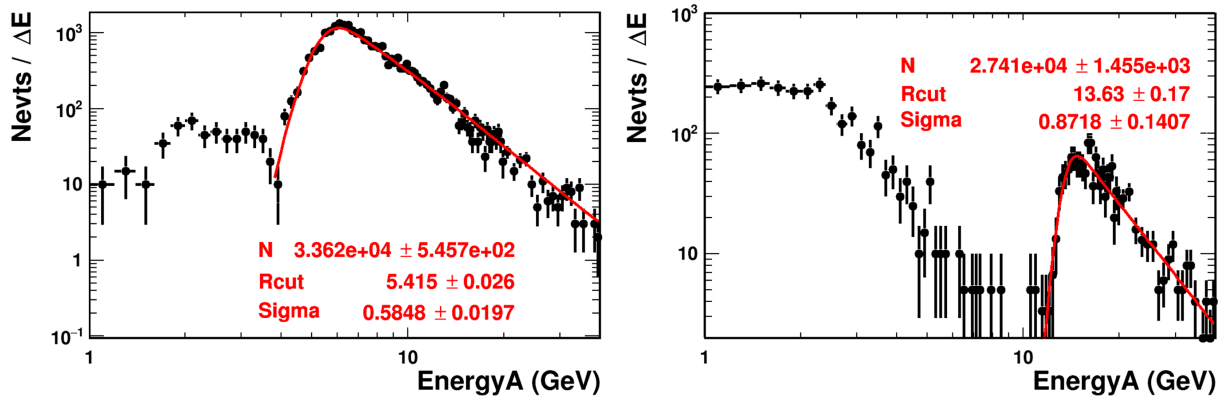


Figure 3.29: Electron spectra of the time period January 2012 to June 2012, fitted with $\mathcal{F}(x)$ for R_{cut} between 5.7 - 5.9 GV (left) and between 13.4 - 13.6 GV (right). The measured R_{cut} results are respectively 5.42 ± 0.03 and 13.63 ± 0.17 .

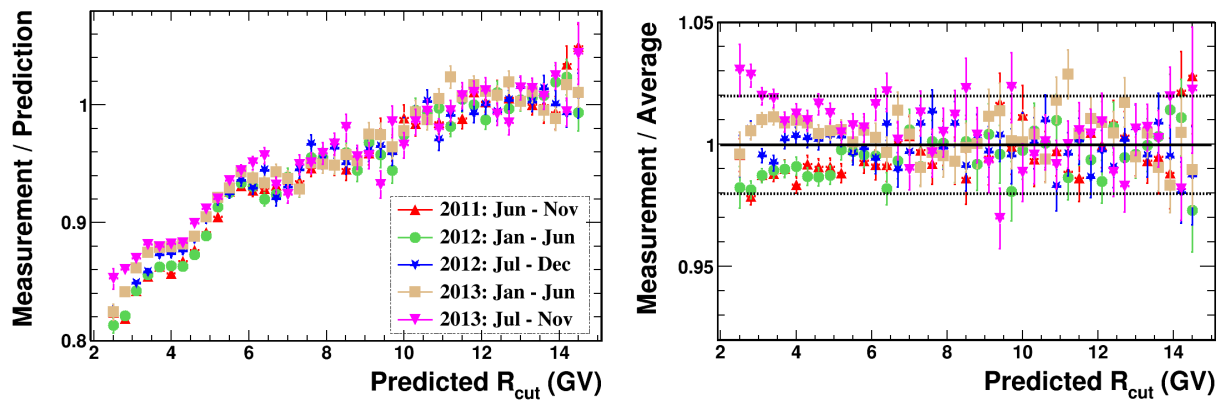


Figure 3.30: Left: ratios of measured R_{cut} over predicted R_{cut} for time ranges: July 2011 - November 2011, January 2012 - June 2012, July 2012 - December 2012, January 2013 - June 2013 and July 2013 - November 2013. Right: ratios of the five results in the left plot over their average. The dashed black line indicates boundaries of $1 \pm 2\%$.

In the regions of $R_{\text{cut}} > 10$ GV, the measurement/prediction ratios are fitted with constant function for each time period as shown in Figure 3.31. The fit results are all very close to 1 with a standard deviation of $\sim 0.3\%$. The small deviation shows that the energy scale is stable with time.

3.3.6 Conclusions on energy scale with R_{cut}

An in-space calibration method is developed using the geomagnetic cutoff rigidity, which is independent of the measurement of momentum P and the related uncertainties. This method can provide an absolute energy scale without using the MIPs, with a systematic uncertainty of 1% from MC studies.

Geomagnetic cutoff rigidities estimated with Störmer approximation and with IGRF model

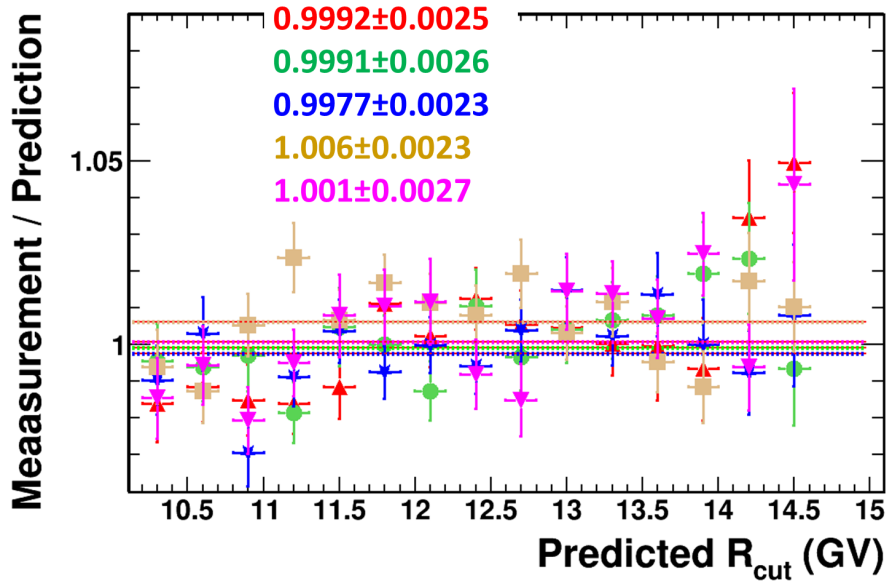


Figure 3.31: Ratios of the measured R_{cut} over predicted for five time periods, fitted with constant functions in the range of $R_{\text{cut}} > 10$ GV.

are studied and compared. As expected, IGRF prediction is more compatible with the results measured with ISS electrons.

For R_{cut} between 10 and 14.5 GV, the energy scale is controlled to a precision of $\sim 0.2\%$ with 29 months of ISS electrons. The stability of energy scale is monitored every 6 months with a precision of 0.3%. No time variation is observed. For R_{cut} below 10 GV, back-tracing must be applied. Effects of the residual solar modulation and back-tracing cannot be excluded and are to be studied.

In the future studies, the same calibration can be repeated with ISS positrons. More established geomagnetic cutoff models are to be tested and compared.

3.4 Energy reconstruction in simulation

The energy scale calibration is performed with MC data by checking the ratio of reconstructed energy over true energy ($E_{\text{rec}}/E_{\text{true}}$) and the reconstructed energy over rigidity (E/P). The scale is checked over the energy range of 1 GeV - 1 TeV.

3.4.1 $E_{\text{rec}}/E_{\text{true}}$

EnergyA of MC electrons of version B620dev is used as E_{rec} in this analysis. Similar to the $E_{\text{rec}}/E_{\text{beam}}$ study with test beam, $E_{\text{rec}}/E_{\text{true}}$ distributions are fitted with Gaussian functions around the peak position. Figure 3.32 shows the distribution and fit for energy bins of 4.5 - 5.0 GeV and 260 - 350 GeV. The energy scale and resolution are obtained from the fit results.

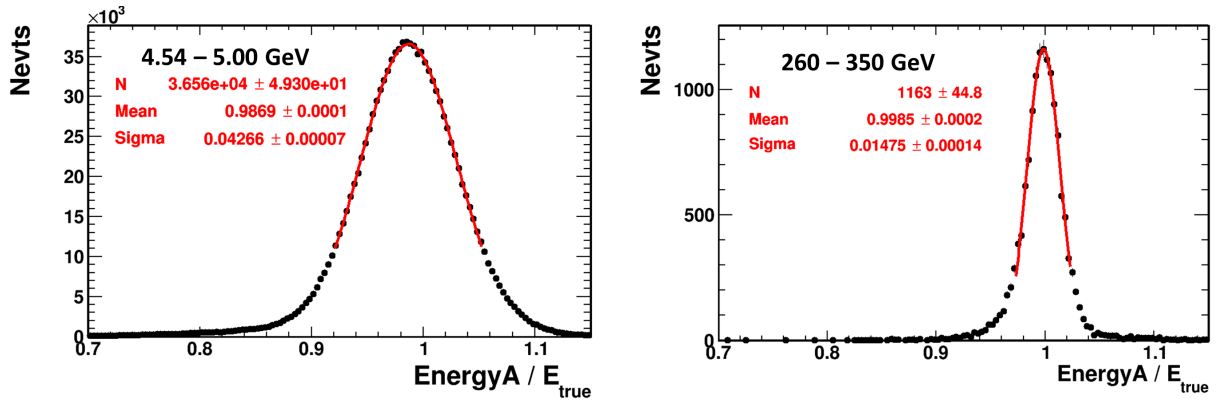


Figure 3.32: $E_{\text{rec}}/E_{\text{true}}$ with EnergyA for energy bins 4.54 - 5.00 GeV (left) and 260 - 350 GeV (right), with a fitted Gaussian function shown in red curve. The mean of the Gaussian is used to determine the energy scale and the width refers to the energy resolution.

The scale is controlled for 65 energy bins defined on the range of 1 GeV to 1 TeV. The binning is the same as used in flux measurement, which is given in Table 5.5. Variation of $E_{\text{rec}}/E_{\text{true}}$ as a function of energy is shown in Figure 3.33 and Figure 3.34.

The energy is reconstructed with 0.5% difference from the E_{true} above 10 GeV. At 2 GeV,

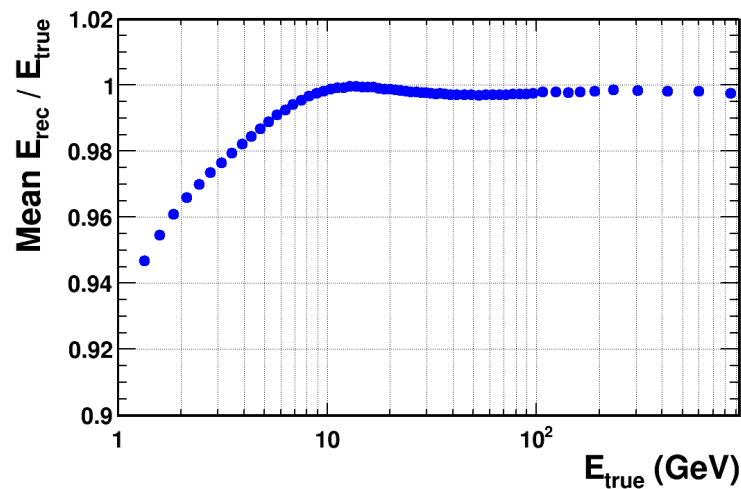


Figure 3.33: Variation of the Mean $E_{\text{rec}}/E_{\text{true}}$ as a function of E_{true} . Error bars are fit errors of the parameter Mean.

the E_{rec} is underestimated by 4%. This low-energy region is affected by the description of the

material in the detector, which will be improved with the new MC data. The energy resolution

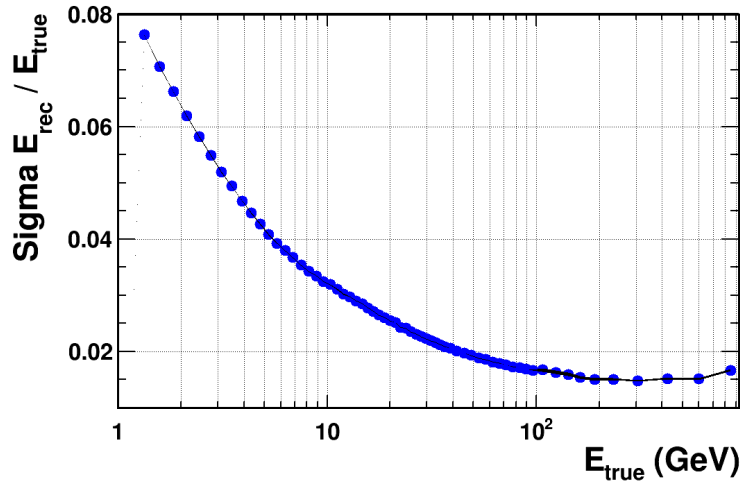


Figure 3.34: Variation of E_{rec}/E_{true} resolution as a function of E_{true} . Error bars are fit errors of the parameter Sigma.

of EnergyA in MC data improves with energy, approximately 6% at 2 GeV, 2% at 40 GeV and 1 % at 700 GeV.

3.4.2 E/P control

The E/P control is performed with MC data over the energy range of 5 GeV to 1 TeV. Similar selection as for ISS electrons in Section 3.2 requiring track pattern L1L9. Figure 3.35 shows the E/P distribution fitted with Crystal Ball function for energy bins 5.0 - 5.5 GeV and 260 - 350 GeV.

The energy dependence of E/P peak position is shown in Figure 3.36 with the same binning

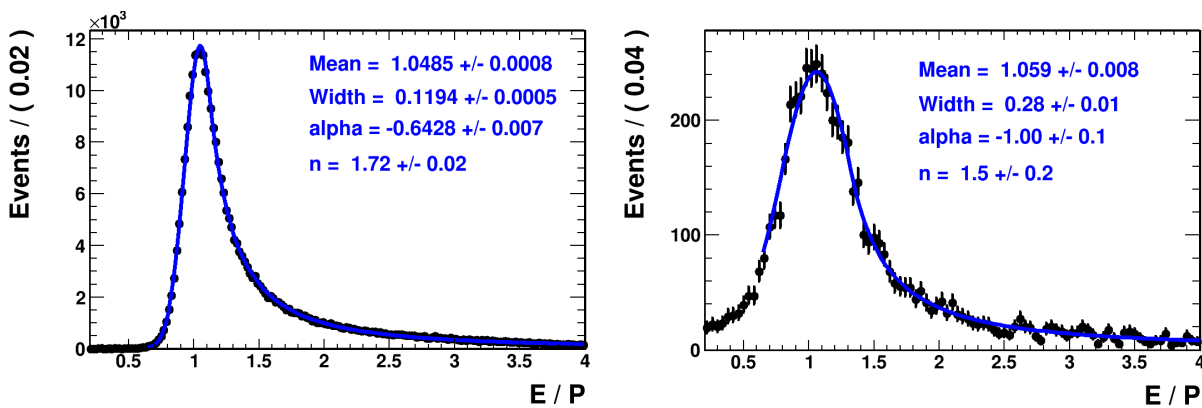


Figure 3.35: E/P distribution with MC data for energy bins 5.0 - 5.5 GeV (left) and 260 - 350 GeV (right), fitted with Crystal Ball function (blue curve) on the interval (0.6, 4). The mean of the CB function is used to determine the energy scale.

as used in $E_{\text{rec}}/E_{\text{true}}$ study. It is observed that the peak position is at 1.05 at 10 GeV and

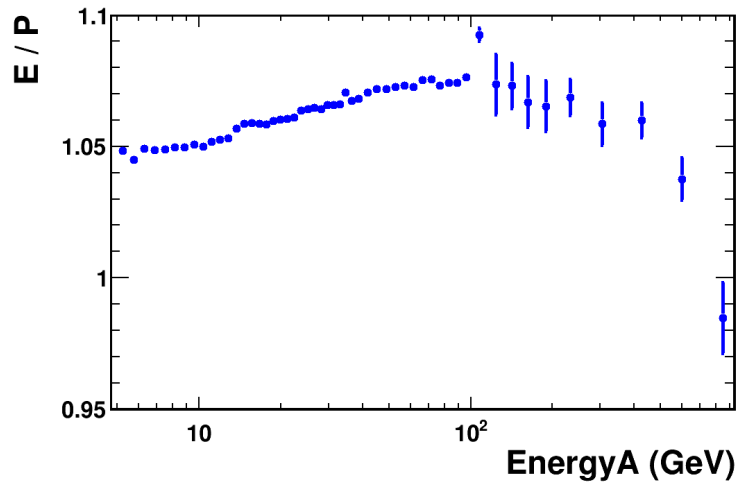


Figure 3.36: E/P peak position as a function of EnergyA. Error bars are uncertainty of the parameter Mean from the fit.

slowly increases to 1.07 at 100 GeV. After 100 GeV, the value drops to about 1 at 500 GeV. The difference with results from ISS data is partly due to less material simulated in MC, which will be improved in the next round of MC generation.

3.5 Conclusions on the ECAL energy measurement

The energy measurement is checked with test beam 2010 data in Section 3.1. The reconstructed linearity is within 0.5% and the angle dependence is $\sim 2\%$. Figure 3.37 shows the energy reso-

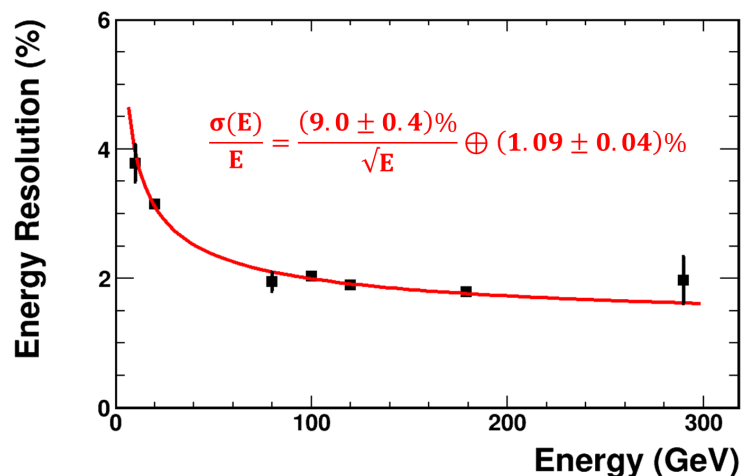


Figure 3.37: ECAL energy resolution from test beam.

lution, $\sigma(E)/E$, as a function of the beam energy.

The E/P control method is performed using test beam and 29 months of ISS data in Section 3.2. Comparison of the positions of the E/P peaks between test beam and ISS data shows good agreement. The energy scale uncertainty is of the order of 1% in the energy range of 20 to 200 GeV.

Alternative method for in-space absolute calibration is developed in Section 3.3 using the geomagnetic cutoff rigidity, leading to an uncertainty of 1%, which is dominated by the resolution tested on MC data.

To conclude, the overall ECAL energy uncertainty is determined as follows:

- 1 - 10 GeV: 4% at 1 GeV, coming from studies of $E_{\text{rec}}/E_{\text{true}}$ with MC data in Figure 3.33. This will be better determined in the future with the cut-off method at low energy.
- 10 - 300 GeV: 2% determined with test beam, dominated by the angle dependence shown in Figure 3.10. The absolute scale is controlled with E/P and R_{cut} .
- 300 - 1 TeV: 5% at 1 TeV, dominated by uncertainty from rear leakage correction as mentioned in Section 2.1.5.1

The ECAL energy uncertainty is drawn in Figure 3.38, which will be taken into account in the flux measurement.

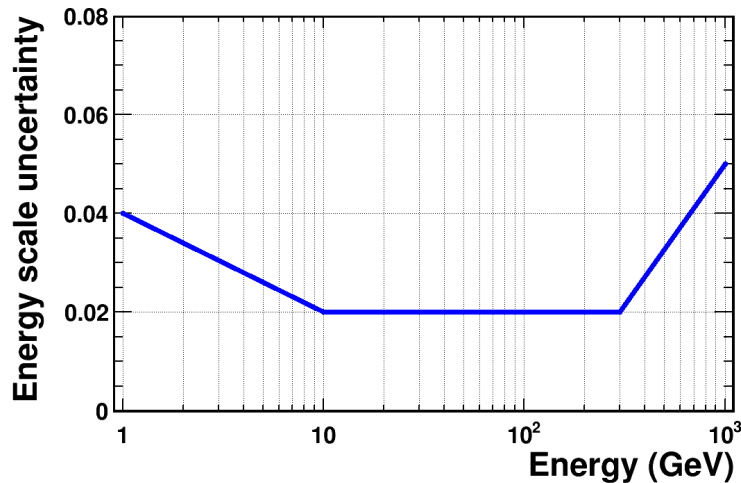


Figure 3.38: ECAL energy scale uncertainty for the energy range of 1 GeV - 1 TeV.

Chapter 4

Lepton and Electron Counting

Lepton or electron flux is calculated with

$$\Phi(E) = \frac{N(E)}{Acc \times \epsilon \times T_{expo} \times \Delta E} \quad (4.1)$$

where Acc is the acceptance of the detector, ϵ is the efficiency, T_{expo} is the exposure time and $N(E)$ is the number of leptons or electrons in the energy range ΔE .

In this chapter, the determination of $N(E)$ with ESE_{V3} and TRD_{LER} is presented using 29 months of ISS data. To achieve a better precision at high energy, the lepton and electron numbers are extracted from data samples using template-fit on the distribution of ESE_{V3} . The numbers counted with TRD_{LER} are used as cross-check.

Figure 4.1 illustrates the fit method using ESE_{V3} for the lepton sample of 115 - 132 GeV. The data sample is selected with preselection (Section 4.1) and lepton selection (Section 4.2) for 64 energy ranges from 1 to 700 GeV. Electron and proton templates are built for each energy bin with ISS data in the form of histograms or analytical functions (Section 4.3). Lepton and electron numbers are extracted from the data samples by fitting the ESE_{V3} distributions with the electron and proton templates (Section 4.4).

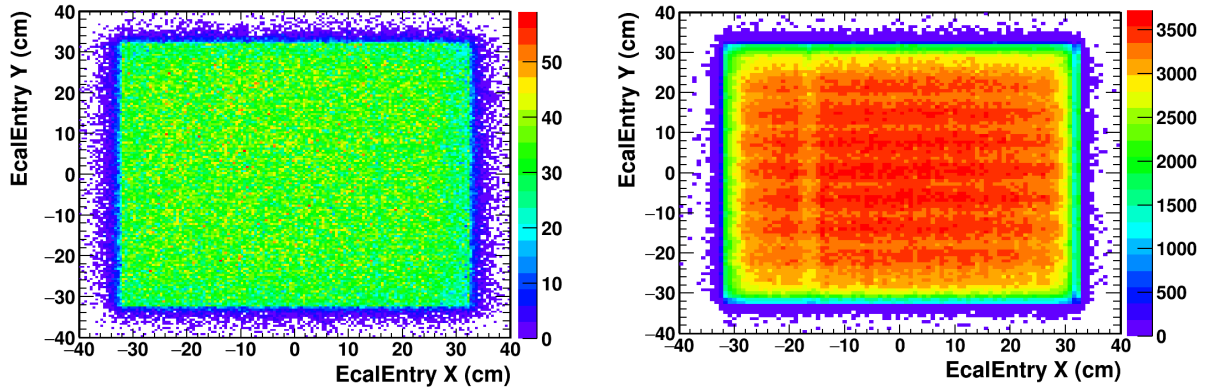


Figure 4.2: Reconstructed ECAL shower entry distribution in 2D: ISS data (Left) and MC data (Right).

on the energy-rigidity matching and performance of ESE_{V3} are also observed.

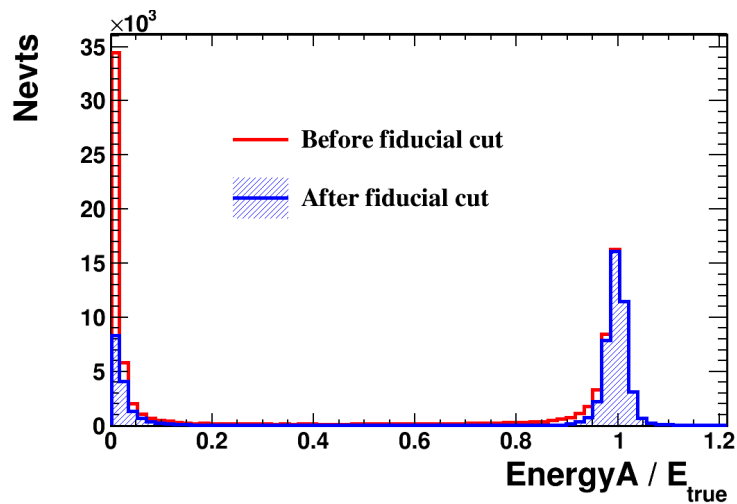


Figure 4.3: $E_{\text{rec}}/E_{\text{true}}$ distribution before and after the fiducial cut for MC data sample with E_{true} in the range of 100 - 150 GeV. The red peak at 0 represents the events with shower at the ECAL border.

Tracker track

Since electric charge and rigidity of the particle are both measured by Tracker, at least 1 successfully reconstructed Tracker track is required. If several tracks are available, the one the closest to the ECAL shower is selected. More matching details are explained in Section 4.2 - Tracker-ECAL matching.

4.2 Lepton selection

The lepton selection is used on the whole dataset, to perform the flux measurement and to build the templates. This selection is controlled with both MC data and ISS data.

Number of showers

For events with more than one shower in the ECAL, the most energetic shower is selected. The number of showers distributions from ISS data is shown in Figure 4.4. It is observed that

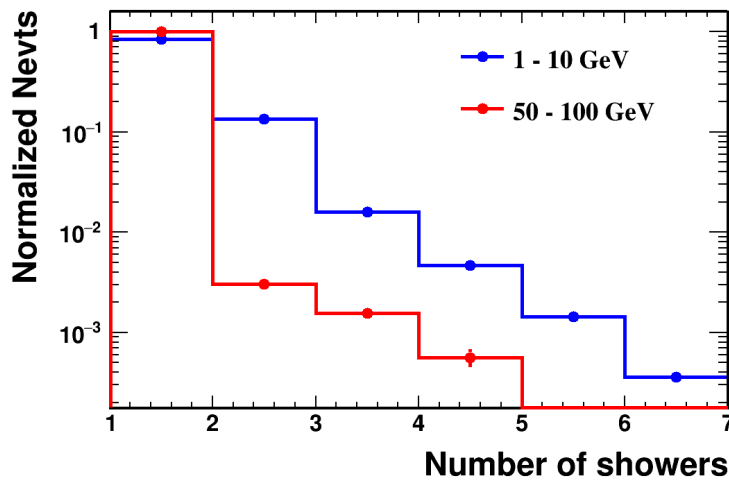


Figure 4.4: Number of showers distributions (normalized to 1) from ISS electrons for energy ranges of 1 - 10 GeV and 50 - 100 GeV.

more than 90% of the events have single shower. And the proportion increases with the energy. Considering the efficiency for low energy electrons, number of showers is required to be less than 2. This cut is justified with MC data. In Figure 4.5, events with more than 2 showers have a $E_{\text{rec}}/E_{\text{true}}$ close to zero, mostly electrons which cannot be exploited.

β from TOF

The velocity, β , measured by TOF is used to reject particles coming from the bottom ($\beta < 0$) and slow particles ($\beta \ll 1$), such as heavy ions. For relativistic leptons, β is around 1. The measured β distributions are given in Figure 4.6. A loose cut $\beta \geq 0.5$ is applied on data.

χ^2 of tracker track

χ^2 of the track is used to evaluate the track quality. Its distribution is shown in Figure 4.7 in

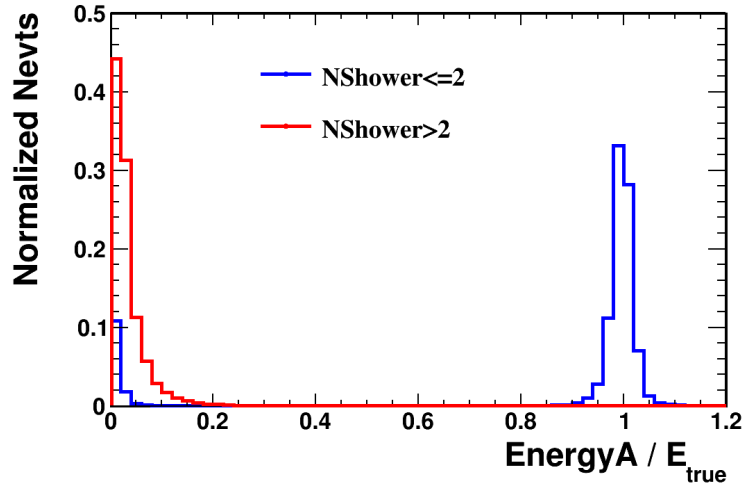


Figure 4.5: Normalized distributions of EnergyA/E_{true} for events with less or equal to 2 showers (blue) and events with more than 2 showers (red). MC data in the energy range of 100 - 150 GeV are used.

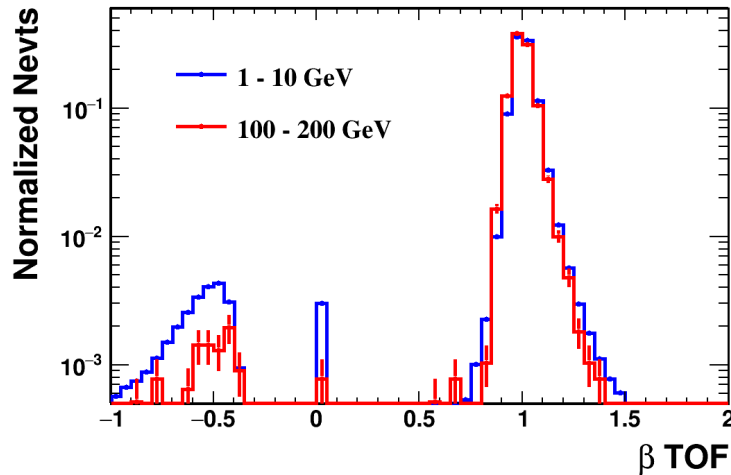


Figure 4.6: Normalized distributions of β measured by TOF from ISS electrons: 1-10 GeV in blue and 50-100 GeV in red. β exceeds 1 due to the resolution of time measurement of TOF.

X and Y directions. $\chi_Y^2 < 20$ is required to reject bad tracks. Loose cut of $\chi_X^2 < 100$ is added to enhance the quality.

Tracker-ECAL matching

For each reconstructed event, the Tracker track is required to match the ECAL shower. The matching is performed by calculating the distance of the shower entry and the tracker track extrapolation at the ECAL surface ($Z = -143.2$ cm). The distances in X and Y direction are respectively denoted as ΔX and ΔY . If more than one track is available, the track with the minimum $\sqrt{\Delta X^2 + \Delta Y^2}$ is selected. 2D distributions of ΔX and ΔY are shown in Figure 4.8.

Events with ΔX and ΔY close to zero (center of the figure) have good Tracker-ECAL matching.

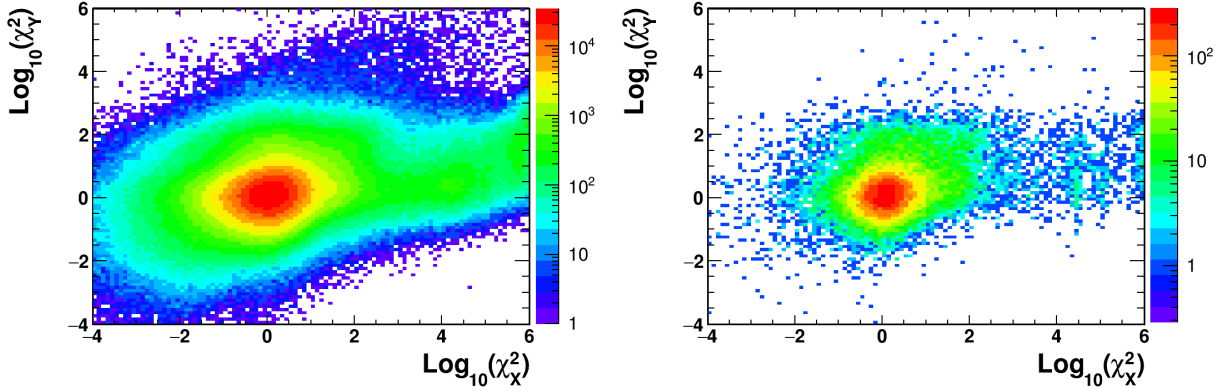


Figure 4.7: 2D distribution of χ^2 for 1 - 10 GeV (left) and 50 - 100 GeV (right) with 18 months of ISS electrons.

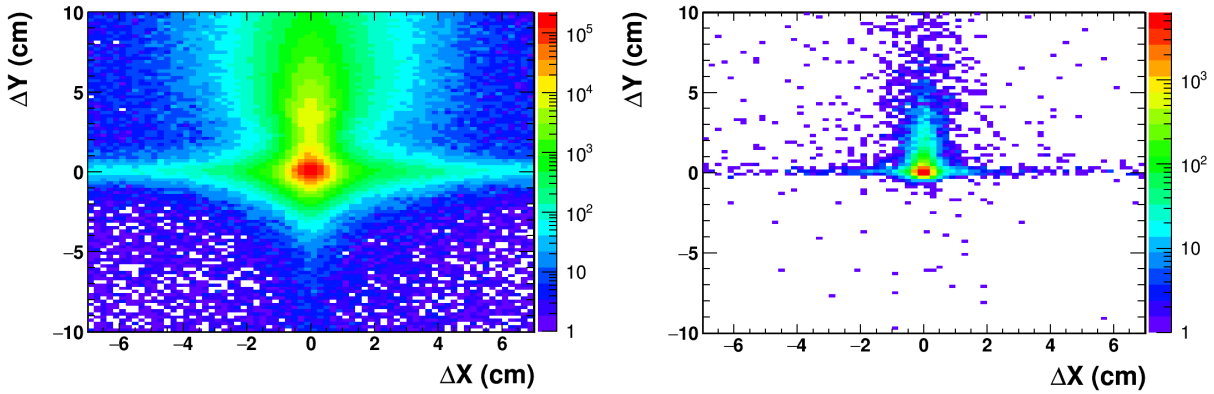


Figure 4.8: $\Delta X - \Delta Y$ distribution with ISS electrons at 1 - 5 GeV (left) and 50 - 100 GeV (right).

Distribution of ΔX is symmetric, whereas ΔY is asymmetric due to curvature of the magnetic field in Y direction. Tracker-ECAL matching requires $|\Delta X| \leq 3\text{cm}$ and $|\Delta Y| \leq 5\text{cm}$.

Energy-rigidity matching(E/P)

Energy is measured by the ECAL and rigidity by the Tracker. E/P distribution is given in Figure 4.9, where the two populations, hadrons (peak at 0.4) and electrons (peak at 1.1) are clearly observed. Events with $E/P < 0.6$ are rejected.

$E/P \gg 1$ is coupled with Bremsstrahlung and wrong measurements of rigidity, both resulting in significant charge confusion. Charge confusion, defined as the fraction of wrong sign events, indicates the proportion of electrons misidentified by the tracker as positrons. The estimation method is presented in Section 5.4. Positive correlation between charge confusion and E/P value is confirmed in Figure 4.10. To reduce wrong sign events, it is required that $E/P < 10$.

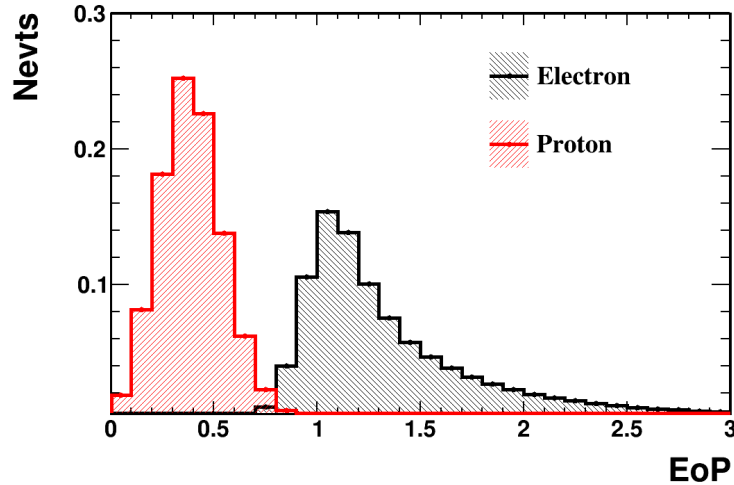


Figure 4.9: Normalized E/P distributions of ISS protons (red) and ISS electrons (black) in the ECAL energy range of 1 - 10 GeV.

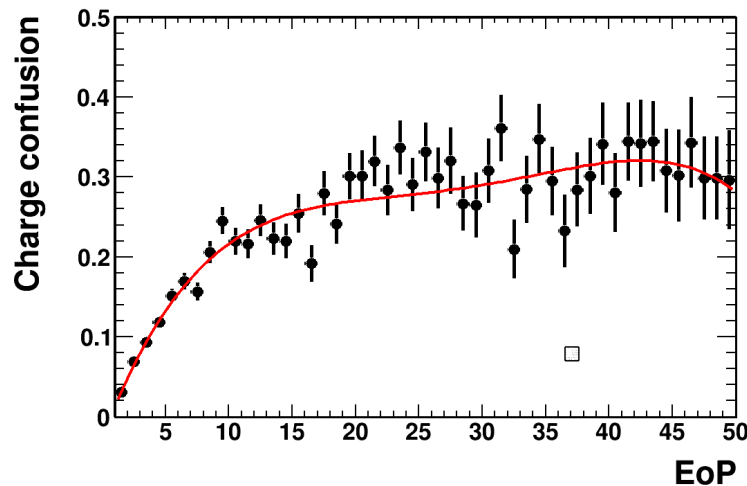


Figure 4.10: Charge confusion as a function of E/P measured by MC data 100 - 300 GeV.

Inner Tracker charge ($Q_{\text{Trk.inn.}}$)

Inner tracker charge is the electric charge measured by the inner layers of the tracker. Different from charge measured by all the layers, $Q_{\text{Trk.inn.}}$ reduces mis-measurements due to interactions on the external layers and back splash from the ECAL. The $Q_{\text{Trk.inn.}}$ distribution is shown in Figure 4.11. Protons and electrons of charge one are well separated from the remaining helium of charge two. The cut of $0.6 < Q_{\text{Trk.inn.}} < 1.5$ is applied to get rid of helium and events with bad tracks in the data sample.

Single track

The number of tracker tracks, N_{Track} , is required to be one and only one. The distribution of number of tracks from ISS data is shown in Figure 4.12. About 80% of the events have single

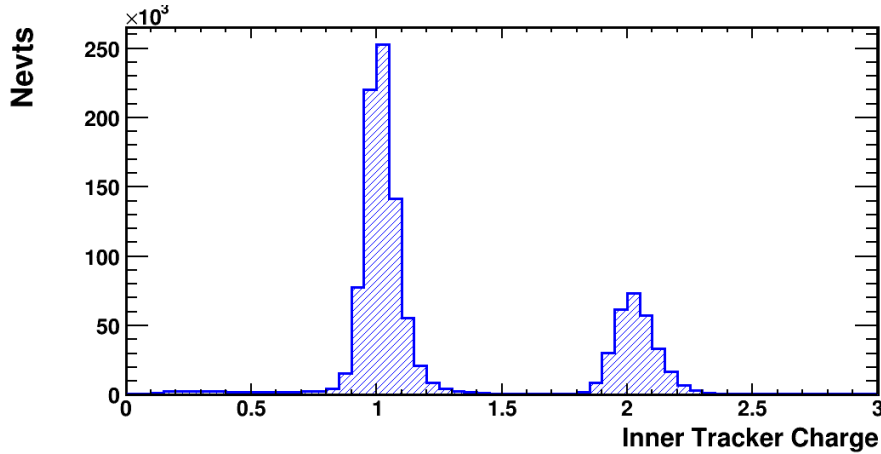


Figure 4.11: Distribution of inner tracker charge $Q_{\text{Trk.inn.}}$ from ISS data.

track. Events with more than 1 track are rejected to reduce charge confusion and interacting protons.

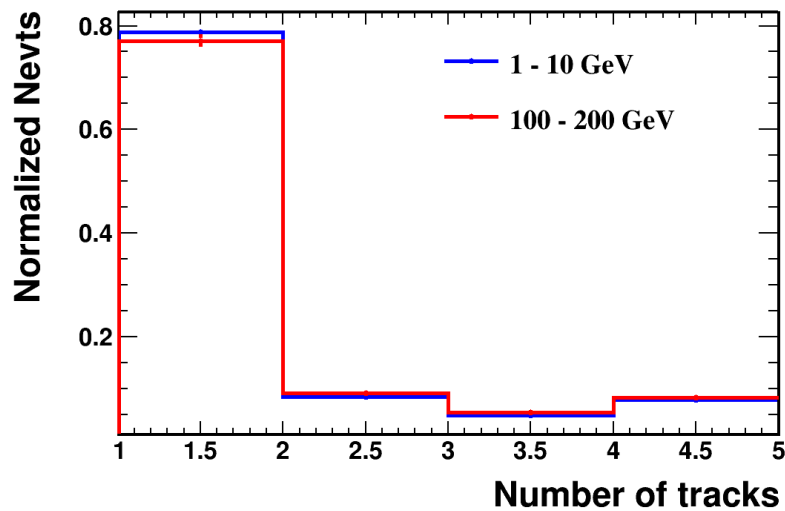


Figure 4.12: Number of Tracker tracks from ISS data electrons, 1-10 GeV in blue and 100-1000 GeV in red.

At this stage, the selection efficiency is shown in Figure 4.13 for 64 energy bins from 1 GeV to 700 GeV. The total efficiency is ~ 0.75 below 10 GeV and drops to 0.5 at 500 GeV. Details of this estimation are developed in the next chapter.

TRD_{LER} cut

To reduce the proton contamination in data samples, a cut on TRD_{LER} is applied to obtain high lepton purity. In Figure 4.14, four distributions of ESE_{V3} with different TRD_{LER} cuts are superimposed. From black dots to green ones, proton number is dramatically reduced by

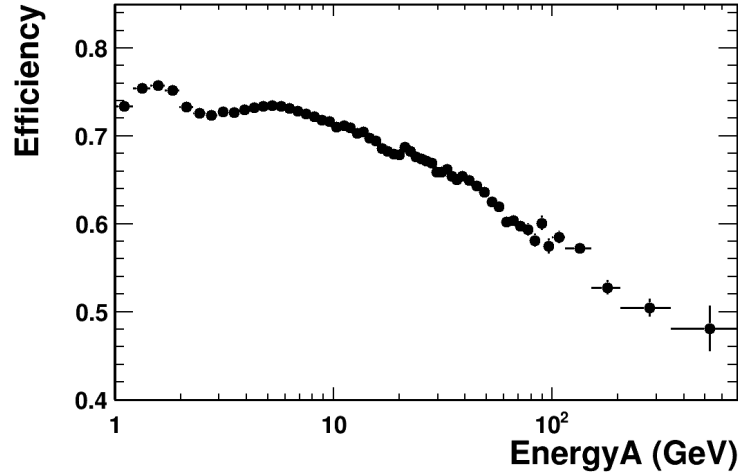


Figure 4.13: Lepton selection efficiency for electrons estimated with ISS electrons from 1 to 700 GeV. 29 months of ISS data are used.

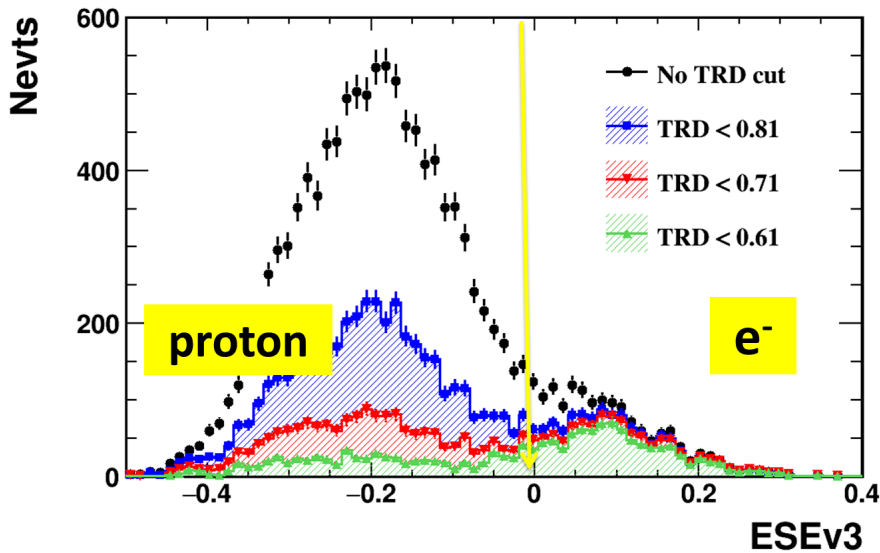


Figure 4.14: ESE_{V3} distribution for energy range 206-260 GeV: all events surviving the lepton selection (black dots), surviving events with $TRD_{LER} < 0.81$ (blue shade), surviving events with $TRD_{LER} < 0.71$ (red shade) and surviving events with $TRD_{LER} < 0.61$ (green shade).

a factor of 10 while lepton efficiency is maintained at 90%. The TRD_{LER} efficiency curves are presented later in Figure 4.33 (Section 4.6.1): below 100 GeV, all the three TRD_{LER} cuts have a high efficiency of 0.95. However, above 100 GeV, efficiency of the tight cut $TRD_{LER} < 0.61$ drops dramatically. Therefore, to select electron samples, a rather loose cut at **0.71** is used for the range of 1 to 500 GeV. For lepton samples, a tight TRD_{LER} cut at **0.65** is applied for energy bins of 1 - 500 GeV, since the proton contamination is more significant. Above 500 GeV, $TRD_{LER} < 0.61$ is used for both electron and lepton samples.

Figure 4.15 shows the ESE_{V3} distribution for lepton samples after TRD_{LER} cut for two energy bins. Even with $TRD_{LER} < 0.61$, the proton contamination in the bin above 500 GeV is about

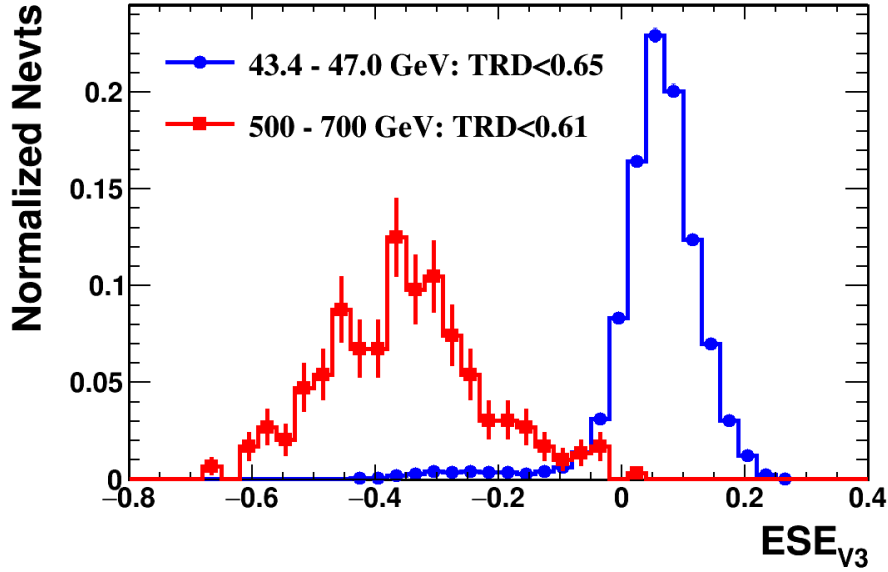


Figure 4.15: Normalized ESE_{V3} distributions of lepton samples in the energy bins of 43.4 - 47.0 GeV (blue) and 500 - 700 GeV (red), with TRD_{LER} cuts respectively at 0.65 and 0.61.

90%.

4.3 Proton and electron templates for ESE_{V3}

The templates of electrons (signal) and protons (background) for ESE_{V3} are built with ISS data, for each energy bin. Besides the lepton selection previously presented, template samples are obtained by applying tight cuts on TRD_{LER} .

The cuts on TRD_{LER} are examined for different energy ranges as illustrated in Figure 4.16, where the ISS samples are selected with $ESE_{V3} > -0.15$. As is also observed in Figure 2.22, below 500 GeV the proton distribution peaks at above 0.8 while the electron distribution peaks at below 0.6. As energy increases, the two peaks get closer, with electrons shifting to the right and protons to the left. Therefore, different cuts must be used to build electron and proton templates for different energy ranges. The cuts are tight at low energy, where the statistics are sufficient. At high energy, the cuts are looser to keep enough statistics. In addition, since the separation of protons and electrons with TRD_{LER} is less good at high energy, the extraction of good template is more difficult.

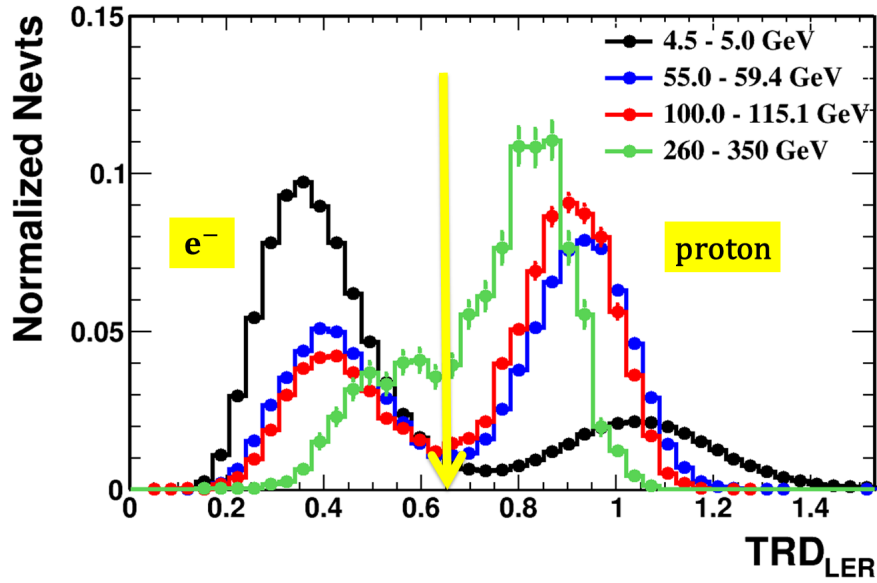


Figure 4.16: TRD_{LER} distributions obtained with ISS samples for energy ranges 4.5 - 4.0 GeV, 55.0 - 59.4 GeV, 100 - 115 GeV and 260 - 350 GeV. Peak on the left are electrons and peak on the right protons.

4.3.1 Templates at low energy: below 15 GeV

Below 15 GeV, the electron and proton template samples have sufficient statistics. Histograms are used to fit the samples, because they better take into account the potential irregularity of the shape.

Electrons

To obtain pure electron samples, protons and helium are greatly reduced by requiring **negative rigidity** and $TRD_{LER} < 0.4$. Moreover, tracker track with good pattern of L1L9 or L2L9 (defined in Section 2.1.3) is required to mitigate charge confusion; cut on the charge measured with TOF is applied to remove the surviving helium and the hadronic interactions in the detector (cf. Table 4.1). The ESE_{V3} distributions of these samples are then fitted with smoothed histogram. Two examples are shown in Figure 4.17.

Protons

To obtain pure proton samples, electrons are removed by additionally requiring **positive rigidity** and $TRD_{LER} > 0.8$. The ESE_{V3} distributions of these samples are then fitted with smoothed histogram, as shown in Figure 4.18.

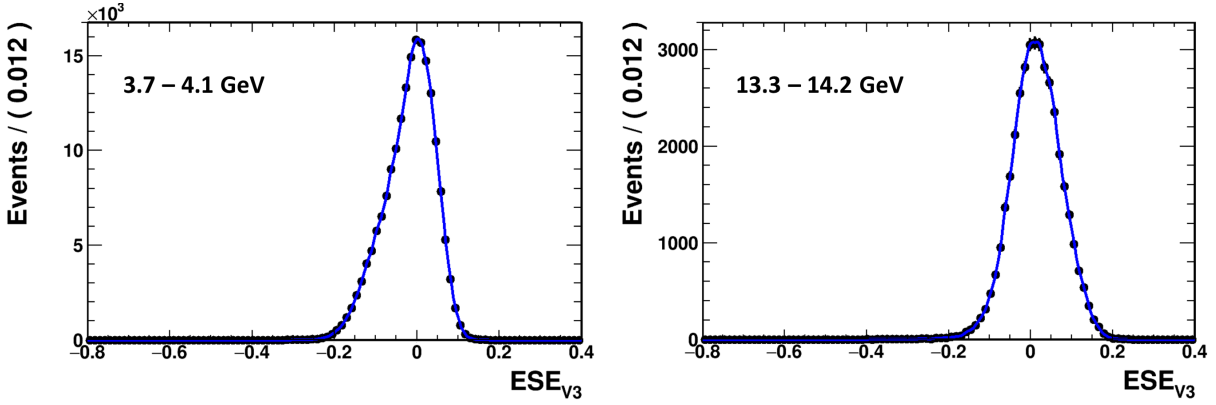


Figure 4.17: Electron samples (black dots) and templates (blue curves) for two energy bins: 3.7-4.1 GeV (left) and 13.3 - 14.2 GeV (right), both fitted with histogram. 29 months of data are used.

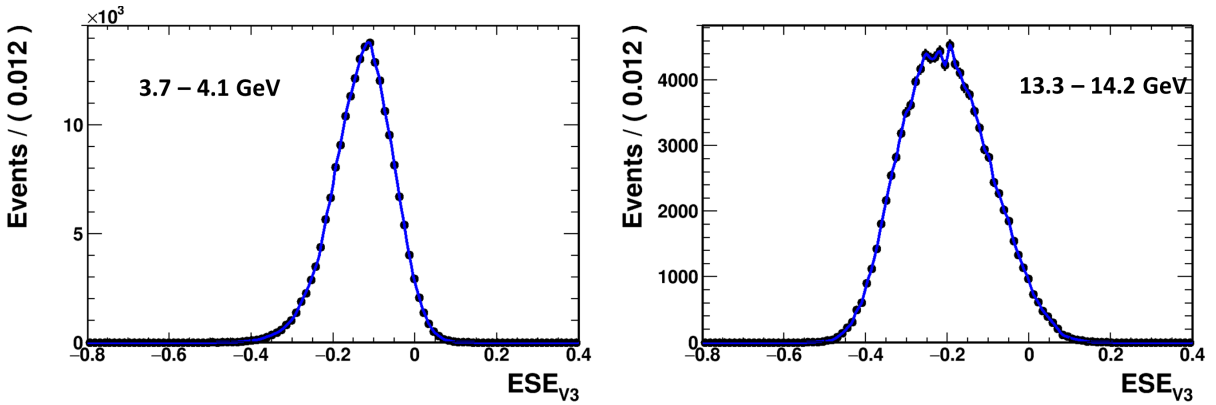


Figure 4.18: Proton samples (black dots) and templates (blue curves) for two energy bins: 3.7-4.1 GeV (left) and 13.3 - 14.2 GeV (right), both fitted with histogram. 29 months of data are used.

4.3.2 Templates at intermediate energy range: 15 - 200 GeV

In this energy range, the electron samples are selected with the same cuts as below 15 GeV, $TRD_{LER} < 0.4$. For proton samples, the same TRD_{LER} cuts as for the lepton samples are used, $TRD_{LER} < 0.65$ or 0.71 , because the proton peak position of ESE_{V3} is observed to be dependent on TRD_{LER} cuts.

Electrons

Below 30 GeV, the ESE_{V3} distributions are still fitted with histograms. Above 30 GeV, the shape of ESE_{V3} gets regular and can be well described by Crystal Ball (CB) function. Electron

templates for two energy bins are shown in Figure 4.19.

The values of the four parameters in CB function, alpha, mean, n and width, are fixed and

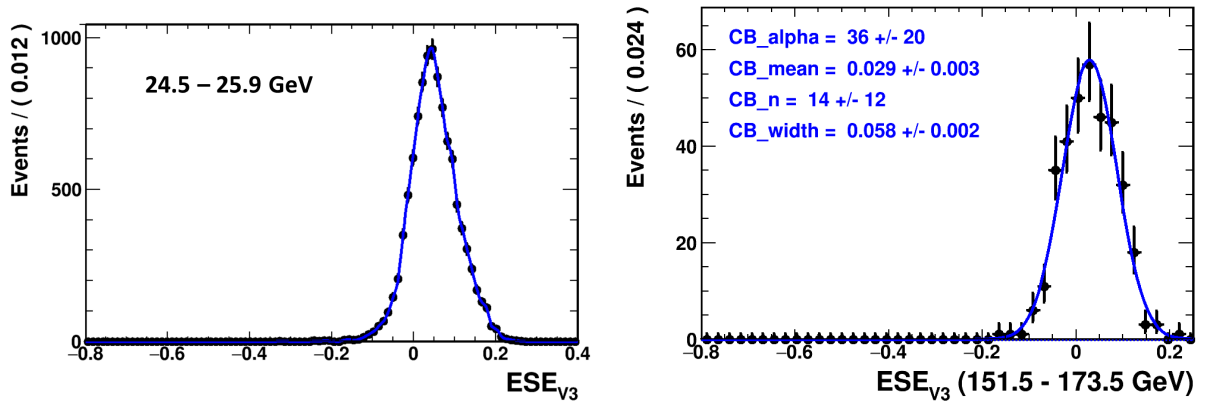


Figure 4.19: Electron samples (black dots) and templates (blue curves) for two energy bins: 24.5 - 25.9 GeV (left) fitted with histogram and 151.5 - 173.5 GeV (right) fitted with crystal ball function. 29 months of data are used.

will be used for template fits on lepton and electron samples.

Protons

Above 15 GeV, a shift is observed between ESE_{V3} distributions of protons selected with $TRD_{LER} < 0.71$ and $TRD_{LER} > 0.8$ as is shown in Figure 4.20. The red curve is shifted to the right compared to the black one. This means that the proton template must be built with

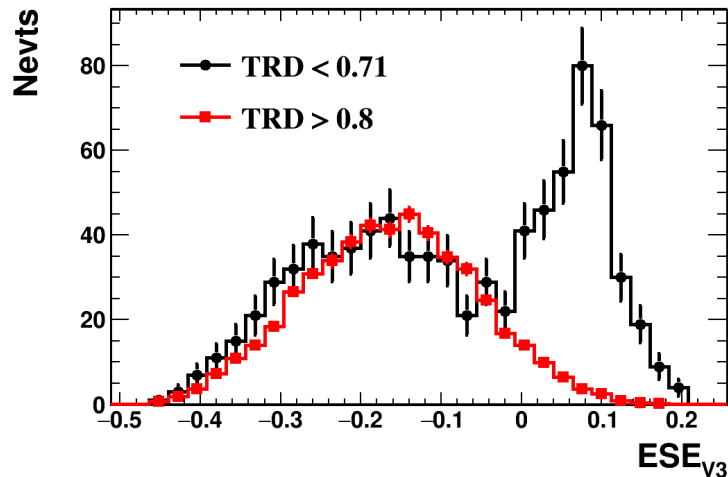


Figure 4.20: ESE_{V3} distributions for ISS positive samples in the energy range of 92.5 - 100 GeV selected with $TRD_{LER} < 0.71$ (black) and $TRD_{LER} > 0.8$ (red). The red curve is scaled to be at the same level as the black one to put in light the shift of the distribution.

the same TRD_{LER} cut as for data.

Consequently, a large proportion of the positive samples selected with $TRD_{LER} < 0.65$ or

$TRD_{LER} < 0.71$ are positrons or charge confused electrons. To remove this contribution, the electron template built for the same energy bin is used. The ESE_{V3} distribution is fitted with combined PDF of the electron template and a Novosibirsk (**Novo**) function. The extraction of proton template with this method is demonstrated in Figure 4.21 for two energy bins.

The values of the three parameters in Novo function, eta, mean and width, are fixed and will

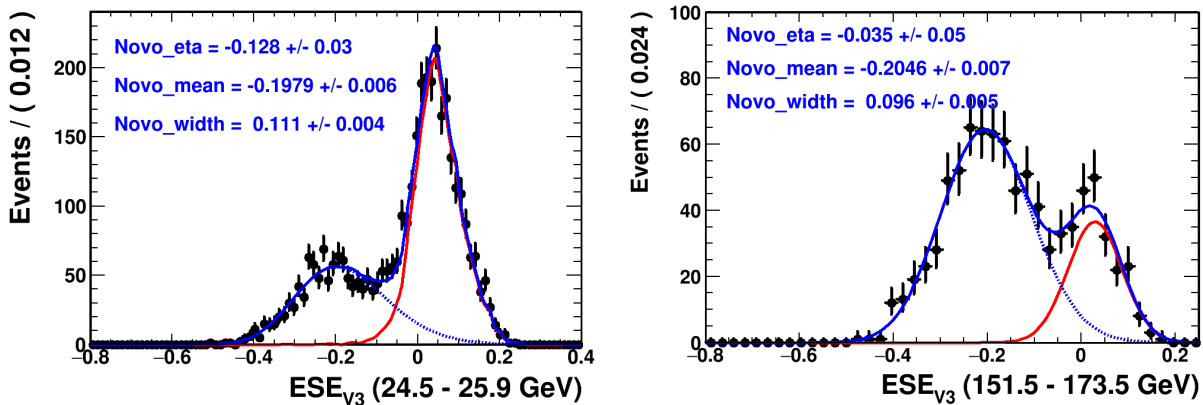


Figure 4.21: Proton template samples (black dots) selected with $TRD_{LER} < 0.71$ for two energy bins: 24.5 - 25.9 GeV (left) and 151.5 - 173.5 GeV (right). Proton templates are fitted with Novosibirsk function in blue dashed curve. 29 months of data are used.

be used for template fits on lepton and electron samples.

4.3.3 Templates at high energy: above 200 GeV

Above 200 GeV, the TRD_{LER} distribution for electrons peaks above 0.4. To gain statistics, the TRD_{LER} cut for electron template samples is loosened to be 0.5. Above 300 GeV, the cut is again loosened to be 0.55 and above 500 GeV, it is at 0.58. Looser TRD_{LER} cuts result in a non negligible proton contamination in the samples.

The proton template samples are selected in the same way as for the intermediate energy range, $TRD_{LER} < 0.65$ for leptons and $TRD_{LER} < 0.71$ for electrons. Since both the electron and proton template samples have contamination, a simultaneous fit on the two samples is used to obtain the two templates at the same time supposing that the electron template has CB shape and the proton template has Novo shape.

In this energy range, unbinned data and fit are used to build templates. The result of this method is shown in Figure 4.22 for the bin of 260 - 350 GeV. The values of the four parameters in CB function and of the three parameters in Novo function are fixed.

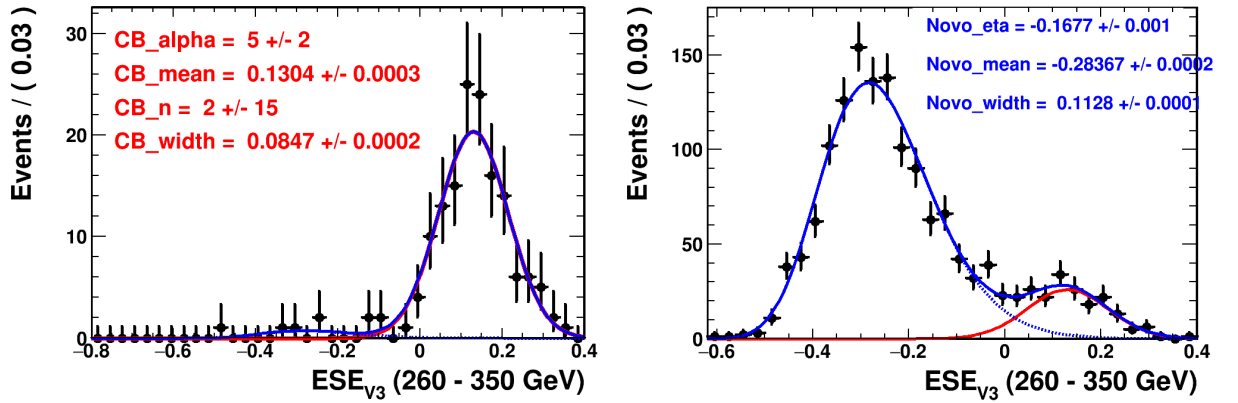


Figure 4.22: Simultaneous fit performed on the electron sample (left) and proton sample (right) for the energy range of 260 - 350 GeV. The electron and proton PDFs displayed in the two plots are the same. The electron PDF is described by CB function (red curve) and the proton PDF by Novo function (blue dashed line).

4.3.4 Summary of the template building

The template building for different energy ranges has been presented and the method is summarized in Table 4.1. To conclude, CB function is used for electron template and Novo for

	Proton template	Electron template
Selection	<ul style="list-style-type: none"> • Positive rigidity 	<ul style="list-style-type: none"> • Negative rigidity • Track pattern L1L9 or L2L9 • TOF charge <ul style="list-style-type: none"> – $Q_{upperTOF} < 1.8$ – $Q_{lowerTOF} < 2.8$
TRD_{LER}	<ul style="list-style-type: none"> • 1 - 15 GeV: > 0.8 • Above 15 GeV: < 0.65 (0.71) 	<ul style="list-style-type: none"> • 1 - 200 GeV: < 0.4 • 200 - 300 GeV: < 0.5 • 300 - 500 GeV: < 0.55 • Above 500 GeV: < 0.58
Fit function	<ul style="list-style-type: none"> • 1 - 15 GeV: histogram • 15 - 200 GeV: Novo (+ e^- contamination) • Above 200 GeV: Novo (simultaneous fit) 	<ul style="list-style-type: none"> • 1 - 30 GeV: histogram • 30 - 200 GeV: Crystal Ball • Above 200 GeV: CB (simultaneous fit)

Table 4.1: Summary of the template building for protons and electrons using ISS data.

proton. Below 30 GeV, statistics allow a histogram fit to describe the irregular shape of ESE_{V3} distribution.

4.4 Lepton and electron numbers counting

The template-fit is performed on the ISS data samples to extract lepton and electron numbers for each energy bin. The proton and electron templates are combined into one PDF, which has only two free parameters, the number of leptons (electrons) and the number of protons. This combined PDF is used to count the number of leptons (electrons) using the ESE_{V_3} distribution. The ISS lepton samples are selected with lepton selection presented in Section 4.2, which mainly contain leptons and survived protons. The ISS electron samples are selected with the lepton selection and in addition requiring the track to have a negative rigidity.

Low energy range: below 15 GeV

In this energy range, the proton and electron templates are histograms. The fit components are shown in Figure 4.23 for the energy range of 10.7 - 11.5 GeV, where leptons are selected with $TRD_{LER} < 0.65$ and electrons with $TRD_{LER} < 0.71$.

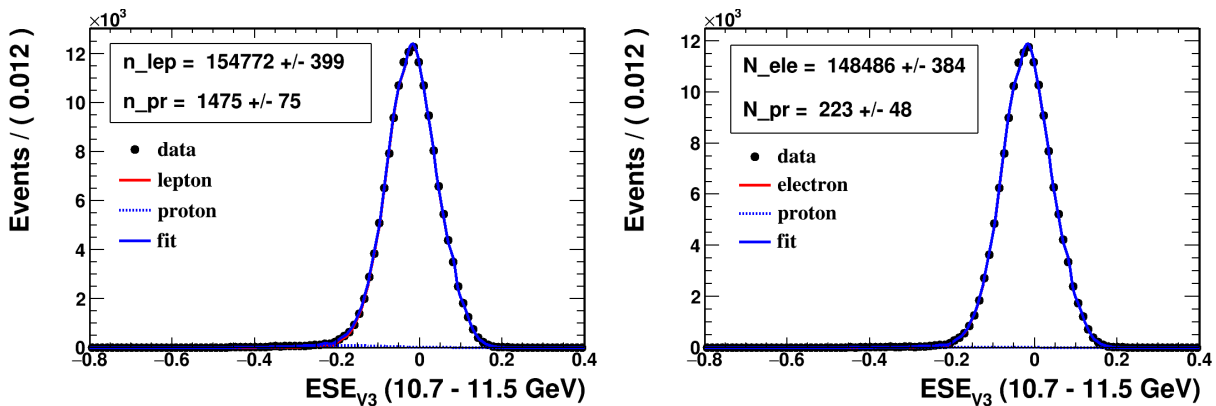


Figure 4.23: Template fits on lepton (left) and electron (right) samples at energy bin 10.7 - 11.5 GeV : lepton (electron) contribution in red, proton contribution in blue dashed line. n_{lep} and N_{ele} are respectively the fitted lepton and electron numbers with their statistical uncertainty.

Intermediate energy range: 15 - 200 GeV

In this energy range, the proton PDF is Novosibirsk function. Above 30 GeV, the electron PDF is crystal ball function. The template-fits are shown in Figure 4.24 and Figure 4.25 for the bin 27.3 - 28.9 GeV and with leptons selected by $TRD_{LER} < 0.65$ and electron selected by $TRD_{LER} < 0.71$.

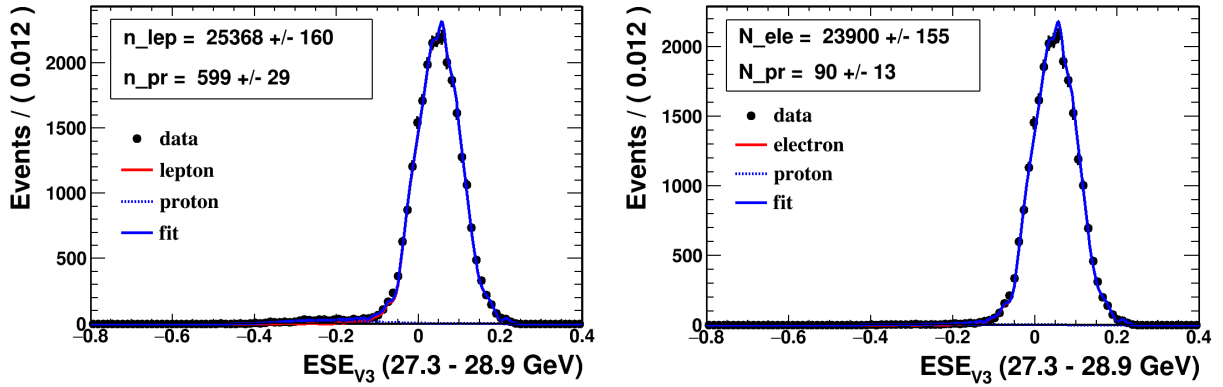


Figure 4.24: Template fits on lepton (left) and electron (right) samples of the energy bin 27.3 - 28.9 GeV : lepton (electron) contribution in red, proton contribution in blue dashed line. n_{lep} and N_{ele} are respectively the fitted lepton and electron numbers with their statistical uncertainty.

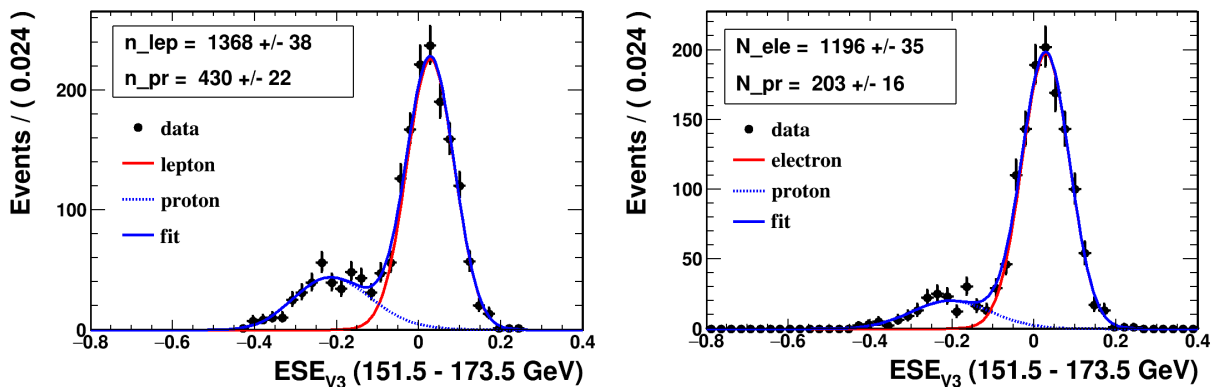


Figure 4.25: Template fits on lepton (left) and electron (right) samples of the energy bin 151.5 - 173.5 GeV : lepton (electron) contribution in red, proton contribution in blue dashed line. n_{lep} and N_{ele} are respectively the fitted lepton and electron numbers with their statistical uncertainty.

High energy range: above 200 GeV

Above 200 GeV, unbinned fit is performed with proton PDF described by Novosibirsk function and electron PDF by crystal ball. The fit results of bins 260 - 350 GeV and 350 - 500 GeV are shown in Figure 4.26.

For the last energy bin 500 - 700 GeV, $TRD_{LER} < 0.61$ is required for both electron and lepton samples to reduce the proton contamination. Figure 4.27 shows the fit results of the last bin.

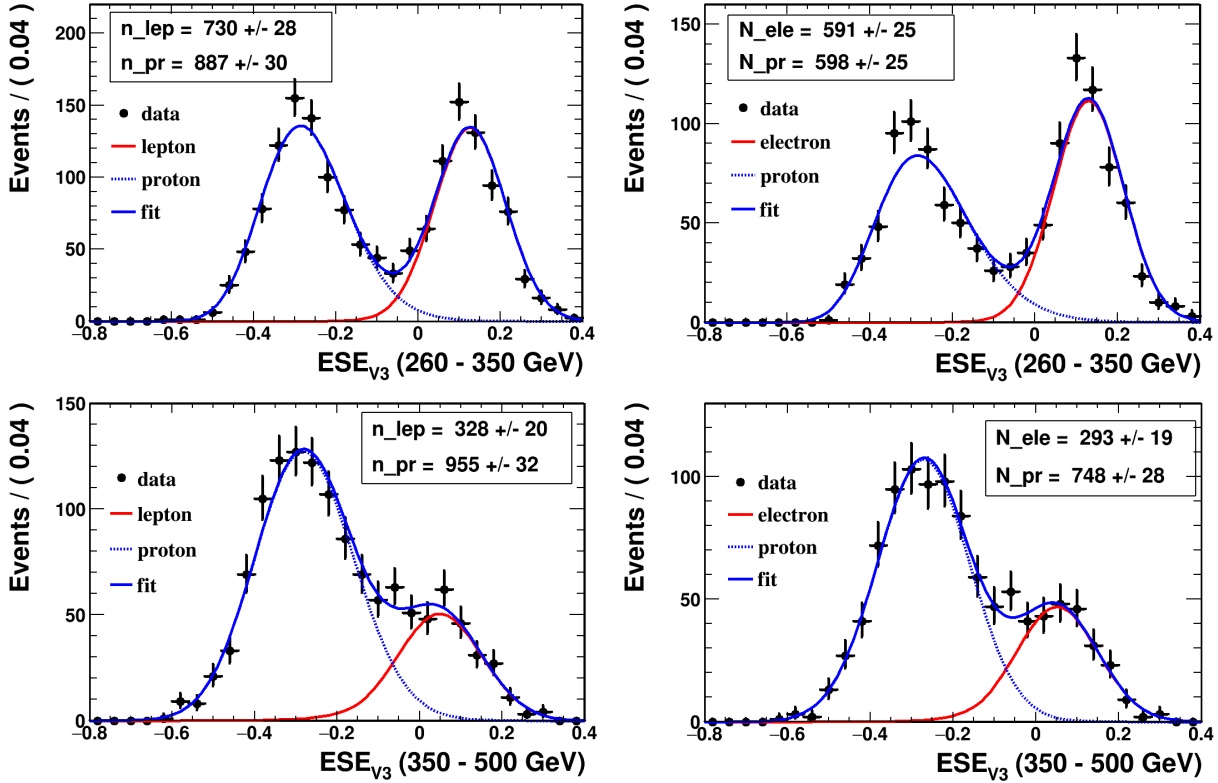


Figure 4.26: Template fits on lepton and electron samples for the energy bins of 260 - 350 GeV (upper) and 350 - 500 GeV (lower): lepton (electron) contribution in red, proton contribution in blue dashed line. n_{lep} and N_{ele} are respectively the fitted lepton and electron numbers with their statistical uncertainty. 29 months of data are used.

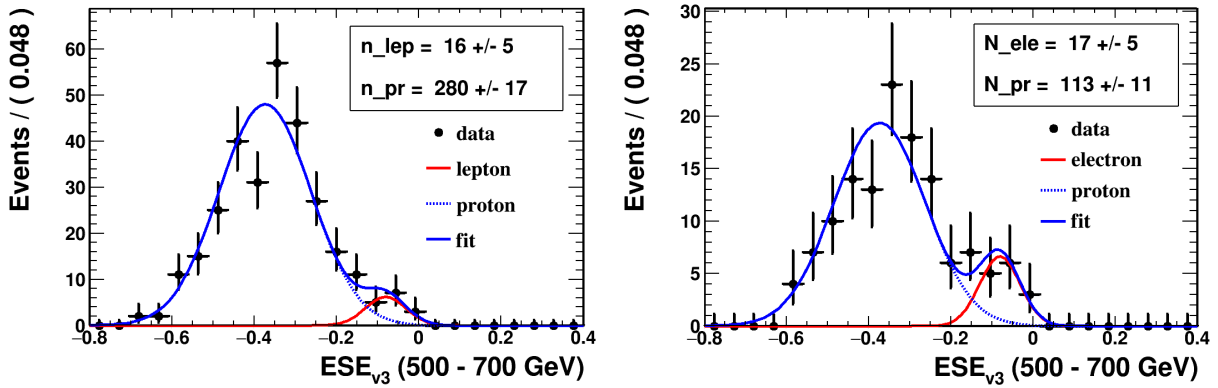


Figure 4.27: Template fits on lepton (left) and electron (right) samples of the energy bin 500 - 700 GeV : lepton (electron) contribution in red, proton contribution in blue dashed line. n_{lep} and N_{ele} are respectively the fitted lepton and electron numbers with their statistical uncertainty. 29 months of data are used.

4.5 Lepton and electron numbers

The raw lepton number and electron number, as well as their statistical uncertainty, are obtained using template-fit methods.

The lepton number is counted with template-fits on ISS data samples requiring $TRD_{LER} < 0.65$. The result using 29 months of data is given in Figure 4.28, which shows dN/dE for the energy range of 1 GeV to 700 GeV.

The electron number is counted on the negative samples requiring $TRD_{LER} < 0.71$. The result

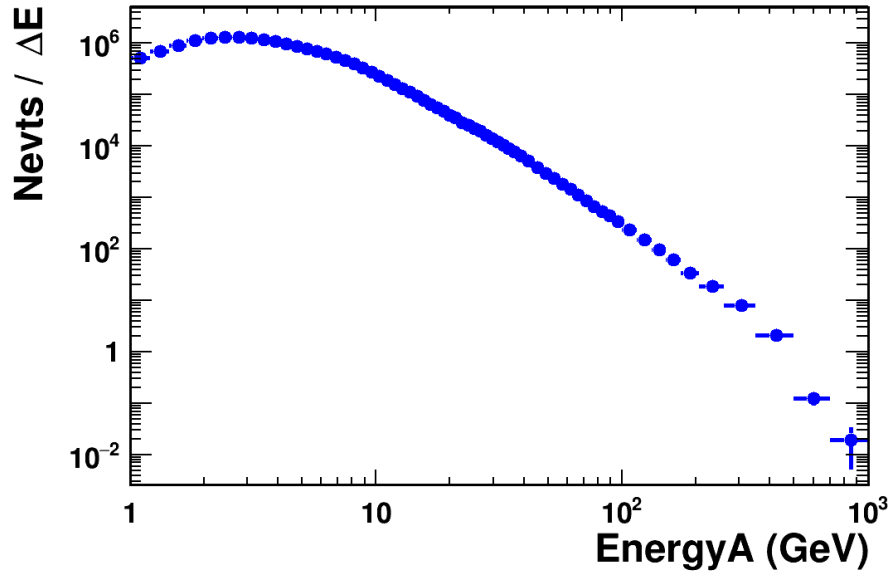


Figure 4.28: Number of leptons divided by bin width for the energy range of 1 GeV to 700 GeV using 29 months of ISS data. Only statistical uncertainty from the fits is shown. Error bars at low energy are smaller than the marker size.

is shown in Figure 4.29.

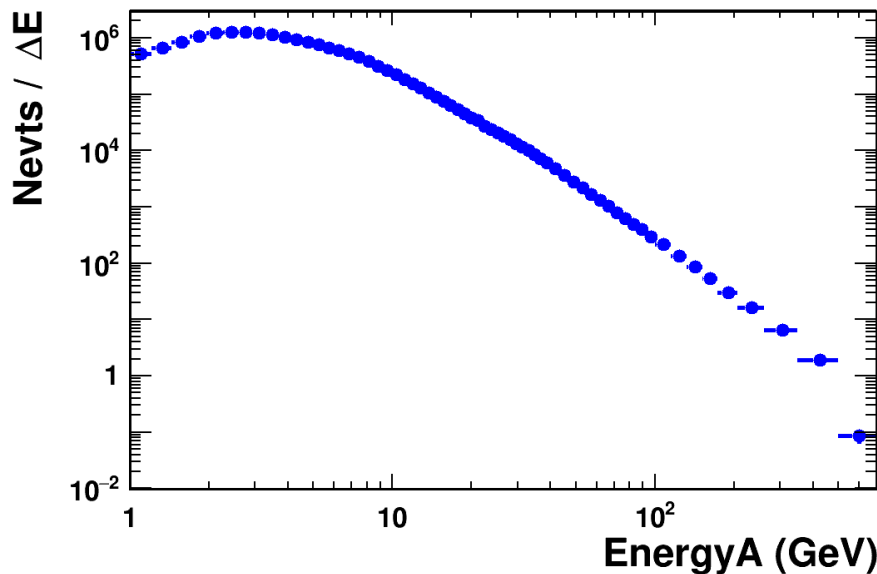


Figure 4.29: Number of electrons divided by bin width for the energy range of 1 GeV to 700 GeV using 29 months of ISS data. Only statistical uncertainty from the fits is shown. Error bars at low energy are smaller than the marker size.

4.6 Cross check using TRD_{LER}

In this section, the number counting analysis is repeated using the TRD_{LER} as a cross-check. TRD_{LER} electron and proton templates are obtained with ISS data for 64 energy bins from 1 GeV to 700 GeV. The cut of $ESE_{V3} > -0.15$ is applied on the data samples to reduce the proton background. Figure 4.30 shows the fit results for $e^+ + e^-$ at 11.5 - 12.4 GeV and e^- at 350 - 500 GeV. Novosibirsk function is used to fit both electron and proton templates.

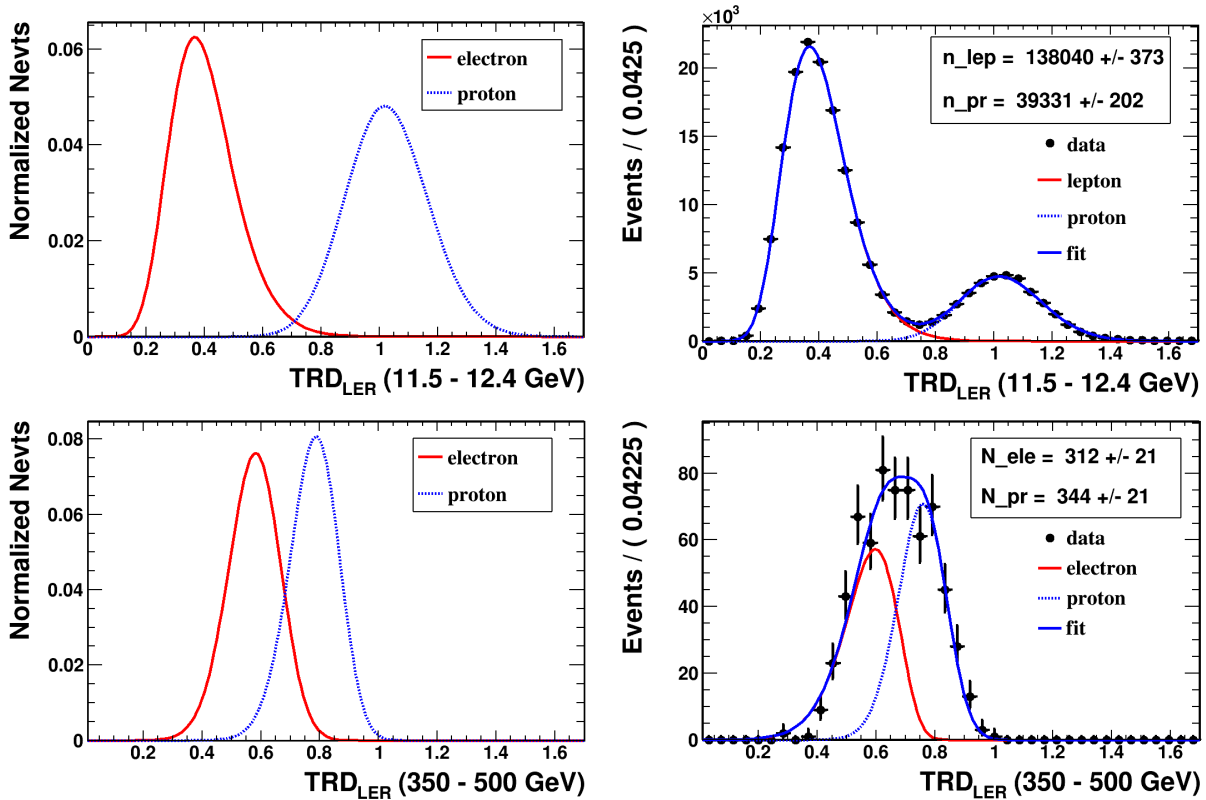


Figure 4.30: Upper left: electron (red) and proton (dashed blue) templates used for the bin 11.5 - 12.4 GeV. Upper right: fit on the lepton sample for the same energy bin. The two lower figures are templates and fit on the electron sample of the bin 350 - 500 GeV.

The lepton and electron numbers are shown in Figure 4.31. To compare this result with that obtained with ESE_{V3} , the efficiency of the cuts $TRD_{LER} < 0.61$, $TRD_{LER} < 0.65$, $TRD < 0.71$ and $ESE_{V3} > -0.15$ needs to be calculated.

4.6.1 TRD_{LER} cut efficiency

The efficiency of TRD_{LER} cuts used in lepton and electron number counting can be estimated with the TRD_{LER} electron template.

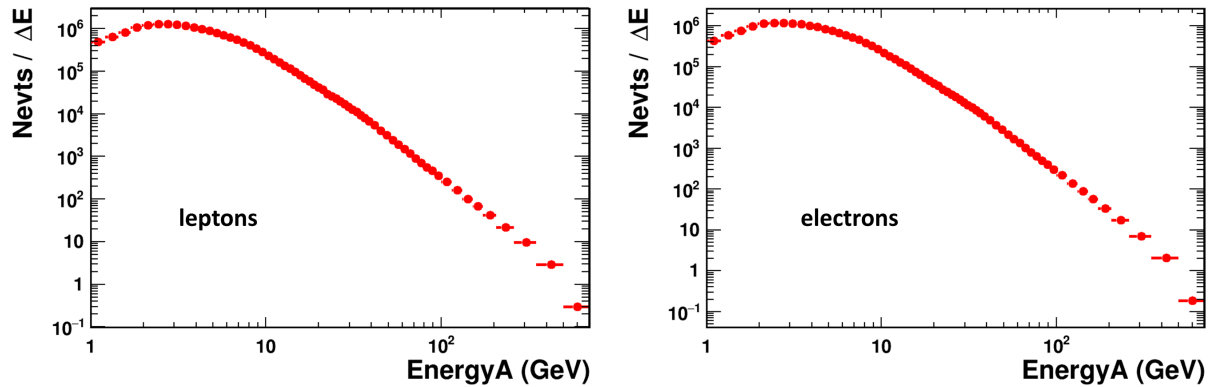


Figure 4.31: Results obtained by template fits on TRD_{LER} : number of leptons (left) and number of electrons (right) divided by the bin width for the energy range of 1 to 700 GeV using 29 months of ISS data. Only statistical uncertainty from the fits is shown. Error bars are smaller than the marker size.

The method is illustrated in Figure 4.32 with the bin of 43.4 - 47.0 GeV. The electron template

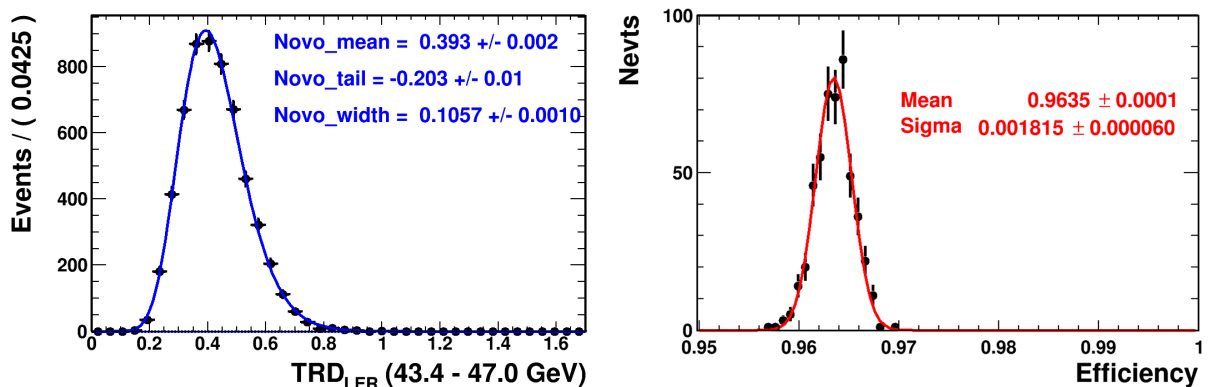


Figure 4.32: Left: electron template for the bin 43.4 - 47.0 GeV fitted with Novosibirsk function. Right: distribution of the integral results performed on the range $TRD_{LER} \in (0, 0.65)$ using 500 PDFs generated from the Novosibirsk function. The red curve is the Gaussian function used to fit the efficiency distribution.

is fitted with a Novosibirsk function, whose normalized integral on the range $TRD_{LER} \in (0, x)$ gives the efficiency of cut $TRD_{LER} < x$. To estimate the uncertainty of this method, 500 PDFs are generated using the fitted parameters, which take into account the uncertainties of the three parameters (mean, width and tail) and the correlation between them. The distribution of the 500 integration results is fitted with Gaussian function. The mean of the Gaussian is the efficiency and the sigma is the uncertainty.

The same procedure is repeated for all the energy bins from 1 to 700 GeV and for different cut values. Figure 4.33 shows the efficiency for the cuts $TRD_{LER} < 0.71$, $TRD_{LER} < 0.65$ and $TRD_{LER} < 0.61$. It is observed that between 2 GeV and 200 GeV, the efficiency is stable at ~ 0.99 for $TRD_{LER} < 0.71$ and ~ 0.94 for $TRD_{LER} < 0.61$. Above 200 GeV, the cut efficiency

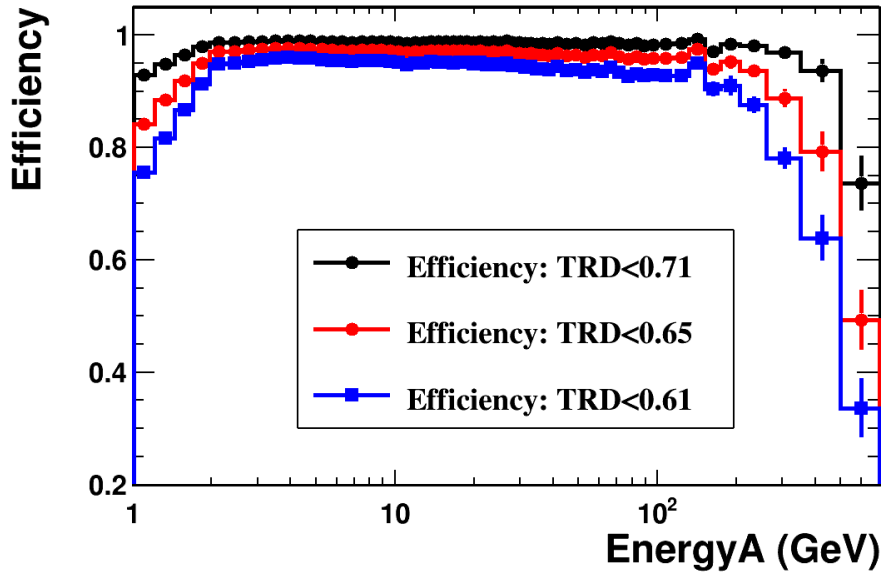


Figure 4.33: Efficiency of TRD_{LER} cuts at 0.71 (black), 0.65 (red) and 0.61 (blue) for the energy range of 1 - 700 GeV.

rapidly drops with energy. At 500 - 700 GeV, the efficiency is ~ 0.74 for $TRD_{LER} < 0.71$ and ~ 0.33 for $TRD_{LER} < 0.61$.

4.6.2 ESE_{V3} cut efficiency

Similarly, the ESE_{V3} cut efficiency is estimated using the electron template for ESE_{V3} . Integral of the normalized electron PDF on the interval of $(-0.15, 0.4)$ yields the efficiency of cut $ESE_{V3} > -0.15$. Figure 4.34 shows the efficiency as a function of energy. Between 5 and 300

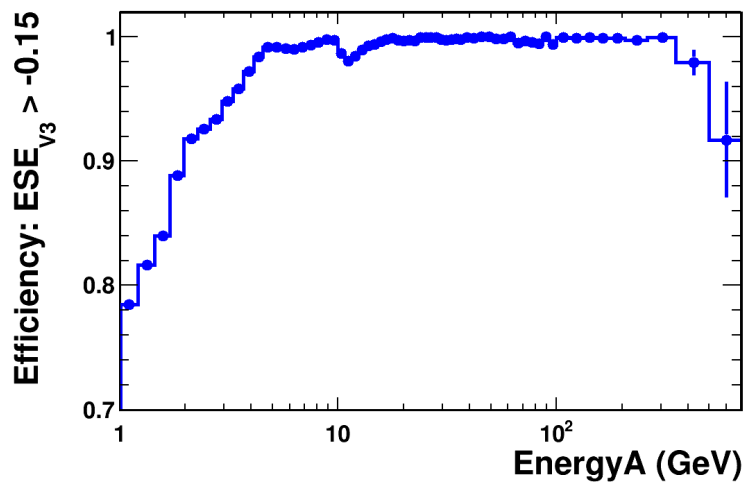


Figure 4.34: Efficiency of the cut $ESE_{V3} > -0.15$ for the energy range of 1 - 700 GeV.

GeV, the efficiency is stable at 1 and then drops to ~ 0.9 at 500 - 700 GeV.

4.6.3 Comparison of results from ESE_{V3} and from TRD_{LER}

The comparison of electron and lepton numbers measured with ESE_{V3} and TRD_{LER} is shown in Figure 4.35 and Figure 4.36. Both are corrected by the efficiency of TRD_{LER} or ESE_{V3} cut.

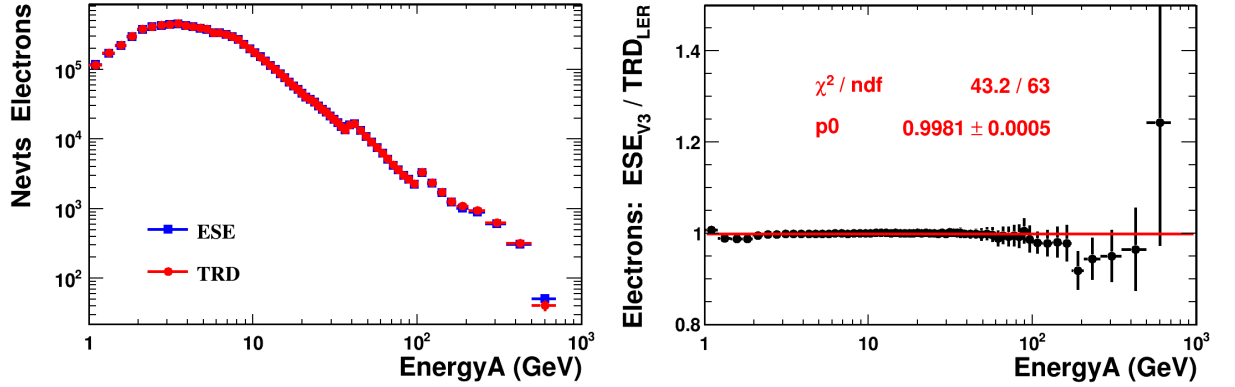


Figure 4.35: Left: electron numbers counted with ESE_{V3} (blue) and TRD_{LER} (red). ESE_{V3} result is corrected by the efficiency of cut $TRD_{LER} < 0.71$. TRD_{LER} result is corrected by the efficiency of cut $ESE_{V3} > -0.15$. Right: ratio of electron numbers ESE_{V3} / TRD_{LER} , which is fitted with a constant function (red curve).

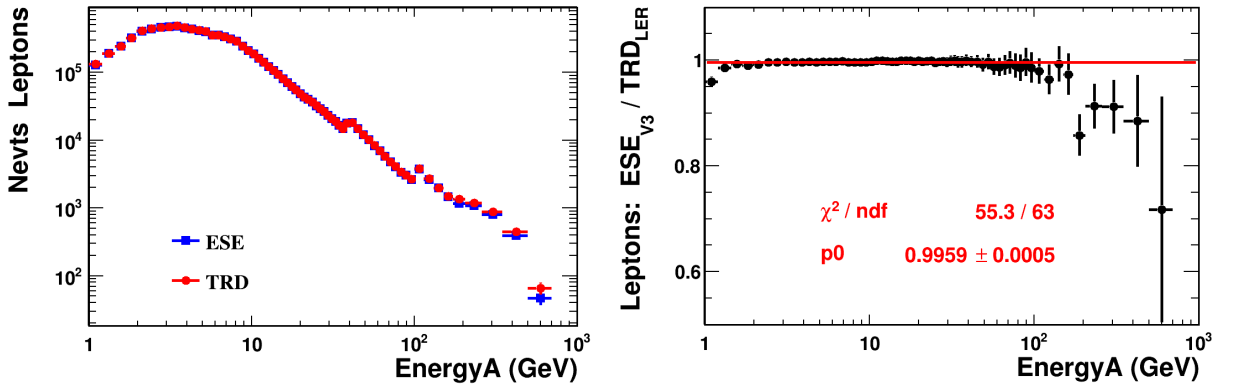


Figure 4.36: Left: lepton numbers counted with ESE_{V3} (blue) and TRD_{LER} (red). ESE_{V3} result is corrected by the efficiency of cut $TRD_{LER} < 0.65$. TRD_{LER} result is corrected by the efficiency of cut $ESE_{V3} > -0.15$. Right: ratio of electron numbers ESE_{V3} / TRD_{LER} , which is fitted with a constant function (red curve).

The two results are in good agreement below 200 GeV. The discrepancy is within 0.5%. At high energy, the number counted with ESE_{V3} is 1-sigma lower than that with TRD_{LER} . However, the separation between electron and proton is better with ESE_{V3} .

4.7 Systematic uncertainties

Two systematic uncertainties of the lepton and electron numbers are estimated here, one due to the template uncertainties and the other due to the estimation of signal purity in the data samples.

4.7.1 Template uncertainties

In the fit method previously presented, all the parameters of the electron and proton templates are fixed. The systematic uncertainty due to the templates is estimated by varying all the parameters within their statistical uncertainties. The energy bins below 15 GeV are not studied, since they are fitted with histograms.

Let's take the electron number of the energy bin of 260 - 350 GeV as an example. 1000 new electron PDF functions and 1000 proton PDF functions are respectively generated using the nominal template PDFs shown in Figure 4.22. Figure 4.37 shows the 1000 generated electron

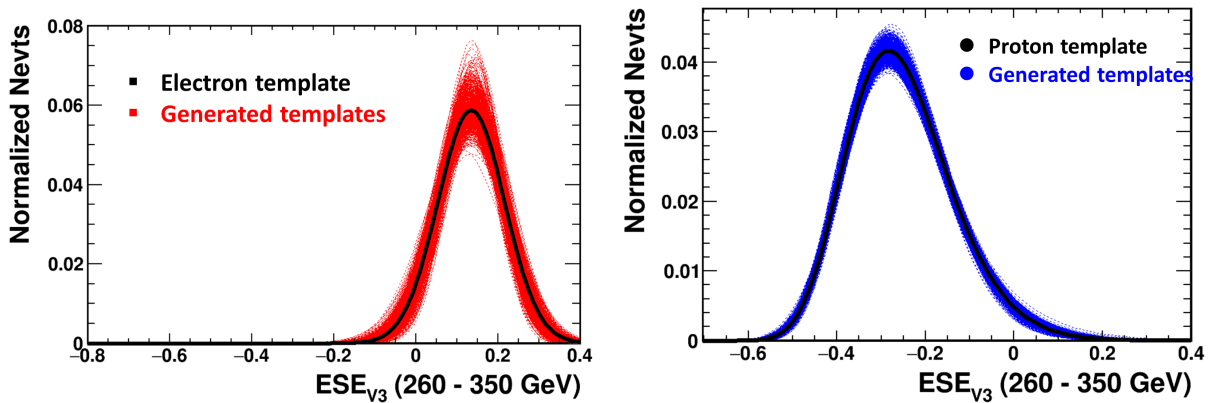


Figure 4.37: Bands of 1000 generated electron (left red) and proton (right blue) templates for the energy bin of 260 - 350 GeV. The fixed-parameter electron and proton templates are drawn in black.

and proton templates. Electron number, N_{e^-} , is obtained by fitting the data samples 1000 times using these generated pairs of functions. The distribution of N_{e^-}/N_0 of the 1000 fit results is shown in Figure 4.38, where N_0 is the number of electrons counted with fixed templates, equal to 591 as given in Figure 4.26. The width of the Gaussian function is taken as the systematic uncertainty due to the templates.

The same analysis is repeated for electrons and leptons, for all the energy bins between 15 and

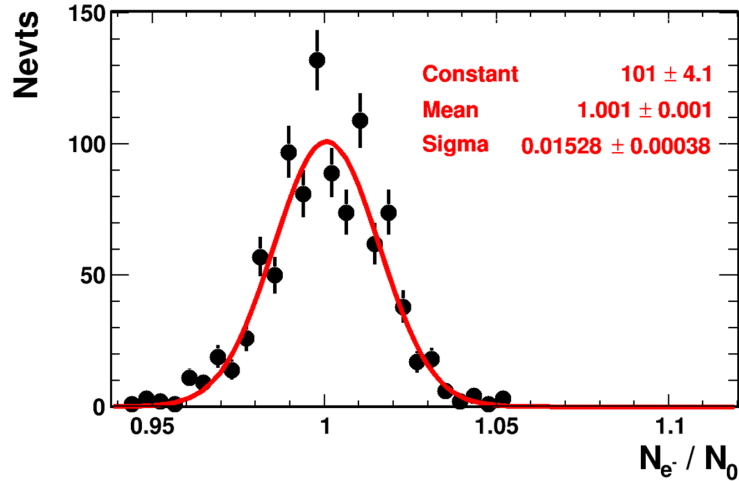


Figure 4.38: Distribution of the ratio N_{e^-}/N_0 for the energy bin of 260 - 350 GeV, where N_{e^-} is the electron number measured using generated templates and N_0 is the number using fixed-parameter templates. The distribution is fitted by Gaussian function with a mean of 1.001 and a width of 0.015.

700 GeV. Uncertainty of the electron number is shown in Figure 4.39. The ratio is very close

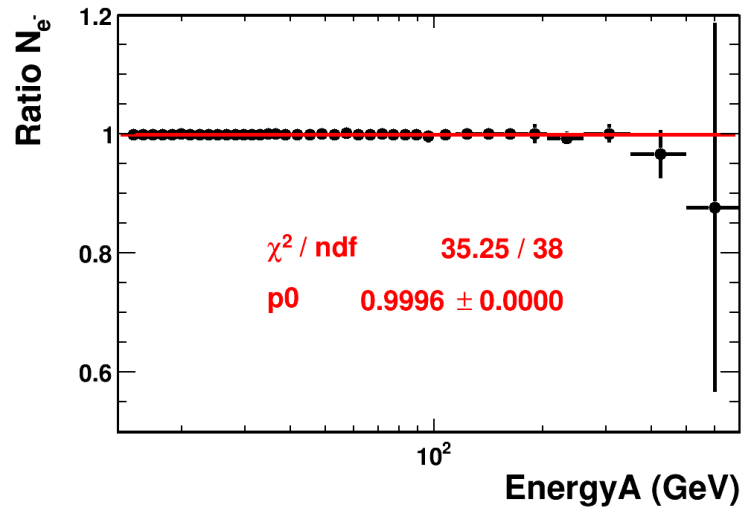


Figure 4.39: Ratio of the electron number measured using generated templates and fixed templates for the energy range of 15 - 700 GeV, fitted by the constant function (red line) of $f(x) = 0.9996$.

to 1 below 300 GeV. Above 300 GeV, large uncertainty is observed due to lack of statistics in template building. A systematic uncertainty of 1.5% at 300 GeV and 43% at 700 GeV is attributed to the electron number result.

Uncertainty of the lepton number is shown in Figure 4.40. Same with the electron number, it is within 1% below 100 GeV. A systematic uncertainty of 2% at 300 GeV and 34% at 700 GeV is attributed to the lepton number result.

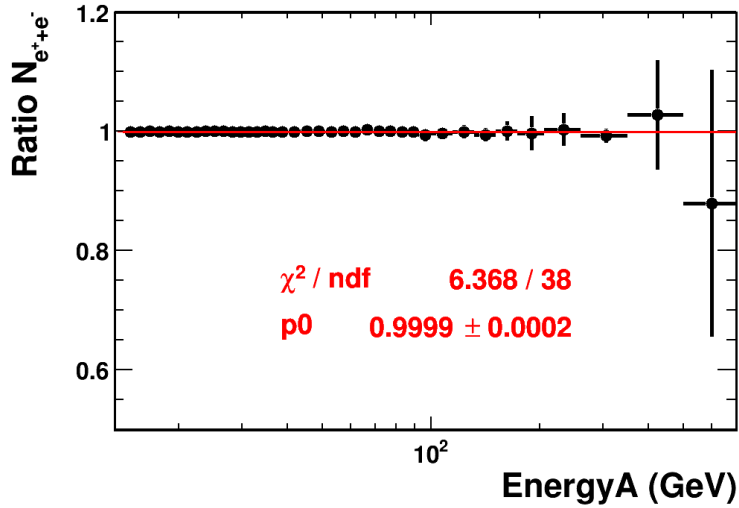


Figure 4.40: Ratio of the lepton number measured using generated templates and fixed templates for the energy range of 15 - 700 GeV, fitted by the constant function (red line) of $f(x) = 0.9999$.

4.7.2 Different TRD_{LER} cuts

The signal purity in our case is defined as $\frac{N_e}{N_e + N_p}$, where N_e is the number of electrons or leptons and N_p is the number of protons in the data sample. The TRD_{LER} cut changes the lepton and electron purity of the data samples, which affects the goodness of template-fit results. Usually, the results are more reliable if the data samples have high signal purity.

Figure 4.41 shows the purities of electron samples as a function of energy for three TRD_{LER} cuts at 0.61, 0.65 and 0.71. The purity is estimated using ISS electron data samples. It is ob-

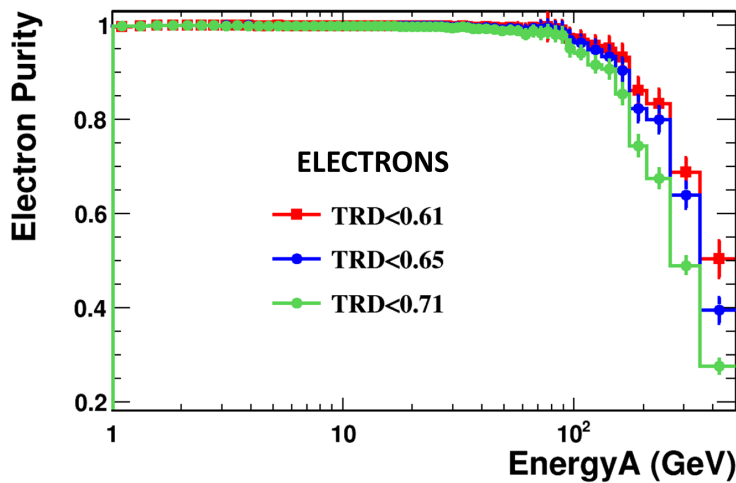


Figure 4.41: Purity of the electron data samples in the energy range of 1 - 500 GeV, for TRD_{LER} cuts at 0.61 (red), 0.65 (blue) and 0.71 (green). Estimated using 29 months of ISS data.

served that the purity is stable at 1 below 100 GeV. Above 100 GeV, the purity drops rapidly.

At 500 GeV, the purity for $TRD_{LER} < 0.71$ is even below 0.3.

Similarly, the purity of lepton samples is checked in Figure 4.42. Generally, the purity is lower

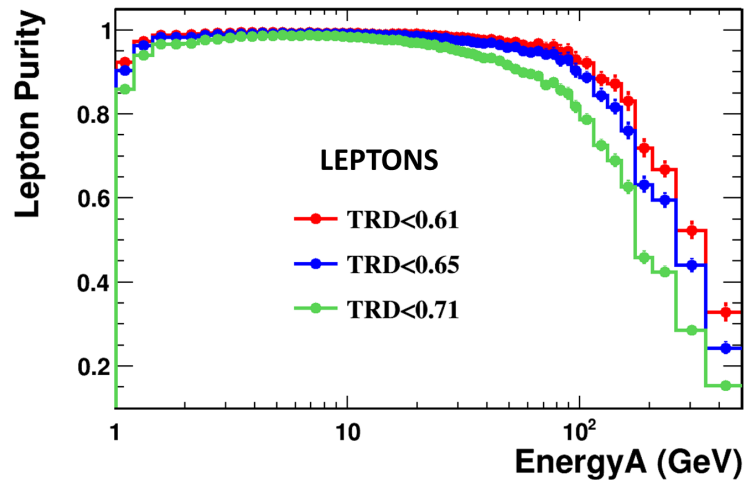


Figure 4.42: Purity of the lepton data samples in the energy range of 1 - 500 GeV, for TRD_{LER} cuts at 0.61 (red), 0.65 (blue) and 0.71 (green). Estimated using 29 months of ISS data.

than that of the electron samples. Purity for loose cut such as $TRD_{LER} < 0.71$ starts to drop at 20 GeV. With $TRD_{LER} < 0.65$, the purity of lepton samples at 500 GeV is ~ 0.25 .

The impact of data sample purity can be studied by varying the TRD_{LER} cut. Therefore, the systematic uncertainty of the electron and lepton numbers due to the purity is examined using data samples with different TRD_{LER} thresholds: 0.61, 0.63, 0.65, 0.67, 0.69, 0.71, 0.73 and 0.75.

The fit is repeated on the 8 data samples with different TRD_{LER} cuts and the efficiency for each TRD_{LER} cut is computed. The N_{e^-}/ϵ_{TRD} and $N_{e^+e^-}/\epsilon_{TRD}$ with different TRD_{LER} thresholds are compared in Figure 4.43 and Figure 4.44 for the energy range of 1 - 500 GeV. The last bin of 500 - 700 GeV is not checked, since the TRD_{LER} cut has to be fixed at 0.61 to reduce the large proton background.

The electron number is rather stable over the whole energy range. Ratios of the numbers are close to 1, though some discrepancies are observed below 2 GeV and above 200 GeV. A systematic uncertainty of 1% is attributed to the range of 2 - 60 GeV. At 1 GeV, the uncertainty is 5% and at 500 GeV, the uncertainty is also 5%.

At high energy, samples are less pure as proton contamination becomes more important, especially for lepton samples. The performance of template fit method is reduced. As a result, the lepton number is less stable than the electron number at high energy. A systematic uncertainty of 1% is attributed to the range of 2 - 60 GeV. At 1 GeV, the uncertainty is 5%. At 500 GeV, the uncertainty is 10%.

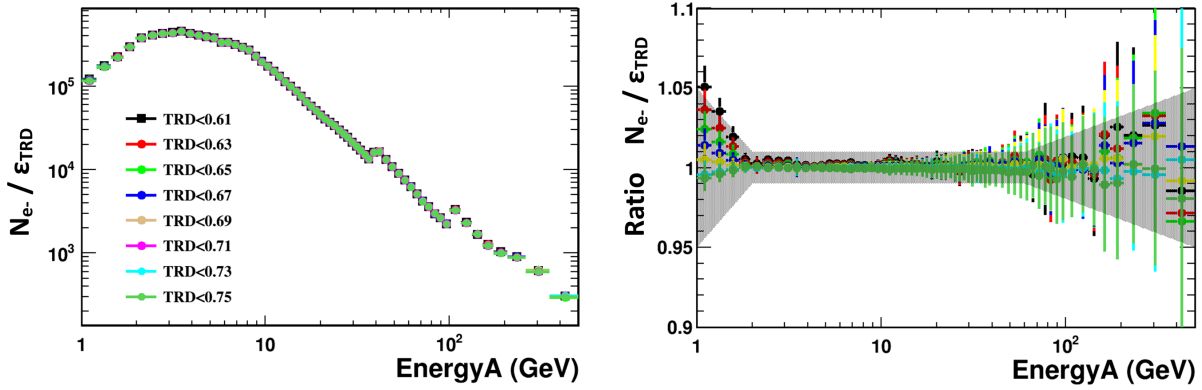


Figure 4.43: Left: electron numbers measured with different TRD_{LER} cuts. Each result is corrected by the corresponding TRD_{LER} efficiency. Right: electron numbers normalized by the number measured with $TRD_{LER} < 0.71$. The grey shade is the systematic uncertainty: 5% at 1 GeV, 1% between 2 and 60 GeV and 5% at 500 GeV.

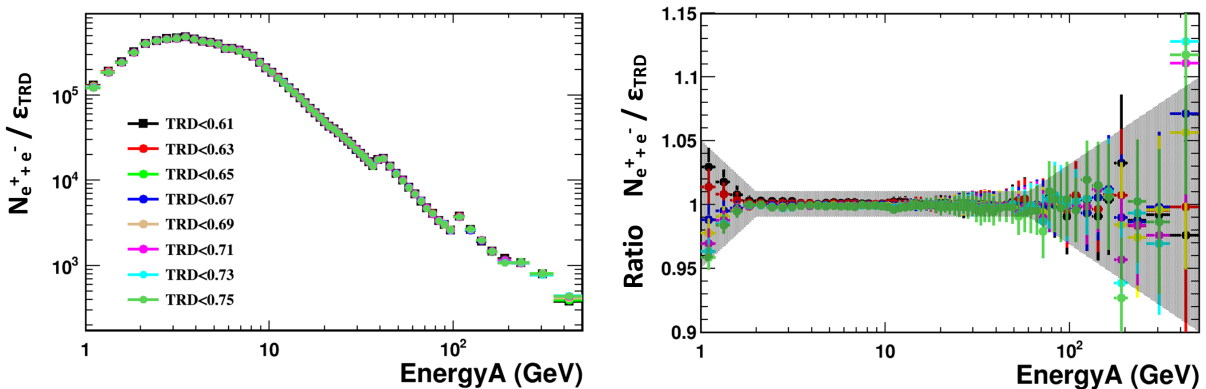


Figure 4.44: Left: lepton numbers measured with different TRD_{LER} cuts. Each result is corrected by the corresponding TRD_{LER} efficiency. Right: lepton numbers normalized by the number measured with $TRD_{LER} < 0.65$. The grey shade is the systematic uncertainty: 5% at 1 GeV, 1% between 2 and 60 GeV and 10% at 500 GeV.

Chapter 5

Electron Flux Measurement

The cosmic-ray lepton ($e^+ + e^-$) flux or electron (e^-) flux, Φ_e at energy E , is computed with the following formula

$$\Phi_e(E) = \frac{N_e(E)}{\underbrace{Acc(E) \times \epsilon_{sel}(E)}_{MC} \times \underbrace{corr_{data/MC}(E)}_{MC \text{ and ISS data}} \times \underbrace{\epsilon_{TRD}(E) \times \epsilon_{phys.trig.}(E) \times T_{expo}(E)}_{ISS \text{ data}} \times \Delta E} \quad (5.1)$$

where N_e is the measured number of electrons, Acc the geometrical acceptance, ϵ_{sel} the selection efficiency, $corr_{data/MC}$ the efficiency correction Data/MC, ϵ_{TRD} the TRD_{LER} cut efficiency, $\epsilon_{phys.trig.}$ the physics trigger efficiency, T_{expo} the exposure time and ΔE the energy bin width. The energy range of this measurement is 1 to 700 GeV. As indicated in Equation (5.1), some of the terms are obtained from ISS data, others from MC events.

The event selection as well as the lepton counting have been explained in the previous chapter. In this chapter, firstly, the geomagnetic cutoff threshold and exposure time are defined. Secondly, the lepton selection efficiency and the trigger efficiency, as well as their systematic uncertainty, are estimated. Then effects of unfolding are studied. Finally the results and consistency checks are reported.

5.1 Exposure time

Exposure time, $T_{expo}(R)$ in Equation (5.1) which depends on rigidity, is the cumulated time of measurement at which the detector is sensitive to particles with a rigidity greater than R . For a given rigidity R , it is calculated as the sum of the good seconds for which $R > f_{safety} \times R_{cut}(t)$ is satisfied, where f_{safety} is called safety factor, normally chosen arbitrarily between 1.0 to 1.5, and $R_{cut}(t)$ is the maximum geomagnetic cutoff¹ rigidity at the position of the detector at time t (cf. Section 1.3.2.3). Similar requirement is applied on data to get consistent electron count. For each electron or positron with energy E , it is required that $E = R > f_{safety} \times R_{cut}$. Otherwise, the event is rejected. In this analysis, f_{safe} is chosen as 1.3 to ensure that the secondary particles produced by the interaction of primary cosmic rays with the atmosphere are removed.

To determine the quality of each second, a few basic cuts are utilized such as:

- Livetime, defined as the time interval between two incoming particles, is greater than 0.5
- AMS is not in the South Atlantic Anomaly (SAA) region
- AMS zenith angle is smaller than 40° (see Figure 5.1)

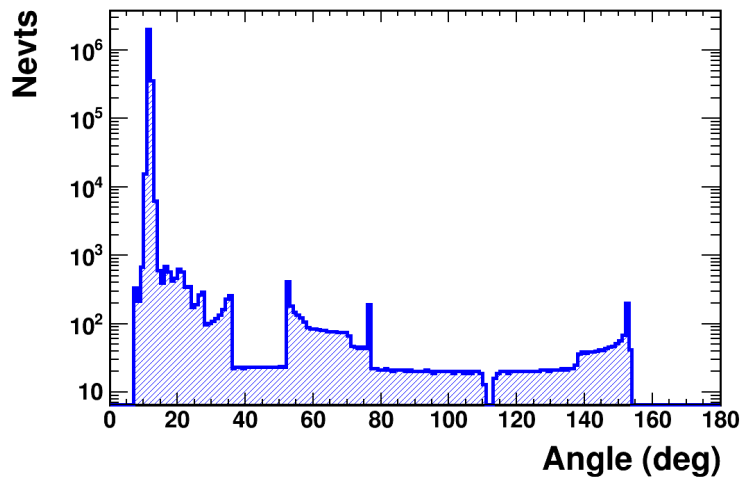


Figure 5.1: Distribution of zenith angle of AMS, measured with 1 month of ISS data.

The R_{cut} for each second is computed with the information of the AMS location and the opening angle. Opening angle of 40° is used for R_{cut} calculation.

The integrated exposure time for 29 months is shown in Figure 5.2. It is seen that the time is

¹Maximum geomagnetic cutoff is the maximum of geomagnetic cutoff values for a specified opening angle.

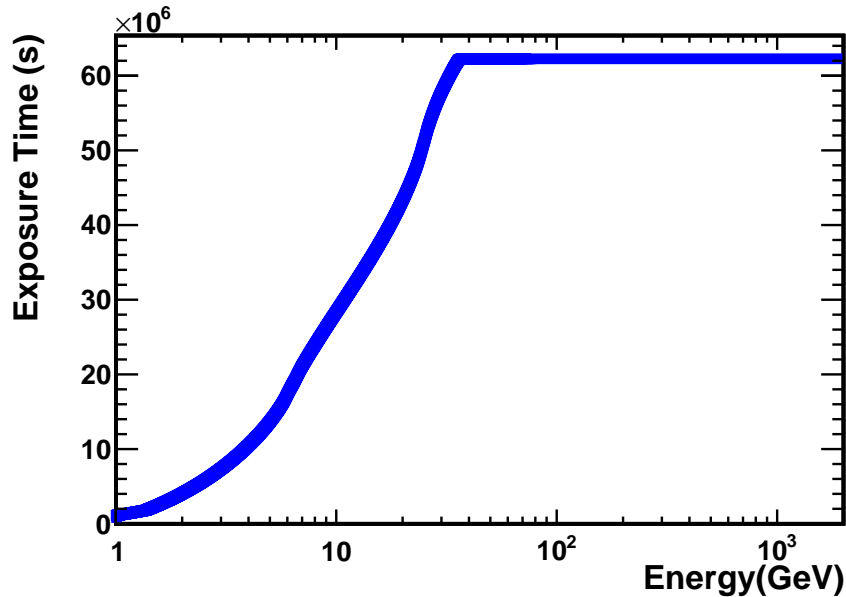


Figure 5.2: Exposure time measured for 29 months from June 2011 to November 2013 (without December 2011).

stable after 40 GeV. Below 40 GeV, it is affected by geomagnetic cutoff effect.

5.1.1 Systematic uncertainty due to geomagnetic cutoff

Uncertainty due to geomagnetic cutoff is estimated by varying the safety factor and opening angle. Exposure time measurements corresponding to different combinations of f_{safety} and opening angle are shown in Figure 5.3

N_e/T_{expo} is to be measured using the 12 combinations. The uncertainty is yielded from the dispersion of the 12 results. The measured N_e/T_{expo} for the 12 thresholds are normalized to the nominal one, safety factor of 1.3 and opening angle of 40° . Their ratios are shown in Figure 5.4. The lepton rate measured using the lowest cutoff rigidity (blue dots) is significantly lower than the others. A systematic uncertainty of 0.5% is attributed to the geomagnetic cutoff estimation.

5.2 Physics Trigger Efficiency

AMS trigger system as well as physics triggers (bits 1 to 5 defined in Table 2.1) has been explained in Section 2.3.1. The trigger efficiency for electrons and its systematic uncertainty are here estimated with the ISS data.

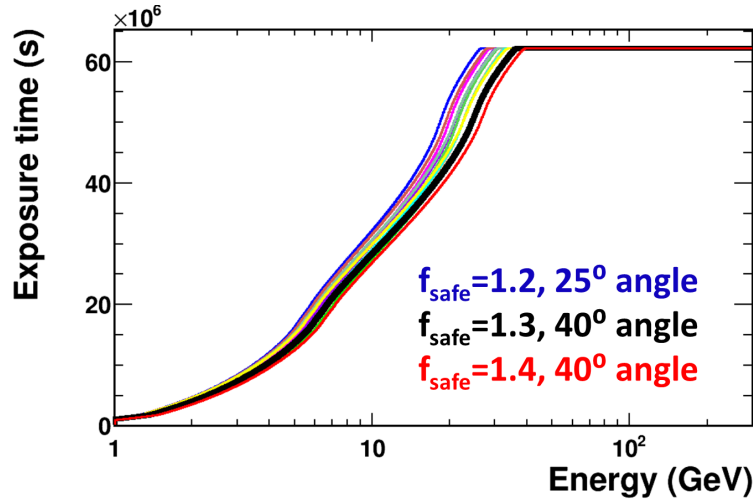


Figure 5.3: Exposure time 12 combinations of safety factor and opening angle used in geomagnetic cutoff calculation: respectively with safety factor of 1.2, 1.3 and 1.4 and opening angle of 25°, 30°, 35° and 40°. The highest exposure time with lowest R_{cut} is the blue line, with safety factor of 1.2 and opening angle of 25°. The lowest exposure time, which has the highest R_{cut} is the red line, with safety factor of 1.4 and opening angle of 40°.

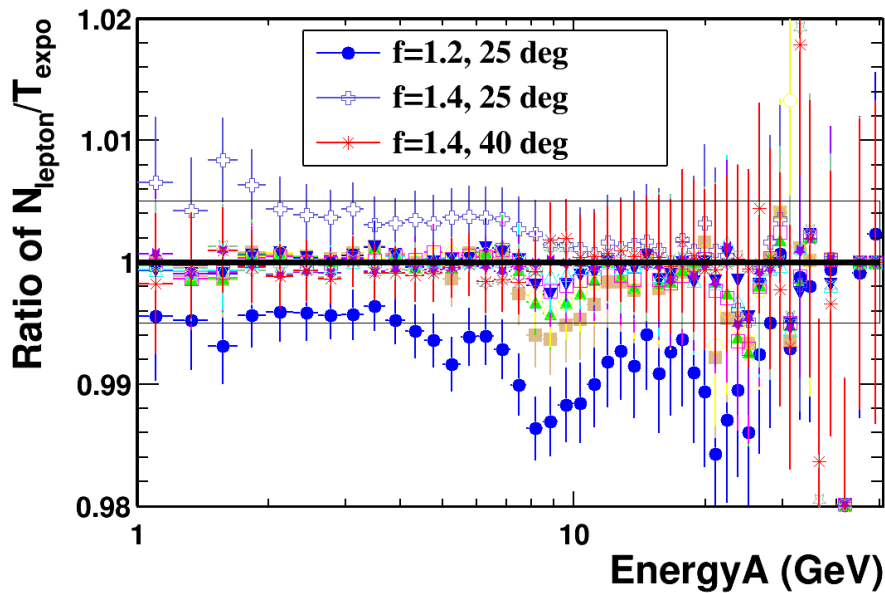


Figure 5.4: Ratios of lepton rates measured using different cutoff thresholds and the nominal one for the energy range of 1 - 50 GeV. Boundary of $1 \pm 0.5\%$ is drawn in black.

5.2.1 Physics trigger efficiency for electrons

Unbiased TOF and unbiased ECAL triggers are designed for trigger efficiency estimation as they are expected to be 100% efficient. With ISS electron events, the physics trigger efficiency is given by

$$\epsilon_{\text{phys.trig.}} = \frac{N_{\text{phys.trig.}}}{N_{\text{phys.trig.}} + f_{\text{prescale}} \times N_{\text{unbias.trig.}}} \quad (5.2)$$

where $N_{phys.trig.}$ is the number of events which have at least 1 physics trigger, $f_{prescale}$ is the prescaling factor and $N_{unbias.trig.}$ is the number of events which only have unbiased triggers. The prescaling factor is designed to be 100 for unbiased TOF and 1000 for unbiased ECAL. As electrons are charged particles, unbiased triggers are essentially unbiased TOF (bit 0) with a prescaling factor of 100.

The ISS electron sample is selected with identification selection presented in Section 4.2 plus a tight cut on ESE_{V3} (>-0.1). Figure 5.5 shows the trigger efficiency calculated for the energy range of 1 to 700 GeV. From 3 GeV above, the physics trigger efficiency for electrons are stable

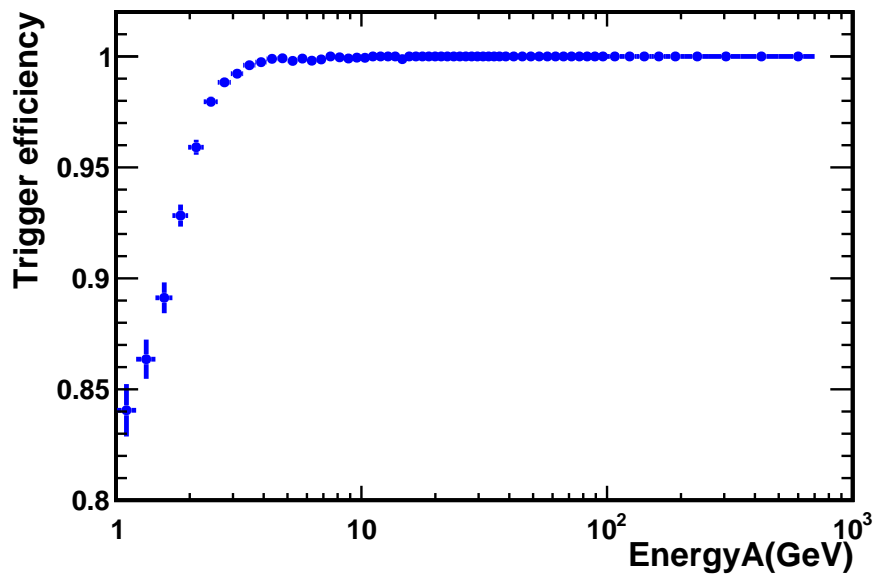


Figure 5.5: Physics trigger efficiency for electrons measured with 29 months of ISS data.

at 1.

5.2.2 Systematic uncertainty of the trigger efficiency using the electron trigger

Since the unbiased trigger is more precisely a minimal biased trigger, another method using the electron trigger has been developed to estimate the systematic uncertainty. The **electron trigger** is one of the five physics triggers, corresponding to the Bit 4 in Table 2.1. There are two methods to measure its efficiency. The difference of the results from the two methods yields the systematic uncertainty of trigger efficiency.

Nominal method using unbiased triggers

The same as for physics trigger efficiency, electron trigger efficiency is calculated with

$$\epsilon_{el.trig.} = \frac{N_{el.trig.}}{N_{phys.trig.} + f_{prescale} \times N_{unbias.trig.}} \quad (5.3)$$

where $N_{el.trig.}$ is the number of events with electron trigger. The result is shown in Figure 5.7.

Method using TOF and ECAL triggers

In this method, TOF (FTCT1) and ECAL (ECALF&) triggers are used. As TOF and ECAL triggers are independent, the efficiency of electron trigger can be split into:

$$\epsilon_{el.trig.} = \epsilon_{FTCT1\&(ECALF\&)} = \epsilon_{FTCT1} \times \epsilon_{ECALF\&} \quad (5.4)$$

where the TOF and ECAL trigger efficiencies can be respectively calculated using the number of events triggered by the proton ($N_{pr.trig.}$), the photon ($N_{ph.trig.}$) and electron and photon ($N_{el.trig.\&ph.trig.}$). The formula is

$$\epsilon_{FTCT1} = \frac{N_{FTCT1\&(ECALF\&)\&(ECALA\&)}}{N_{ECALA\&}} = \frac{N_{el.trig.\&ph.trig.}}{N_{ph.trig.}} \quad (5.5a)$$

$$\epsilon_{(ECALF\&)} = \frac{N_{(ECALF\&)\&FTCT1\&ACC0}}{N_{FTCT1\&ACC0}} = \frac{N_{el.trig.\&ACC0}}{N_{pr.trig.}} \quad (5.5b)$$

In Equation (5.5), $N_{ph.trig.}$ is the number of events with Bit 5 in physics triggers (Table 2.1), $N_{pr.trig.}$ is the number of events with Bit 1 in physics triggers. The results of TOF and ECAL trigger efficiency are given in Figure 5.6. Combining the TOF and ECAL efficiencies, the

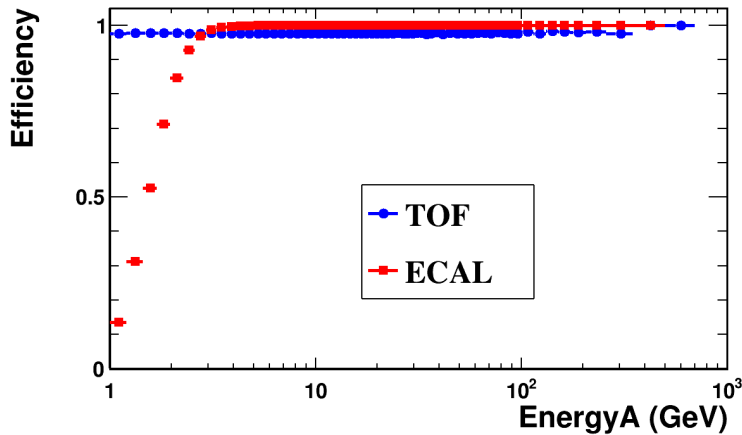


Figure 5.6: TOF (blue) and ECAL (red) trigger efficiency measured with 29 months of ISS data.

electron trigger efficiency is obtained with Equation (5.4).

Comparison of the trigger efficiency calculated with the two methods is shown in Figure 5.7.

Their difference gives the systematic uncertainty of the trigger efficiency. Figure 5.8 shows the

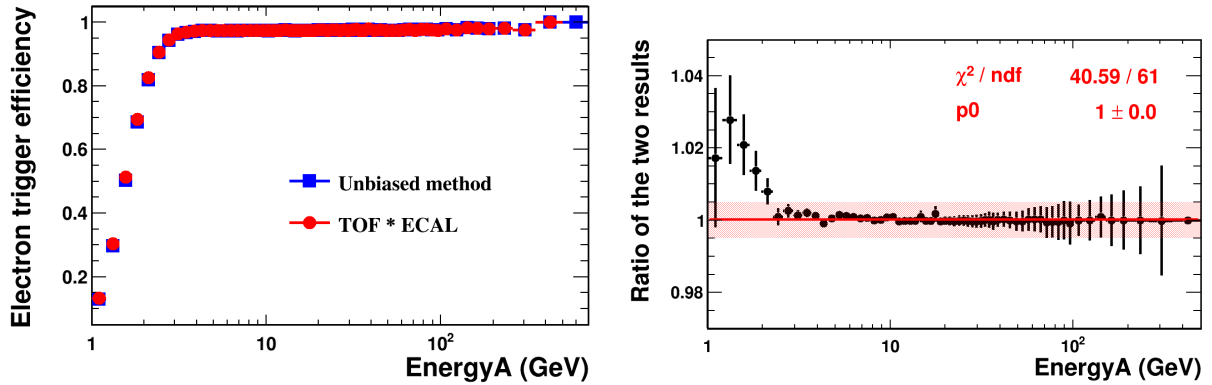


Figure 5.7: Electron trigger efficiency measured with the two methods, flat after 3 GeV. The product of the TOF and ECAL efficiency gives the red points. On the right is the ratio of the two results (unbiased/TOF-ECAL), which is fitted with a constant function. The red shade indicates the boundary of $1 \pm 0.5\%$.

uncertainty as a function of ECAL energy, which is smaller than 10^{-3} above 3 GeV.

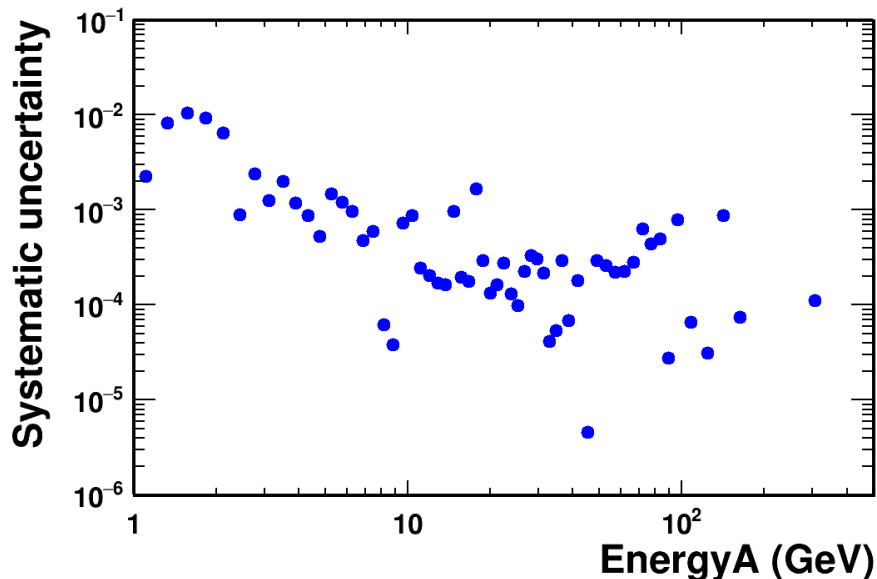


Figure 5.8: Systematic uncertainty estimated by the difference of electron trigger efficiency measured with Unbiased and TOF&ECAL methods. The uncertainty goes smaller than 10^{-3} above 3 GeV.

5.2.3 TOF and ECAL triggers yearly monitoring

To monitor the performance of TOF and ECAL trigger, their efficiencies are measured for each year. Figure 5.9 and Figure 5.10 show the TOF and ECAL trigger efficiency measured with data collected in the year 2011, 2012 and 2013.

A decrease with time is observed in the TOF trigger efficiency over the energy range of 1 to

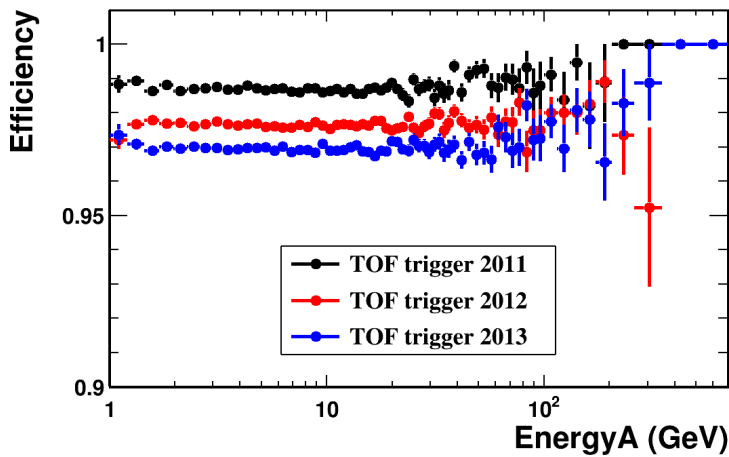


Figure 5.9: Efficiency of the TOF trigger measured with data collected in 2011, 2012 and 2013.

700 GeV. The ECAL trigger efficiency stays stable at 1 above 3 GeV over the three years.

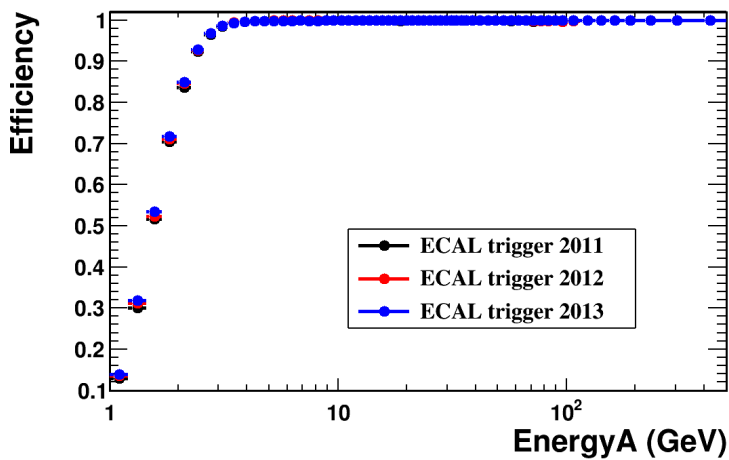


Figure 5.10: Efficiency of the ECAL trigger measured with data collected in 2011, 2012 and 2013.

5.3 Acceptance and selection efficiency

The acceptance, Acc , and selection efficiency, ϵ_{sel} , are measured with MC data. The ϵ_{sel} is also estimated with ISS control samples. The difference between efficiency measured with ISS and MC control samples is corrected on ϵ_{sel} and the associated systematic uncertainty is estimated by using different control samples.

5.3.1 MC reweighting

To estimate the acceptance, the selection efficiency and the charge confusion, the MC input spectrum must be reweighted to have the same dN/dE as in the real observation of cosmic-ray electrons with AMS. From Equation (4.1), dN/dE is equal to $\Phi \times Acc \times \epsilon \times T_{expo}$, where Acc is a constant and ϵ is 1 for MC. As a result, dN/dE of MC should be proportional to $\Phi \times T_{expo}$. Here, the electron flux (Φ_{e^-}) published by AMS-02 collaboration 2014 [46] is used as real flux. The exposure time has been measured with 29 months of data in Section 5.1. The shape of $\Phi_{e^-} \times T_{expo}$ is used to reweight the MC data from 1 GeV to 700 GeV.

The initial dN/dE of MC is a power law of degree -1, which is presented in Section 2.3.3. Therefore, the weight for each MC event is

$$w(E_{true}) = K \times E_{true} \times \Phi_{e^-}(E_{true}) \times T_{expo}(E_{true}) \quad (5.6)$$

where K is a normalization coefficient independent of energy. Figure 5.11 shows the dN/dE spectrum of the reweighted MC in comparison with the unweighted generated spectrum.

The MC data used in the following studies are always reweighted with the weight calculated by Equation (5.6).

The impact of this reweighting method is studied by changing the input spectrum in Section 5.3.4.

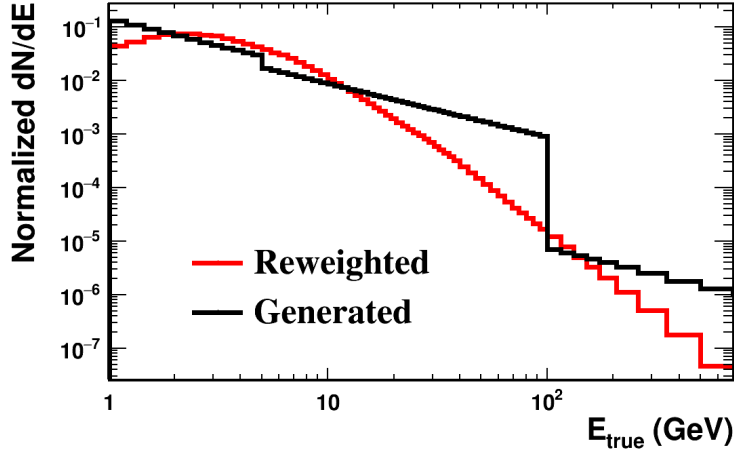


Figure 5.11: Reweighted MC dN/dE (red) as a function of E_{true} in comparison with the generated dN/dE (black).

5.3.2 Estimation of the acceptance with MC events

The effective acceptance is defined as

$$A_{\text{eff}} = A_{\text{gen}} \times \epsilon_{\text{sel}} = A_{\text{gen}} \times \frac{N_{\text{selected}}}{N_{\text{generated}}} = 47.8 \times \frac{N_{\text{selected}}[E_{\text{rec}}]}{N_{\text{generated}}[E_{\text{true}}]} \quad [\text{m}^2 \cdot \text{sr}] \quad (5.7)$$

where A_{gen} is the generation acceptance of MC electrons ($47.8 \text{ m}^2 \cdot \text{sr}$), N_{selected} is the number of events after the selection and $N_{\text{generated}}$ is the number of generated events.

Figure 5.12 shows the acceptance after each cut in the selection defined in Section 4.2. After the preselection, the acceptance is around $0.06 \text{ m}^2 \cdot \text{sr}$ and it lowers with each cut. For instance, the cut ΔY affects the acceptance at low energy and $\text{EoP} < 10$ affects the high energy. The final acceptance after the single track cut is $\sim 0.04 \text{ m}^2 \cdot \text{sr}$ at 10 GeV and $\sim 0.03 \text{ m}^2 \cdot \text{sr}$ at 300 GeV.

The final acceptance is smoothed with polynomial functions. Systematic uncertainty is attributed to the fluctuations in this estimation, 0.3% for the energy bins below 40 GeV, 1.3% at 100 GeV and 3% above 200 GeV.

5.3.3 Data-driven correction on the acceptance

The selection efficiency is measured for each energy bin using control samples, which are e^- samples selected from ISS data and from MC data. Difference between the results given by ISS and MC samples is applied as Data-MC correction on the acceptance.

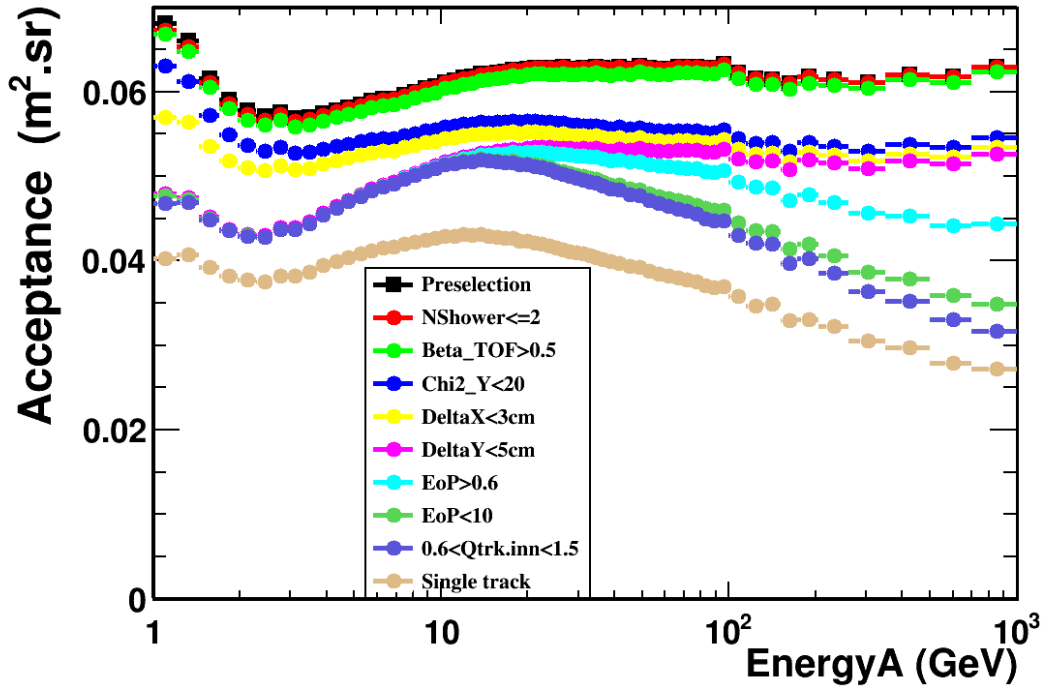


Figure 5.12: Preselection acceptance (black) and acceptance after each cut, calculated in the hierarchical order. The khaki curve is the final acceptance after lepton selection, which is used in the flux measurement.

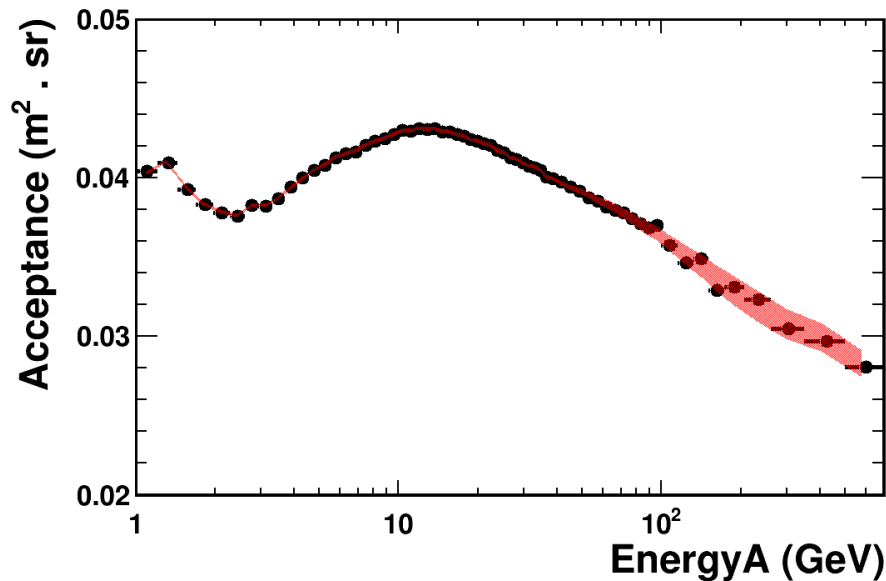


Figure 5.13: The final acceptance after the lepton selection smoothed with a spline function below 40 GeV and a polynomial of degree three above 40 GeV. The red shade is the systematic uncertainty of the acceptance estimation with MC.

5.3.3.1 Control of the preselection efficiency

The preselection consists of three basic quality cuts: the availability of TRD_{LER} estimator (TRD_{LER}), at least one shower in the ECAL, and at least one track in the tracker. The

efficiency of these three cuts is respectively estimated using ISS electrons and MC data.

Availability of TRD_{LER}

To estimate the efficiency of the availability of TRD_{LER} using ISS data, pure electron samples are selected by cutting on the variables of TOF, tracker and ECAL.

- TOF: velocity $\beta > 0.8$, charge $Q_{TOF} < 1.8$
- Tracker: number of tracks $N_{track} > 0$, rigidity $R < 0$, pattern L1L9
- ECAL: number of showers $N_{shower} > 0$, $ESE_{V3} > 0$

The same cuts are also applied on MC data. The TRD_{LER} availability estimated using the ISS and MC samples as a function of energy is shown in Figure 5.14, as well as their ratio, plotted as a function of E_{rec} .

Above 5 GeV, the efficiency is stable at 1; ISS and MC show good agreement. Below 5 GeV,

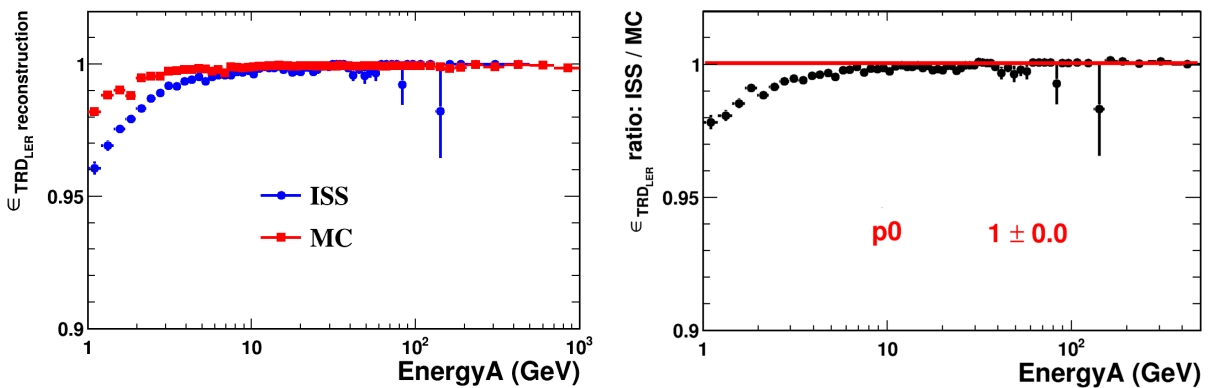


Figure 5.14: Left: efficiency of TRD_{LER} available estimated using control samples from ISS data (blue) and MC data (red). Right: ratio of the efficiency ISS / MC, fitted by constant function $f(x) = p0$.

efficiency drops as energy decreases; the MC efficiency is higher than that of ISS. This difference between ISS and MC is taken into account in the systematic uncertainty.

Number of shower > 0

ISS and MC control samples are selected by cutting on the variables of TOF, TRD and tracker.

- TOF: $\beta > 0.8$, $Q_{TOF} < 1.8$
- TRD: $TRD_{LER} < 0.6$

- Tracker: $N_{track} > 0$, $R < 0$, pattern L1L9, track extrapolation enters the ECAL surface (four cells away from the ECAL border).

The shower reconstruction efficiency estimated using the ISS and MC samples is shown in Figure 5.15, plotted as a function of deposited energy. The ratio of efficiency ISS / MC is

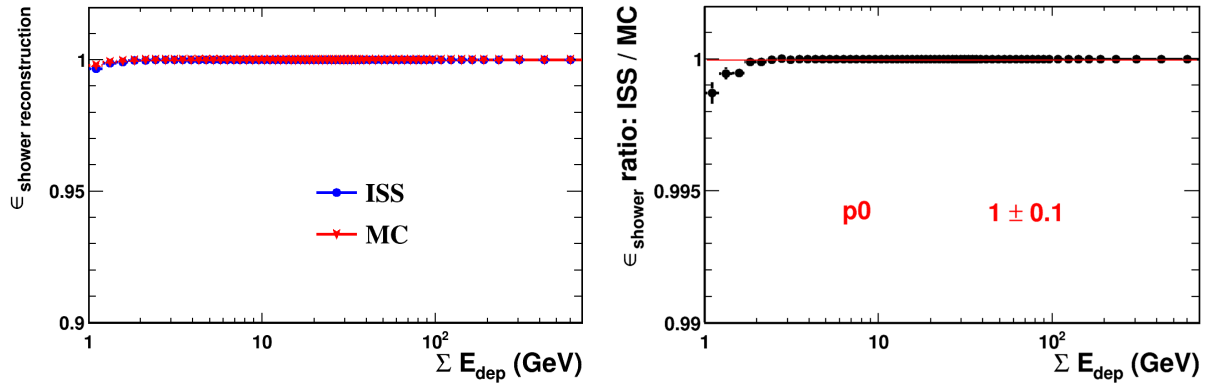


Figure 5.15: Left: efficiency of $N_{shower} > 0$ estimated using control samples from ISS data (blue) and MC data (red). Right: ratio of the efficiency ISS / MC.

stable at 1. The slight difference below 2 GeV, which is about 0.2% is added to the systematic uncertainty.

The ECAL fiducial cut efficiency is also checked on ISS and MC, for events with at least one shower. The result is shown in Figure 5.16. ISS and MC electrons show the same energy

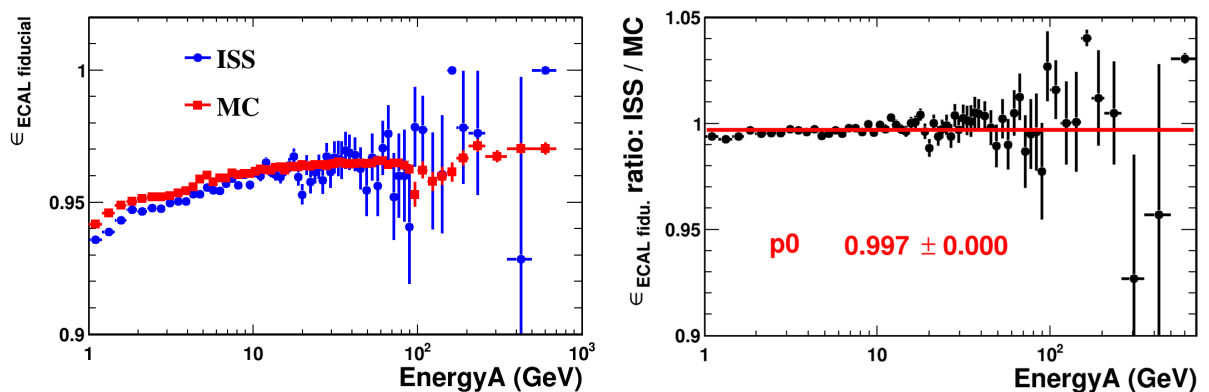


Figure 5.16: Left: efficiency of ECAL fiducial cut estimated using control samples from ISS data (blue) and MC data (red). Right: ratio of the efficiency ISS / MC.

dependence and the efficiency ratio is 1. No correction is needed.

Number of track > 0

ISS and MC control samples are selected by cutting on the variables of TOF, TRD and ECAL.

- TOF: $\beta > 0.8$, $Q_{\text{TOF}} < 1.8$
- TRD: $TRD_{\text{LER}} < 0.6$
- ECAL: only 1 shower, the shower is well contained in fiducial volume, $ESE_{V3} > 0$.

The track reconstruction efficiency estimated using the ISS and MC samples is shown in Figure 5.17, plotted as a function of E_{rec} . It is observed that the ratio of efficiency ISS/MC is

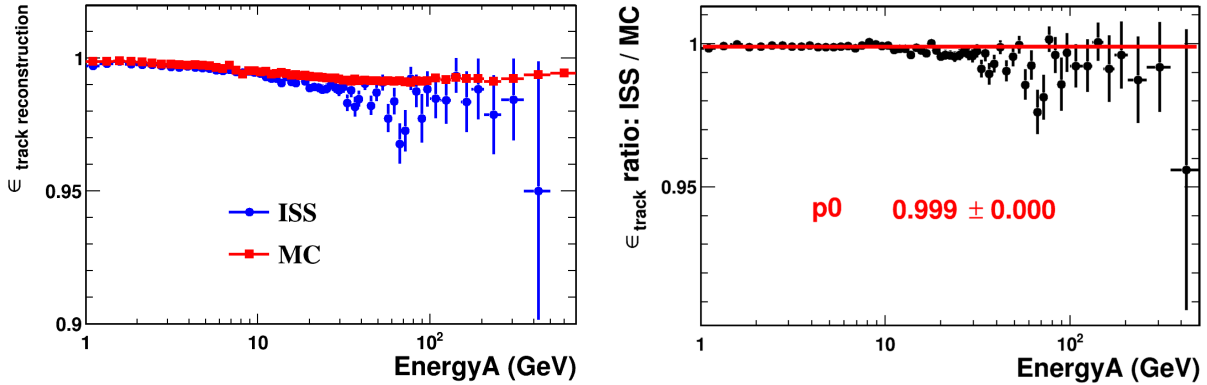


Figure 5.17: Left: efficiency of $N_{\text{track}} > 0$ estimated using control samples from ISS data (blue) and MC data (red). Right: ratio of the efficiency ISS / MC, fitted by constant function $f(x) = p0$.

stable at 1. No correction is needed.

5.3.3.2 Selection efficiency estimated with ISS electrons

The ISS samples are selected by applying cuts on TRD_{LER} and ESE_{V3} , which are the least correlated variables to the cuts to be evaluated in the lepton selection. The cut thresholds are listed below:

- Negative rigidity to select e^-
- $TRD_{\text{LER}} < 0.6$ to remove protons
- $TRD_{e\text{He}} < 0.5$ to remove helium
- $ESE_{V3} > -0.1$ to remove protons and helium

Statistics of the selected control samples are $\sim 1.9 \times 10^5$ events for the bin at 10 GeV, ~ 3500 for the bin at 100 GeV and ~ 400 events for the bin above 350 GeV. Efficiencies of the cuts in

the lepton selection are calculated consecutively using the control samples. The results for cuts of $\chi_Y^2 < 20$, $\Delta Y < 5$ cm, $EoP > 0.6$ and single track are shown in Figure 5.18.

It is observed that the efficiency of χ^2 and single track cuts is significantly lower than 1 over

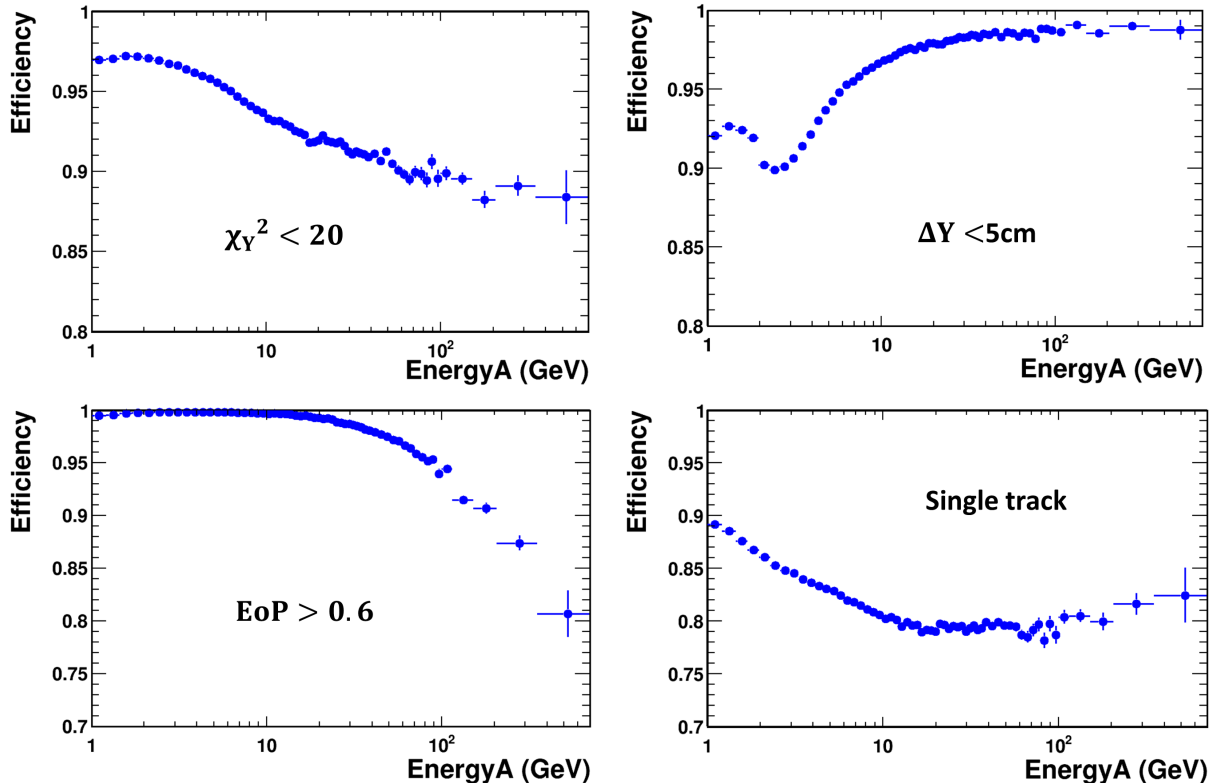


Figure 5.18: Efficiency for cuts of track χ^2 (upper left), ΔY (upper right), $EoP > 0.6$ (lower left) and single track (lower right). 29 months of ISS data are used.

the whole energy range. Other cuts like Tracker-ECAL matching reduces the efficiency at low energy. And the drop of efficiency at high energy is dominated by the EoP cut.

5.3.3.3 Selection efficiency estimated with MC electrons

To estimate the selection efficiency on MC data, MC control samples are built with the same cuts as previously presented for ISS data. However, both TRD_{LER} and ESE_{V3} lepton distributions don't peak at the same position in data and in MC, as shown in Figure 5.19. Therefore, the cut thresholds of TRD_{LER} and ESE_{V3} must be adjusted accordingly.

Figure 5.20 and Figure 5.21 show the peak positions of TRD_{LER} and ESE_{V3} in data and MC, as well as the suggested adjustment value. For instance, at 30 GeV, the threshold for ISS data is chosen as -0.1 (cf. Section 5.3.3.2). Figure 5.21 shows that the ESE_{V3} distribution peaks at ~ 0.12 in MC and peaks at ~ 0.07 in data. As a result, the equivalent threshold for MC is -0.05.

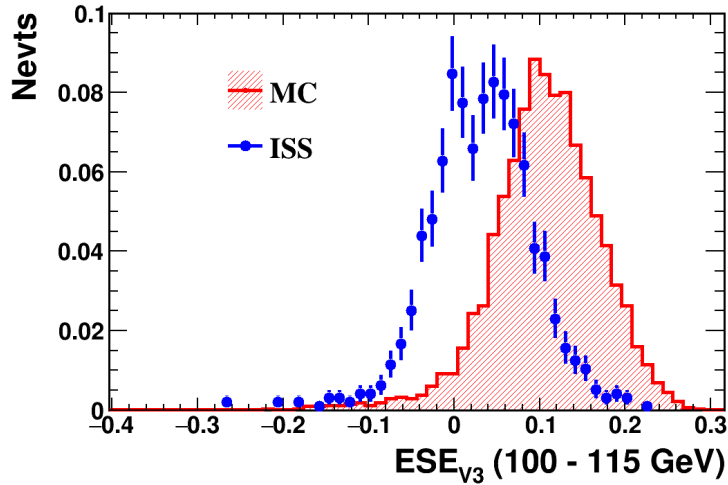


Figure 5.19: ESE_{V3} distributions for MC (red) and ISS (blue) electrons in the energy range of 100 - 115 GeV.

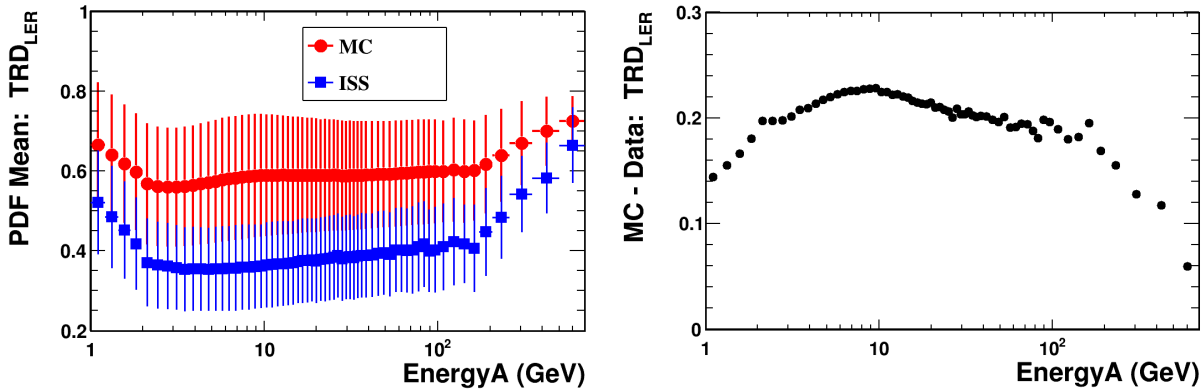


Figure 5.20: Left: peak position of TRD_{LER} distributions in MC data (red) and ISS data (blue). The error bars represent width of the distributions. Right: difference of the peak positions, MC - ISS.

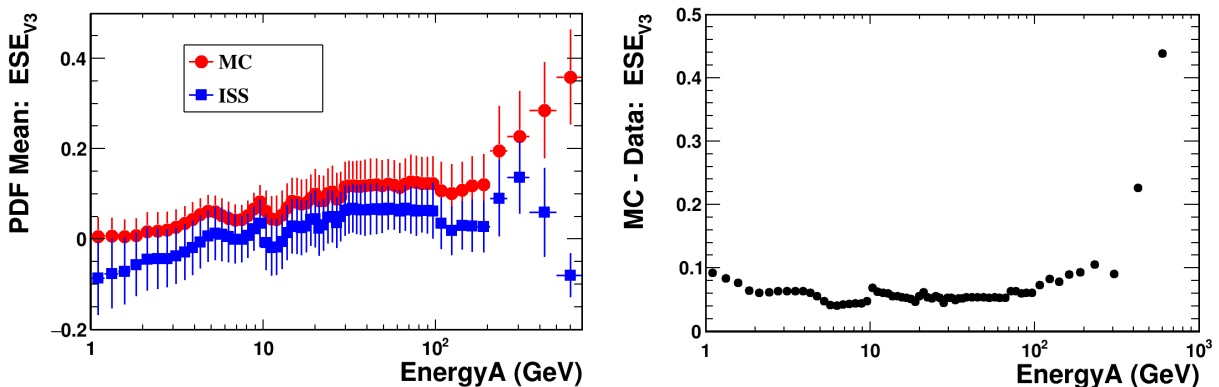


Figure 5.21: Left: peak position of ESE_{V3} distributions in MC data (red) and ISS data (blue). The error bars represent width of the distributions. Right: difference of the peak positions, MC - ISS.

Four cut efficiencies estimated using MC control samples are shown in Figure 5.22. For comparison, efficiencies estimated using ISS electrons for the same cuts are superimposed. The

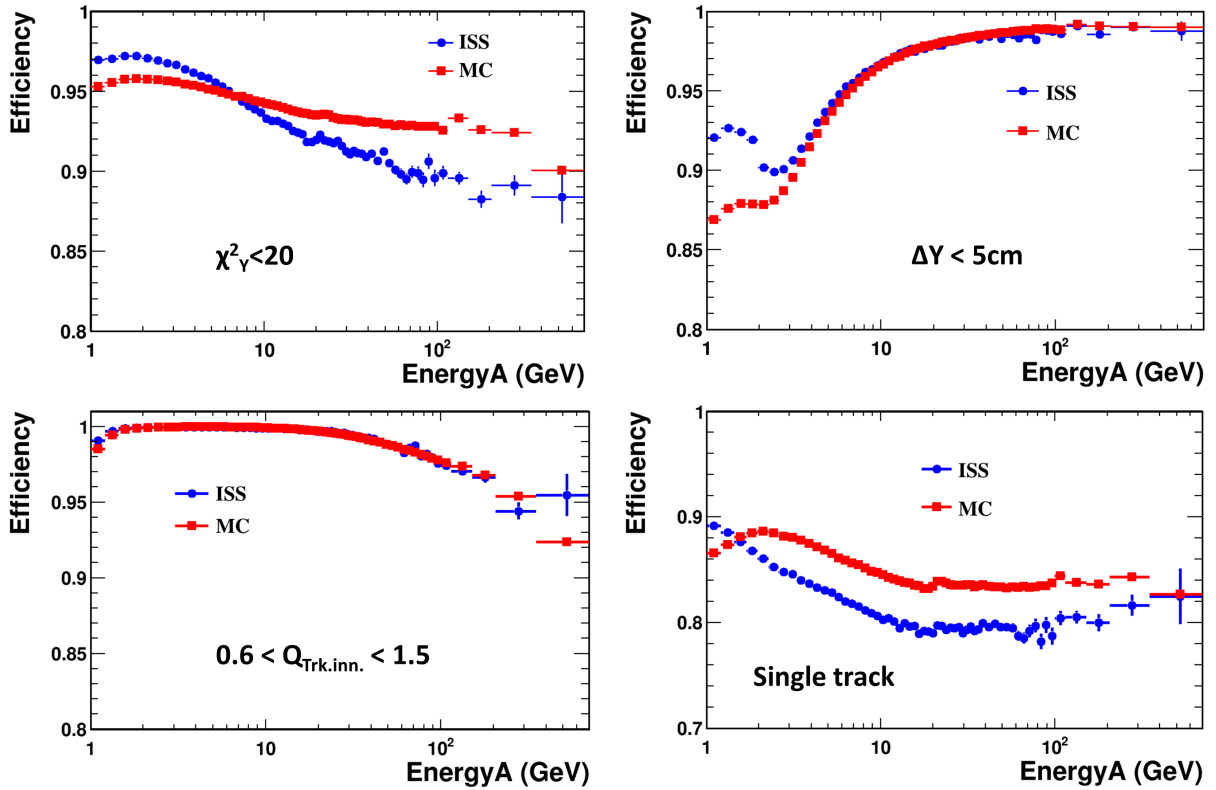


Figure 5.22: Comparison of efficiencies calculated with ISS data (blue) and MC data (red) for cuts of track χ^2 (upper left), ΔY (upper right), $Q_{\text{Trk.inn.}}$ (lower left) and single track (lower right).

efficiencies of ISS and MC follow the same trend and have good agreement for cuts such as ΔY and $Q_{\text{Trk.inn.}}$. However, the cuts such as χ^2 and single track have significant discrepancy between ISS data and MC.

The comparison of efficiencies of the whole lepton selection is shown in Figure 5.23. The

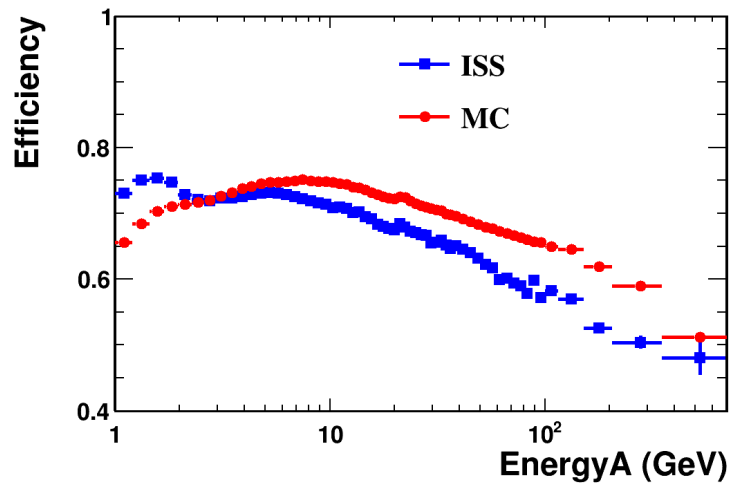


Figure 5.23: Efficiency of lepton selection calculated with 29 months of ISS data (blue) and MC data (red). The error bars represent statistical uncertainty.

discrepancy between ISS and MC grows larger with energy, which is due to the material description and alignment in MC and will be improved in the next version of MC. For now, this discrepancy needs to be taken into account in the acceptance correction.

5.3.3.4 Data-MC efficiency correction

The acceptance is estimated with MC data in Section 5.3.2. Previously, discrepancy on the selection efficiency between ISS data and MC is observed. A correction factor $\text{corr}_{\text{data}/\text{MC}}$ must be applied on the acceptance.

$$\text{corr}_{\text{data}/\text{MC}}(E) = \frac{\epsilon_{\text{sel.}}^{\text{data}}(E)}{\epsilon_{\text{sel.}}^{\text{MC}}(E)} \quad (5.8)$$

where ϵ is the efficiency.

Figure 5.24 shows the correction factor for the two cuts, χ_Y^2 and single track, which have the most significant discrepancy between ISS and MC. For χ^2 cut, the $\text{corr}_{\text{data}/\text{MC}}$ is 1.02 at 1 GeV

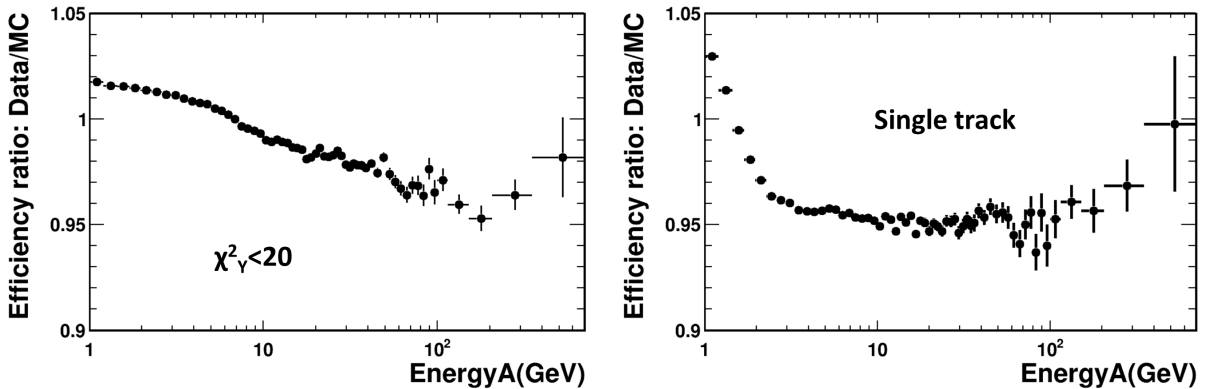


Figure 5.24: Ratio of efficiency between ISS and MC, $\text{corr}_{\text{data}/\text{MC}}$, for cuts of χ_Y^2 (left) and single track (right). The error bars are statistical uncertainty of the ISS data and MC data.

and decreases with energy to ~ 0.95 at 200 GeV. For single track cut, the $\text{corr}_{\text{data}/\text{MC}}$ is constant about 0.95 between 3 GeV and 300 GeV. Below 3 GeV and above 300 GeV, the $\text{corr}_{\text{data}/\text{MC}}$ factor rises.

Figure 5.25 shows the correction factor for the whole lepton selection as a function of EnergyA. At 1 GeV, the $\text{corr}_{\text{data}/\text{MC}}$ is about 1.1 and then decreases with energy. Above 200 GeV, the $\text{corr}_{\text{data}/\text{MC}}$ is stable at ~ 0.86 . The last point is unstable due to lack of statistics. This $\text{corr}_{\text{data}/\text{MC}}$ will be used for the acceptance correction.

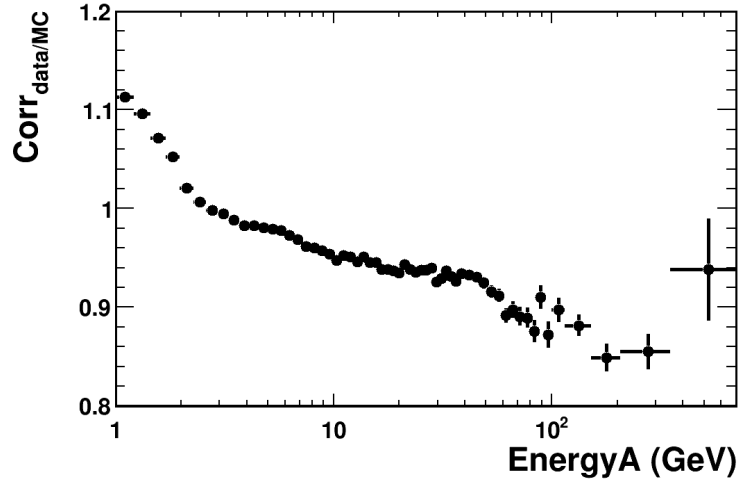


Figure 5.25: Factor $\text{corr}_{\text{data}/\text{MC}}$ for the whole lepton selection. The error bars represent statistical uncertainty.

5.3.3.5 Systematic uncertainty of the data-MC efficiency correction

The systematic uncertainty of the data-MC correction is estimated by changing the control samples. The standard deviation of the efficiency results from different control samples is taken as the systematic uncertainty. Compared to the nominal sample which is selected with ESE_{V3} and TRD_{LER} , the new set of samples have different cut thresholds and additional cuts. The selection of 14 control samples is listed in Table 5.1. The cut thresholds vary around the nominal cut.

Figure 5.26 and Figure 5.27 show the efficiency results from the control samples for the χ^2 cut and $\text{EoP} < 10$ cut. At high energy above 200 GeV, large statistical uncertainties are observed

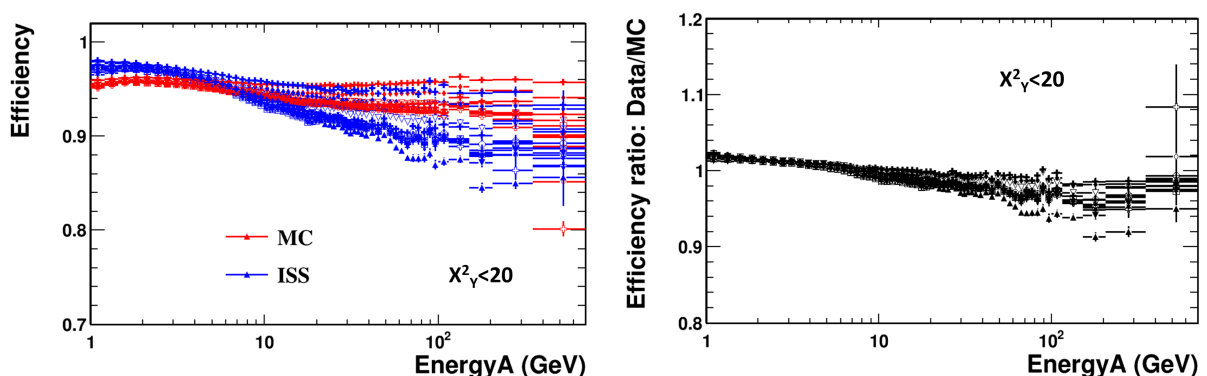


Figure 5.26: Left: efficiency of χ^2 cut calculated with the 14 pairs of control samples. Right: ratios of ISS efficiency over MC efficiency.

for some control samples. To mitigate the dispersion due to lack of statistics, the RMS is calculated using weighted efficiency ratios with a weight of $w_i = 1/\sigma_{\text{stat}}^2$, where σ_{stat}^2 is the

Control sample (Negative rigidity)		ISS data	MC data
ESE_{V3}	A1	-0.17	$-0.17 + \delta 1$
	A2	-0.12	$-0.12 + \delta 1$
	A3	-0.07	$-0.07 + \delta 1$
TRD_{LER}	B1	0.63	$0.63 + \delta 2$
	B2	0.58	$0.58 + \delta 2$
	B3	0.53	$0.53 + \delta 2$
	B4	0.48	$0.48 + \delta 2$
TRD_{eHe}	C1	0.65	0.8
	C2	0.55	
	C3	0.45	
Q_{TOF}	D1	2.2	2.2
	D2	2.0	2.0
	D3	1.8	1.8
$Q_{Trk.inn.}$	E1	1.5	1.5

Table 5.1: Different cuts used to select control samples in ISS data and MC data. One cut is changed at a time while the other cuts stay the same as the nominal sample. $\delta 1$ and $\delta 2$ are respectively MC-ISS shifts for ESE_{V3} and TRD_{LER} . Q_{TOF} is charge measured by TOF.

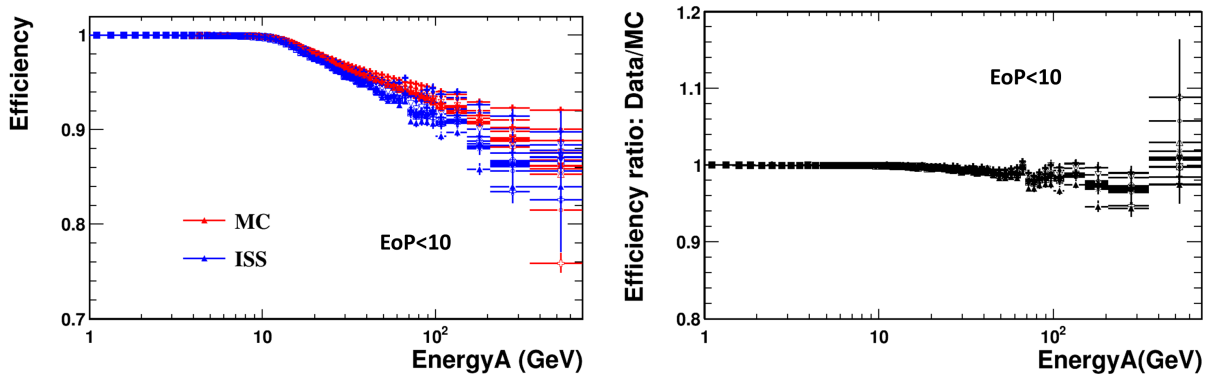


Figure 5.27: Left: efficiency of EoP<10 cut calculated with the 14 pairs of control samples. Right: ratios of ISS efficiency over MC efficiency.

statistical uncertainty of the data/MC ratio. Detailed calculations are given in Equation (5.9).

$$\text{Weighted efficiency mean of cut } j: \quad \bar{\epsilon}_j = \frac{\sum_{CS_i} w_i \epsilon_i}{\sum_{CS_i} w_i} \quad (5.9a)$$

$$\text{Weighted variance of cut } j: \quad \sigma_j^2 = \sum_{CS_i} (w_i \epsilon_i - \bar{\epsilon})^2 \quad (5.9b)$$

$$\text{Weighted standard deviation:} \quad \sigma_{total} = \sqrt{\sum_{cut_j \in ele.sel.} \sigma_j^2} \quad (5.9c)$$

The results of the weighted RMS are shown in Figure 5.28. It is observed that the systematic uncertainty of $\text{corr}_{\text{data}/\text{MC}}$ is dominated by the cuts of $\Delta Y < 5$ cm (in beige) and single track (in purple) below 10 GeV. Above 10 GeV, it is dominated by the cut of $\chi_Y^2 < 20$. The systematic

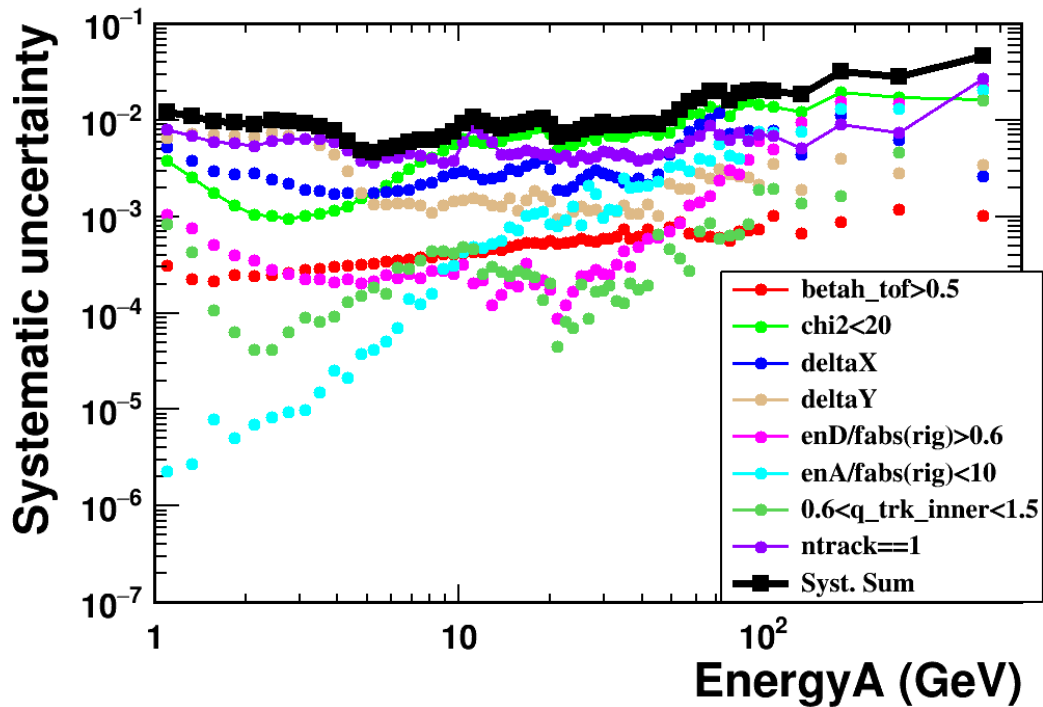


Figure 5.28: Total systematic uncertainty of the data-MC efficiency correction (black). Contribution from each cut is drawn in different colors.

uncertainty breakdown for three energy bins 2.9 - 3.3 GeV, 47 - 51 GeV and 206 - 350 GeV is given in Table 5.2.

Energy/GeV	β_{TOF}	χ^2	ΔX	ΔY	EoP > 0.6	EoP < 10	$Q_{\text{Trk.inn.}}$	NTrack=1	Total
2.9 - 3.3	3e-4	0.001	0.002	0.006	2e-4	1e-7	9e-5	0.006	0.009
47 - 51	8e-4	0.001	0.004	0.002	7e-4	0.003	5e-4	0.005	0.011
206 - 350	0.001	0.017	0.006	0.003	0.015	0.013	0.005	0.008	0.028

Table 5.2: Breakdown of the efficiency correction systematic uncertainty for three energy ranges.

Combining the $\text{corr}_{\text{data}/\text{MC}}$ calculated in Figure 5.25 and the systematic uncertainty in Figure 5.28, the final data-MC efficiency correction is shown in Figure 5.29. This correction is to be applied in the flux measurement, as the term $\text{corr}_{\text{data}/\text{MC}}(E)$.

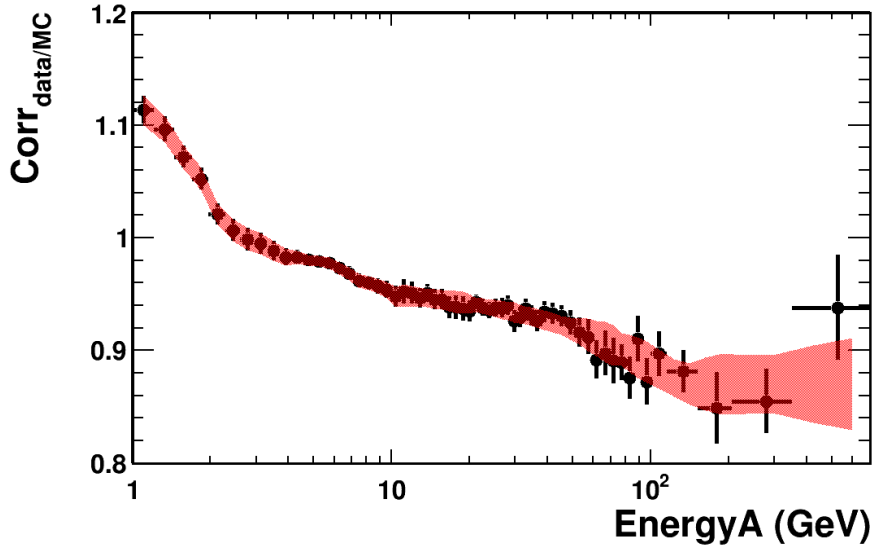


Figure 5.29: Efficiency correction factor $\text{corr}_{\text{data}/\text{MC}}$ for the whole lepton selection. The error bars represent the systematic uncertainty calculated in Figure 5.28. The correction is smoothed with the red curve, which is spline function from 1 to 10 GeV, polynomial function of degree 2 from 10 to 150 GeV and constant above 150 GeV. The shade band width is the systematic uncertainty of this efficiency correction.

5.3.4 Study of the impact of MC reweighting

The MC reweighting affects two terms in the flux measurement, $A_{\text{eff}} \times \text{corr}_{\text{data}/\text{MC}}$. Uncertainty due to the MC reweighting is estimated by varying the input flux index at high energy. Four indices close to that of the true flux are tested: -2.8, -3.1, -3.4 and -3.7. Figure 5.30 shows the shape of four input fluxes in comparison with the true flux. The comparison is to be studied

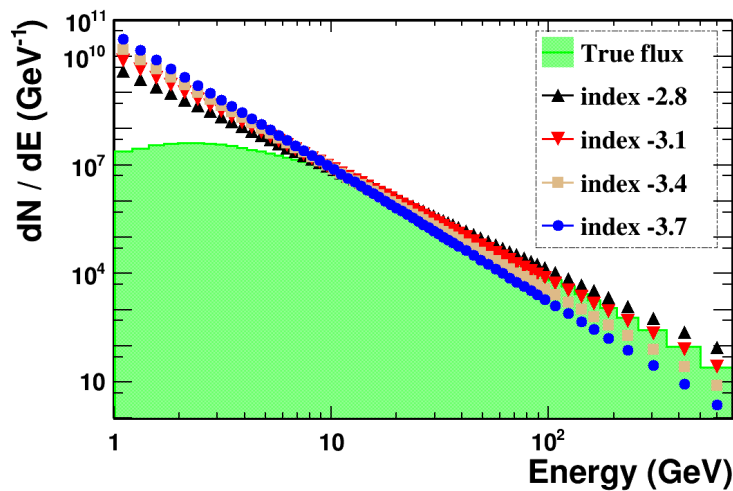


Figure 5.30: Shape of input power-law fluxes with the index of -2.8 (black), -3.1 (red), -3.4 (maroon) and -3.7 (blue). The green area is the true measured flux.

for the energy range above 10 GeV, since below 10 GeV, the true flux cannot be described by

a single power law.

The selection efficiency estimated by ISS data, $\epsilon_{sel.}^{data}$, does not depend on the MC reweighting. Therefore, the impact of reweighting is simplified into comparing the $A_{eff}/\epsilon_{sel.}^{MC}$ measured using different indices. The result is shown in Figure 5.31. The ratios are stable at 1. Effect of input

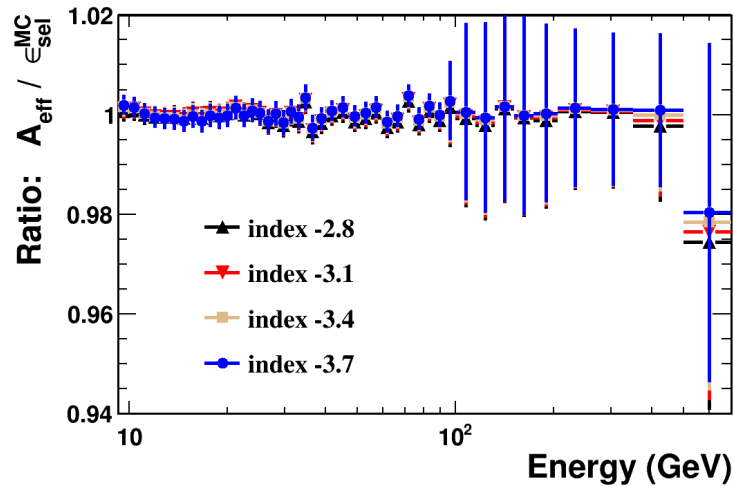


Figure 5.31: Ratio of $A_{eff}/\epsilon_{sel.}^{MC}$ measured using different reweighting power law indices and the one using true flux. Error bars are MC statistical uncertainty.

flux index used for MC reweighting is negligible above 10 GeV.

5.4 Charge confusion for electrons

Charge confusion describes the fact that for some events, the sign of the charge is wrongly reconstructed. The proportion of charge confusion events is quantified as the ratio of the number of wrong sign events over the total number of events, by which is defined f_{CC} as written in Equation (5.10)

$$f_{CC} = \frac{N_{wrong.sign}}{N_{wrong.sign} + N_{good.sign}} \quad (5.10)$$

The f_{CC} can be measured with MC events by counting the fraction of wrong sign events after applying the lepton selection. For electrons, correction of charge confusion is applied to subtract the small contribution of false electrons and to retrieve the lost electrons.

5.4.1 Impact of track pattern on charge confusion

Six tracker patterns are defined in Section 2.1.3. Figure 5.32 shows the charge confusion for each pattern estimated by MC electrons. It is observed that the charge confusion is dependent

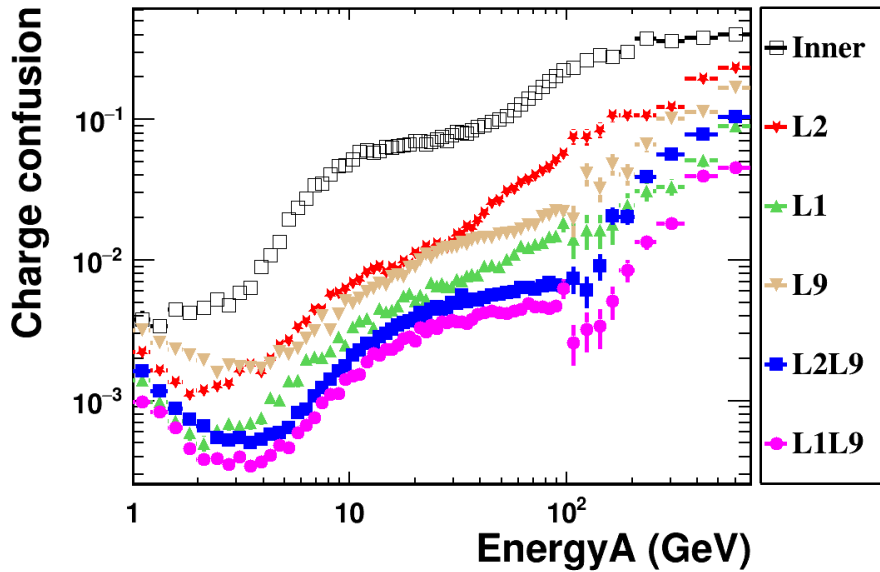


Figure 5.32: Charge confusion f_{CC} measured using MC data for the energy range of 1 - 700 GeV for six tracker patterns.

on tracker patterns. The pattern of L1L9 has the minimum charge confusion, whereas the inner pattern is more charge confused.

The proportions of the two dominant patterns are shown in Figure 5.33 for ISS and MC data. For charge confusion estimation, the difference in proportion between ISS and MC is corrected for each pattern using the fit result p_0 . The corrected f_{CC} is

$$f_{CC} = \frac{\sum N_i f_{CC}^i}{\sum N_i} = \sum p_i \times f_{CC}^i \quad (5.11)$$

where N_i is the number of electrons of one pattern, f_{CC}^i is the charge confusion for this pattern, p_i is the corrected proportion of this pattern. Charge confusion after pattern correction is shown in Figure 5.34. At 5 GeV, the f_{CC} is 0.1% and at 300 GeV, it is 5%. From 3 GeV above, the charge confusion increases with energy.

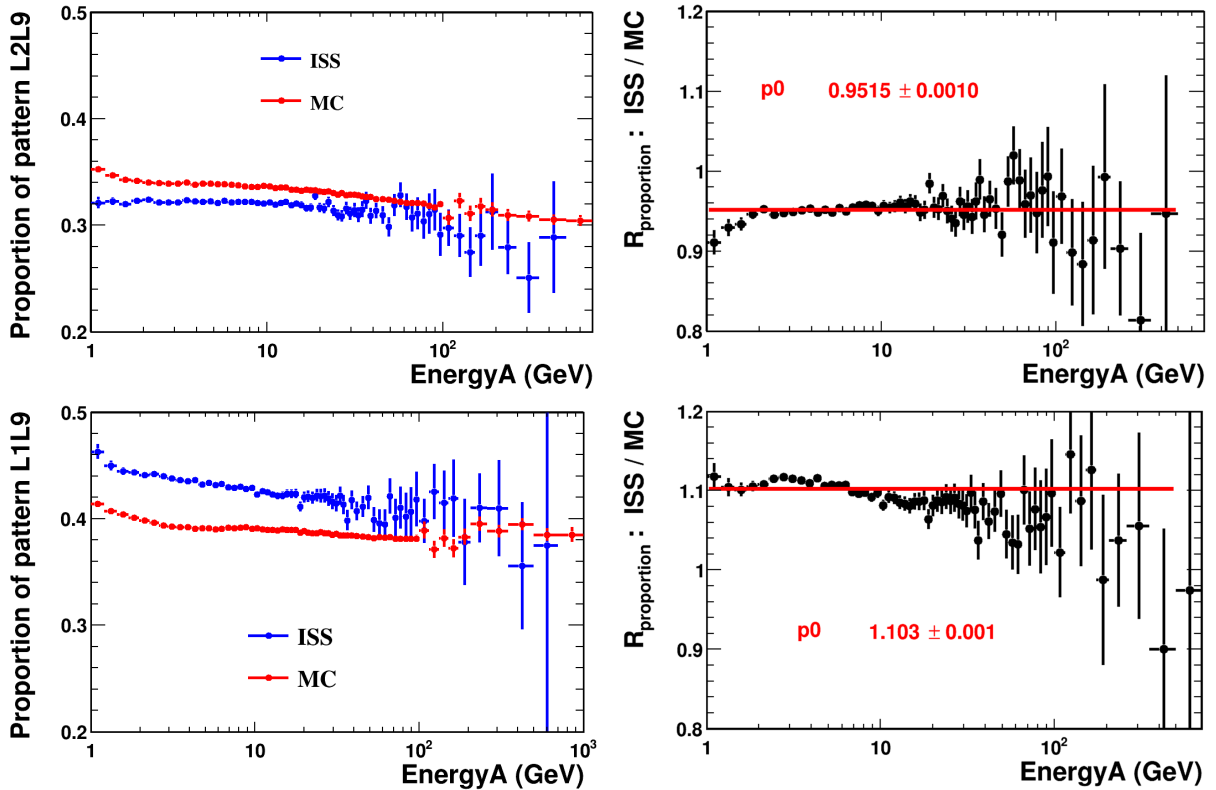


Figure 5.33: Proportions of electrons with tracker pattern L2L9 (upper) and L1L9 (lower) observed in ISS data and MC data. The ratio of proportions in ISS and MC is fitted with constant function $f(x) = p_0$.

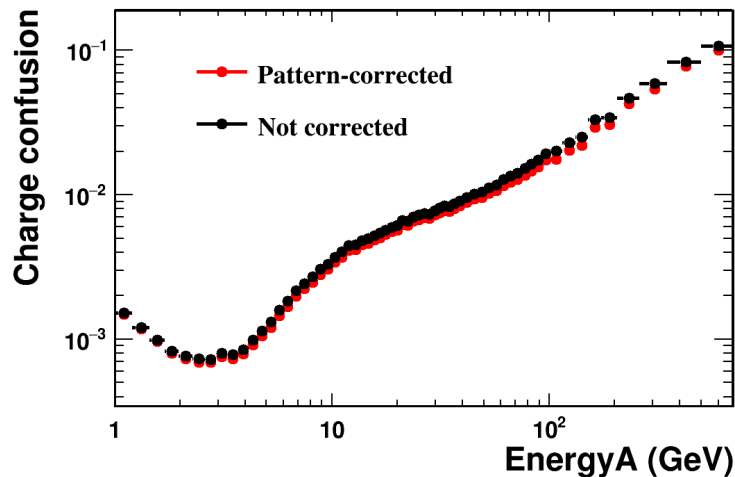


Figure 5.34: Charge confusion measured with MC data for the energy range of 1 to 700 GeV, before (black) and after (red) the pattern correction.

5.4.2 Charge confusion correction of electron number

Raw electron number is measured and shown in Figure 4.29. To get the true electron number ($N_{e^-}^{true}$) from the raw number ($N_{e^-}^{raw}$), charge confusion correction is applied using the raw lepton number ($N_{e^-+e^+}^{raw}$) and the charge confusion factor (f_{CC}) estimated with MC data. The

correction is given by

$$\begin{cases} N_{e^+e^-}^{raw} = N_{e^+e^-}^{true} = N_{e^+}^{true} + N_{e^-}^{true} \\ N_{e^-}^{raw} = (1 - f_{CC})N_{e^-}^{true} + f_{CC}N_{e^+}^{true} \end{cases} \rightarrow N_{e^-}^{true} = \frac{N_{e^-}^{raw} - f_{CC}N_{e^+e^-}^{raw}}{1 - 2f_{CC}} \quad (5.12)$$

where $N_{e^+}^{true}$ is the number of positrons at the same energy.

The electron number for each energy bin is corrected with Equation (5.12). The result is shown in Figure 5.35. For the energy bin of 260 - 350 GeV, the corrected electron number is 610 ± 26

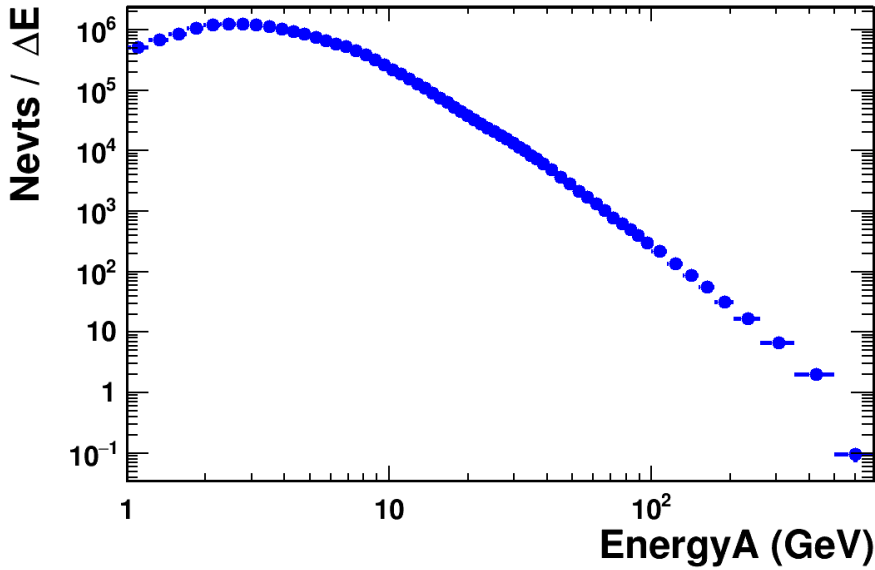


Figure 5.35: Corrected number of electrons divided by bin width for the energy range of 1 to 700 GeV using 29 months of ISS data. Only statistical uncertainty is drawn.

compared to before correction 583 ± 25 .

The statistical uncertainty of corrected electron number is obtained by propagating the uncertainties of the $N_{e^+e^-}^{raw}$ ($\sigma_{e^+e^-}$) and $N_{e^-}^{raw}$ (σ_{e^-}). As the correlation between $N_{e^+e^-}^{raw}$ and $N_{e^-}^{raw}$ is linear, the final statistical uncertainty on the corrected electron number is simply $|\sigma_{N_{e^-}} - f_{CC} \times \sigma_{N_{e^+e^-}}| / (1 - 2f_{CC})$.

5.4.3 Systematic uncertainty of the charge confusion correction

The charge confusion can also be measured with ISS data using charge confusion estimators, such as tracker BDT and E/P as shown in Figure 4.10. Comparison of the f_{CC} predicted by MC and f_{CC} measured on ISS data using E/P shows a good agreement in the energy range of 5 to 500 GeV [47].

The systematic uncertainty on the charge confusion is estimated using the difference between f_{CC} from MC and data, which has been published in the positron fraction paper of AMS-02 in 2014 for the range of 1 to 500 GeV [48]. Systematic uncertainty for the last energy bin 500 - 700 is obtained by a linear extrapolation. The result is shown in Figure 5.36.

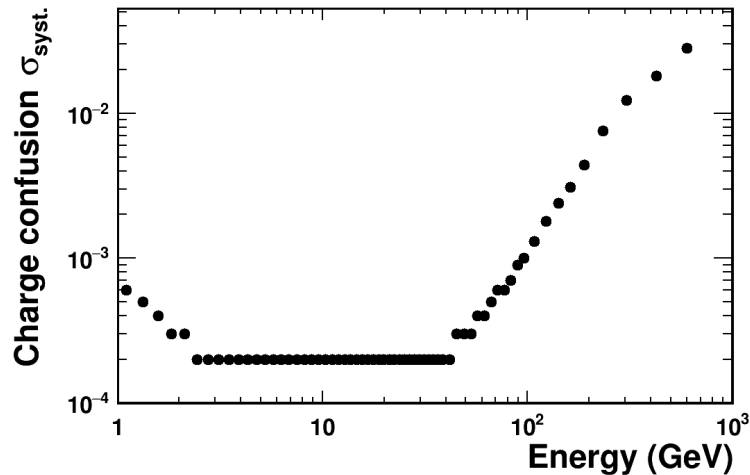


Figure 5.36: Systematic uncertainty of the charge confusion estimation [48]. Uncertainty for the energy of 500 - 700 GeV is obtained by a linear extrapolation from the lower energy bins.

5.5 Summary of uncertainties in flux measurement

The uncertainty estimation of each term in the flux measurement Equation (5.1) has been presented. All the statistical and systematic uncertainties are summarized in Table 5.3.

The statistical uncertainty of lepton and electron fluxes σ_{stat} is calculated by

$$\sigma_{stat} = \Phi \times \sqrt{\left(\frac{\sigma_N^{stat}}{N}\right)^2 + \left(\frac{\sigma_{\epsilon_{phys.trig.}}^{stat}}{\epsilon_{phys.trig.}}\right)^2}$$

The relative statistical uncertainties of lepton flux and electron flux are shown in Figure 5.37, which are very similar. At 10 GeV, the relative uncertainty is $\sim 0.2\%$; at 100 GeV, it is 2%; between 500 - 700 GeV, it is 30%.

The systematic uncertainty σ_{syst} for lepton flux is calculated by

$$\sigma_{syst} = \Phi \times \sqrt{\left(\frac{\sigma_N^{syst}}{N}\right)^2 + \left(\frac{\sigma_{Acc \times \epsilon_{sel}}}{Acc \times \epsilon_{sel}}\right)^2 + \left(\frac{\sigma_{corr_{data/MC}}}{corr_{data/MC}}\right)^2 + \left(\frac{\sigma_{\epsilon_{TRD}}}{\epsilon_{TRD}}\right)^2 + \left(\frac{\sigma_{\epsilon_{phys.trig.}}^{syst}}{\epsilon_{phys.trig.}}\right)^2 + \left(\frac{\sigma_{T_{expo}}}{T_{expo}}\right)^2}$$

Statistical uncertainties on:

- $N_{e^+e^-}$ and N_{e^-} : computed by the template fit procedure
- $\epsilon_{phys.trig.}$: trigger efficiency estimation using selected ISS electron samples

Systematic uncertainties on:

- $N_{e^+e^-}$ and N_{e^-} :
 - statistical uncertainties of the templates (cf. Section 4.7)
 - different TRD_{LER} cuts on the data samples (cf. Section 4.7)
- N_{e^-} : charge confusion correction (cf. Section 5.4.3)
- $Acc \times \epsilon_{sel.}$: statistical uncertainty of the MC data (cf. Section 5.3.2)
- $corr_{data/MC}$: preselection and lepton selection (cf. Section 5.3.3.4)
- ϵ_{TRD} : statistical uncertainty of the TRD_{LER} electron template (cf. Section 4.6.1)
- $\epsilon_{phys.trig.}$: estimated using electron trigger (cf. Section 5.2)
- $T_{expo.}$: geomagnetic cutoff thresholds (cf. Section 5.1.1)
- E: energy scale uncertainty (cf. Section 3.5)

Table 5.3: List of the statistical and systematic uncertainties in the flux measurement, as well as their sources and estimation method.

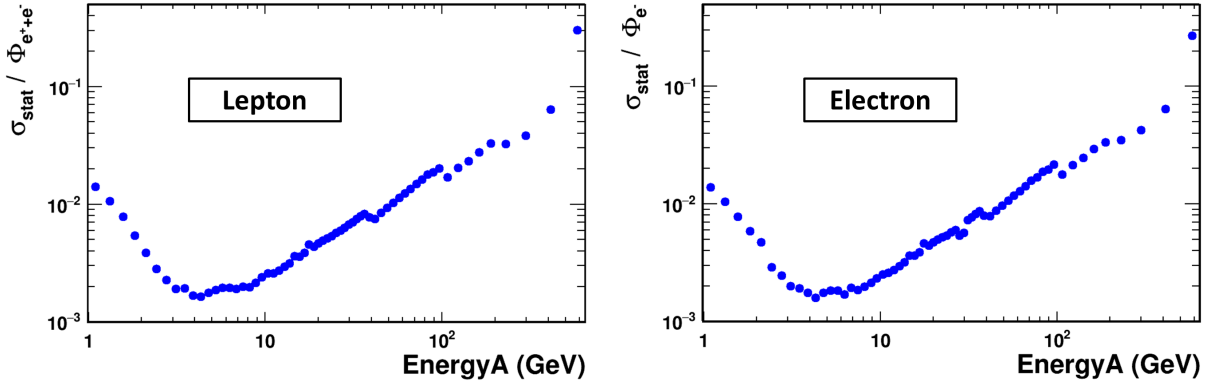


Figure 5.37: Statistical uncertainty of the lepton flux (left) and electron flux (right).

The total systematic uncertainty of the lepton flux measurement is shown in Figure 5.38. In the energy range of 2 - 40 GeV, the uncertainty is about 1.5%. Above 40 GeV, it increases with energy due to the energy dependence of σ_N^{syst} , $\sigma_{corr_{data/MC}}$ and $\sigma_{\epsilon_{TRD}}$. Above 300 GeV, the uncertainty is dominated by the uncertainty of lepton number due to template statistics.

For electrons, an extra term of systematic uncertainty on the electron number due to charge confusion, σ_N^{CC} , needs to be added. It is calculated by

$$\frac{\sigma_{N_{e^-}}^{CC}}{N_{e^-}} = \frac{\sigma\left(\frac{N_{e^-} - f_{CC}N_{e^+e^-}}{1 - 2f_{CC}}\right)}{N_{e^-}} = \left(2 + \frac{N_{e^+e^-}}{N_{e^-}}\right) \frac{\sigma_{f_{CC}}}{(1 - 2f_{CC})^2}$$

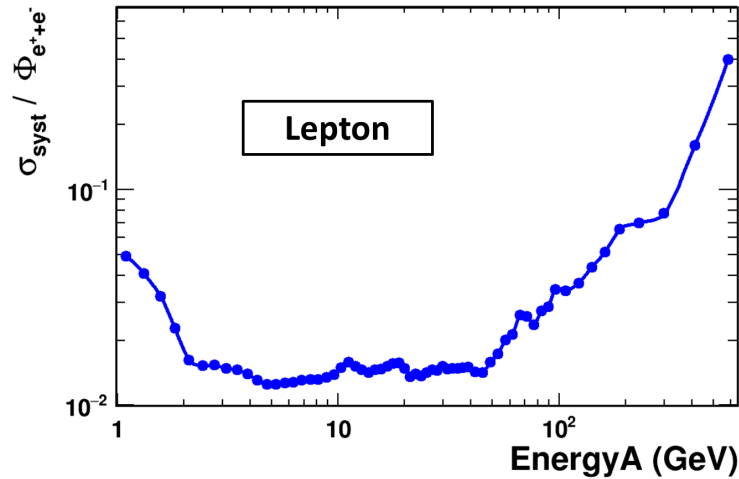


Figure 5.38: Systematic uncertainty of the lepton flux in the energy range of 1 - 700 GeV.

Electron flux uncertainty exhibits the same energy dependence as the lepton flux. The uncer-

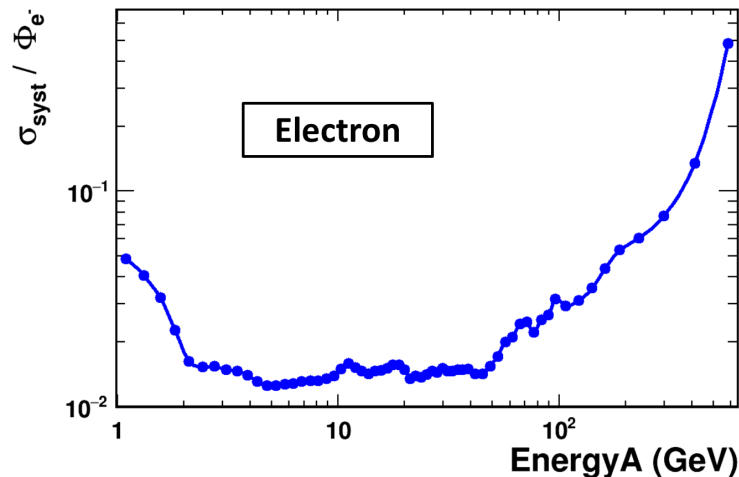


Figure 5.39: Systematic uncertainty of the electron flux in the energy range of 1 - 700 GeV.

tainty of the last bin, 500 - 700 GeV, is about 50%.

Dominant uncertainties of the electron flux due to different sources are given for six energies in Table 5.4. It can be seen that below 100 GeV, the uncertainty is dominated by selection efficiency correction, while at higher energies, the statistical uncertainty dominates. In fact, a great part of the systematic uncertainty of σ_N^{syst} is accounted for by the statistical uncertainty of electron templates.

$\tilde{E}(\text{GeV})$	σ_N^{stat}	σ_N^{syst}	$\sigma_{Ne^-}^{CC}$	$\sigma_{corr_data/MC}$	$\sigma_{\epsilon_{TRD}}$
2.11	0.318%	1.0%	0.09%	0.908%	0.0534%
10.3	0.234%	1.0%	0.06%	0.938%	0.0484%
48.9	0.971%	1.0%	0.10%	1.06%	0.108%
107	1.78%	1.5%	0.44%	1.99%	0.346%
411	6.58%	8.5%	8.96%	3.94%	2.23%
583	26.8%	44%	13.0%	4.69%	15.7%

Table 5.4: Dominant uncertainties of electron flux for six energies, presented in percentage. σ_N^{stat} is statistical uncertainty given by template fit; σ_N^{syst} is systematic uncertainty on number counting; $\sigma_{Ne^-}^{CC}$ is systematic uncertainty due to charge confusion estimation; $\sigma_{corr_data/MC}$ is systematic uncertainty due to selection efficiency correction; $\sigma_{\epsilon_{TRD}}$ is systematic uncertainty due to the estimation of TRD_{LER} cut efficiency.

5.6 Results of the flux measurement

The measured lepton flux and electron flux are respectively shown in Figure 5.40 and Figure 5.41. The results are presented in Table 5.5.

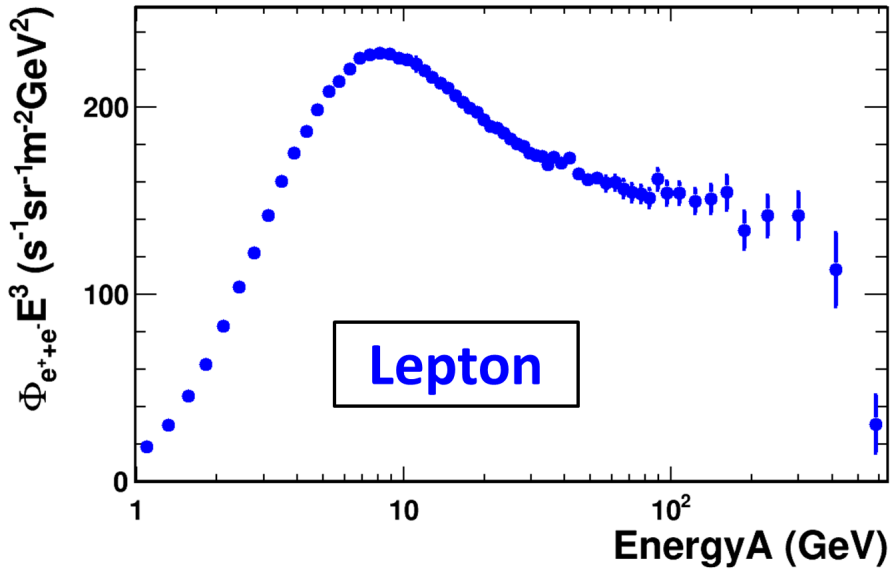


Figure 5.40: Lepton flux normalized by E^3 for the energy range of 1 - 700 GeV, measured using 29 months of ISS data. Error bars are quadratic sum of statistical and systematic uncertainties.

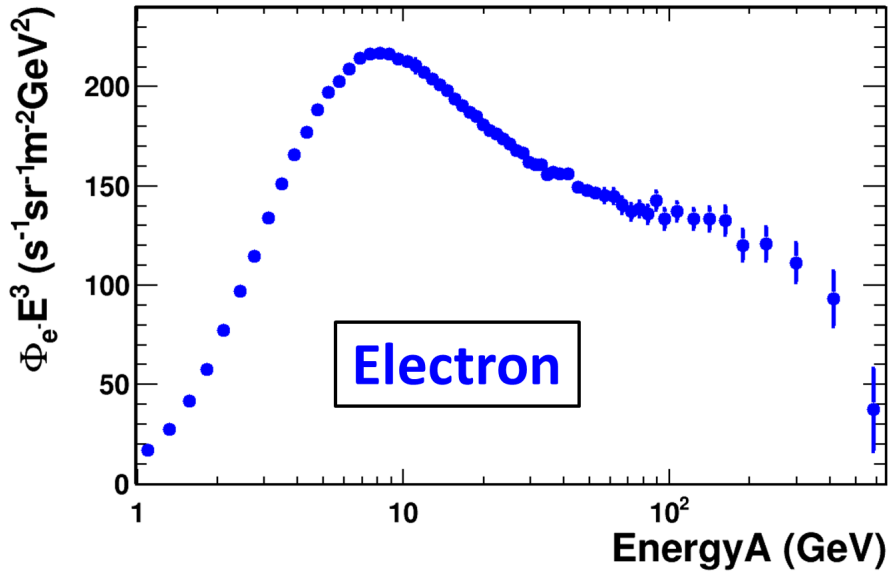


Figure 5.41: Electron flux normalized by E^3 for the energy range of 1 - 700 GeV, measured using 29 months of ISS data. Error bars are quadratic sum of statistical and systematic uncertainties.

Table 5.5: Results for the lepton and electron fluxes in units of $[m^2 \cdot sr \cdot s \cdot GeV]^{-1}$ with statistical and systematic uncertainties. \tilde{E} as described in the text with its systematic error derived from the energy scale uncertainty. The lepton number and electron number from this analysis are given, where the electron number is corrected for charge confusion.

Energy(GeV)	\tilde{E} (GeV)	$N_{e^+e^-}$	$\Phi_{e^+e^-} \pm \sigma_{stat} \pm \sigma_{syst}$	N_{e^-}	$\Phi_{e^-} \pm \sigma_{stat} \pm \sigma_{syst}$
1.0-1.2	1.1±0.0	106146	$(1.42 \pm 0.02 \pm 0.08) \times 10^1$	107639	$(1.31 \pm 0.02 \pm 0.07) \times 10^1$
1.2-1.4	1.3±0.1	165288	$(1.32 \pm 0.01 \pm 0.06) \times 10^1$	160288	$(1.20 \pm 0.01 \pm 0.05) \times 10^1$
1.4-1.7	1.6±0.1	221024	$(1.19 \pm 0.01 \pm 0.04) \times 10^1$	211742	$(1.09 \pm 0.01 \pm 0.04) \times 10^1$
1.7-2.0	1.8±0.1	300129	$(1.03 \pm 0.01 \pm 0.03) \times 10^1$	286929	$(9.52 \pm 0.06 \pm 0.28) \times 10^0$
2.0-2.3	2.1±0.1	388952	$(8.79 \pm 0.03 \pm 0.21) \times 10^0$	369650	$(8.21 \pm 0.04 \pm 0.20) \times 10^0$
2.3-2.6	2.4±0.1	419733	$(7.26 \pm 0.02 \pm 0.16) \times 10^0$	399341	$(6.78 \pm 0.02 \pm 0.15) \times 10^0$
2.6-2.9	2.8±0.1	441490	$(5.82 \pm 0.01 \pm 0.13) \times 10^0$	420792	$(5.46 \pm 0.01 \pm 0.12) \times 10^0$
2.9-3.3	3.1±0.1	449923	$(4.73 \pm 0.01 \pm 0.10) \times 10^0$	430083	$(4.46 \pm 0.01 \pm 0.10) \times 10^0$
3.3-3.7	3.5±0.1	465683	$(3.77 \pm 0.01 \pm 0.08) \times 10^0$	445704	$(3.56 \pm 0.01 \pm 0.07) \times 10^0$
3.7-4.1	3.9±0.1	439826	$(2.97 \pm 0.00 \pm 0.06) \times 10^0$	421395	$(2.80 \pm 0.00 \pm 0.05) \times 10^0$
4.1-4.5	4.3±0.1	417364	$(2.33 \pm 0.00 \pm 0.04) \times 10^0$	400551	$(2.21 \pm 0.00 \pm 0.04) \times 10^0$
4.5-5.0	4.8±0.2	400454	$(1.84 \pm 0.00 \pm 0.03) \times 10^0$	384945	$(1.75 \pm 0.00 \pm 0.03) \times 10^0$
5.0-5.5	5.2±0.2	385634	$(1.45 \pm 0.00 \pm 0.02) \times 10^0$	371022	$(1.37 \pm 0.00 \pm 0.02) \times 10^0$
5.5-6.0	5.7±0.2	341481	$(1.13 \pm 0.00 \pm 0.02) \times 10^0$	328998	$(1.07 \pm 0.00 \pm 0.02) \times 10^0$

Continued on next page

Table 5.5 – *continued from previous page*

Energy(GeV)	\tilde{E} (GeV)	$N_{e^+e^-}$	$\Phi_{e^+e^-} \pm \sigma_{stat} \pm \sigma_{syst}$	N_{e^-}	$\Phi_{e^-} \pm \sigma_{stat} \pm \sigma_{syst}$
6.0-6.6	6.3±0.2	342147	$(8.95 \pm 0.02 \pm 0.14) \times 10^{-1}$	329694	$(8.49 \pm 0.01 \pm 0.13) \times 10^{-1}$
6.6-7.2	6.8±0.2	323266	$(7.04 \pm 0.01 \pm 0.10) \times 10^{-1}$	311731	$(6.68 \pm 0.01 \pm 0.10) \times 10^{-1}$
7.2-7.8	7.5±0.2	298517	$(5.48 \pm 0.01 \pm 0.08) \times 10^{-1}$	287740	$(5.20 \pm 0.01 \pm 0.07) \times 10^{-1}$
7.8-8.5	8.1±0.2	275472	$(4.25 \pm 0.01 \pm 0.06) \times 10^{-1}$	265395	$(4.03 \pm 0.01 \pm 0.06) \times 10^{-1}$
8.5-9.2	8.8±0.2	233513	$(3.30 \pm 0.01 \pm 0.05) \times 10^{-1}$	225188	$(3.13 \pm 0.01 \pm 0.04) \times 10^{-1}$
9.2-9.9	9.6±0.2	202446	$(2.58 \pm 0.01 \pm 0.04) \times 10^{-1}$	195037	$(2.45 \pm 0.01 \pm 0.03) \times 10^{-1}$
9.9-10.7	10.3±0.2	178351	$(2.05 \pm 0.01 \pm 0.03) \times 10^{-1}$	171450	$(1.93 \pm 0.00 \pm 0.03) \times 10^{-1}$
10.7-11.5	11.1±0.2	154772	$(1.62 \pm 0.00 \pm 0.03) \times 10^{-1}$	148651	$(1.53 \pm 0.00 \pm 0.02) \times 10^{-1}$
11.5-12.4	11.9±0.2	135331	$(1.29 \pm 0.00 \pm 0.02) \times 10^{-1}$	130107	$(1.22 \pm 0.00 \pm 0.02) \times 10^{-1}$
12.4-13.3	12.8±0.3	116484	$(1.03 \pm 0.00 \pm 0.01) \times 10^{-1}$	112021	$(9.70 \pm 0.03 \pm 0.14) \times 10^{-2}$
13.3-14.2	13.7±0.3	102326	$(8.24 \pm 0.03 \pm 0.12) \times 10^{-2}$	98475	$(7.80 \pm 0.02 \pm 0.11) \times 10^{-2}$
14.2-15.2	14.7±0.3	89255	$(6.66 \pm 0.02 \pm 0.10) \times 10^{-2}$	85681	$(6.29 \pm 0.02 \pm 0.09) \times 10^{-2}$
15.2-16.1	15.6±0.3	77975	$(5.39 \pm 0.02 \pm 0.08) \times 10^{-2}$	74650	$(5.08 \pm 0.02 \pm 0.07) \times 10^{-2}$
16.1-17.2	16.6±0.3	67635	$(4.39 \pm 0.02 \pm 0.07) \times 10^{-2}$	64665	$(4.13 \pm 0.02 \pm 0.06) \times 10^{-2}$
17.2-18.2	17.7±0.4	59487	$(3.60 \pm 0.02 \pm 0.06) \times 10^{-2}$	56735	$(3.37 \pm 0.02 \pm 0.05) \times 10^{-2}$
18.2-19.4	18.8±0.4	52997	$(2.97 \pm 0.01 \pm 0.05) \times 10^{-2}$	50662	$(2.79 \pm 0.01 \pm 0.04) \times 10^{-2}$
19.4-20.5	19.9±0.4	46925	$(2.44 \pm 0.01 \pm 0.04) \times 10^{-2}$	44691	$(2.28 \pm 0.01 \pm 0.03) \times 10^{-2}$
20.5-21.8	21.1±0.4	41736	$(2.01 \pm 0.01 \pm 0.03) \times 10^{-2}$	39841	$(1.89 \pm 0.01 \pm 0.03) \times 10^{-2}$
21.8-23.1	22.4±0.4	38562	$(1.68 \pm 0.01 \pm 0.02) \times 10^{-2}$	36694	$(1.57 \pm 0.01 \pm 0.02) \times 10^{-2}$
23.1-24.4	23.7±0.5	34893	$(1.39 \pm 0.01 \pm 0.02) \times 10^{-2}$	33197	$(1.30 \pm 0.01 \pm 0.02) \times 10^{-2}$
24.4-25.9	25.1±0.5	31053	$(1.15 \pm 0.01 \pm 0.02) \times 10^{-2}$	29560	$(1.08 \pm 0.01 \pm 0.02) \times 10^{-2}$
25.9-27.3	26.6±0.5	27977	$(9.58 \pm 0.06 \pm 0.14) \times 10^{-3}$	26522	$(8.92 \pm 0.05 \pm 0.13) \times 10^{-3}$
27.3-28.9	28.1±0.6	25368	$(8.10 \pm 0.05 \pm 0.12) \times 10^{-3}$	23983	$(7.53 \pm 0.04 \pm 0.11) \times 10^{-3}$
28.9-30.4	29.6±0.6	22297	$(6.73 \pm 0.05 \pm 0.10) \times 10^{-3}$	21037	$(6.23 \pm 0.04 \pm 0.09) \times 10^{-3}$
30.4-32.1	31.3±0.6	20099	$(5.69 \pm 0.04 \pm 0.08) \times 10^{-3}$	18930	$(5.26 \pm 0.04 \pm 0.08) \times 10^{-3}$
32.1-33.8	32.9±0.7	18028	$(4.87 \pm 0.04 \pm 0.07) \times 10^{-3}$	16998	$(4.50 \pm 0.03 \pm 0.07) \times 10^{-3}$
33.8-35.6	34.7±0.7	15857	$(4.07 \pm 0.03 \pm 0.06) \times 10^{-3}$	14919	$(3.75 \pm 0.03 \pm 0.06) \times 10^{-3}$
35.6-37.4	36.5±0.7	14513	$(3.56 \pm 0.03 \pm 0.05) \times 10^{-3}$	13445	$(3.23 \pm 0.03 \pm 0.05) \times 10^{-3}$
37.4-40.0	38.7±0.8	16965	$(2.95 \pm 0.02 \pm 0.04) \times 10^{-3}$	15918	$(2.71 \pm 0.02 \pm 0.04) \times 10^{-3}$
40.0-43.4	41.6±0.8	17847	$(2.39 \pm 0.02 \pm 0.03) \times 10^{-3}$	16473	$(2.16 \pm 0.02 \pm 0.03) \times 10^{-3}$

Continued on next page

Table 5.5 – *continued from previous page*

Energy(GeV)	\tilde{E} (GeV)	$N_{e^+e^-}$	$\Phi_{e^+e^-} \pm \sigma_{stat} \pm \sigma_{syst}$	N_{e^-}	$\Phi_{e^-} \pm \sigma_{stat} \pm \sigma_{syst}$
43.4-47.0	45.1±0.9	14055	$(1.79 \pm 0.02 \pm 0.03) \times 10^{-3}$	13079	$(1.63 \pm 0.01 \pm 0.02) \times 10^{-3}$
47.0-50.9	48.9±1.0	11497	$(1.38 \pm 0.01 \pm 0.02) \times 10^{-3}$	10781	$(1.27 \pm 0.01 \pm 0.02) \times 10^{-3}$
50.9-55.0	52.8±1.1	9596	$(1.10 \pm 0.01 \pm 0.02) \times 10^{-3}$	8868	$(9.92 \pm 0.11 \pm 0.17) \times 10^{-4}$
55.0-59.4	57.1±1.1	7929	$(8.56 \pm 0.10 \pm 0.17) \times 10^{-4}$	7398	$(7.81 \pm 0.09 \pm 0.16) \times 10^{-4}$
59.4-64.0	61.6±1.2	6663	$(6.83 \pm 0.08 \pm 0.15) \times 10^{-4}$	6191	$(6.20 \pm 0.08 \pm 0.13) \times 10^{-4}$
64.0-69.0	66.4±1.3	5511	$(5.33 \pm 0.07 \pm 0.14) \times 10^{-4}$	5058	$(4.80 \pm 0.07 \pm 0.12) \times 10^{-4}$
69.0-74.3	71.6±1.4	4557	$(4.21 \pm 0.06 \pm 0.11) \times 10^{-4}$	4146	$(3.74 \pm 0.06 \pm 0.09) \times 10^{-4}$
74.3-80.0	77.0±1.5	3846	$(3.36 \pm 0.05 \pm 0.08) \times 10^{-4}$	3558	$(3.03 \pm 0.05 \pm 0.07) \times 10^{-4}$
80.0-86.0	82.9±1.7	3179	$(2.66 \pm 0.05 \pm 0.07) \times 10^{-4}$	2925	$(2.39 \pm 0.04 \pm 0.06) \times 10^{-4}$
86.0-92.5	89.1±1.8	2900	$(2.28 \pm 0.04 \pm 0.07) \times 10^{-4}$	2631	$(2.02 \pm 0.04 \pm 0.05) \times 10^{-4}$
92.5-100.0	96.1±1.9	2519	$(1.74 \pm 0.04 \pm 0.06) \times 10^{-4}$	2238	$(1.50 \pm 0.03 \pm 0.05) \times 10^{-4}$
100.0-115.1	107.0±2.1	3591	$(1.26 \pm 0.02 \pm 0.04) \times 10^{-4}$	3289	$(1.12 \pm 0.02 \pm 0.03) \times 10^{-4}$
115.1-132.1	123.0±2.5	2523	$(8.04 \pm 0.16 \pm 0.30) \times 10^{-5}$	2307	$(7.17 \pm 0.15 \pm 0.22) \times 10^{-5}$
132.1-151.5	141.1±2.8	1896	$(5.37 \pm 0.13 \pm 0.23) \times 10^{-5}$	1706	$(4.75 \pm 0.12 \pm 0.17) \times 10^{-5}$
151.5-173.5	161.8±3.2	1368	$(3.65 \pm 0.10 \pm 0.19) \times 10^{-5}$	1223	$(3.14 \pm 0.09 \pm 0.14) \times 10^{-5}$
173.5-206.0	188.4±3.8	1107	$(2.01 \pm 0.07 \pm 0.13) \times 10^{-5}$	1025	$(1.80 \pm 0.06 \pm 0.10) \times 10^{-5}$
206.0-260.0	229.9±4.6	1019	$(1.17 \pm 0.04 \pm 0.08) \times 10^{-5}$	909	$(9.95 \pm 0.35 \pm 0.60) \times 10^{-6}$
260.0-350.0	298.4±6.0	730	$(5.35 \pm 0.21 \pm 0.41) \times 10^{-6}$	610	$(4.19 \pm 0.18 \pm 0.32) \times 10^{-6}$
350.0-500.0	411.8±10.2	328	$(1.62 \pm 0.10 \pm 0.26) \times 10^{-6}$	304	$(1.34 \pm 0.09 \pm 0.18) \times 10^{-6}$
500.0-700.0	583.3±18.8	16	$(1.54 \pm 0.47 \pm 0.62) \times 10^{-7}$	19	$(1.88 \pm 0.50 \pm 0.91) \times 10^{-7}$

The comparison of fluxes measured in this analysis with the published results is shown in Figure 5.42 and Figure 5.43. The two results show an agreement within 1 to 2 sigmas in the energy range of 3 - 500 GeV. The difference between them is due to some different estimation approaches:

- The published results are based on TRD estimators, using either TRD_{LER} in the case of electrons, or universal templates in the case of leptons (one template for all the energy bins). Below 2 GeV, the performance of ESE_{V3} is reduced.

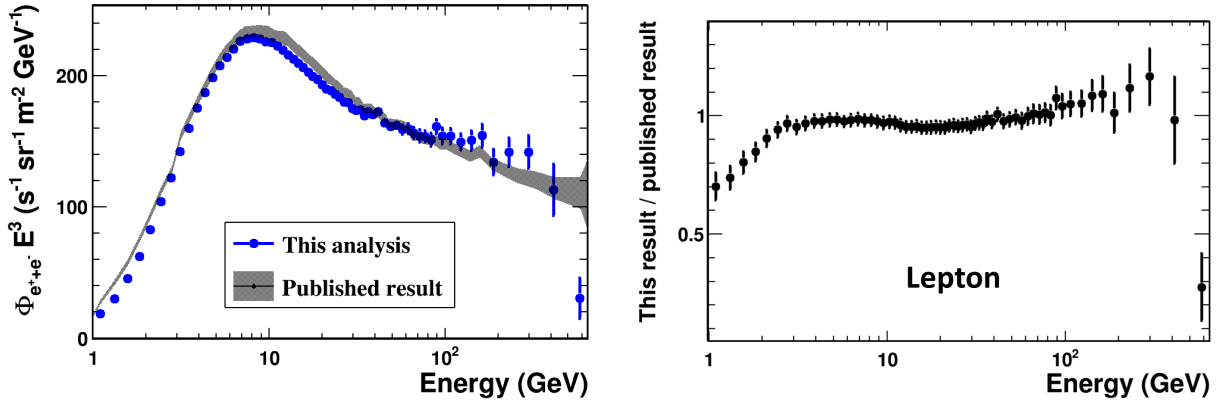


Figure 5.42: Left: lepton flux measured in this analysis (blue dots) in comparison with the AMS result published in [49] (black shade), both plotted as $\Phi \times E^3$. Right: The ratio of lepton flux measured in this analysis over the published result. The two results are compatible within 1 to 2 sigmas except at low energy.

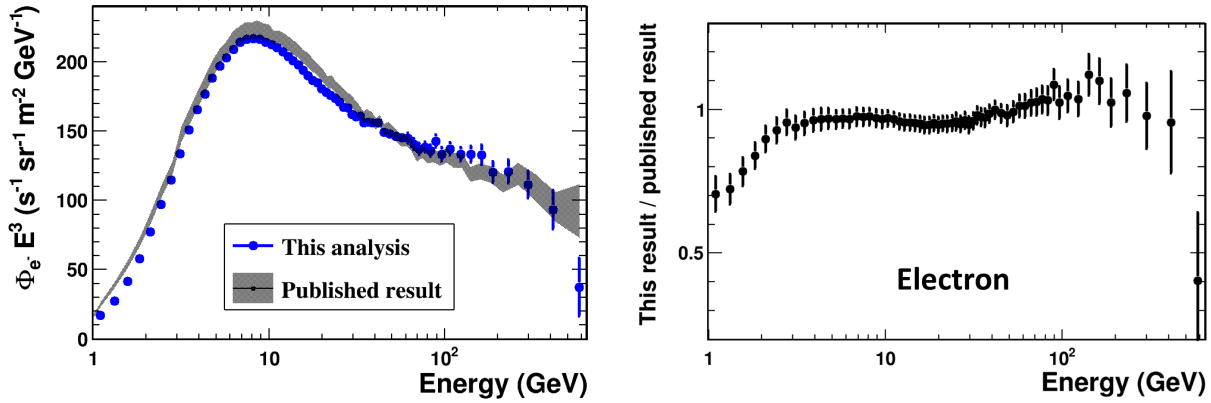


Figure 5.43: Left: electron flux measured in this analysis (blue dots) in comparison with the AMS result published in [50] (black shade), both plotted as $\Phi \times E^3$. Right: The ratio of electron flux measured in this analysis over the published result. The two results are compatible within 1 to 2 sigmas except at low energy.

- The efficiency correction ($\text{corr}_{\text{data}/\text{MC}}$) method is different.
- The published results use a different reconstructed energy than EnergyA, which affects low energy range where the binning is fine compared to the energy resolution. It should also be noted that the uncertainty of the energy scale adds 5% to 10% on the total error, which is not plotted in Figure 5.42 and Figure 5.43.

5.7 Consistency check of unfolding

Unfolding procedure is often used in spectrum measurements to remove the known effects of energy measurement resolution and to recover the true spectrum. Here, unfolding is applied

on the lepton energy spectrum to check the effects of energy resolution of ECAL. A priori estimation is that the effect of unfolding should on the lepton and electron fluxes should be negligible, since the size of bins is large compared to the ECAL energy resolution.

5.7.1 Mathematical formulation

The following mathematical formulation is extracted from [51]. Two notations:

- **True** histogram: distribution of number of counts in true energy
- **Smeared** histogram: distribution of number of counts in measured/reconstructed energy

Suppose that the counts in each bin of the true histogram, \vec{x} , are Poisson distributed with means of $\vec{\lambda}$. The propagation of events to neighboring bins is multinomial and independent for each true bin. It follows that the counts in each bin of the smeared histogram, \vec{y} , are also Poisson distributed with means of $\vec{\mu} = K\vec{\lambda}$. K is defined as the unfolding response matrix, which is often obtained from MC data in practice.

The unfolding problem can be formulated as:

Given the smeared observations \vec{y} and the Poisson regression model (K), what can be inferred about $\vec{\lambda}$?

The problem can be solved via different approaches, such as maximum likelihood iteration (Expectation-Maximization) and Bayes. Details of the regularized MLE method are described in [52].

5.7.2 Unfolding result

The unfolding response matrix is determined using MC electrons, as shown in Figure 5.44 as a function of E_{rec} vs. E_{true} . Most of the events are located along the diagonal, with $E_{\text{rec}} \simeq E_{\text{true}}$. Only terms in Equation (5.1) measured in E_{rec} need to be unfolded. Therefore, the unfolding is performed on $N_e/(\epsilon_{TRD} \times \epsilon_{trig})$. Precisely, *RooUnfoldSvd* [53] is used with a regularization term of 20. The results with and without unfolding are shown in Figure 5.45. A slight difference is observed between the two. The acceptance accounts for part of this difference. In Section 5.3.2, the acceptance is measured using E_{rec} . For the unfolded spectrum, E_{true} has to be used. The two "fluxes" to be compared are:

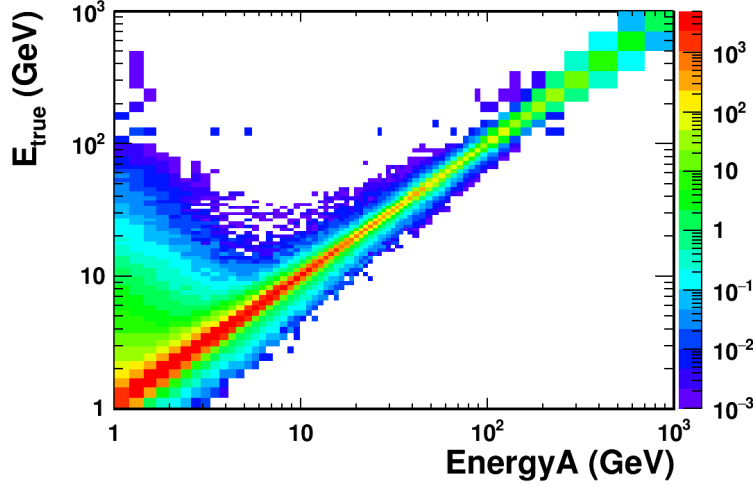
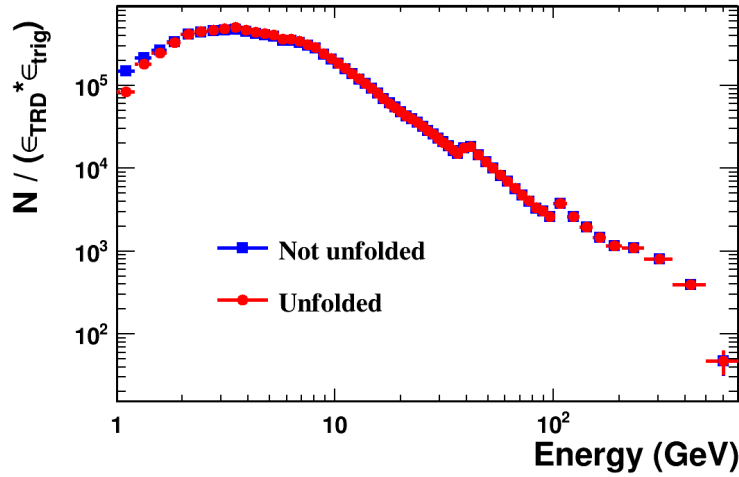


Figure 5.44: The unfolding matrix obtained using MC data.


 Figure 5.45: Energy spectrum of $N_e / (\epsilon_{TRD} \times \epsilon_{trig})$ with (red) and without (blue) unfolding.

- Without unfolding: $\frac{N(E_{rec})}{A_{eff}(E_{rec}) \times \epsilon_{TRD}(E_{rec}) \times \epsilon_{trig}(E_{rec})}$
- Unfolded: $\frac{1}{A_{eff}(E_{true})} \times \left(\frac{N(E_{rec})}{\epsilon_{TRD}(E_{rec}) \times \epsilon_{trig}(E_{rec})} \right)_{unfold}$

where Acc_{eff} is effective acceptance, defined as $Acc_{geo} \times \epsilon_{sel}$. The effective acceptances measured using E_{rec} and E_{true} are superimposed in Figure 5.46. Ratio of the unfolded electron flux over the non-unfolded is shown in Figure 5.47. Above 2 GeV, the ratio is flat and close to 1. At 1 GeV, the difference between unfolded and non-unfolded is 20%, which is larger than the quoted uncertainty of energy scale (4%). This is to be understood.

The results with and without unfolding are very well consistent, which confirms the good energy resolution of ECAL. Therefore, the unfolding is not necessary for lepton measurements in AMS.

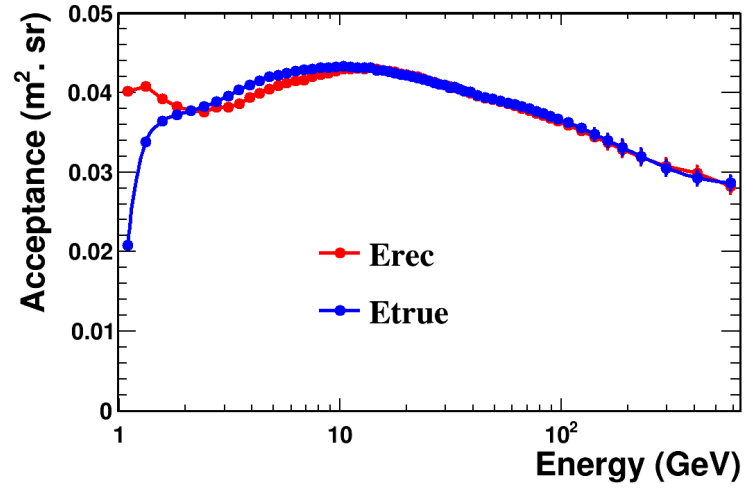


Figure 5.46: Effective acceptance, $Acc_{geo} \times \epsilon_{sel.}$, as a function of E_{rec} (red) and E_{true} (blue).

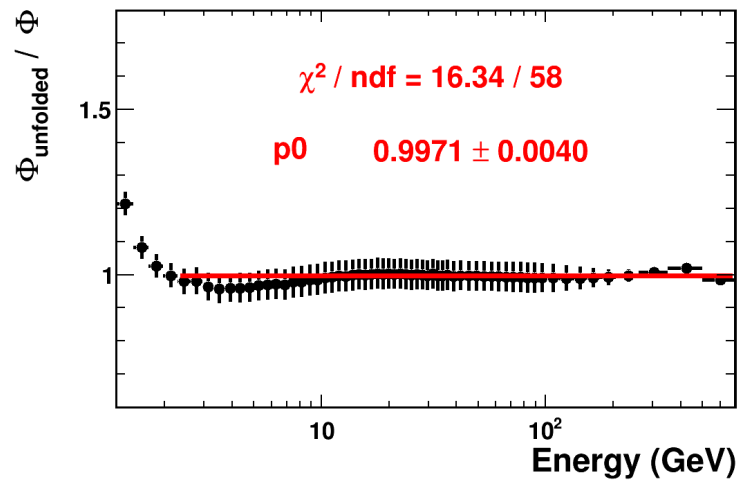


Figure 5.47: Ratio of unfolded electron flux over the non-unfolded flux, fitted by constant function $f(x) = p_0$ in the energy range of 2.5 - 700 GeV.

Chapter 6

Conclusion and outlook

In this analysis, the first 30 months of AMS-02 data have been used to measure the electron flux and lepton (positron plus electron) flux in the energy range of 1 GeV to 700 GeV. Different from the AMS published results, this analysis is based on the ECAL estimator, ESE_{V3} , which provides a better discriminating power between electrons and protons at high energy.

After the quality preselection, cuts on the TRD likelihood estimator and E/p variables are applied to enrich the samples in electron and lepton by rejecting protons. The selection efficiency at 10 GeV (resp. 700 GeV) is $\sim 70\%$ (50%) (cf. Section 4.2). The numbers of electrons and leptons are then extracted from the samples by fitting templates on the distribution of ESE_{V3} : 8 million leptons are selected (cf. Section 4.5). A cross-check is performed by fitting alternatively the distribution of TRD_{LER} , which yields compatible results (cf. Section 4.6.3). At low energy (below 100 GeV), the main systematic uncertainties on the flux measurements come from selection efficiency correction of Data/MC. Above 100 GeV, uncertainty due to the template fits dominates and for electrons, the uncertainty due to charge confusion also becomes important (cf. Section 5.5). In total, at 100 GeV (resp. 600 GeV), ~ 3600 (16) leptons are selected, the statistic uncertainty of the lepton flux is 1.6% (30%) and the systematic uncertainty is 3.2% (40%).

The uncertainty on the ECAL energy scale is determined using test beam data, MC data and eventually ISS data. The ratios of $E_{\text{rec}}/E_{\text{beam}}$, E/p , $E_{\text{rec}}/E_{\text{true}}$ on one hand, and geomagnetic cutoff on the other hand are used to control the energy measurement (Section 3.5). At 10 GeV (resp. 500 GeV), the uncertainty is 2% (5%), which is translated into $\sim 5\%$ ($\sim 10\%$) extra uncertainty on lepton and electron fluxes due to the power-law spectrum.

Up to now, AMS has been collecting data for 50 months, and is expected to operate for at least 10 years. A key feature of AMS, compared to future experiments such as CALET, is the presence of the magnet, and thus its ability to identify positrons. The electron (positron) measurements are limited by charge confusion. Currently, the charge confusion at 500 GeV is $\sim 10\%$. However, it can be improved by requiring a good track pattern. For instance, for pattern L1L9, at the price of losing 60% of the statistics, the charge confusion is significantly reduced to $\sim 4.5\%$ at 600 GeV. Therefore, positrons can be separated from electrons to a higher energy.

Presently, the ECAL estimator, ESE_{V3} , does not perform as well as anticipated at high energy (above 500 GeV), the loss of performance essentially due to the use of non-optimal training samples. In the future, a better version of MC data will be available as well as more ISS data: the separation power of ESE_{V3} is expected to be stable, which will push the lepton measurement to a higher energy range.

To measure energy of leptons beyond 1 TeV, one technical issue to be resolved is the ECAL energy saturation. Under current settings, the ECAL energy measurement saturates at 1 TeV. However, with proper corrections, it was shown by MC studies that the energy can be reconstructed with a reasonable resolution at 2 TeV (cf. Figure 2.15). An alternative solution is to lower the High Voltage on the photo-multipliers of ECAL, which raises the energy saturation threshold. Drawback of this method is that we lose signals of minimum ionizing protons. For calibration and related work, we will have to switch to minimum ionizing helium, which is not fully studied.

Meanwhile, besides AMS, there are other interesting experiments showing promising results. High Energy Stereoscopic System (H.E.S.S.), system of imaging Cherenkov telescopes, has measured lepton flux up to 5 TeV exhibiting a cutoff at 1 - 2 TeV. CALorimetric Electron Telescope (CALET), designed to perform high precision measurements of the lepton energy spectrum from 1 GeV to 20 TeV, will be flying to the ISS in 2015. Hopefully, in the coming years, all these exciting experiments will shed light on the unresolved puzzles in the cosmos and lead physics research into new era.

Appendix A

Solar Energetic Particles events during AMS flight

The SEP events are high-energy particles coming from the sun. They originate from two processes: energetization at a solar-flare site or by shock waves associated with Coronal Mass Ejections (CME) [54].

Major SEP events are recorded in the SOHO-LASCO catalog [55]. Days with SEP events during AMS flight, from June 2011 to November 2013, are listed in Table A.1.

SEP Date	
2011	Jun: 4, 7 Aug: 4, 8, 9, 11 Sep: 22, 23, 24 Oct: 1, 4
2012	Jan: 2, 19, 23, 26, 27 Mar: 4, 5, 7, 10, 13, 18, 21, 24, 26, 27 Apr: 15, 16 May: 17, 26 Jun: 2, 13, 23, 28 Jul: 6, 8, 9, 19, 23 Aug: 31 Sep: 20, 27 Nov: 23
2013	Feb: 6, 11 Mar: 5 May: 13, 14, 15, 17, 22 Jun: 16, 21, 25 Aug: 17 Sep: 29 Oct: 11, 28 Nov: 7

Table A.1: Solar energetic particle dates from CME catalog

Bibliography

- [1] C. Goy et al., “Lepton/proton separation, positron fraction and lepton fluxes with the ECAL vased estimator ESE. A description of the analysis tools,” Tech. Rep. AMS note 2014-11-01, LAPP, November 2014.
- [2] M. Longair, *High Energy Astrophysics*. Cambridge University Press, 2011.
- [3] Particle Data Group, “Review of particle physics,” *Phys. Rev. D*, vol. 86, p. 010001, July 2012.
- [4] F. Barao, “Cosmic rays observations near Earth,” 2013. IDPASC.
- [5] K. Yoshida, “High-energy cosmic-ray electrons in the galaxy,” *Advances in Space Research*, vol. 42, no. 3, pp. 477 – 485, 2008.
- [6] A. Panov, “Electrons and Positrons in Cosmic Rays,” *J.Phys.Conf.Ser.*, vol. 409, p. 012004, 2013.
- [7] “WMAP’s Universe.” http://map.gsfc.nasa.gov/universe/uni_matter.html. Accessed 2015-05-22.
- [8] E. Corbelli and P. Salucci, “The extended rotation curve and the dark matter halo of m33,” *Monthly Notices of the Royal Astronomical Society*, vol. 311, no. 2, pp. 441–447, 2000.

BIBLIOGRAPHY

- [9] L. Bergstrom, “Cosmology and the Dark Matter Frontier,” *Phys.Scripta*, vol. T158, p. 014014, 2013.
- [10] G. Aad *et al.*, “Search for dark matter candidates and large extra dimensions in events with a jet and missing transverse momentum with the ATLAS detector,” *JHEP*, vol. 1304, p. 075, 2013.
- [11] M. Boudaud, S. Aupetit, S. Caroff, A. Putze, G. Belanger, *et al.*, “A new look at the cosmic ray positron fraction,” *Astron.Astrophys.*, vol. 575, p. A67, 2015.
- [12] V. Poireau, “Recent results from ams,” October 2014. LHC Days in Split.
- [13] M. Potgieter, “Solar modulation of cosmic rays,” *Living Reviews in Solar Physics*, vol. 10, p. 3, june 2013.
- [14] L. J. Gleeson and W. I. Axford, “Solar modulation of galactic cosmic rays,” *Astrophysical Journal*, vol. 154, p. 1011, dec 1968.
- [15] I. G. Usoskin, G. A. Bazilevskaya, and G. A. Kovaltsov, “Solar modulation parameter for cosmic rays since 1936 reconstructed from ground-based neutron monitors and ionization chambers,” *Journal of Geophysical Research: Space Physics*, vol. 116, no. A2, 2011. A02104.
- [16] *The Evolution of Galactic Cosmic Ray Element Spectra from Solar Minimum to Solar Maximum: ACE Measurements*, 2001. International Cosmic Ray Conference 2001.
- [17] N. Weiss, “Dynamoes in planets, stars and galaxies,” *Astronomy & Geophysics*, vol. 43, no. 3, pp. 3.9–3.14, 2002.
- [18] G. Glatzmaier and P. Roberts, “A three-dimensional self-consistent computer simulation of a geomagnetic field reversal,” *Nature*, vol. 377, pp. 203 – 209, September 1995.
- [19] M. Walt, *Introduction to Geomagnetically Trapped Radiation*, vol. 10 of *Camb. Atmos. Space Sci. Ser., Vol. 10.*, Cambridge University Press, 1994.
- [20] “L shell global dipole.” http://en.wikipedia.org/wiki/Dipole_model_of_the_Earth's_magnetic_field. Licensed under CC BY-SA 3.0.
- [21] “International geomagnetic reference field.” <http://www.ngdc.noaa.gov/IAGA/vmod/igrf.html>. Accessed: 2015-03-13.

-
- [22] J. Davis, “Mathematical modeling of earth’s magnetic field,” tech. rep., Virginia Tech, Blacksburg, May 2004.
- [23] “Magnetospheres.” <http://science.nasa.gov/heliophysics/focus-areas/magnetosphere-ionosphere/>. Accessed: 2015-03-26.
- [24] D. Smart and M. Shea, “Fifty years of progress in geomagnetic cutoff rigidity determinations,” *Advances in Space Research*, vol. 44, no. 10, pp. 1107 – 1123, 2009. Cosmic Rays From Past to Present.
- [25] AMS Collaboration, “Protons in near earth orbit,” *Phys.Lett.*, vol. B472, pp. 215–226, 2000.
- [26] D. Smart and M. Shea, “A review of geomagnetic cutoff rigidities for earth-orbiting spacecraft,” *Advances in Space Research*, vol. 36, no. 10, pp. 2012 – 2020, 2005. Solar Wind-Magnetosphere-Ionosphere Dynamics and Radiation Models.
- [27] D. Smart, M. Shea, and E. Flückiger, “Magnetospheric models and trajectory computations,” *Space Science Reviews*, vol. 93, no. 1-2, pp. 305–333, 2000.
- [28] “NASA ISS tracker.” <http://spaceflight.nasa.gov/realdata/tracking/index.html>. Accessed: 2015-01-06.
- [29] C. Chung, “Ams-02 trd general,” September 2011. AMS internal courses @ CERN.
- [30] H. Ikeda et al., “A detailed test of the CsI calorimeter for BELLE with photon beams of energy between 20 MeV and 5.4 GeV,” *Nuclear Instruments and Methods in Physics Research Section A: Accelerators, Spectrometers, Detectors and Associated Equipment*, vol. 441, no. 3, pp. 401 – 426, 2000.
- [31] Z. Weng, *Particle Identification Using Transition Radiation Detector and Precision Measurement of Cosmic Ray Positron Fraction with the AMS-02 Experiment*. PhD thesis, School of Physics and Engineering SUN YAT-SEN University, May 2013.
- [32] V. Bindi et al., “The AMS-02 time of flight (TOF) system: construction and overall performances in space,” in *Proceedings of the 33rd International Cosmic Rays Conference, Rio Janeiro, Brazil*, July 2013.

BIBLIOGRAPHY

- [33] G. Ambrosi, “The ams02 tracker lecture,” October 2011. AMS internal courses @ CERN.
- [34] F. Giovacchini, “AMS-RICH Design and Construction,” 2011. AMS internal courses @ CERN.
- [35] C. Adloff et al., “The ams-02 lead-scintillating fibres electromagnetic calorimeter,” *Nuclear Instruments and Methods in Physics Research Section A: Accelerators, Spectrometers, Detectors and Associated Equipment*, vol. 714, no. 0, pp. 147 – 154, 2013.
- [36] L. Basara, *Performance of the electromagnetic calorimeter of the AMS-02 experiment on the International Space Station and measurement of the positron fraction in the 1.5-350 GeV energy range*. PhD thesis, Ecole Doctorale de Physique de Grenoble, LAPP, May 2014.
- [37] C. Goy and S. Rosier, “The AMS calorimeter performance studies with the 2007 Test Beam Data,” Tech. Rep. AMS note 2008-07-01, LAPP, July 2008.
- [38] C. Goy, “Control of the impact correction using iss electrons.” <https://indico.cern.ch/event/254089/contribution/0/material/slides/0.pdf>, May 2013. AMS ECAL Meeting.
- [39] “Crystal Ball function.” http://en.wikipedia.org/wiki/Crystal_Ball_function. Accessed: 2014-12-17.
- [40] S. Ting, “The ams experiment.”
- [41] S. Schael, “Precision measurements of the electron spectrum and the positron spectrum with ams,” in *Proceedings of the 33rd International Cosmic Rays Conference, Rio Janeiro, Brazil*, July 2013.
- [42] C. LIN, “Trigger Logic Design Specification,” Tech. Rep. AMS-JT-JLV1-LOGIC-R02c, NCU, November 2005.
- [43] A. Kounine and V. Koutsenko, “Flight Software for xDR and JINx nodes in AMS-02,” tech. rep., AMS Collaboration, February 2011.
- [44] H. Chen, “Ecal energy absolute scale,” May 2014. AMS meeting.

-
- [45] Fermi-LAT collaboration, “In-flight measurement of the absolute energy scale of the fermi large area telescope,” *Astroparticle Physics*, vol. 35, no. 6, pp. 346 – 353, 2012.
- [46] AMS Collaboration, “Electron and positron fluxes in primary cosmic rays measured with the alpha magnetic spectrometer on the international space station,” *Phys. Rev. Lett.*, vol. 113, p. 121102, September 2014.
- [47] Z. Weng and V. Vagelli, “Ams-02 measurement of cosmic ray positrons and electrons.” Proceedings of the 37 International Conference on High Energy Physics (ICHEP 2014) in Valencia, Spain, July 2014.
- [48] AMS Collaboration, “High statistics measurement of the positron fraction in primary cosmic rays of 0.5–500 gev with the alpha magnetic spectrometer on the international space station,” *Phys. Rev. Lett.*, vol. 113, p. 121101, Sep 2014.
- [49] AMS Collaboration, “Precision measurement of the ($e^+ + e^-$) flux in primary cosmic rays from 0.5 gev to 1 tev with the alpha magnetic spectrometer on the international space station,” *Phys. Rev. Lett.*, vol. 113, p. 221102, Nov 2014.
- [50] AMS Collaboration, “Electron and positron fluxes in primary cosmic rays measured with the alpha magnetic spectrometer on the international space station,” *Phys. Rev. Lett.*, vol. 113, p. 121102, Sep 2014.
- [51] M. Kuusela, “Introduction to unfolding in high energy physics.” http://mkuusela.web.cern.ch/mkuusela/ETH_workshop_July_2014/slides.pdf. Advanced Scientific Computing Workshop.
- [52] V. Blobel, “An Unfolding method for high-energy physics experiments,” pp. 258–267, 2002.
- [53] T. Adye, “Unfolding algorithms and tests using roounfold,” *ArXiv e-prints*, May 2011.
- [54] “Solar energetic particles.” http://en.wikipedia.org/wiki/Solar_energetic_particles. Accessed: 2015-02-04.
- [55] N. Gopalswamy, “SOHO LASCO CME CATALOG: A Brief Description.” http://cdaw.gsfc.nasa.gov/CME_list/catalog_description.htm, 2005. Accessed: 2015-02-04.